UNIVERSITÉ DU LUXEMBOURG

PhD-FSTM-2023-068
The Faculty of Science, Technology and Medicine

DISSERTATION

Presented on 13/07/2023 in Esch-sur-Alzette

to obtain the degree of

DOCTEUR DE L'UNIVERSITÉ DU LUXEMBOURG

EN PHYSIQUE

by

Taowen WANG
Born on 5 June 1993 in Chongzhou (China)

COMPREHENDING AND MITIGATING BACKSIDE RECOMBINATION IN CU(IN,GA)SE_2 SOLAR CELLS

Dissertation defence committee

Dr. Susanne Siebentritt, dissertation supervisor
Professor, Université du Luxembourg

Dr. Eva Unger
Professor, Humboldt University Berlin
HZB, Helmholtz-Zentrum Berlin

Dr. Phillip Dale, Chairman
Professor, Université du Luxembourg

Dr. Romain Carron
Empa, Swiss Federal Laboratories for Materials Science and Technology

Dr. Thomas Kirchartz, Vice Chairman
Professor, Forschungszentrum Jülich GmbH

Contents

List of Abbreviations

ARC	Anti-reflection coating
ALD	Atomic layer deposition
BSF	Back surface filed
BR	Backside reflector
C-V	Capacitance-Voltage
CBD	Chemical bath deposition
CVD	Chemical vapor deposition
Cu(In,Ga)Se_2-CIGSe	Copper Indium Gallium Diselenide
CGI	Cu/(Ga+In)
J-V	Current-Voltage
DSC	Differential scamming calorimeter
EDF	Electric diode factor
ETL	Electron selective transport layer
EQE	External quantum efficiency
GBG	Ga back grading
GGI	Ga/(Ga+In)
GIXRD	Grazing incidence X-ray diffraction
HTL	Hole selective transport layer
ODF	Optical diode factor
OVC	Ordered vacancy compound
PL	Photoluminescence
PVD	Physical vapor deposition
PDT	Post-deposition treatment
qFLs	Quasi-Fermi level splitting
QNR	Quasi-neutral region
SCAPS	Solar cell capacitance simulator
SCS	Solution combustion synthesis
SCR	Space charge region

SEM	Scanning electron microscopy
SQ limit	Shockley-Queisser limit
SRH	Shockley-Read-Hall
TCO	Transparent conductive oxides
TEM	Transmission electron microscopy
TRPL	Time-resolved Photoluminescence
XRD	X-ray diffraction

List of symbols

$\alpha(E)$	Absorption coefficient
$a(E)$	Absorptivity
N_A	Acceptor density
$\phi_{bb}(E)$	Black body radiation flux
k_b	Boltzmann constant
τ_{bulk}	Bulk lifetime
C	Capacitance
E_c	Conduction band
N_c	Conduction band effective density of states
ΔE_c	Conduction band offset
J_m	Current density at maximum power point
E_t	Defect energy level
N_t	Defects density
N_D	Donor density
S_b^{eff}	Effective back surface recombination velocity
k	Electric diode factor
σ_n	Electron capture cross-section
n	Electron density
τ_n	Electron lifetime
μ_e	Electron mobility
q	Element charge
E_F	Fermi level
E_{Fn}	Fermi level of electron
E_{Fp}	Fermi level of hole
FF	Fill factor
Δn	Free electron density
G	Generation flux

G'	Generation rate
σ_p	Hole capture cross-section
p	Hole density
τ_p	Hole lifetime
μ_p	Hole mobility
P_{in}	Input power
n_i	Intrinsic carrier density
E_i	Intrinsic energy level
ε	Material permittivity
P_m	Maximum output power
V_{oc}	Open-circuit voltage
A	Optical diode factor
J_{ph}	Photon current density
η	Power conversion efficiency
ΔE_F	Quasi-Fermi level splitting
$\phi(E)$	Radiation flux
τ_r	Radiative lifetime
B	Radiative recombination coefficient
ϕ_r	Radiative recombination/flux
$\hbar$	Reduced Planck's constant
J_0	Saturation current density
R_s	Series resistance
R_{SRH}	Shockley-Read-Hall recombination
J_{sc}	Short-circuit current density
R_{sh}	Shunt resistance
c	Speed of light
τ_s	Surface lifetime
R_s	Surface recombination
S_n	Surface recombination velocity of electron
S_p	Surface recombination velocity of hole

T	Temperature
v_{th}	Thermal velocity of carriers
ρ	Total charge density
E_{u}	Urbach energy
N_{v}	Valance band effective density of states
ΔE_{v}	Valance band offset
E_{v}	Valence band
V_{m}	Voltage at maximum power point

Physical Constants

k_b	Boltzmann constant	1.38×10^{-23} J·K^{-1}
q	Elementary charge	1.6×10^{-19} C
$\hbar$	Reduced Planck's constant	1.05×10^{-34} J·s
c	Speed of light	3.0×10^{8} m/s

Abstract

The aim of this thesis is to comprehend and mitigate backside recombination in $Cu(In,Ga)Se_2$ solar cells. The record $Cu(In,Ga)Se_2$ solar cell has the highest efficiency reaching up to 23.35%[1] at the time of writing this thesis. To achieve such an efficiency level, CsF post-deposition treatments are used to improve the absorber quality in the bulk and on the front surfaces. A good quality absorber and front interface is necessary to make a high efficiency solar cell. Meanwhile, the interface between the metal back contact (molybdenum) and the absorber must be passivated to avoid non-radiative recombination losses due to high backside recombination. Traditionally, this is accomplished by constructing a Ga gradient that creates a higher conduction band gradient towards the backside. Unfortunately, the Ga gradient also introduces an inhomogeneous absorber, leading to higher non-radiative and radiative losses in the solar cells, limiting further improvement in power conversion efficiency. To solve this issue, a functional hole selective transport structure is proposed in this work. One of the critical issues of using hole selective transport layers for $Cu(In,Ga)Se_2$ is that they must withstand the harsh growth condition of $Cu(In,Ga)Se_2$, e.g. high temperature and Se pressure. It means that the introduced hole selective layers should have a good thermal stability to avoid massive diffusion. In this work, we developed a thermally stable hole transport layer which shows comparable passivation effects and transport of holes to the Ga gradient, but with a homogeneous absorber. Since the Ga gradient is not required with the hole selective transport structure, the absorber thickness can be reduced to less than 1.0 μm, thereby lowering manufacturing costs and making $Cu(In,Ga)Se_2$ more cost-competitive with other solar cell technologies.

Firstly, to gain a better understanding of how backside recombination affects the quasi-Fermi level splitting or open circuit voltage of solar cells, this study investigates the traditional backside passivation strategies of Ga gradient and metal oxide dielectric layers. The results confirm that reducing backside recombination can improve quasi-Fermi level splitting by at least 40 meV, even with a short minority carrier lifetime of only dozens of nanoseconds. These findings are supported by SCAPS simulations, which also demonstrate similar results.

Secondly, after gaining an understanding of the quasi-Fermi level splitting losses caused by backside recombination, this study investigates several candidate hole selective transport layers,

which are supposed to mitigate the backside recombination and transport holes simultaneously. Some single layers prove to be thermally unstable due to the harsh growth conditions of $Cu(In,Ga)Se_2$, which causes a negative impact on quasi Fermi-level splitting or open-circuit voltage on solar cells. Others show good thermal stability but provide negligible passivation. To address this issue, the study proposes a combination of a hole transport layer with a metal oxide stabilizer, $CuGaSe_2/In_2O_3$, which significantly improves thermal stability and provides a good passivation effect that enhances quasi-Fermi level splitting by approximately 80 meV. Beside the good passivation effect, we found that the hole transport properties depend on the excess Cu of the hole selective transport layer. The Cu annealing of $CuGaSe_2/In_2O_3$ can remove the current blocking effects, which improves the FF from ~40% to ~77%.

Thirdly, backside recombination can also impact the optical diode factor, and thus fill factor of solar cells. The optical diode factor (ODF) discussed in this thesis is based on injection level dependent metastable defects that transition from donors to acceptor, which additionally shifts down the Fermi level of the holes, thus leading to a higher ODF. Both experiments and simulation found that the higher backside recombination and doping density can lower the optical diode factor. In general, a lower optical diode factor is desired to achieve a higher fill factor. However, it has been found that a lower optical diode factor resulting from higher backside recombination is unfavorable due to significant losses in quasi-Fermi level splitting. Conversely, improving the doping density has been found to be preferable, as it enhances quasi-Fermi level splitting while simultaneously lowering the optical diode factor.

This thesis presents a thorough investigation of the impact of backside recombination on the quasi-Fermi level splitting of $Cu(In,Ga)Se_2$ solar cells. Using this understanding, a novel hole selective transport structure is proposed that enables the construction of a high-efficiency solar cell with a homogeneous absorber, making a significant shift in the paradigm of $Cu(In,Ga)Se_2$ solar cells. With this shift, the non-radiative and radiative loss of solar cells due to inhomogeneity, e.g. Ga profile, can be removed. Additionally, the results presented in this thesis shed light on the relationship between the optical diode factor, backside recombination, and doping level, providing a direction for further optimization of $Cu(In,Ga)Se_2$ solar cells to achieve even higher power conversion efficiency.

Chapter 1 INTRODUCTION: Why solar cells and What boundary have we pushed?

There are various reasons why someone may choose to pursue a Ph.D., and these motivations are often shaped by an individual's unique personality and interests. For me, the driving force behind my decision to embark on this journey is my insatiable curiosity and passion for research. It is this deep-seated desire to explore and uncover new knowledge that fuels my focus and dedication to this project and the writing of this thesis.

But why did I choose the topic about renewable energy, particularly solar cells that directly convert solar power into electricity? The answer is simply because photovoltaic power (PV) technology offers a low-carbon emission solution, promoting carbon neutralization and offering a viable pathway towards resolving the urgent environmental challenges we are facing. The responsibility to address the climate crisis falls on everyone, especially those who are well-educated and living in favorable conditions. Human activities, characterized by the massive emission of carbon-based greenhouse gases (GHGs) into the atmosphere, are the primary drivers of the climate crisis. These emissions contribute to the rise in global mean temperature, resulting in extreme weather events such as floods, droughts, hurricanes, wildfires, and more. Extensive research and statistical data consistently demonstrate the strong correlation between global warming and the concentration of CO_2 in the atmosphere [2-4]. Despite the international commitment through agreements like the Paris Agreement, aimed at reducing GHGs emissions and limiting the global mean temperature increase to below 2°C compared to pre-industrial levels, the reality remains concerning. Reports from the Intergovernmental Panel on Climate Change (IPCC) indicate that the global mean temperature continues to rise, and it is highly likely that the warming will exceed 1.5°C during the 21st century, making it challenging to stay below the 2°C target. This discrepancy between projected emissions based on implemented policies and the nationally determined contributions (NDCs) results in the existing gap[5].

The reality of climate change extends far beyond words on paper; it is a tangible presence in our daily lives. In 2022, China, the EU, and the US experienced a series of droughts, leading to the drying up of vital rivers and lakes[6]. Additionally, devastating wildfires, fiercer and faster than ever before, have become more frequent worldwide, resulting in deforestation and increased

carbon emissions[7]. Closer to where I am currently living, Luxembourg faced its worst flooding in history in 2021[8]. These events are not isolated incidents; rather, they are clear indications of the rising global mean temperature and the catastrophic consequences of climate change. It is imperative that we move beyond mere slogans and take immediate action.

As an individual, I recognize that I cannot directly influence current policy implementation. However, I have chosen to contribute to the fight against climate change by studying $Cu(In,Ga)Se_2$ solar cells with the aim of achieving higher efficiency. Improving the efficiency of solar cells reduces the cost of production and installation of solar modules, thereby accelerating the adoption of PV applications. Among the various PV technologies available, thin-film-based technologies like $Cu(In,Ga)Se_2$ have the lowest carbon footprint[9]. Furthermore, these solar cells represent the cutting-edge of technology and have proven to be stable for long-term use in large-scale power stations, boasting a record efficiency of 23.35%[1]. To achieve such high efficiency, it is essential to introduce a Ga lateral gradient in the absorber layer to minimize unwanted backside recombination. However, the presence of composition inhomogeneity resulting from the Ga gradient introduces higher non-radiative and radiative losses, which limit further improvements in solar cell efficiency. To address this challenge, the $Cu(In,Ga)Se_2$ research community is advocating for a paradigm shift. They propose combining a homogeneous absorber layer with a hole selective transport layer to passivate the backside[10, 11]. However, constructing such a structure poses difficulties due to the harsh growth conditions of $Cu(In,Ga)Se_2$, which can potentially damage the underlying hole transport layers.

Addressing this issue leads to the initial propose and motivation of this thesis. But it is not a straightforward work that can be done at once. To essentially achieve this goal, the different scenarios at each phase of this project are conducted to understand the influence of the backside recombination on performance of solar cells and finally come up with a structure to mitigate the backside recombination. The results of these investigations are discussed in this thesis within different chapters, which is briefly summarized as bellow:

Chapter 4: First of all, to have an impression about how much the backside recombination can influence the quasi-Fermi level splitting of the $Cu(In,Ga)Se_2$. Chapter 4 involves the typical strategies such as Ga back grading and metal oxides dielectric layers to mitigate the backside recombination. The results suggest that both strategies can improve the quasi-Fermi level splitting

of ~50 meV even with a short lifetime of ~13 ns and a thick film of ~1.5 μm. Moreover, the specific backside recombination of different samples is quantified by implementation of SCAPS simulation, which suggests that the backside recombination can be as low as ~10^3 cm/s by using Ga back grading or Al_2O_3. Meanwhile, the SCAPS simulation results also confirm the similar improvement in quasi-Fermi level splitting by reducing the backside recombination. And the higher quasi-Fermi level splitting improvement of ~100 meV can be realized by further reducing the front recombination and improving the minority carrier lifetime.

Chapter 5: The achievable improvement in quasi-Fermi level splitting by reducing the backside recombination is clear, but it requires a good passivation. In this chapter, the different potential candidates to work as a hole selective transport layer are investigated. Some single layers like NiO_x, $CuCrO_x$ and CuO_x show an low thermal instability that can not withstand the harsh growth condition of $Cu(In,Ga)Se_2$, leading to a interaction with the absorber. Consequently, on the one hand, the diffusion of Ni and Cr, which are unwanted impurities for $Cu(In,Ga)Se_2$, completely degrades the quality of the absorber. On the other hand, the diffusion of hole selective transport layers underneath also destroys their selectivity, meaning no obvious passivation effects can be observed. Other layer such as GaO_x shows a good thermal stability but without clear passivation effects.

To address the issue of thermal stability and passivation, a novel structure of hole selective transport layer covered with a metal oxide stabilizer is proposed. For the combination of $CuGaSe_2$ or CuO_x/GaO_x, it seems that GaO_x prepared by solution combustion synthesis lacks the ability of stabilizing the layers underneath. Meanwhile, it may not have good enough electronic properties that are required for a functional HTL. As a result, no passivation effects are observed but rather causing higher non-radiative recombination loss. For $CuGaSe_2/In_2O_3$, the two individual layers can be clearly identified after the absorber growth. But because of the element exchange between Ga and In, it is very likely that these two layers end up with $CuInSe_2/GaO_x$. With this element exchange, the layers at the backside show an impressive passivation effect, which most likely attributes to the high conduction band spike between GaO_x and absorber. This spike reduces the minority carrier concentration at the backside, which consequently reduces backside recombination that is proportional to minority carrier concentration. Compared to reference sample without passivation, the quasi-Fermi level splitting is improved by ~80 meV in both $CuInSe_2$ and

submicron $Cu(In,Ga)Se_2$. Moreover, a good hole selective transport layer is more than the passivation since the good hole transport property is also essential to maintain a high fill factor of solar cells. It is found out that the transport ability is highly related to excess Cu in this dual layer. The excess Cu likely modifies the electric properties of the oxides, which allows the hole transporting through and thus ensuring a good fill factor of $Cu(In,Ga)Se_2$ solar cells up to 77%. Inversely, lack of Cu results in poor hole transport, leading to low current density and fill factor.

Chapter 6: The influence of backside recombination and its mitigation have been figured out in previous chapters. But on other hand, the backside recombination can also influence the fill factor by dominating the optical diode factor since the lower diode factor leads to a higher fill factor. In this chapter, the theory of optical diode factor based on the metastable defects transition is explained. Based on which, the influence of backside recombination and doping density on the optical diode factor is investigated. The presented results suggest that both high backside recombination and doping density can lead to a lower optical diode factor. However, the low diode factor due to the high backside recombination is unfavorable because it causes massive losses in quasi-Fermi level splitting at the same time. The low diode factor due to the high doping density is preferable because it improves the quasi-Fermi level splitting. These discoveries are important because it points out the further optimization of our solar cells should focus on reducing backside recombination and improving the doping density.

Chapter 7: This chapter is about efficiency loss analysis of our best submicron solar cell. To further improve efficiency of solar cells, it is important to figure out where do our solar cells loss the efficiency. For V_{oc} loss analysis, the analysis model based on detailed balance shows V_{oc} loss due to non-radiative recombination is about 220 mV, which dominates the V_{oc} loss. With further optimization of absorber and front surface, we predict a reduction in V_{oc} loss of 100 mV, leading to a V_{oc} of 753 mV (E_g^{EQE} =1.15 eV). In terms of FF, the influence of V_{oc} and diode factor on FF is simulated based on a one-diode model. With V_{oc} of 753 mV and diode factor of 1.1, the simulation suggests that FF can be improved to 81%. In addition, according to our EQE simulations by SCAPS, it suggests that the J_{sc} can be potentially improved by adding anti-reflection coating (ARC) and using Zn(O,S) buffer. The ARC and Zn(O,S) contributes to a J_{sc} gain of 2.1 mA/cm^2 and 1.4 mA/cm^2, respectively. With implementing both optimizations, the predicted

J_{sc} is 36.7 mA/cm^2. Ideally, if all of these parameters can be further optimized, we predict an efficiency of 22.4% for a sub-micron Cu(In,Ga)Se_2 solar cell.

Chapter 2 Basic knowledge

The purpose of this thesis is to understand and mitigate the backside recombination in chalcopyrite [$Cu(In,Ga)Se_2$] solar cells. To provide a comprehensive understanding of the topic, **section 2.1** discusses the fundamental working principles of solar cells. **Section 2.2** focuses on the absorber layer and the typical structure of devices, which covers its properties and growth methods. As this work involves multiple characterization techniques, **section 2.3** explains the setups and measuring conditions. Because the photoluminescence (PL) is widely employed in this work to characterize our samples. Specific details regarding PL are discussed in this section. Since diode factor presented in this thesis is an important indicator to show the dominant recombination and also has an impact on the fill factor of solar cells, **Section 2.4** explains the model of high diode factor based on metastable defects transition. Meanwhile, backside recombination velocity and doping density of the solar cells will be widely discussed in this thesis, **Section 2.5** shows the model involved in this thesis to estimate backside recombination velocity and doping density.

2.1 Basics of solar cells

Solar cells are semiconductor devices capable of converting solar energy into electricity. The absorber layer, a semiconductor material, plays a crucial role in the process of energy conversion. It absorbs photons, which generate electron-hole pairs as a function of absorber depth. However, the generation of electron-hole pairs alone is insufficient to generate current and power. The electrons and holes must be separated and collected at two contacts assisted by an asymmetry of chemical potential, band structure or conductivity, typically a p-n junction or carrier selective transport structure. Unfortunately, no ideal energy converter exists, including solar cells, which suffer from energy losses[12]. These losses lead to the Shockley-Queisser (SQ) limit[13] on the maximum efficiency of solar cells. Despite this limit, solar cells tend to lose even more efficiency due to additional radiative and non-radiative recombination processes. Compared to the radiative loss, non-radiative loss is more pronounced because its high recombination rate, which is usually assisted by defects in bulk and at interface. In this work, a significant achievement is the reduction

of non-radiative recombination at the backside of the $Cu(In,Ga)Se_2$ solar cell by employing a hole selective transport layer (HTL).

2.1.1 Absorption and Generation

The initial step in generating current or power from solar cells involves the absorption of photons, which creates free electron/hole pairs that can be separated and collected[14-16]. Ideally, all photons from the sun would be absorbed, and their energy would be converted to electricity. However, in reality, a small percentage of incident photons reflects off the absorber's surface, while the remaining photons interacts with the absorber, where not all are absorbed, and their energy is not fully converted. Only photons with energy higher than the absorber's bandgap can be absorbed, and the energy equal to the absorber's bandgap can be utilized. As depicted in **Figure 2.1 (a)**, the standard AM1.5G spectrum[17], with an integrated power of 1000 $W \cdot m^{-2}$, is used to assess the efficiency of terrestrial solar cells. The sun's photon energy ranges from approximately 0 eV to 4 eV. The absorber interacts with the incident photons in three different ways, depending on the photons' energy compared to the absorber's bandgap.

I. When the energy of photons (E_{photon}) is equal to the bandgap energy (E_g), the photons can excite electrons from the maximum of the valence band to the minimum of the conduction band, generating electron/hole pairs. Since there is no excess energy over the bandgap energy, all the energy of the photons can be utilized without thermalization losses.

II. When E_{photon} is greater than E_g, the photons are strongly absorbed and generate electrons with energy higher than the conduction band minimum or holes below the valance band maximum. However, the excess energy over the bandgap energy is wasted, as the electrons or holes quickly thermalize back to the near conduction band minimum or valance band maximum.

III. When E_{photon} is less than E_g, the photons with energy lower than the bandgap energy cannot be absorbed. They transmit through the absorber and are either reflected back into the absorber or absorbed by the metal contacts, such as molybdenum for $Cu(In,Ga)Se_2$ solar cells.

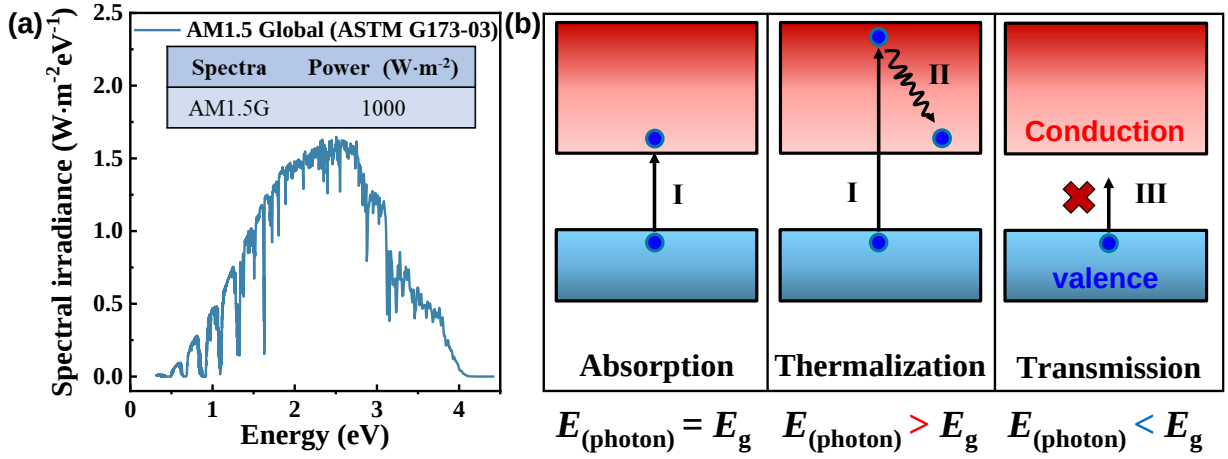

Figure 2.1(a) AM1.5G sun spectra with an integrated power intensity of 1000 W·cm^{-2}, which is the standard sun spectra for the terrestrial solar cells to quantify efficiency; (b) The absorption of incoming photons: I. when $E_{photon} = E_g$, the photons have just enough energy to be absorbed and generate electron/hole pairs without losing energy. II. when $E_{photon} > E_g$, the photons have high enough energy to excite the electrons going beyond the bandgap energy. The excess energy beyond bandgap energy is lost by thermalization. III. when $E_{photon} < E_g$, the photons do not have enough energy to excite electron/hole pairs.

The absorption of photons in a solar cell leads to the generation of free electrons and holes, which can be categorized as minority or majority carriers in a doped absorber. For most solar cells, including Cu(In,Ga)Se_2, the photon-generated minority carrier density (10^{13}~10^{14} cm^{-3}) is significantly lower than the doping density (10^{15}~10^{16} cm^{-3}) under illumination at AM1.5G (one-Sun intensity), which implies that the solar cells operate under low injection conditions. The photon-generated majority carriers have a negligible effect on the majority carrier density due to doping, whereas the minority carrier density is primarily influenced by the photon-generated minority carriers. It is critical background knowledge for us to subsequently understand and discuss the diode factor in **Chapter 6**.

As discussed above, the absorption of photons in a semiconductor material depends on the energy of the photons and the properties of the absorber. Photons with energy greater than the bandgap energy can be absorbed by the absorber, with the strength of absorption increasing as the energy of the photons increases. The absorption coefficient (α) is a measure of the ability of the semiconductor to absorb photons and describes how far the photons can penetrate the absorber

before being absorbed. For $CuInSe_2$ (as shown in **Figure 2.2** [18]), the absorption coefficient exhibits a rapid increase as the photon energy approaching the bandgap energy. However, even for photons with energy higher than the bandgap, a certain thickness of absorber is required to efficiently absorb the photons. For example, for a photon with energy of 1.1 eV (where E_g = 1.0 eV), a film thickness of ~0.33 μm is necessary for absorption (around 63% photons are absorbed, 1-1/e). In this work, the absorber thickness studied is above 0.8 μm, which is thick enough to absorb all high-energy photons and supports the assumption of absorptivity $a(E)$=1. This assumption is important for calculating ΔE_F by fitting the high-energy wing of absolute PL spectra, which will be discussed in detail in **Section 2.3.2**. However, for photons with low energy that is almost equal to the bandgap, an absorber thickness of ~1.7 μm is needed for effective absorption.

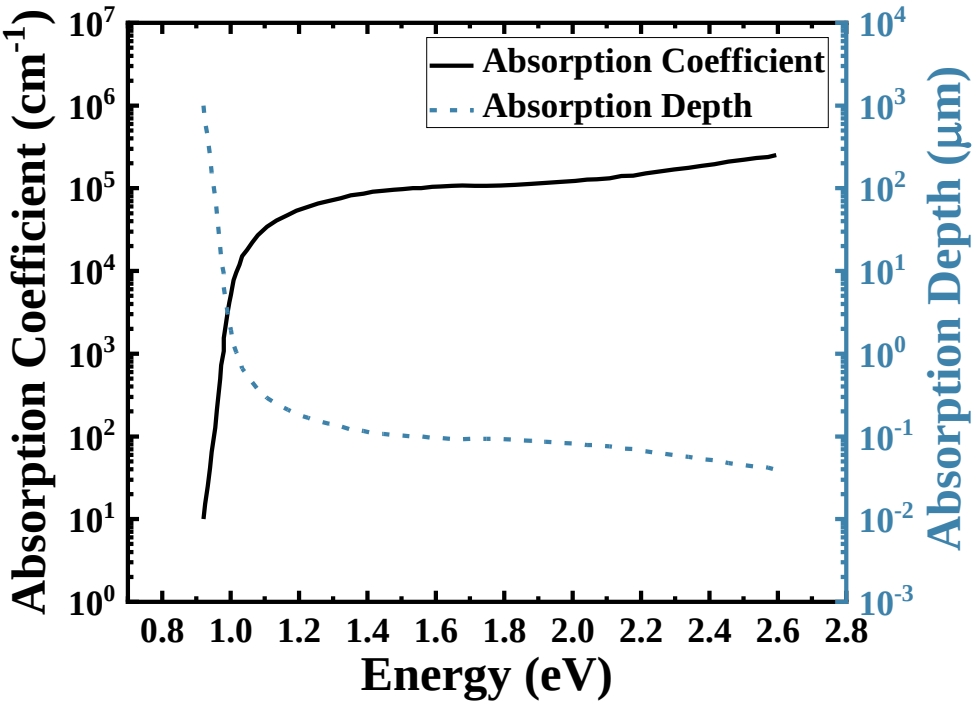

Figure 2.2 The absorption coefficient and absorption depth of photon with different energy for polycrystalline $CuInSe_2$. The absorption depth is the inverse of the absorption coefficient. With this thickness around 63% of photons will be absorbed. This Figure is reproduced from Ref. [18]

2.1.2 p-n junction: photon generated carrier separation

In solar cells, efficient separation and collection of the free electron/hole pairs generated upon photon absorption are crucial for generating useful power. To extract these carriers, an asymmetry in chemical potential for electrons and holes is essential to provide a driving force. Several approaches can be used to create this chemical potential, including p-n junctions and carrier selective transport contacts[19-22].For Cu(In,Ga)Se_2 solar cells, p-n junction is the most commonly used and analyzed structure for building efficient solar cells. In recent years, a new approach based on hole selective transport has been called for shifting the paradigm of Cu(In,Ga)Se_2, aiming to improve the efficiency of chalcopyrite solar cells[10, 11], which will be discussed in **Chapter 5**.

The built-in potential of a p-n junction is established under thermal equilibrium conditions, but in the absence of illumination, the net current of the junction is zero. Consequently, solar cells cannot generate power in the dark because there is no electrochemical potential or fermi-level gradient to drive the flow of current. To induce the flow of current, illumination is required to create free carriers that will be separated by a p-n junction and then collected at the two contacts. A simulated band energy diagram of the $CuInSe_2$ under illumination ant at maximum power point is shown in **Figure 2.3**. The excitation of free carriers by illumination splits the quasi-Fermi level of electrons (E_{Fn}) and holes (E_{Fp}), creating a quasi-Fermi level splitting (qFLs or ΔE_F) equal to the difference between E_{Fn} and E_{Fp}, $\Delta E_F = E_{Fn} - E_{Fp}$. The ΔE_F sets the upper limit of the open-circuit voltage (qV_{oc}) that can be achieved in the finished solar cells and is an important indicator of its performance before device fabrication. It is widely used in this work to quantify the quantity of the absorbers and predict the performance of solar cells. The ΔE_F can be determined by absolute PL, as discussed in **Section 2.3.2**. To determine the maximum power output and efficiency of a solar cell under specific illumination conditions, it is necessary to determine the current density (J) as a function of generated or applied voltage (V). This requires solving three equations:

I. The **Poisson's Equation** that shows the relation between the electric field and charges:

$$\frac{\mathrm{d}^2V(x)}{\mathrm{d}x^2} = \frac{\rho}{\varepsilon} = -\frac{q}{\varepsilon}\left(N_D^+(x) + p(x) - N_A^-(x) - n(x)\right) \qquad \textbf{2.1}$$

II. The **Transport Equation** that describes the movement of the carriers. It shows that the flowing current is driven by the Fermi level gradient:

$$\begin{cases} J_{\mathrm{n}} = \mathrm{q}\mu_{\mathrm{n}} n \dfrac{\mathrm{d}E_{\mathrm{Fn}}}{\mathrm{d}x} \xrightarrow{n=N_{\mathrm{c}}\exp\left(\frac{E_{\mathrm{Fn}}-E_{\mathrm{c}}}{\mathrm{k_b}T}\right)} \mathrm{q}\mu_{\mathrm{n}} n \dfrac{\mathrm{d}E_{\mathrm{c}}}{\mathrm{d}x} + \mathrm{q}D_{\mathrm{n}} \dfrac{\mathrm{d}n(x)}{\mathrm{d}x} \\ J_{\mathrm{p}} = \mathrm{q}\mu_{\mathrm{p}} p \dfrac{\mathrm{d}E_{\mathrm{Fp}}}{\mathrm{d}x} \xrightarrow{p=N_{\mathrm{v}}\exp\left(\frac{E_{\mathrm{v}}-E_{\mathrm{Fp}}}{\mathrm{k_b}T}\right)} \mathrm{q}\mu_{\mathrm{p}} p \dfrac{\mathrm{d}E_{\mathrm{v}}}{\mathrm{d}x} + \mathrm{q}D_{\mathrm{p}} \dfrac{\mathrm{d}p(x)}{\mathrm{d}x} \\ J_{\mathrm{total}} = J_{\mathrm{n}} + J_{\mathrm{p}} \end{cases} \quad \textbf{2.2}$$

In which, the $J_{\mathrm{n(p)}}$ is the current density of electrons (holes), $\mu_{\mathrm{n(p)}}$ is the mobility of electrons (holes) and $D_{\mathrm{n(p)}}$ is the diffusivity of electrons (holes). The first term is the drift current, and the second term is the diffusion current. The drift term contains contribution from both electric field in space charge region (SCR) and band gradients, e.g. the conduction band gradients for Cu(In,Ga)Se_2 solar cells as shown in **Figure 2.9 (a)**.

III. The **Continuity Equation** that tracks the changes of carrier density by considering the current flow, generation rate (G') and recombination rate (R) in the solar cells:

$$\begin{cases} \dfrac{\mathrm{d}n(x)}{\mathrm{d}t} = \dfrac{\mathrm{d}J_{\mathrm{n}}}{\mathrm{d}x} + G' - R = 0 \\ \dfrac{\mathrm{d}p(x)}{\mathrm{d}t} = -\dfrac{\mathrm{d}J_{\mathrm{p}}}{\mathrm{d}x} + G' - R = 0 \end{cases} \quad \textbf{2.3}$$

With some boundary conditions and rigorous derivation that can be found in Ref. [16, 23], the classical Shockley Equation that shows the current density is proportional to applied voltage. Assuming the photon generated current density (J_{ph}) is independent of the applied voltage, the total current ($J(V)$) of solar cell follows the superposition of diode current and photon generated current. It is notable that the assumption of voltage independence of J_{ph} may be incorrect for Cu(In,Ga)Se_2 solar cells due to voltage dependent carrier collection[23]. Without considering the effect of parasitic resistance, the *J-V* behavior of a solar cell under illumination can be described by:

$$J(V) = \mathrm{J_0}\left[\exp\left(\frac{\mathrm{q}V}{\mathrm{k}\mathrm{k_b}T}\right) - 1\right] - J_{\mathrm{sc}} \quad \textbf{2.4}$$

Where the J_0 is the saturation current density that depends on material properties and the recombination in solar cells, J_{sc} is the short circuit current density that equals to J_{ph}, and k is the electric diode factor (EDF). The EDF is equivalent to optical diode factor (ODF) in case no additional recombination is introduced in finished devices, which is discussed in **Section 2.4**. The diode factor has a strong impact on FF, thus the efficiency of solar cells. The further discussion of its impact is shown in **Chapter 7**.

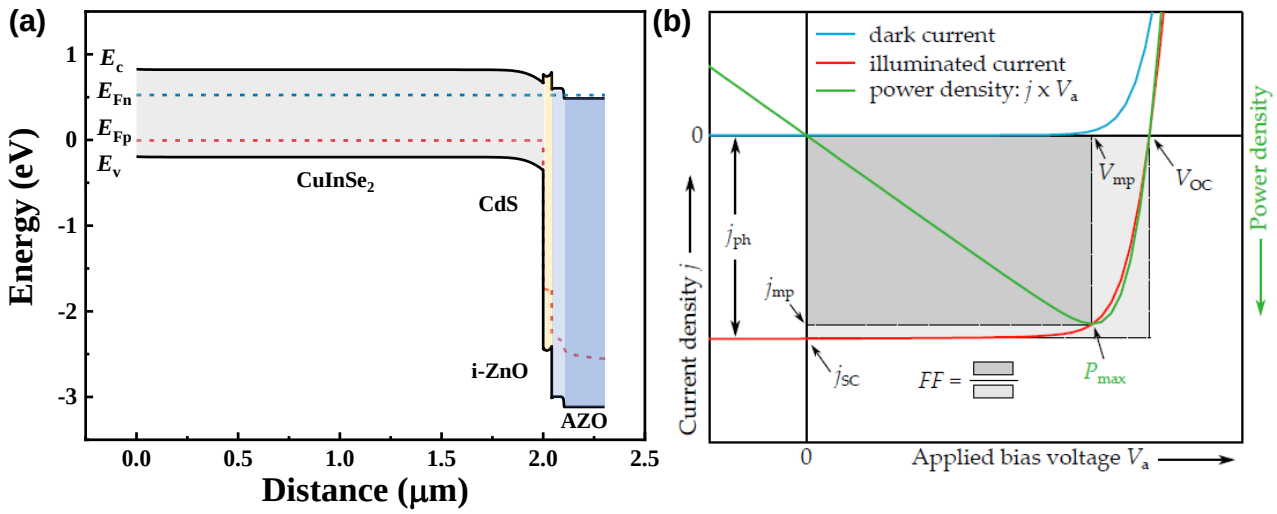

Figure 2.3 (a) The simulated band energy diagram of the $CuInSe_2$ solar cell under illumination ant at the maximum power point. The excited free carriers result in splitting of the Fermi levels of electrons (E_{Fn}) and holes (E_{Fp}); (b) The typical current density (J) – applied bias voltage (V) curve of a solar cell under illumination.

The *J-V* curve of a solar cell, as described by **Equation 2.4**, exhibits an exponential relationship between current density and applied voltage, as shown by the red curve in **Figure 2.3 (b)**. Under short circuit conditions, the solar cell operates at zero voltage, producing the maximum current density, or short circuit current density (J_{sc}). Conversely, under open circuit conditions, the solar cell operates at zero current density, producing the maximum voltage, or open circuit voltage (V_{oc}). However, neither condition generates any output power because power is the product of current density and voltage. To determine the maximum output power, the power curve of the solar cell is plotted using the equation $P = J(V)\times V$, as shown by the green curve in **Figure 2.3 (b)**. By calculating the maximum output power (P_{max}), it is possible to determine the efficiency of the solar cell using a simple equation:

$$\eta = \frac{P_{max}}{P_{in}} = \frac{J_{max}V_{max}}{P_{in}} = \frac{FF \cdot J_{sc}V_{oc}}{P_{in}} \qquad \textbf{2.5}$$

Where the P_{in} is the incident power of the sun, the J_{max}/V_{max} is the current density/voltage at the maximum power point and the FF is the fill factor. FF is the geometric factor of the *J-V* curve, which is an important parameter to determine the efficiency of the solar cells.

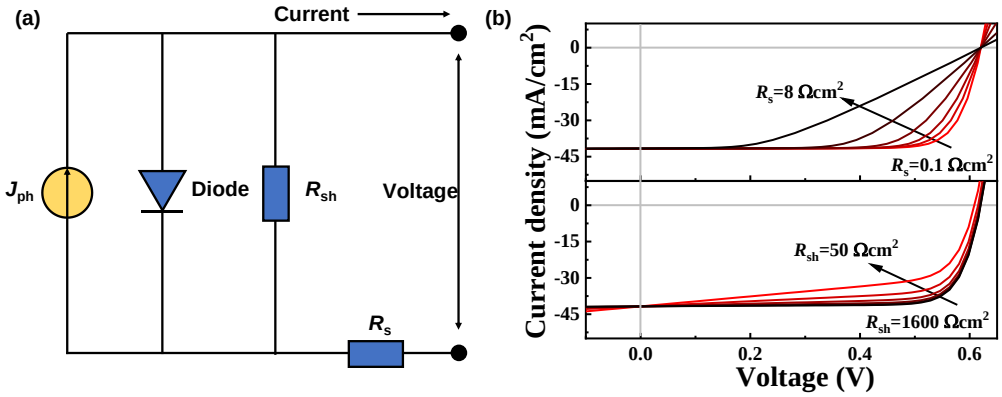

Figure 2.4 (a) The equivalent circuit of the working solar cell with the influence of shunt resistance and series resistance; (b) The example of the influence of shunt resistance or series resistance on FF. When discussing the influence of one parameter, either R_s or R_{sh}, the influence of the other is screened. These results are simulated by SCAPS.

In discussing the *J-V* curve of solar cells, the influence of parasitic resistance, such as shunt resistance (R_{sh}) and series resistance (R_s), is overlooked before. However, in realistic solar cells, parasitic resistance is a widespread issue that can significantly reduce the FF of solar cells, especially when R_s and R_{sh} do not have good enough values. **Figure 2.4 (a)** shows the equivalent circuit of a working solar cell with the influence of R_s and R_{sh}. To account for the impact of parasitic resistance on the *J-V* curve of solar cells, **Equation 2.4** can be generalized as:

$$J(V) = J_0\left\{\exp\left[\frac{q(V + J(V)R_s)}{kk_bT}\right] - 1\right\} + \frac{V + J(V)R_s}{R_{sh}} - J_{sc} \qquad \textbf{2.6}$$

The short-circuit path for current in R_{sh} results in reduced current flowing through the load at the same voltage, while the barrier for voltage in R_s shares the voltage from the load at the same current density, both causing a loss of FF, as depicted in **Figure 2.4 (b)**. The results are from SCAPS simulation. Typically, a good solar cell has R_s values lower than 0.5 Ω·cm² and R_{sh} values higher than 1000 Ω·cm².

2.1.3 Recombination

As discussed earlier, solar cells operate under steady state, meaning that the excited electrons in the conduction band are metastable. To stabilize the system, these electrons return to the valence

band and recombine with holes, either by interacting with photons or phonons. Recombination is the inverse process to generation and occurs in both the bulk and surface of the absorber. There are two primary recombination mechanisms that occur in the bulk for Cu(In,Ga)Se_2 solar cells:

1. Radiative recombination by releasing photons.

2. Shockley-Read-Hall (SRH) recombination via defects.

Beside the recombination taking place in the bulk, the surface recombination is a defects-assisted recombination, which is the main issue discussed and solved in this thesis for the Cu(In,Ga)Se_2 solar cells by using a carrier selective transport structure.

Bulk Recombination

For solar cells made with direct band semiconductors, such as Cu(In,Ga)Se_2, the dominant recombination mechanisms are radiative and Shockley-Read-Hall recombination. Auger recombination is only considerable when the solar cells are working under high injection conditions, where the carrier concentration is high enough to make Auger recombination comparable to radiative and SRH recombination. Radiative recombination occurs due to the band-to-band transition between carriers and is a reciprocal process of absorption. The rate of radiative recombination rate (R_r) is given by the following equation[16]:

$$R_r = B(np - n_i^2) \quad \textbf{2.7}$$

Where B is radiative recombination coefficient. If the semiconductor is p-type with $p_0 \approx p >> n_0$, in the low injection condition ($n_0 << n << p_0$), the **Equation 2.7** can be simplified as:

$$R_r \approx \frac{\Delta n}{\tau_r} \quad \textbf{2.8}$$

where τ_r is the radiative lifetime:

$$\tau_r = \frac{1}{Bp_0} \quad \textbf{2.9}$$

The similar relation can be gained for the n-type semiconductor. The Radiative recombination from a semiconductor can also be described by the Planck's Generalized Law[14, 24], which will be discussed later in **Section 2.3.2**.

SRH recombination is a defects-assisted non-radiative recombination, which is one of the most import efficiency loss paths for Cu(In,Ga)Se_2 solar cells. Another important recombination path is surface recombination that will be discussed later. The SRH recombination (R_{SRH}) rate is given by [16]:

$$R_{\mathrm{SRH}} = \frac{np - n_{\mathrm{i}}^2}{\tau_{\mathrm{n}}\left[p - n_{\mathrm{i}}\exp\left(\frac{E_{\mathrm{i}} - E_{\mathrm{t}}}{k_{\mathrm{b}}T}\right)\right] + \tau_{\mathrm{p}}\left[n - n_{\mathrm{i}}\exp\left(\frac{E_{\mathrm{t}} - E_{\mathrm{i}}}{k_{\mathrm{b}}T}\right)\right]} \qquad \textbf{2.10}$$

Where E_i and E_t is the intrinsic Fermi level and defect energy level, τ_n and τ_p is electron and hole lifetime, respectively. The recombination rate via Shockley-Read-Hall mechanism is influenced by the E_t, as well as the τ_n and τ_p. When E_t is located deeper inside the bandgap and closer to E_i, R_{SRH} increases. This is because when E_t is shallow, captured carriers are readily released back to the conduction or valence band through thermal activation. Only with deep defects, the capturing time is long enough for recombination. Additionally, R_{SRH} depends on carrier lifetime; longer carrier lifetime leads to lower R_{SRH}. For p-type semiconductors with $p_0 \approx p >> n_0$, under low injection conditions ($n_0 << n << p_0$), and with E_t near E_i ($E_t \approx E_i$), **Equation 2.10** can be simplified to:

$$R_{\mathrm{SRH}} = \frac{\Delta n}{\tau_{\mathrm{n}}} \qquad \textbf{2.11}$$

Where the τ_n is:

$$\tau_{\mathrm{n}} = \frac{1}{\sigma_{\mathrm{n}} v_{\mathrm{th}} N_{\mathrm{t}}} \qquad \textbf{2.12}$$

And σ_n is the electron capture cross-section of the corresponding defect, N_t is the defects concentration and v_{th} is the thermal velocity of the electrons. The efficiency of a solar cell is greatly affected by the rate of SRH recombination, which is inversely proportional to the minority carrier lifetime. When non-radiative recombination increases, the minority carrier lifetime becomes short and results in higher efficiency deficits. This short lifetime is typically caused by abundant defects or large carrier capture cross-sections of the defects. To increase the efficiency of solar cells, it is necessary to grow high-quality absorbers with as few recombinant defects as possible. This will ensure a long enough minority carrier lifetime, comparable to the radiative lifetime, and minimize non-radiative recombination[11, 25, 26].

Surface Recombination

The surface of a semiconductor is a region where the periodic crystal structure is disrupted, creating an interface that is prone to contamination from the environment or adjacent layers. The disruption of the crystal lattice generates discontinuity, which act as recombination centers. The high surface recombination depletes minority carriers at the surface, which in turn causes an influx of minority carriers from the bulk to diffuse towards the surface. This diffusion can result in a concentration gradient of minority carriers near the surface, which reduces minority carrier concentration and leads to a decrease in the ΔE_F of the solar cells. For p-type semiconductors in low injection condition, the surface recombination rate (R_s) can be simplified as follows[16]:

$$R_s \approx S_n \Delta n \qquad \textbf{2.13}$$

Where S_n is surface recombination velocity of electrons. The surface recombination velocity of electrons is a measure of the rate at which electron-hole pairs recombine at the surface of a material. Compared to bulk recombination that represents recombination rate per unit volume, the surface recombination represents the recombination rate per unit area. In this research, the main objectives are to study the impact of backside recombination on the performance of $Cu(In,Ga)Se_2$ solar cells and to develop strategies for mitigating this negative effect by using an HTL structure. Achieving a surface recombination velocity below 10^2 cm/s is critical for producing high-efficiency solar cells[11, 25, 27]. These topics will be discussed in more detail in the following chapters.

2.1.4 The influence of recombination on V_{oc} (ΔE_F)

The non-radiative recombination assisted by the defects is the main loss path of solar cells compared to the radiative recombination. In a p-type semiconductor and in low injection condition, non-radiative recombination taking place in the bulk directly cases the carriers recombining in the bulk and lowering the bulk lifetime of minority carriers. For surface recombination, it shows an obvious impact when the bulk lifetime is long enough to guarantee a long diffusion length (L_n) of electrons that is comparable to the absorber thickness. The diffusion length of electrons can be determined by[15]:

$$L_n = \sqrt{D_n \tau_n^b} \qquad \textbf{2.14}$$

With both recombination taking place in the bulk and at the surface, the total recombination rate of the solar cell is:

$$R_{\mathrm{n}}^{\mathrm{e}} = R_{\mathrm{n}}^{\mathrm{b}} + R_{\mathrm{n}}^{\mathrm{s}} = \frac{\Delta n}{\tau_{\mathrm{n}}^{\mathrm{e}}} = \frac{\Delta n}{\tau_{\mathrm{n}}^{\mathrm{b}}} + \frac{\Delta n}{\tau_{\mathrm{n}}^{\mathrm{s}}} \qquad \textbf{2.15}$$

According to **Equation 2.15**, the effective lifetime of electrons is determined by:

$$\frac{1}{\tau_{\mathrm{n}}^{\mathrm{e}}} = \frac{1}{\tau_{\mathrm{n}}^{\mathrm{b}}} + \frac{1}{\tau_{\mathrm{n}}^{\mathrm{s}}} \qquad \textbf{2.16}$$

In which, $\tau_{\mathrm{n}}^{\mathrm{e}}$, $\tau_{\mathrm{n}}^{\mathrm{b}}$ and $\tau_{\mathrm{n}}^{\mathrm{s}}$ is effective lifetime, bulk lifetime and surface lifetime, respectively. The surface lifetime represents the inverse of the surface recombination velocity occurring in a small slice of δx, and it is influenced by the defects density and capture cross-section of carriers. Several strategies have been introduced to minimize the interface recombination rate, such as implementing a band gradient (Ga gradient), utilizing a dielectric layer, and incorporating a hole selective transport layer. These strategies primarily focus on reducing the minority carrier density (Δn) at the backside. Therefore, when referring to the longer surface lifetime achieved through these approaches, it essentially implies an equivalent extension of surface lifetime accomplished by reducing Δn. Consequently, the high non-radiative recombination lowers the effective lifetime, which reduces the excess electron density and makes solar cells deviate from the radiative limit in which the radiative recombination is the only recombination channel. Assuming the Fermi level in a p-type semiconductor is flat and in low injection condition, the excess carrier density generated by illumination is expressed as:

$$\Delta n = G \times \frac{\tau_{\mathrm{n}}^{\mathrm{eff}}}{d} \qquad \textbf{2.17}$$

Where $\tau_{\mathrm{n}}^{\mathrm{eff}}$ is the electron effective lifetime and d is the absorber thickness, G is the generation flux that is usually equal to one-sun equivalent flux. The higher non-radiative recombination leads to a short effective lifetime, which results in a lower excess electron density. Since the electron Fermi level is logarithmically proportional to excess electron density, the higher non-radiative recombination leads to a lower electron Fermi level, thus reducing the Fermi-level splitting that is the upper limit of V_{oc}.

If considering the influence non-radiative recombination on V_{oc} from the devices, in an ideal case without considering the impact of parasitic resistance, at open-circuit condition, the Equation **2.4** can be modified as:

$$V_{oc} = \frac{kk_b T}{q} \ln\left(\frac{J_{sc}}{J_0}\right) \quad \textbf{2.18}$$

The J_0 is a recombination related term which includes both contributions from radiative and non-radiative recombination. The higher non-radiative recombination increases the J_0, as a result, reducing the V_{oc} of solar cells.

2.2 Cu(In,Ga)Se_2 solar cells

The solar cell studied in this work uses Cu(In,Ga)Se_2 as an absorber layer, which is a I-III-VI_2 compound semiconductor composed of Copper (Cu), Indium (In), Gallium (Ga), and Selenium (Se). This semiconductor is a tetrahedrally bonded crystal with a chalcopyrite crystal structure and is discussed in more detail in **Section 2.2.1**. It is a solid solution of $CuInSe_2$ and $CuGaSe_2$, with a tunable bandgap between 1.02 eV and 1.68 eV depending on the ratio of Ga/(Ga+In) (GGI), as described in **Section 2.2.2**.With this advantage, a structure with a bandgap gradient towards both surfaces was developed by building a Ga gradient, which mitigates surface recombination and achieves a record efficiency of 23.35%[28-31]. Moreover, Cu(In,Ga)Se_2 is a complex compound, and other phases can form depending on the growth conditions. Only the chalcopyrite phase is suitable for producing high-quality solar cells, as explained in **section 2.2.3** with the Pseudo binary In_2Se_3-Cu_2Se phase diagram. Then in **Section 2.2.4,** the 1-stage and 3-stage processes used to prepare the absorbers are explained. To achieve high efficiency, other functional layers such as contacts, window layers, and buffers are essential. The typical structure of a Cu(In,Ga)Se_2 solar cell is explained in **Section 2.2.5**.

2.2.1 Crystal structure

The chalcopyrite crystal structure of $CuInSe_2$ is derived from two zincblende unit cells, as shown in **Figure 2.5**. Zincblende belongs to the cubic crystal structure system, which has the same atomic arrangement as diamond but with alternative atoms occupying different lattice positions, as depicted in **Figure 2.5 (a)**. It can also be viewed as a face-centered cubic lattice of atom A, where half of the tetrahedral voids are occupied by atom B. Each ion is 4-coordinated and exhibits local tetrahedral geometry. To form the chalcopyrite structure of $CuInSe_2$ from the zincblende structure, the atom A in zincblende is replaced alternatively by Cu and In, as illustrated in **Figure 2.5 (b)**. This replacement causes a distortion in the tetragonal structure, as the bond lengths between Cu-Se and In-Se are different, resulting in a lattice distance "a" (5.784 Å) that is not exactly half of "c" (11.616 Å) [32]. The advantage of $Cu(In,Ga)Se_2$ lies in its ability to form a solid solution between $CuInSe_2$ and $CuGaSe_2$ by replacing In with its congener, such as Ga, in all ranges of composition. This allows for the tuning of the optoelectronic properties of the absorber layer to achieve the desired characteristics for different solar cell applications by adjusting the GGI. Similarly, it is possible to replace Cu/Se by Ag/S, which enhances the versatility of this material[33, 34].

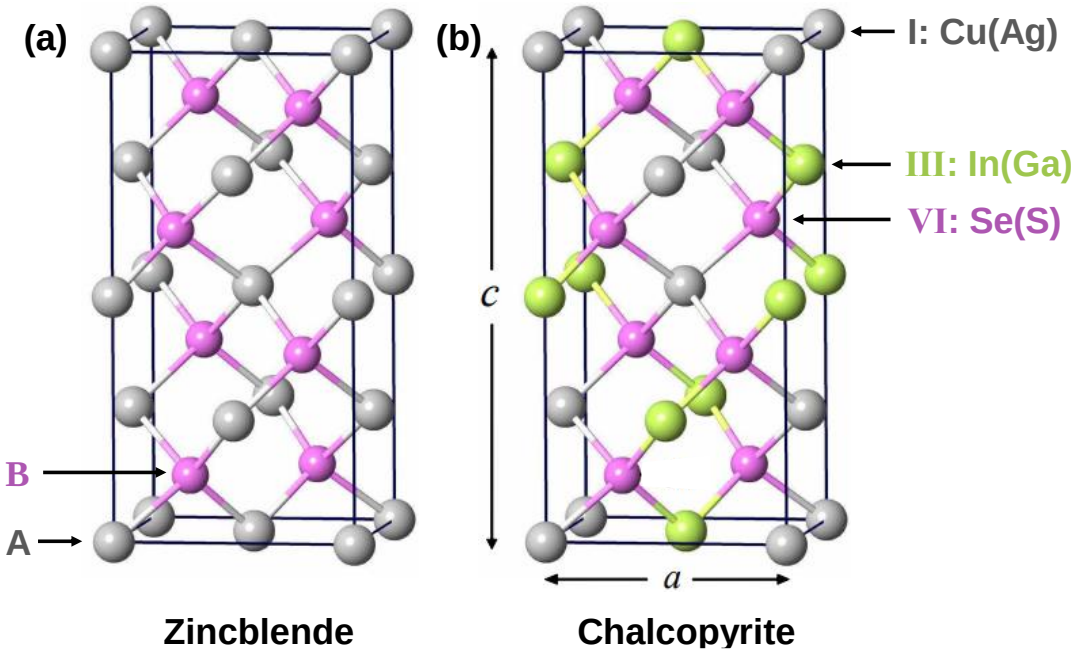

Figure 2.5 (a) Two unit cells of zincblende crystal structure; (b) Tetragonal unit cell of chalcopyrite crystal structure. The chalcopyrite is formed by alternatively replacing cations in zincblende by Cu and In. The Figure is reproduced from Ref.[35]

2.2.2 The tunable bandgap

As discussed, the bandgap of $Cu(In,Ga)Se_2$ is tunable from 1.02 eV to 1.68 eV by adjusting GGI from 0 to 1. The bandgap does not increase strictly linear with increase in GGI but follows a quadratic dependence, which cases a deviation to the linear relation and can be described by the following Equation[36]:

$$E_g^{CIGSe} = 1.68 * GGI + (1 - GGI) * 1.02 - GGI(1 - GGI) * 0.12 \quad \textbf{2.19}$$

The bowing factor, which is "0.12," represents the degree to which the relationship between the bandgap and composition deviates from linearity. It is worth to mention that **Equation 2.19** is slightly different from the relations reported from other literatures[37, 38], in which, they are also slightly different from each other. In semiconductors, the bandgap can be increased by either raising the conduction band minimum or lowering the valence band maximum. For $Cu(In,Ga)Se_2$, the increase in bandgap is mainly due to the upward shift of the conduction band, while the change in the valence band is negligible[39, 40]. This allows us making $Cu(In,Ga)Se_2$ solar cells with band gradients, which is critical for achieving high efficiency in conventional $Cu(In,Ga)Se_2$ solar cells.

2.2.3 Phase diagram

During the growth of $Cu(In,Ga)Se_2$, several phases can form, but only the chalcopyrite phase serves as a suitable absorber for solar cells. A phase diagram provides valuable information on the optimal growth conditions for preparing high-quality absorbers. The binary phase diagram of Cu_2Se and In_2Se_3 as a function of temperature and Cu content is depicted in **Figure 2.6**. The stoichiometric point, where Cu/In equals 1, occurs at 25% Cu. In Cu-rich conditions (Cu% > 25% or Cu/In > 1), the chalcopyrite phase (α) with the secondary phase Cu_2Se forms over a wide temperature range. Some evidence suggests that Cu-rich films possess better transport and recombination properties than Cu-poor samples, but Cu-rich chalcopyrite solar cells typically exhibit lower efficiency than Cu-poor solar cells[41]. One of the reasons is the Cu_2Se accumulation mostly on the chalcopyrite film surface, leading to significant surface recombination and reduced V_{oc} of the solar cells[42]. To address this issue, the films are typically grown under Cu-poor

conditions within the red-colored region of the phase diagram, where only the single chalcopyrite phase is obtained. The largest tolerance of Cu content for obtaining a single chalcopyrite phase is growing sample with substate temperature of around 600 °C. In addition, Cu-poor chalcopyrite can tolerate a high Cu deficit due to the formation of Cu vacancy-related defects (e.g., V_{Cu} and In_{Cu})[43]. With low Cu concentrations and high temperatures, there is no ordering of Cu and In, which results in the formation of the δ phase with a zincblende crystal structure.

With lower temperatures or very low Cu concentration around 16%, it starts forming the β phase also known as the ordered vacancy compound (OVC). Notably, another OVC phase (γ-$CuIn_5Se_8$) can form at even lower Cu content, though it is not shown in **Figure 2.6**. The similar binary phase diagram of Cu_2Se-Ga_2Se_3 was also reported in Ref.[44]. Since $Cu(In,Ga)Se_2$ is the solid solution of the two compounds, it behaves similarly to $CuInSe_2$ and $CuGaSe_2$.

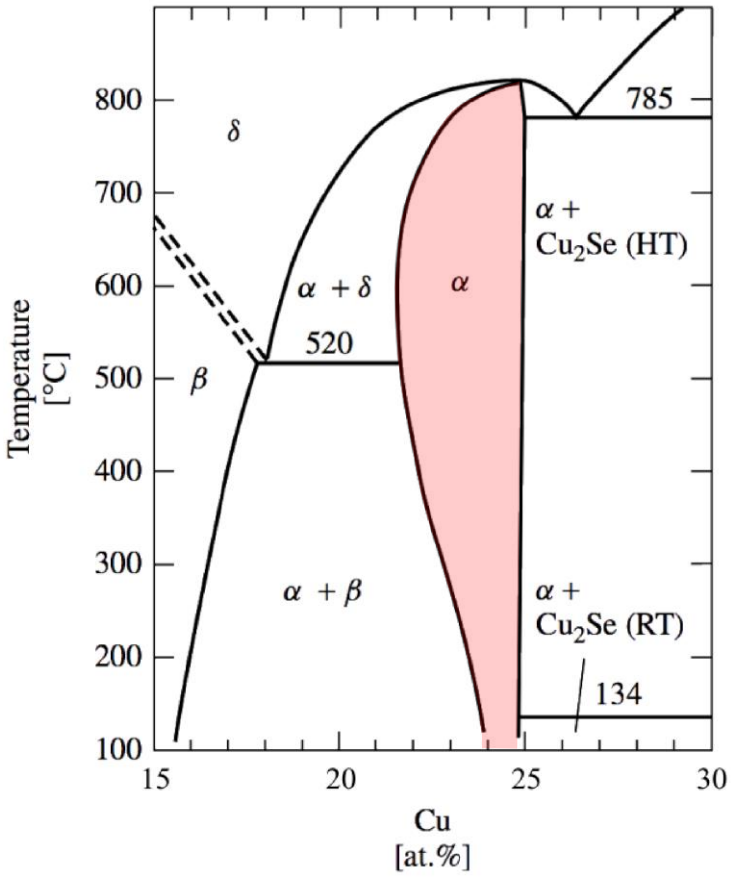

Figure 2.6 The binary phase diagram of Cu_2Se and In_2Se_3. The single α phase that is marked in red shows the right temperature and Cu content range to grow chalcopyrite. The Figure is reproduced from Ref. [45].

2.2.4 The growth of $Cu(In,Ga)Se_2$

The phase diagram presented in **Figure 2.6** indicates that a high substrate temperature and a Cu-poor condition are crucial factors for producing suitable absorbers. In this study, both one-stage and three-stage processes were utilized to grow the samples in a PVD system, as illustrated in **Figure 2.7 (a)**. The PVD system contains four crucial sources, including Cu, In, Ga and Se which provide a stable molecular beam flux. To ensure stable metal flux, the metals were loaded into a ceramic crucible, which was heated by a dual-filament heater. The Se source is unique, as it is composed of an individual crucible and a long Se cracker. The cracker is uniformly heated by the surrounding filaments and can be heated to 1000 °C. The Se flux can be precisely controlled by adjusting the temperature of the crucible and cracker, as well as by manipulating the needle valve between them. These features ensure the PVD system's long-term stability, critical to guarantee the reproducibility of samples prepared using the same recipe but in different runs. Additionally, the system includes a NaF and KF source, which provides Na/K precursors or incorporates Na/K post-deposition treatment (PDT). The substrate temperature mentioned in this study refers to the setting temperature of the substrate heater, which is measured by the thermocouple at the center of the substrate holder without touching the samples. The pyrometer's temperature reading is usually lower than the setting temperature, and this temperature gap increases as the setting temperature increases. For instance, the temperature readings are similar when the setting temperature is below 350 °C, while the pyrometer's temperature is ~60 °C lower than the setting temperature at 590 °C.

Figure 2.7 (b) shows the typical 1-stage process utilized in this work to grow $CuInSe_2$ films. Prior to film deposition, the substrate is cleaned by ramping up the temperature in vacuum to 500°C with all sources closed. This process takes 20 minutes to remove any contaminants on the substrates. Cu, In(Ga) and Se are then supplied simultaneously to the substrate, with the temperature maintained at 40°C lower than the highest setting temperature. The highest growth temperature ranges from 540°C to 590°C, depending on the specific experiments. For instance, in **Chapter 4**, the lower growth temperature of 540°C is used to reduce the diffusion of Ga from the backside to the frontside.

In contrast, the 3-stage process[46], depicted in **Figure 2.7 (c)**, involves a similar cleaning process to the 1-stage process, but after the cleaning, the substrate temperature is cooled down to 356°C

and only Se is supplied for typically 5 minutes before first stage to promote the formation of a thin $MoSe_2$ layer. In the first stage, an $(In,Ga)_2Se_3$ precursor layer is deposited by supplying In(Ga) and Se. The thickness of this layer is monitored using the signal from the pyrometer, which oscillates as a function of the film thickness due to the interference of the infrared light from the samples[47]. In this work, a 3.5 oscillation period is used to obtain a final absorber thickness of approximately 2.0 μm. To obtain a thinner $Cu(In,Ga)Se_2$ film with a thickness of 800-900 nm, the oscillation is reduced to 1.5. In the second stage, the substrate temperature is ramped up to the highest growth temperature, and only Cu and Se are supplied. The chalcopyrite phase forms as the Cu content increases, and the stoichiometry can be identified by the point where the substrate heating power begins to increase due to the formation of Cu_2Se on the surface of the chalcopyrite, which has higher emissivity[47]. The Cu-rich growth duration lasts 15%-20% of the first stage, after which In(Ga) and Se are supplied again in the third stage to finish the film with a Cu-poor composition.

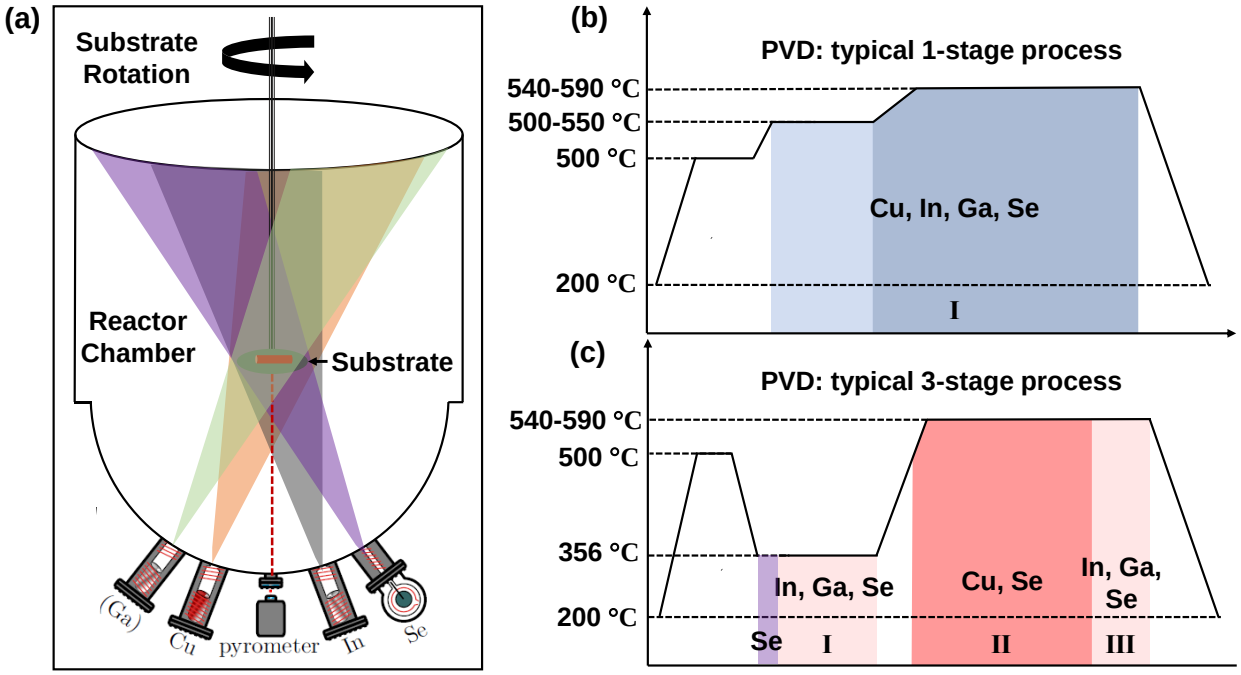

Figure 2.7 (a) Sketch of the PVD system used to grow absorber layers, the Figure is reproduced from Ref.[48]; (b)(c) The growth procedure of the typical 1-stage and 3-stage processes.

The 1-stage process is simple and straightforward, but compared to the 1-stage process, the 3-stage process with Cu-rich growth gives better absorbers that have larger grains and less defects[49-51]. Additionally, the 3-stage process can easier control the final Cu content by tuning the duration of the 3rd stage. With this advantage, it is easier to make slightly Cu-poor samples close to

stoichiometry, which has less defects compared to highly Cu-poor films[41, 50]. Because the diffusivity of Ga is lower than the In, 3-stage process is also generally applied to prepare high efficiency Cu(In,Ga)Se_2 solar cells with the Ga double gradient from the backside to the frontside[49, 52].

2.2.5 Structure of Cu(In,Ga)Se_2 solar cells

In order to create functional solar cells, additional layers are required. As shown in **Figure 2.8** (left), a typical Cu(In,Ga)Se_2 solar cell with a substrate configuration is constructed from the bottom up. The substrate typically consists of soda-lime glass, which supplies Na during the growth of Cu(In,Ga)Se_2. This dopant is essential for high-efficiency solar cells because it improves V_{oc}[53-55]. Alternatively, Na-free glass or glass with a Na diffusion barrier can be used, but Na precursor or Na PDT is required to achieve high efficiency solar cells[56-58]. A layer of ~500 nm Mo is sputtered on top of the glass to serve as a back contact for the collection of free holes, followed by a layer of Cu(In,Ga)Se_2 deposited using the 1-stage or 3-stage process described in **Section 2.2.4**. To reduce front surface recombination, a layer of ~50 nm CdS is deposited on top of the Cu(In,Ga)Se_2 using chemical bath deposition (CBD). Prior to this deposition, a soft KCN etching is typically used to remove impurities and oxides from the surface of the Cu(In,Ga)Se_2. To create a p-n junction for separating the photon-generated free carriers, ~80 nm intrinsic ZnO (i-ZnO) and ~450 nm ZnO:Al (AZO) n-type window layers are deposited sequentially. Finally, Ni/Al grids are evaporated onto the top of the window layer to enhance the collection of free electrons. SEM cross-section film stacks corresponding to the sketch on the left side of **Figure 2.8** are shown on the right side.

Without specific explanation of solar cells preparation, the solar cells are made with baseline processes as described below:

Mo: Roughly 500 nm Molybdenum is prepared by the DC sputtering with a power of 240 W and Argon gas pressure of 2 mTorr.

KCN solution etching: The KCN solution etching process involves immersing the samples in a 5% KCN aqueous solution for 30 seconds, followed by rinsing with deionized (DI) water to remove

any residual KCN. The sample surface is then rapidly dried using a stream of dry N_2 gas. This etching process is commonly used in our processes to remove impurities and oxides from the surface of materials before subsequent processing steps.

CdS: Prior to deposition, all samples undergo chemical etching using a 5% aqueous KCN solution for 30 seconds to eliminate residual oxides. The CBD process involved depositing the CdS layer for 6-7 minutes at 67°C with a mixture of 2 mM $CdSO_4$, 50 mM thiourea, and 1.5 M NH_4OH. Typical growth rates suggest a resulting thickness of 40-50 nm. The CdS layer is crucial for passivating the front surface of the samples and preventing surface degradation during PL characterization.

i-ZnO/AZO: The ~80 nm i-ZnO and 450 nm AZO are prepared by AC sputtering. The working power is around 125 W. And the Argon gas pressure is 4 mTorr and 1 mTorr for depositing i-ZnO and AZO, respectively.

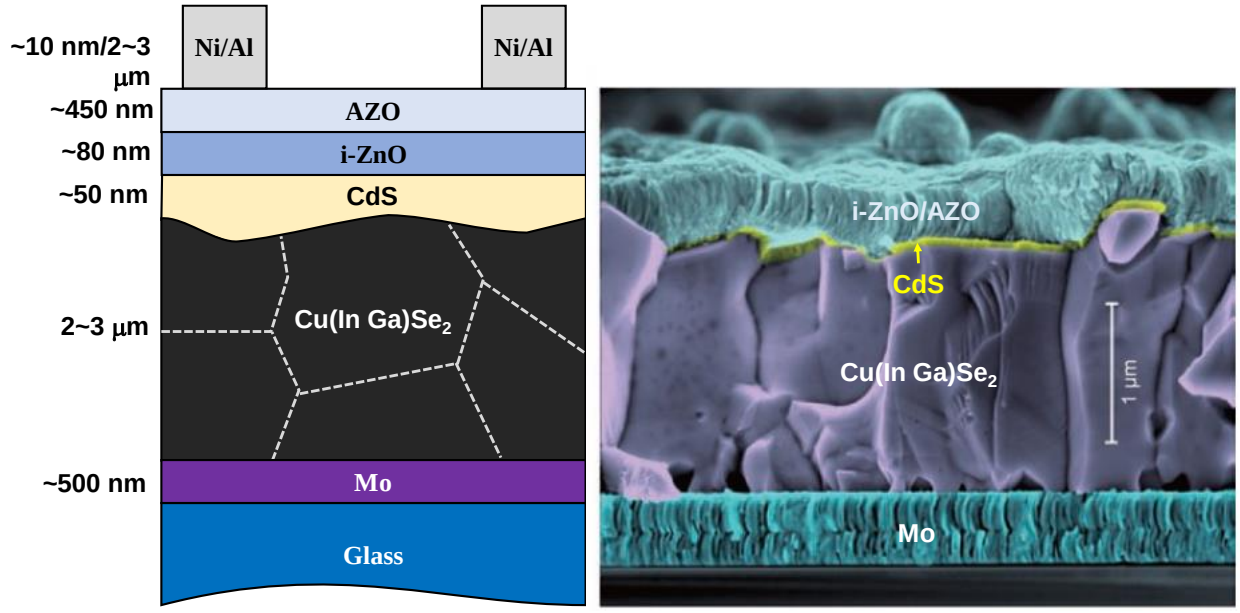

Figure 2.8 The general structure of $Cu(In,Ga)Se_2$ solar cells (left); The typical SEM cross-section image of $Cu(In,Ga)Se_2$ solar cells, the figure is captured from Ref.[59].

Corresponding to the structure of solar cells, **Figure 2.9** shows band diagrams under thermal equilibrium, which are critical to understanding the design principles of efficient solar cells. **Figure 2.9 (a)** depicts the classical band diagram of a $Cu(In,Ga)Se_2$ solar cell with a Ga double gradient from the backside to the frontside. The Ga grading which leads to higher V_{oc} forms during

the 3-stage process. This is attributed to the fact that In is more reactive with Cu than Ga, and the diffusivity of Ga is lower than In through Cu vacancies, as observed in previous studies[46, 60].

In terms of front gradient, some experimental results have suggested that a sharp and steep front grading can impede electron transport and increase non-radiative recombination in SCR[28], later results from ZSW have indicated that a steeper front Ga grading can lead to record efficiency compared to flat grading samples[61]. The discrepancies in findings are thought to be strongly correlated with the presence of KF-PDF on the absorber's surface, which can heal surface defects[61]. Moreover, recent studies have shown that optimized results for solar cells with a Ga back single grading (GBG) exhibit similar V_{oc} deficits compared to record solar cells with double gradients[62, 63]. Achieving the best results is likely to depend on optimizing the heavy PDT to improve surface quality, as well as implementing a high-quality buffer layer to reduce surface defects and ensure a suitable $+\Delta E_c$ (spike) value of approximately 0.2 eV[64-66]. For the backside, the use of Ga grading can act as a back surface field (BSF) that drifts photon-generated carriers into the depletion region (**Equation 2.2**) and improves carrier collection[67]. By removing minority carriers from the backside, the backside recombination rate, which is proportional to minority carrier concentration (as shown in **Equation 2.13**), can be mitigated.

Taking advantages of Ga gradient, the record Cu(In,Ga)Se_2 solar cells are generally built with this structure. However, the use of a gradient in Cu(In,Ga)Se_2 solar cells can result in various losses, which limits its further improvement in efficiency to 29%[11]. These losses include:

I. Due to the thin zone of the minimum band gap, which determines the absorption edge, non-absorption losses may occur in the short circuit current[37].

II. The gradual absorption onset can cause radiative losses in the open circuit voltage[68, 69].

III. High Ga regions near the back contact have shown to exhibit a carrier lifetime below 100ps[70], which can be attributed to additional deep defects in high bandgap chalcopyrite[43, 71].

In addition, when it comes to homogeneous $CuInSe_2$, as illustrated in **Figure 2.9 (b)**, the absence of a Ga grading on the backside can lead to significant backside recombination, thereby limiting the efficiency of $CuInSe_2$ solar cells. Despite this limitation, the photovoltaic community is particularly interested in $CuInSe_2$ solar cells due to their low bandgap of approximately 1.0 eV, which is an ideal match for high bandgap solar cells in a tandem application[72, 73]. Moreover,

building a proper band gradient asks for a thick film which is unnecessarily thick in terms of absorption of photons, consequently increasing production costs. Given these shortcomings of the standard gradient in Cu(In,Ga)Se_2 solar cells, several investigations have called for a paradigm shift by replacing the gradient with a HTL at the back contact[10, 11].

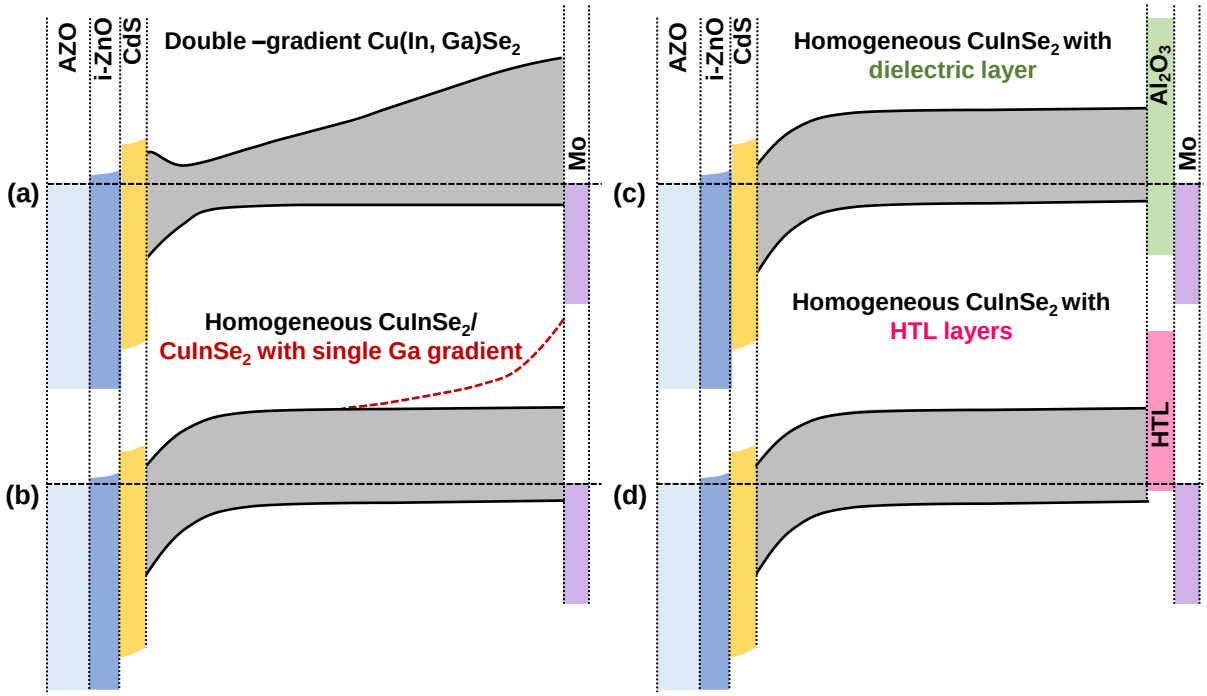

Figure 2.9 Sketch of band diagrams: (a) the Cu(In,Ga)Se_2 with double Ga gradient, which results in higher conduction band minimum toward backside and frontside; (b) The $CuInSe_2$ with and without Ga back single grading; (c) the $CuInSe_2$ with backside passivation of dielectric layers (Al_2O_3); (d)The $CuInSe_2$ with backside passivation of hole selective transport layer.

After evaluating the advantages and drawbacks of using a homogeneous absorber in Cu(In,Ga)Se_2 solar cells, it is concluded that it can increase efficiency and reduce production costs, but backside recombination must be addressed. One strategy to mitigate this issue is to keep a homogenous low bandgap part on the front side and introduce a Ga single grading towards the backside, as shown in **Figure 2.9 (b)** with the red dashed line. While this approach has been shown to reduce backside recombination[62, 63], it still requires a thick film for the Ga grading and does not fully address the issue of inhomogeneity in the high-Ga content region.

Another option for passivation is to use metal oxide dielectric layers, such as Al_2O_3, as shown in **Figure 2.9 (c)**. These layers generate a negatively charged interface that repels minority carriers

away from the backside, reducing recombination[74]. However, the trade-off between hole transport and passivation must be considered, as a thicker layer offers better passivation but worse hole transport, and a thinner layer behaves in the opposite way[75].

The most promising method for achieving good passivation and hole transport simultaneously is to use an HTL. A high conduction band spike (>0.2 eV) between the absorber and HTL can lower minority carrier population at the backside, reducing recombination[11, 76], and a low valence band spike (<0.2 eV) allows holes to transport freely into the HTL[23]. In addition, good p-type conductance of this layer can improve hole transport and reduce series resistance[19].

2.2.6 Submicron $Cu(In,Ga)Se_2$ solar cells

Reducing the thickness of $Cu(In,Ga)Se_2$ solar cells offers several advantages, including shorter manufacturing time and increased cost-effectiveness. The investigation of submicron $Cu(In,Ga)Se_2$ solar cells began approximately 30 years ago with studies by Shafarman et al. in 1997[77] and Negami et al. in 1998[78]. However, submicron $Cu(In,Ga)Se_2$ solar cells prepared using a shorter 3-stage process exhibited a decrease in efficiency due to a decline in all parameters (FF, V_{oc}, and J_{sc}). Several factors contribute to this reduction, such as insufficient absorption thickness resulting in low J_{sc}[79, 80], shunt-related lower FF[77], and backside recombination leading to lower V_{oc} and J_{sc}[81], collectively resulting in decreased overall efficiency.

Among these factors, mitigating the loss due to backside recombination presents one of the most challenging hurdles. In thicker $Cu(In,Ga)Se_2$ absorbers, the longer deposition duration allows for the development of a suitable Ga gradient towards the backside, thereby reducing backside recombination. However, the deposition duration for submicron films is too short to create the necessary Ga grading, leading to significant losses in V_{oc} and J_{sc}. M. Gloeckler et al. conducted simulations to explore the influence of backside recombination on the performance of $Cu(In,Ga)Se_2$ solar cells with varying thicknesses[81]. The results indicated that implementing effective passivation techniques, such as a conduction band gradient or electron reflector, could improve the V_{oc} and J_{sc} of a solar cell with 500 nm $Cu(In,Ga)Se_2$ by 100 mV and 5 mA/cm^2, respectively. Additionally, the utilization of a hole selective transport structure proves to be one of

the most promising solutions to address this issue. This structure eliminates the need for concerns regarding the Ga gradient while simultaneously improving backside passivation. Further details regarding the implementation of the hole selective transport layer for submicron Cu(In,Ga)Se_2 solar cells will be discussed in **Section 5.3**.

2.3 Characterization techniques

To quantify the quality of solar cells, various characterization techniques are employed. This section explains the measuring conditions for involved measurements. Given that photoluminescence (PL) is the most important method used in this thesis, relevant characterizations are discussed in detail. **Section 2.3.1** explains the photoluminescence and Planck's generalized law. **Section 2.3.2** explains absolute PL, which is used to determine the ΔE_F according to Planck's generalized law. In **Section 2.3.3**, we introduce illumination-intensity dependent PL and explain how to determine the optical diode factor (ODF) based on it. **Section 2.3.4** describes time-resolved PL (TRPL), which is widely used in this work to determine the effective minority carrier lifetime. Finally, we briefly introduce other characterization techniques involved in this study in **Section 2.3.5**.

2.3.1 Photoluminescence

The photoluminescence is the reciprocal process to generation as discussed in **Section 2.1.1**, in which excited free electrons in a semiconductor thermally stabilizing back to the conduction band minimum and recombine radiatively by emitting photons. This luminescence can be classified as photoluminescence (PL), electroluminescence (EL), and cathodoluminescence (CL), depending on the method of excitation (photons, electric field, or electrons, respectively). They are widely involved in photovoltaic research community to study optoelectronic properties of solar cells. Photoluminescence is the focus of this work, which allows for the measurement of spectral photon flux density emitted from the semiconductor absorber during the band-to-band transition.

Since semiconductor is a grey body, the absorptivity is a function of energy of photons, with ΔE_F, the photon flux emitted radiatively from the semiconductor can be described by Planck's generalized law[14, 24]:

$$\emptyset(E) = \frac{1}{4\pi^2\hbar^3 c^2}\frac{a(E)E^2}{\exp\left(\frac{E-\Delta E_F}{k_b T}\right)-1} \quad \textbf{2.20}$$

Where the $\emptyset(E)$ is the radiation (photon) flux ($cm^{-2}s^{-1}eV^{-1}$), c is the speed of light and $a(E)$ is the absorptivity. It shows that the photon flux emitted from an excited semiconductor is determined by the black body radiation at each energy interval, absorptivity, and quasi-Fermi level splitting of the absorber.

With the Boltzmann approximation that shows the exponential term is way larger than 1, the total radiation over the energy is given by:

$$\emptyset_r = \int_0^\infty \emptyset(E)dE = C_b \exp\left(\frac{\Delta E_F}{k_b T}\right) \quad \textbf{2.21}$$

C_b is a constant that represents the integrated black body radiation related term times absorptivity.

2.3.2 Absolute Photoluminescence

To get the ΔE_F under the absolute condition, e.g. the one-Sun equivalent illumination intensity, the home-built PL set-up must be calibrated. Basically, all the samples studied in this thesis are excited by a 660 nm diode layer with a spot diameter of ~2.6 mm in the air at ambient temperature. The photoluminescence from the sample is collected by two off-axis parabolic mirrors, and then redirected into a 550 μm optical fiber. The focus lengths of two parabolic mirrors are carefully chosen to make the incident angle smaller than the acceptance angle of the fiber, which avoids the reflection loss of photons. In front the entrance of the fiber, the long pass filters are inserted to remove unwanted singles, e.g. the reflection of the laser from the sample surface. Through the coupling of the fiber, the photons are sent to monochromator that splits them into different energy intervals. Then, they are detected by the corresponding detectors, Si-CCD camera (200 nm-1100 nm) or InGaAs-array detector (800 nm-1600 nm). The detector can only show the arbitrary number

with a unit of "Counts". The arbitrary number of photons can be changed into absolute photon flux with a unit of "$cm^{-2}s^{-1}eV^{-1}$" by calibrating the system, which is briefly discussed in this thesis (The specific details of calibration process is well explained in Ref.[82]):

1. A standard halogen lamp is measured, which gives us a spectrum with a unit of "Counts" ($\emptyset_{\mathrm{Hal}}$).

2. By comparing the $\emptyset_{\mathrm{Hal}}$ with the standard spectrum of the Halogen lamp given by the supplier with a unit of "$cm^{-2}s^{-1}eV^{-1}$" ($\emptyset_{\mathrm{Sd-Hal}}$), the spectrum correction function [SF(E)] as a function of energy of photons can be determined:

$$\mathrm{SF}(E) = \frac{\emptyset_{\mathrm{Sd-Hal}}}{\emptyset_{\mathrm{Hal}}} (\mathrm{cm^{-2}s^{-1}eV^{-1}Counts^{-1}}) \qquad \textbf{2.22}$$

3. Applying SF(E) to the measured PL spectrum with a unit of "Counts" ($\emptyset_{\mathrm{PL-C}}$), the relative photon flux ($\emptyset_{\mathrm{PL-F}}$) from the sample with a unit of "$cm^{-2}s^{-1}eV^{-1}$" is:

$$\emptyset_{\mathrm{PL-F}} = \mathrm{SF}(E)\emptyset_{\mathrm{PL-C}} \qquad \textbf{2.23}$$

4. To know the absolute value of the photon flux, an intensity correction factor (IF) is needed because the lamp has the absolute intensity only in a certain distance and the light shined on the reflector within a certain angle. This is done by comparing the absolute photon flux of the laser ($\emptyset_{\mathrm{Abs-Laser}}$) with a unit of "$cm^{-2}s^{-1}eV^{-1}$" and the relative photon flux measured by the detector ($\emptyset_{\mathrm{Det-Laser}}$) with a unit of "$cm^{-2}s^{-1}eV^{-1}$". Thus, the IF can be described by:

$$\mathrm{IF} = \frac{\emptyset_{\mathrm{Abs-Laser}}}{\emptyset_{\mathrm{Det-Laser}}} \qquad \textbf{2.24}$$

The $\emptyset_{\mathrm{Abs-Laser}}$ is determined by measuring the power of the laser by a power meter and its diameter from a CCD camera. $\emptyset_{\mathrm{Det-Laser}}$ is measured by inserting a spectralon at the sample position, which reflects the laser to the detector. The measured spectrum is corrected by SF(E), which changes it into relative photon flux.

5. By applying the IF to $\emptyset_{\mathrm{PL-F}}$, the absolute photon flux ($\emptyset_{Abs-PL-F}$) is obtained:

$$\emptyset_{\mathrm{Abs-PL-F}} = \mathrm{IF}\emptyset_{\mathrm{PL-F}} = \mathrm{IF} \cdot \mathrm{SF}(E)\emptyset_{\mathrm{PL-C}} \qquad \textbf{2.25}$$

With an absolute PL spectrum, the absolute ΔE_{F} can be determined according to the Planck's generalized law under the certain illumination intensity. To have ΔE_{F} under the one-Sun equivalent illumination, the laser power and its diameter is measured, which gives us the photon flux of the

laser with respect to the laser power. Then the one-Sun equivalent laser power is chosen depending on the bandgap of the absorber, which determines the one-Sun equivalent incident photon flux. Basically, the AM1.5G spectrum is plotted as photon flux ($\emptyset_{\mathrm{AM1.5G}}$, $\mathrm{cm^{-2}s^{-1}eV^{-1}}$) with respect to the energy of photons. The one-Sun equivalent photon flux ($\emptyset_{\mathrm{one-Sun}}$) is an integration of AM1.5G spectrum with energy of photons above the bandgap of the absorber:

$$\emptyset_{\mathrm{one-Sun}} = \int_{E_g}^{\infty} \emptyset_{\mathrm{AM1.5G}}(E)\mathrm{d}E \qquad \textbf{2.26}$$

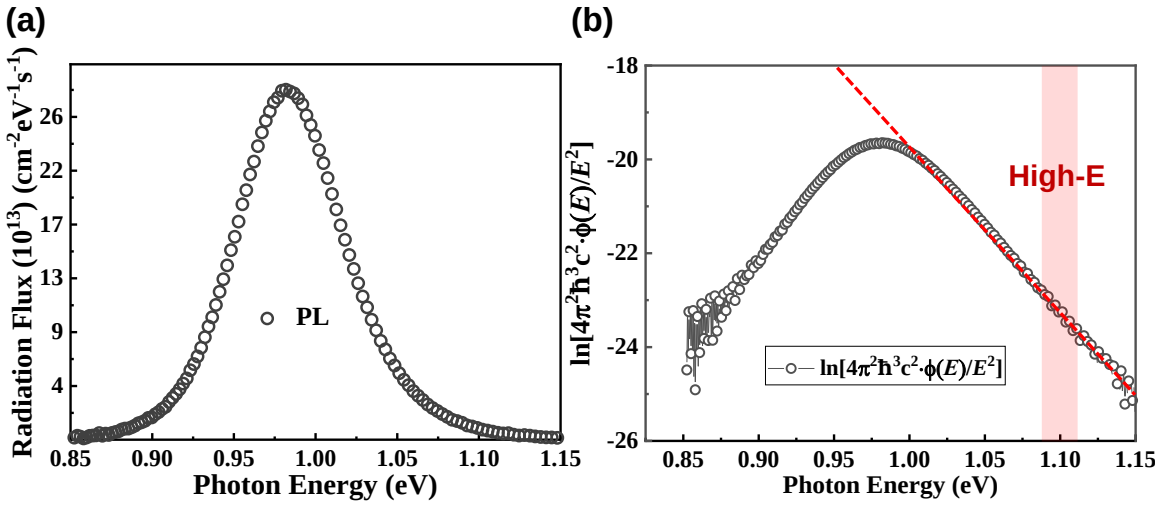

Figure 2.10 (a) The typical PL spectrum of the $CuInSe_2$; (b) The transformed absolute PL within semi-logarithmic scale. By fitting the high energy wing of the spectrum where the $a(E)$ is assumed to be 1, the ΔE_F can be determined based on Planck's generalized law.

With calibrated PL and one-Sun equivalent illumination, the absolute PL spectrum of a typical $CuInSe_2$ under one-Sun illumination is shown in **Figure 2.10 (a)**. With a rearranged **Equation 2.20** with Boltzmann approximation:

$$\ln\left[\frac{4\pi^2\hbar^3c^2\cdot\emptyset(E)}{a(E)\cdot E^2}\right] = -\frac{E-\Delta E_F}{k_b T} \qquad \textbf{2.27}$$

The PL spectrum can be transformed into a semilogarithmic plot as shown in **Figure 2.10 (b)** with the black circled curve. As discussed in **Section 2.1.1**, $Cu(In,Ga)Se_2$ with a thickness of ~2 μm is thick enough to absorb almost all high energy photons with energy 0.1 eV higher that the bandgap energy. Thus, it is reasonable to assume the "a(E) = 1" for the high energy photons. With this assumption, the ΔE_F of the semiconductor under certain illumination can be linearly fitted at the

high energy wing of the semilogarithmic plot as shown in **Figure 2.10 (b)**. The temperature involved in ΔE_F fitting is the ambient temperature that is measured by a thermometer. The ambient temperature is always under control, but a slight change of 2 K from 295 K to 297 K was generally observed in winter and summer. However, these differences were considered when we did a fixed temperature fitting. Additionally, the free temperature fitting can also be applied to estimate ΔE_F. However, in most of cases, the temperature is overestimated around 20 K to 50 K higher than the ambient temperature, which leads to a much lower ΔE_F. This higher temperature is not because the illuminated sample has a higher temperature. The temperature distribution of the sample surface was checked by an infrared camara, which shows the temperature difference is tiny enough (less than 1 K) to be ignored under the one-Sun equivalent illumination (based on AM1.5G). Indeed, we believe this difference of temperature is due to ignorance of reflection and non-absorption of photons. The ΔE_F values presented in this thesis were computed by fixing the fitting temperature. This approach is chosen because the fixed temperature is close to realistic conditions and produced ΔE_F values that are more reliable and higher than the V_{oc}. This result is physically sensible because ΔE_F represents the upper limit of achievable V_{oc}.

The absolute PL also allows us to determine photoluminescence quantum yield (PLQY), which is the ratio between integrated PL flux and generation flux. From PLQY, the non-radiative loss of V_{oc} compared to the SQ value[83] can be calculated (the derivations can be found in [84, 85]):

$$\Delta V_{oc}^{nrad} = \frac{k_b T}{q} \ln(\text{PLQY}) = \frac{k_b T}{q} \ln(\frac{\emptyset_r}{G}) \qquad \textbf{2.28}$$

Besides, it also allows us to measure the PL or the ΔE_F of the samples under the different Suns (illumination intensity), which is involved to measure illumination intensity-dependent PL, and thus determining the optical diode factor of samples. The details of illumination intensity-dependent PL are discussed in **Section 2.3.3**.

2.3.3 Illumination intensity-dependent photoluminescence and the ODF

With the PL system calibrated, it is possible to determine the absolute photon flux emitted from both the sample and the laser. This allows for investigation of illumination intensity-dependent

photoluminescence by changing the incident laser photon flux. **Figure 2.11 (a)** presents a typical illumination intensity-dependent PL, where the spectra, measured from bottom to top, correspond to increasing illumination intensity. By integrating the photon flux over the photon energy interval, the total radiation (ϕ_r) from the sample can be acquired.

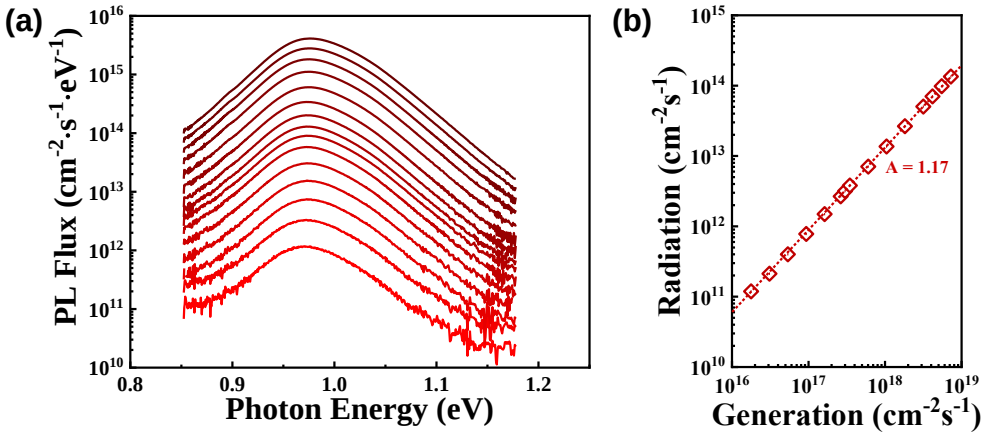

Figure 2.11 (a) Illumination intensity-dependent photoluminescence: from the bottom to the top, the spectra are measured with increasing illumination intensity; (b) The relation between the radiation and the generation (illumination intensity). By linearly fitting the curve, the ODF is the slope.

Empirically, ϕ_r is found to follow a power law dependence on the illumination intensity or generation flux (G) over many orders of magnitude:

$$\emptyset_r \propto G^A \qquad \textbf{2.29}$$

combining **Equation 2.21** and **2.29** gives:

$$G = C_b' \exp\left(\frac{\Delta E_F}{A k_b T}\right) \qquad \textbf{2.30}$$

Where A is the optical diode factor and C′ is a constant. The ODF is the exponent of the exponential relation between radiation and generation, which can be determined by linearly fitting the slope of the logarithmic curve of radiation and generation as shown in **Figure 2.11 (b)**.

2.3.4 Time-resolved photoluminescence (TRPL)

Time-resolved photoluminescence (TRPL) is a technique that employs time-correlated single photon counting (TCSPC) to measure the decay of luminescence in the time domain. In this technique, samples are excited by a pulsed diode laser with a wavelength of 640 nm, and the repetition rate of the laser is adjusted based on the effective lifetime of the sample. The used laser has a diameter of 40.5 μm which is determined from a beam profiler. The typical photon density per pulse is around 1.2×10^{13} cm^{-2} for repetition of 5MHZ and 4.8×10^{12} cm^{-2} for repetition of 2MHZ, which are estimated from the average power of the pulse laser. For samples with an effective lifetime shorter than 100 ns, a repetition rate of 5 MHz is used, while for samples with an effective lifetime longer than 100 ns, a repetition rate of 2 MHz is used. To avoid the pile-up effect, which can lead to the loss of long-lifetime photons, the ratio between the total counts rate and repetition rate is always kept below 2% by optimizing the laser intensity using a waveguide iris filter. The background of shown TRPL spectra is subtracted. And the background counts are accumulated dark counts. When the samples exhibit a 2-exponential decay, a 2-exponential decay function is used to fit the effective lifetime. If the samples exhibit a 1-exponential decay, both 1-exponential and 2-exponential decay functions are utilized to fit the effective lifetime.

$$I = I_0 + \mathrm{A}\exp\left(\frac{-t}{\tau}\right) \qquad \textbf{2.31}$$

$$I = I_0 + \mathrm{A_1}\exp\left(\frac{-t}{\tau_1}\right) + \mathrm{A_2}\exp\left(\frac{-t}{\tau_2}\right) \qquad \textbf{2.32}$$

The **Equation 2.31** and **2.32** are 1-exponential and 2-exponential decay function, respectively. The I_0 and A (A_1 and A_2) are fitting parameters and τ (τ_1 and τ_2) is the effective lifetime. If 2-exponential decay function is used to fit the PL decay curve, and the weighted effective lifetime is considered:

$$\tau_{\mathrm{e}} = \frac{\mathrm{A_1}\tau_1 + \mathrm{A_2}\tau_2}{\mathrm{A_1} + \mathrm{A_1}} \qquad \textbf{2.33}$$

Currently, the exact reason for the 2-exponential decay observed in some of our samples remains uncertain. Existing literature suggests a few possible explanations, including high injection levels[86, 87], carrier transport[88], and fast surface recombination[89], which can lead to 2-exponential decay in TRPL spectra. However, the first two factors are not influenced by recombination under low injection condition. In this situation, incorporating the fast decay lifetime

(τ_1) within **Equation 2.33** may lead to a lower estimated effective lifetime, resulting in a lower estimated backside recombination velocity and a higher estimated doping density. To maintain the consistency of this study, we consistently utilize the weighted effective lifetime. Importantly, this choice does not alter the trends observed in lifetime, backside recombination, and doping density among the various samples, thus preserving the integrity of our final conclusions.

Assuming the carriers are uniformly distributed, according to **Equation 2.17 and 2.40**, the change of ΔE_F due to change of weight effective lifetime can be expressed as:

$$\Delta\Delta E_F = k_b T \ln\left(\frac{\tau_1}{\tau_2}\right) \quad \textbf{2.34}$$

In which, τ_1 and τ_2 is weight effective lifetime determined from TRPL.

2.3.5 Others

Secondary ion mass spectrometry (SIMS)

SIMS was used to measure the element distribution of the samples. The CAMECA SC-ultra instrument (Ametek) was used to conduct measurements. A 1 keV focused Cs^+ ion beam (with a current of 5 nA) was applied to sputter the surface of the sample over an area of 250 μm × 250 μm. Only ions from the central region, with a diameter of 60 μm, were detected as MCs^+ or MCs^{2+}. Here, M represents the ions of interest, such as Cu, In, Ga, Se, and Mo. The measurement presented here is a non-calibrated SIMS measurement. To determine the absolute intensity of each element and quantify the lateral bandgap grading based on the GGI, the data must be calibrated using the PL bandgap of the sample. We assume that this bandgap corresponds to the very front surface where the GGI is minimal. Using the dependency, $E_g^{CIGS} = E_g^{CIS}$+0.65(GGI), provided in Ref[36], E_g^{PL} can be used to calculate the In $[C(In)_{PL}^{Front}]$ and Ga concentration $[C(Ga)_{PL}^{Front}]$ concentrations at the front side. By comparing these concentrations with the intensity measured by non-calibrated SIMS $[I(In)_{SIMS}^{Front}$ or $I(Ga)_{SIMS}^{Front}]$, a quantification factor $\alpha = C(In)_{PL}^{Front}/I(In)_{SIMS}^{Front}$ and $\beta = C(Ga)_{PL}^{Front}/I(Ga)_{SIMS}^{Front}$ can be determined to quantify the non-calibrated SIMS GGI profile and obtain the calibrated Ga profiles.

The error of this calibration may come from the small variation of the PL measured bandgap and the low Ga tracing signal of SIMS measurements. To remove the uncertainty of the calibration, the relative In and Ga yield values (α and β) are shown in **Figure 2.12**. These values for different samples are almost same, which confirms the reliability of this calibration.

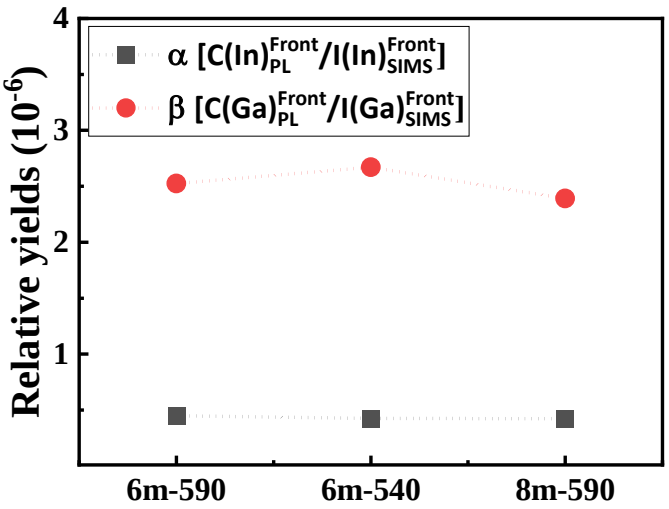

Figure 2.12 Relative yields of In and Ga for different samples.

X-Ray diffraction (XRD)

XRD was used to check the phase composition and crystal structure of SCS synthesized oxides. Grazing incidence X-ray diffraction (GIXRD) patterns with an incidence angle a of 0.5^{o} are recorded on a Bruker D8 Discover diffractometer (Bruker) using Cu-Ka radiation in the 2θ range from 20 to 60^{o} with the step of 0.02^{o}.

Differential Scanning Calorimeter (DSC)

DSC was used to confirm the SCS reaction. The thermal behaviour of the combustion precursor is analyzed by Differential Scanning Calorimeter (DSC, Mettler Toledo 3+). The samples are prepared by drying the solutions at 100 ^{o}C overnight in ambient atmosphere. Measurements are performed from 25 to 350 ^{o}C with a heating rate of 10 ^{o}C/min in the air atmosphere.

Illumination Current-Voltage (J-V)

To determine the efficiency of solar cells, the illumination *J-V* was introduced. Measurements are carried out at 25 °C with a 4-probe configuration. A class AAA solar simulator supplies a simulated

AM1.5G spectrum that is calibrated by a Si reference cell. The forward scanning voltage is applied from -0.3 V to 0.6 V with a step of 0.01 V.

Capacitance-Voltage (C-V)

To determine the doping density of absorber, the *C-V* measurement was used. The capacitance of the solar cell as a function of applied DC voltage is recorded using an inductance capacitance and resistance meter in the frequency range f = 100 Hz to 1 MHz with a controlled small-signal AC voltage pulse of 30 mV rms. The capacitance-voltage measurements were performed at room temperature and low temperature after keeping the device in dark at 300K for 8 hours to ensure a relaxed state.

External quantum efficiency (EQE)

EQE measurements were conducted to some solar cells to determine the collection of photon-generated carriers. The EQE measurements were done by a home-built set-up. The sample were measured at the ambient temperature (~296 K).

2.4 Diode factor

Diode factor is an important parameter that has an impact on the fill factor of the solar cells. With the same J_{sc} and V_{oc}, the lower diode factor leads to a higher fill factor[23, 90, 91], efficiency loss due to diode factor related FF will be discussed in **Chapter 7**. When talking about diode factor[23, 92, 93], electric diode factor (EDF) and optical diode factor (ODF) are discussed. The EDF is an exponent of the exponential relation between current density and voltage, **Equation 2.4**. When it is an open-circuit condition, from the **Equation 2.4**, the J_{ph} can be expressed as:

$$J_{\mathrm{ph}} = J_0 \left[\exp\left(\frac{\mathrm{q}V_{\mathrm{oc}}}{\mathrm{kk_b}T}\right) - 1\right] \approx J_0 \exp\left(\frac{\mathrm{q}V_{\mathrm{oc}}}{\mathrm{kk_b}T}\right) \qquad \textbf{2.35}$$

In which, k is the EDF. Because the J_{ph} is proportional to the generation. The **Equation 2.35** can be further transformed as:

$$J_{\mathrm{ph}} \sim G \sim J_0 \exp\left(\frac{\mathrm{q}V_{\mathrm{oc}}}{\mathrm{kk_b}T}\right) \qquad \textbf{2.36}$$

Meanwhile, as shown in **Equation 2.30**, the ODF is an exponent between generation and ΔE_F. Comparing **Equation 2.30 and 2.36**, they are indeed very similar formulas. Actually, in a *J-V* measurement, a voltage is applied and the resulting current is measured. In an illumination intensity-dependent PL measurement, the generation flux (i.e. the current) is defined by the experimental condition and the quasi-Fermi level splitting (i.e. the voltage) is measured.

Despite the similarity of the EDF and ODF, they can be different depending on the recombination channels. For the EDF, it is a diode factor of the finished devices, which can be influenced by both recombination in the quasi-neutral region (QNR) and space charge region (SCR). For the ODF, it is diode factor in the QNR since the measured samples are only covered by a thin CdS layer (40-50 nm), meaning the formation a narrow SCR that usually can be ignored. Theoretically, for a doped semiconductor in the low injection condition, e.g. p-type semiconductor ($\Delta n << N_A$), the generation can only shift the quasi-Fermi level of minority carrier in the QNR, which leads to a diode factor of 1[15, 23]. Due to carrier depletion in SCR, the density of electron and hole is equal, meaning the recombination in SCR can shift both quasi-Fermi levels of electron and hole simultaneously, which leads to a diode factor of 2 [15, 23]. Thus, the ODF from the QNR is the lowest diode factor that can be realized. In addition, if the recombination taking place at the front interface is sufficiently low, i.e. the differnece between ΔE_F and qV_{oc} is negligible [92].

As discussed above, theoretically, the ODF originating from the QNR is expected to be 1. However, the experimental value of ODF>1 is usually observed, indicating an additional increase in carrier density besides the band-to-band generation. This can be explained by a model proposed by Weiss et.al.[90]. This model is based on illumination intensity-dependent metastable defects transition theory[94], which shows that the donors can transform to acceptors depending the illumination intensity. Because of this transition, the hole density increases upon the increase in illumination intensity, resulting in an extra down shift of Fermi level of hole and thus the ODF>1. The presented results in **Chapter 6** that are about the influence of backside recombination and doping on the ODF is based on this model.

Metastable behavior of defects has been observed in $Cu(In,Ga)Se_2$, which allows donors (acceptors) to convert to acceptors (donors) by capturing free electrons (holes)[94-96]. One of the most well-known metastable defect pairs is (V_{Se}-V_{Cu}) vacancy complex. For the p-type $CuInSe_2$ or $CuGaSe_2$, group III metal atoms (In or Ga) next to the Se vacancy contributes to the formation of metal dimer

bonds[97]. The isolated V_{Se} in $CuInSe_2$ or $CuGaSe_2$ introduces two states, a bonding state and antibonding state. From example in $CuInSe_2$, the In-In bonding state contributes to a lower energy state "*a*", while a high energy state "*b*" is resulted from the In-In antibonding state. And the metastability of anion (Se) vacancies in $CuInSe_2$ compounds is primarily attributed to the significant alterations in atomic and electronic structures resulting from the occupation and de-occupation of the symmetric state formed by the cation (In) dangling bonds. It means that the energy states of V_{Se} depends on its charges. For the neutral V_{Se}^{0}, the bonding state "*a*" is occupied by two electrons with two neighbors In atoms are bond and the distance between them (d_{In-In}) is short. In this defect configuration, the "*a*" level is around 2 eV below the VBM, and the "*b*" level locates at upper part of the VBM. By capturing two holes, the positively ionized state V_{Se}^{2+} results in breaking up the bond of two neighbor In atoms and a longer distance between them. In this defect configuration, both "*a*" and "*b*" are shifted upward above the CBM. Unlike V_{Se}, V_{Cu} always introduce shallow acceptor level (V_{Cu}^{-}) just above the VBM, which is independent on the position of Fermi level.

Since, on the one hand, the V_{Cu} density will excess the V_{Se} even in stoichiometric $CuInSe_2$[23]. On the other hand, the pair binding energy of the (V_{Se}-V_{Cu}) complex is negative[94, 98, 99]. Other calculations also show a weak bounding in case of the (V_{Se}-V_{Cu}) complex in $CuInSe_2$, which may attribute to metastability in $Cu(In,Ga)Se_2$ [100]. It is expected that V_{Cu} will equilibrate to form the (V_{Se}-V_{Cu}) complex at room temperature. In other words, the most of the V_{Se} is bound to the V_{Cu}, thus the density of (V_{Se}-V_{Cu}) complex will be much higher than V_{Se} and the metastability of (V_{Se}-V_{Cu}) rather than V_{Se} should be considered. From the DFT calculation[97], the "*a*" and "*b*" defect-localized states of (V_{Se}-V_{Cu}) complex occurs at the similar energies compared to the isolated V_{Se}. It means that the similar metastability of (V_{Se}-V_{Cu}) complex compared to the isolated V_{Se} should take place, but the corresponding charge of (V_{Se}-V_{Cu}) complex are shifted by -1 relative to the isolated V_{Se} due to V_{Cu}^{-}. According to the calculation[94], for a p-type $CuInSe_2$ (the Fermi level is close to VBM), the $(V_{Se}\text{-}V_{Cu})^{+}$ state in the donor configuration has the longest In-In bonds and lowest energy. Assuming an electron-hole pair is generated by using light or voltage bias, after thermal activation, the $(V_{Se}\text{-}V_{Cu})^{+}$ state in the donor configuration can convert to the $(V_{Se}\text{-}V_{Cu})^{-}$ state in acceptor configuration by capturing one electron and releasing one hole:

$$(V_{Se} - V_{Cu})^{+} + e \rightarrow (V_{Se} - V_{Cu})^{-} + h \qquad \textbf{2.37}$$

During this transition, the bonding state "*a*" is populated by two electrons with forming the In-In bonds, leading to a short $d_{In\text{-}In}$. Similarly, after overcoming the corresponding thermal activation, the reverse reaction can take place by capturing two holes:

$$(V_{Se} - V_{Cu})^{-} + 2h \rightarrow (V_{Se} - V_{Cu})^{+} \qquad \textbf{2.38}$$

During this transition, the bonding state "*a*" is de-populated by capturing two holes with breaking up the In-In bonds, leading to a long $d_{In\text{-}In}$.

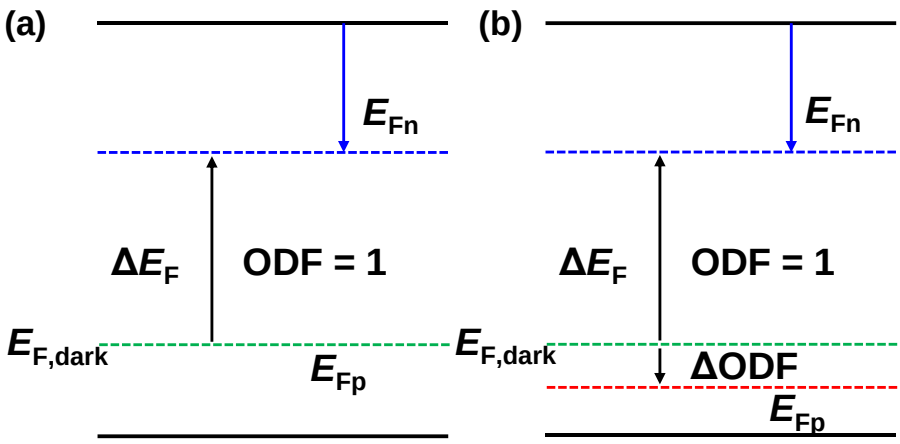

Figure 2.13 (a) In the low injection condition, for a p-type semiconductor, the photon-generated free carriers can only shift the quasi-Fermi level of electron in the QNR which leads to the ODF of 1; (b) With the metastable defects, the extra holes from the metastable defects transition from the donors to acceptors additionally shift the quasi-Fermi level of hole, which leads to ODF=ΔODF+1>1. The figure is recaptured from Ref. [90].

The additional holes from the metastable defects transition shift the quasi-Fermi level of the majority carrier, which increases the ODF. The transition of (V_{Se}-V_{Cu}) complex discussed above can be the reason, but any other potential metastable defects transition from donor to acceptor would contribute to the ODF. As shown in **Figure 2.13 (a)**, in the low injection condition without metastable defects and generation dependent lifetime, the photon generated free carriers can only shift the quasi-Fermi level of electron for a p-type semiconductor in the QNR, which leads to the ODF of 1 (**Equation *2.45***) . With the metastable defects transition as shown in **Figure 2.13 (b)**, the extra holes increased by metastable defects converting (from donors to acceptors) additionally shift the quasi-Fermi level of holes, leading to the ODF>1. This ΔODF can be quantified by

considering the ODF as a function of p and τ_{eff} (effective lifetime). As discussed above, the ODF is the exponent of the exponential relation between radiation flux (ϕ_r) and generation flux (G), which can be determined by the slop of the logarithmic PL flux-Generation flux characteristics (**Section 2.3.3**):

$$\mathrm{A} = \frac{\mathrm{dln}(\emptyset_{\mathrm{r}})}{\mathrm{dln}(G)} \qquad \textbf{2.39}$$

For a p-type semiconductor with uniform distribution of doping and free carriers, meaning the quasi-Fermi levels are straight. In the low injection condition ($\Delta n << p$, $n_0 << \Delta n \approx n$), the position of the electron quasi-Fermi level can be calculated by:

$$E_{\mathrm{F}}^{\mathrm{n}} - E_{\mathrm{c}} = \mathrm{k_b} T \ln\left(\frac{n}{N_{\mathrm{c}}}\right) \approx \mathrm{k_b} T \ln\left(\frac{\Delta n}{N_{\mathrm{c}}}\right) \qquad \textbf{2.40}$$

Where N_c is the conduction band effective density of states, n is the electron density, Δn is the non-equilibrium (free) electron density, $E_{\mathrm{F}}^{\mathrm{n}}$ is the quasi-Fermi level of electrons and E_{c} is the energy of the conduction band minimum. Similarly, for a p-type semiconductor in the low injection condition ($p \approx N_A$), the position of the hole quasi-Fermi level can be calculated by:

$$E_{\mathrm{v}} - E_{\mathrm{F}}^{\mathrm{p}} = \mathrm{k_b} T \ln\left(\frac{p}{N_{\mathrm{v}}}\right) \approx \mathrm{k_b} T \ln\left(\frac{N_{\mathrm{A}}}{N_{\mathrm{v}}}\right) \qquad \textbf{2.41}$$

Where N_v is the valence band effective density of states, p is the hole density, N_A is the doping density, $E_{\mathrm{F}}^{\mathrm{p}}$ is the quasi-Fermi level of holes and E_{v} is the energy of the valence band maximum. Then with the bandgap (E_g), the ΔE_F is:

$$\Delta E_{\mathrm{F}} = E_{\mathrm{g}} + (E_{\mathrm{F}}^{\mathrm{n}} - E_{\mathrm{c}}) + \left(E_{\mathrm{v}} - E_{\mathrm{F}}^{\mathrm{p}}\right) = E_{\mathrm{g}} + \mathrm{k_b} T \ln\left(\frac{N_{\mathrm{A}} \cdot \Delta n}{N_{\mathrm{v}} \cdot N_{\mathrm{c}}}\right) \qquad \textbf{2.42}$$

According to Equations **2.39**, **2.21** and **2.42**, the ODF is:

$$\mathrm{A} = \frac{\mathrm{dln}p}{\mathrm{dln}G} + \frac{\mathrm{dln}n}{\mathrm{dln}G} \approx \frac{\mathrm{dln}N_{\mathrm{A}}}{\mathrm{dln}G} + \frac{\mathrm{dln}\Delta n}{\mathrm{dln}G} \qquad \textbf{2.43}$$

By combining **Equations 2.17 and 2.43**, assuming the τ_{eff} is independent on N_A, the ODF can be expressed as a function of N_A and τ_{eff}:

$$\mathrm{A} = 1 + \frac{\mathrm{dln}p}{\mathrm{dln}G} + \frac{\mathrm{dln}\tau_{\mathrm{eff}}}{\mathrm{dln}G} \approx 1 + \frac{\mathrm{dln}N_{\mathrm{A}}}{\mathrm{dln}G} + \frac{\mathrm{dln}\tau_{\mathrm{eff}}}{\mathrm{dln}G} \qquad \textbf{2.44}$$

If the τ_{eff} is injection level independent or only weakly dependent, meaning that the change of τ_{eff} upon illumination intensity is small enough to be neglected[101], the ODF is determined only by the change of the N_{A} upon illumination intensity, which is due to metastable defects transition:

$$\text{A} = 1 + \frac{\text{d}\ln p}{\text{d}\ln G} \approx 1 + \frac{\text{d}\ln N_{\text{A}}}{\text{d}\ln G} \qquad \textbf{2.45}$$

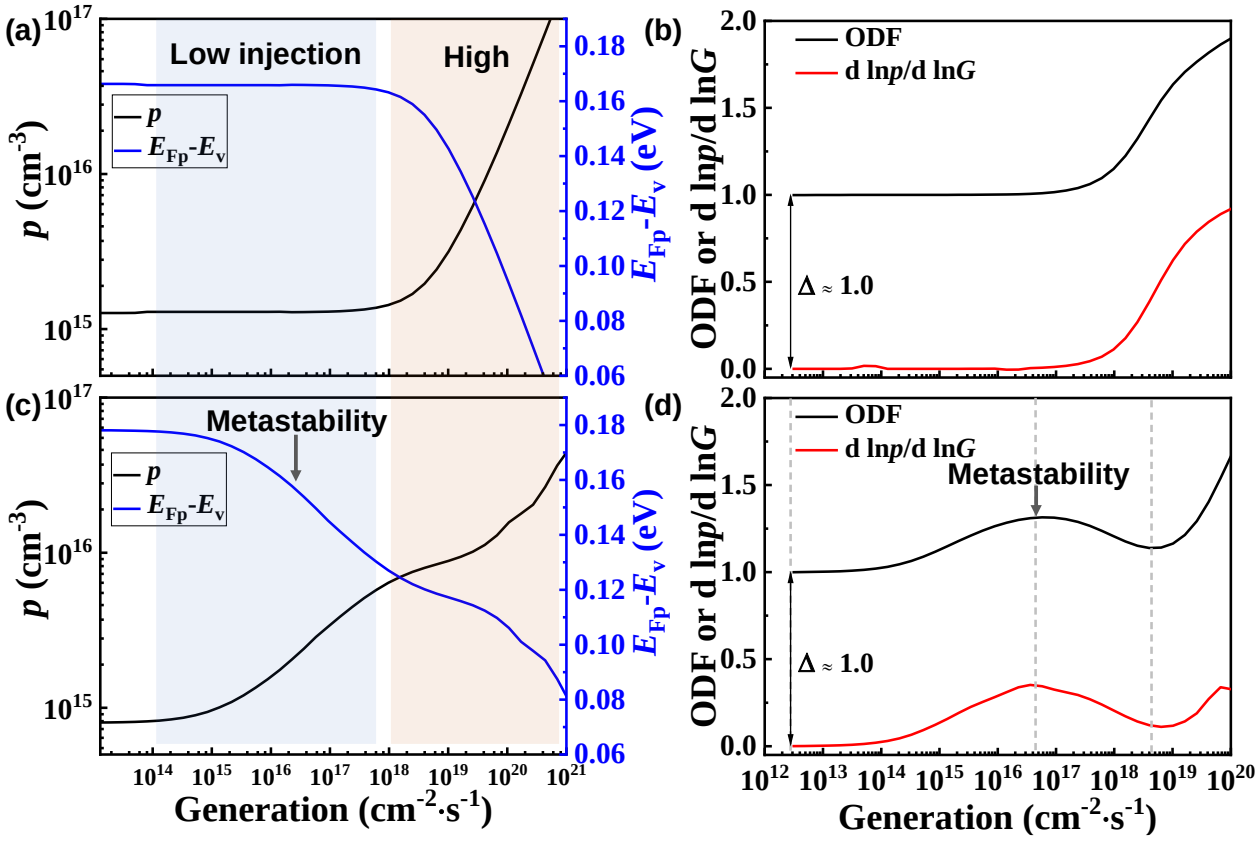

Figure 2.14 The N_{A} and E_{Fp} position as a function of generation: (a) Without metastable defects. When there were no metastable defects, the p is independent with generation in the low injection condition; (c) With metastable defects, the additional holes from the metastable defects transition from donors to acceptors increase the hole density, thus shifting down the E_{Fp}; The ODF and "d ln$p$/d ln$G$" as a function of generation: (b) Without metastable defects, there is no additional increase in N_{A} in the low injection condition, thus leading to the ODF of 1; (d) With metastable defects, the additional holes from the metastable defects transition shift down the E_{Fp}, thus leading to the ODF>1. In the high injection condition, the photon generated free holes and electrons are enough to shift both quasi-Fermi levels, which results in a higher ODF

The change of p as a function of generation is simulated by SCAPS[102], the results are shown in **Figure 2.14**. The details about the simulation set-ups will be discussed in **Section 3.2**. In case there were no metastable defects, the p is independent of generation in the low injection condition as shown in **Figure 2.14 (a)**. As a result, the p related derivative term in **Equation 2.45** can be removed, which leads to the ODF of 1 in the low injection condition as shown in **Figure 2.14 (b)**. In the high injection condition, the amount of photon-generated free holes is comparable to doping level, which shifts both the quasi-Fermi levels of electrons and holes, thus increasing the ODF. When there are metastable defects as shown in **Figure 2.14 (c)**, the hole density increases (shift down of E_{Fp}) with the increase in generation due to the metastable defects transition in the low injection condition, which leads to the ODF>1 as shown in **Figure 2.14 (d)**. Like the situation without metastable defects, in the high injection condition, both quasi-Fermi levels of electrons and holes can be shifted, thus leading to a higher ODF. In addition, the **Equation 2.45** is demonstrated by the simulation as shown in **Figure 2.14 (b) (d)**, which shows the relation between A and "d ln$p$/d ln$G$" follows **Equation 2.45.**

2.5 Doping density and backside recombination velocity

In this thesis, the doping density and backside recombination velocity are critical in determining the efficiency of a solar cell. The doping density of a solar cell refers to the concentration of majority carriers that affects the ΔE_F, while the backside recombination velocity refers to the rate at which charge carriers are lost due to recombination at the backside of the cell.

2.5.1 Determining doping density

With assumptions that doping density and carriers uniformly distribute, the lifetime is independent with doping density, and it is not affected by de-trapping, an optical method based on PL is used to determine the doping density of these samples. Under the steady state, non-equilibrium electron density (Δn) can be estimated by **Equation 2.17**. And the relation between ΔE_F and doping density

is described by **Equation 2.42**. Combining **Equation 2.17** and **Equation 2.42**, the doping density of the absorber can be determined by:

$$N_{\mathrm{A}} \approx p = \frac{\mathrm{d} \cdot N_{\mathrm{c}} N_{\mathrm{v}}}{G \cdot \tau_{\mathrm{n}}^{\mathrm{eff}}} \exp\left(\frac{\Delta E_{\mathrm{F}} - E_{\mathrm{g}}}{\mathrm{k_b} T}\right) \qquad \textbf{2.46}$$

Assuming Fermi-levels are flat and doping are homogeneous, the improvement in V_{oc} due to higher doping density can be estimated by[23]:

$$\Delta V_{\mathrm{oc}} = \frac{\mathrm{k_b} T}{\mathrm{q}} \ln\left(\frac{N_{\mathrm{A1}}}{N_{\mathrm{A2}}}\right) \qquad \textbf{2.47}$$

N_{A1} is improved doping density compared to N_{A2}.

2.5.2 Determining backside recombination velocity

Solving backside recombination velocity graphically from diffusion equation

The lifetime measured by TRPL is an effective lifetime that is influenced by both surface and bulk lifetimes. However, distinguishing between the two can be a significant challenge. To address this issue, a model was previously proposed[103, 104] which provides a mean to separate the contributions of surface and bulk lifetimes. In this section, we summarize the main steps of the derivation for a homogeneous absorber, while the full details can be found in the cited reference[104].

To solve this problem, it is necessary to solve the following equation which describes the transient behavior of carriers:

$$\frac{\partial \Delta n}{\partial t} = D \nabla^2(\Delta n) - \frac{\Delta n}{\tau_{\mathrm{b}}} + G' \qquad \textbf{2.48}$$

In which, Δn is the minority carrier density and G' is the generation rate. D is the diffusivity of minority carrier, which is determined by the Einstein relation, $D = \frac{\mu_{\mathrm{e}} \mathrm{k_b} T}{\mathrm{q}}$, q is elementary charge and μ_{e} is electron mobility. The μ_{e} = 100 $\mathrm{cm^2 V^{-1} s^{-1}}$ used for the calculation is the same as the value involved in the SCAPS simulation. Similar values of μ_{e} were found in Hall measurement on epitaxial n-type films[105].

With two boundary conditions given as:

$$\begin{cases} D\left.\frac{\partial \Delta n}{\partial z}\right|_{z=\mathrm{d}/2} = S_{\mathrm{f}}\Delta n|_{z=\mathrm{d}/2} \\ D\left.\frac{\partial \Delta n}{\partial z}\right|_{z=-\mathrm{d}/2} = -S_{\mathrm{b}}\Delta n|_{z=-\mathrm{d}/2} \end{cases} \quad \textbf{2.49}$$

The *z*-direction corresponds to the depth of the film, with the film thickness denoted by *d*. The midpoint of the film is set to 0, while the front and back surfaces of the film are located at d/2 and -d/2, respectively. **Equation 2.49** states that the surface recombination rate at the semiconductor surface is equal to the minority carrier diffusion flux. The general solution of **Equation 2.48** is:

$$n_{\mathrm{z}}(t) = \sum_{\mathrm{i}=1}^{\infty} \exp\left[-t \cdot \left(\frac{1}{\tau_{\mathrm{b}}} + \alpha_{\mathrm{i}}^2 D\right)\right] \mathrm{A_i} \cos(\alpha_{\mathrm{i}} z + \emptyset_{\mathrm{i}}) \quad \textbf{2.50}$$

Where α_i and $\emptyset_{\mathrm{i}}$ is spatial frequencies and phases, respectively. $\mathrm{A_i}$ is a coefficient. They can be determined by putting the general solution into boundary conditions, **Equation 2.49**, which gives:

$$\tan(\alpha_{\mathrm{i}} d) = \frac{D\alpha_{\mathrm{i}}(S_{\mathrm{f}} + S_{\mathrm{b}})}{(D\alpha_{\mathrm{i}})^2 - S_{\mathrm{f}}S_{\mathrm{b}}} \quad \textbf{2.51}$$

The **Equation 2.50** indicates the total process consists infinitely exponential decay processes. But in most of cases, exponential decay with i > 1 is much faster compared to i = 1, meaning the transient with i > 1 can be ignored. And i = 1 leads to the so-called fundamental mode of recombination. With i = 1, the following equation is given according to **Equation 2.50**:

$$\frac{1}{\tau_{\mathrm{b}}} + \alpha_1^2 D = \frac{1}{\tau_{\mathrm{e}}} = \frac{1}{\tau_{\mathrm{b}}} + \frac{1}{\tau_{\mathrm{s}}} \quad \textbf{2.52}$$

Then τ_{s} is given by:

$$\frac{1}{\tau_{\mathrm{s}}} = \alpha_1^2 D \quad \textbf{2.53}$$

By implementing another assumption that $S_{\mathrm{b}} >> S_{\mathrm{f}}$, **Equation 2.51** (i = 1) and **2.53** can be simplified as[106]:

$$\tau_{\mathrm{s}} = \frac{d}{S_{\mathrm{b}}} + \frac{4}{D}\left(\frac{d}{\pi}\right)^2 \quad \textbf{2.54}$$

The S_b of the reference sample without passivation is assumed to be 10^6 cm/s, based on previous studies[101, 107, 108]. By covering CBD CdS, the S_f can be reduced to 1.4×10^3 cm/s[101]. The ratio of the backside to the front side recombination velocity (S_b/S_f) is approximately 3 orders of magnitude, which satisfies the condition that $S_b >> S_f$. Using **Equation 2.54**, the τ_s of the reference sample can be estimated. Then, by inputting this value of τ_s and the TRPL τ_e into **Equation 2.52**, τ_b of the reference sample can be estimated. Assuming that the τ_b of the studied samples (backside passivated samples) is same to that of the reference sample, as the absorber is prepared using the same method and conditions. Then the τ_b and TRPL measured τ_e of the studied samples can be inputted back into **Equation 2.52** to estimate the τ_s of the studied samples. With the τ_s of the studied samples known, the α_1 of the studied samples can be determined by inputting this value into **Equation 2.53**. To determine the S_b of the studied sample, it is necessary to solve **Equation 2.51** graphically. Using the calculated α_1, the left-hand term of **Equation 2.51** can be plotted, while the right-hand term of **Equation 2.51** can be plotted as a function of S_b on the same scale. The intersection that makes the left-hand term equal to the right-hand term corresponds to the S_b of the studied samples. The experimental results are discussed in **Section 4.4**.

The errors of the S_b estimation

As previously discussed, the model proposed in Ref[103, 104] can be used to estimate τ_b and S_b. However, in realistic cases, not all assumptions of this model are met, leading to potential errors in estimating τ_b and S_b. These deviations include:

1. The model assumes a homogeneous absorber excited by low-energy photons with energy slightly higher than the bandgap of the absorber, meaning a constant generation through the film thickness. However, in our TRPL measurements, we used a laser with a higher energy (1.94 eV) than the bandgap of the absorber (1.0 eV to 1.2 eV), which may result in a non-homogeneous initial carrier generation profile.

2. The model only considers the first term in the summation (i=1) to represent the dominant recombination, resulting in a so-called fundamental lifetime (τ_F). However, it is common in realistic cases to observe biexponential decays, indicating two recombination processes. In this case, a weighted effective lifetime is used to represent the fundamental lifetime.

Although errors in estimating τ_b and S_b may occur, they do not negate the conclusions presented in this thesis. This is supported by the fact that S_b estimated graphically or from SCPAS simulations are similar, and their influence on ΔE_F from experiments agrees well with the simulations.

Chapter 3 Preparation of samples and SCAPS set-ups

Section 3.1 explains the structure of Cu(In,Ga)Se_2 solar cells studied in this work, along with the preparation methods and the function of each layer. Among them, the carrier selective transport structure is particularly interesting and is believed to represent a critical paradigm shift that aims to push efficiency beyond the current record of 23.35%[10, 11, 31]. Additionally, SCAPS simulations give us more insights about working mechanism of solar cells. Therefore, they are widely used in this work to understand the physics of solar cells. The setups for the SCAPS simulation are briefly discussed in **section 3.2**.

3.1 Samples' preparation

This section provides an overview of the samples analyzed in this study. Specifically, we focus on samples with Ga single grading, dielectric layers, and hole selective transport layers. The information presented in this section provides a concise overview of the workflow of this thesis. Subsequent chapters will delve into the results and discussions of these samples in detail.

3.1.1 Samples with Ga back grading (GBG)

To gain insight into the potential improvements in terms of V_{oc} or ΔE_F resulting from reduced backside recombination in our typical 1-stage process prepared $CuInSe_2$, we prepared samples with varying Ga single grading. As illustrated in **Figure 3.1**, we achieved Ga grading by depositing $CuGaSe_2$ precursor layers at a substrate temperature 40°C lower than the highest temperature, followed by 1-stage $CuInSe_2$ deposition. The different Ga gradings were achieved by adjusting either the duration of $CuGaSe_2$ deposition or the highest substrate temperature. Longer periods of Ga supply resulted in a higher Ga content at the backside, producing a higher bandgap gradient towards the backside. Lower substrate temperatures limited the diffusion of Ga from the backside to the frontside, leading to a similar increase in bandgap towards the backside. We prepared three distinct samples, denoted 6m-590, 6m-540, and 8m-590, corresponding to different durations of

$CuGaSe_2$ deposition and highest substrate temperatures, as shown in **Figure 3.1 (b)**. All PL measurements were conducted on samples coated with CBD CdS to minimize frontside recombination.

After annealing our samples on a pre-heated hot plate in air at 200 °C for 2 minutes, we observed an improvement of around 30 meV in V_{oc} (ΔE_F). This annealing was done by putting the samples with CdS on the pre-heated hot plate at the temperature of 200 °C in air. After 2 minutes, the samples were removed from the hot plate onto a glass at the ambient temperature. Then it cooled down naturally in air until reaching ambient temperature. Therefore, the results presented in **Chapter 4** are based on these annealed samples. We also observed a similar improvement in dielectric layer-passivated 1-stage $CuInSe_2$, as discussed in **Section 3.1.2**. However, this improvement was only observed for 1-stage process prepared samples in the early stages of this work and was not involved in the preparation of the other samples studied in **Section 3.1.3**.

To fabricate the solar cells, we deposited the window layers and electrodes sequentially. While not shown in the figure, we also prepared a $CuInSe_2$ reference sample using the same 1-stage process. The results for these samples are discussed in **Chapter 4**.

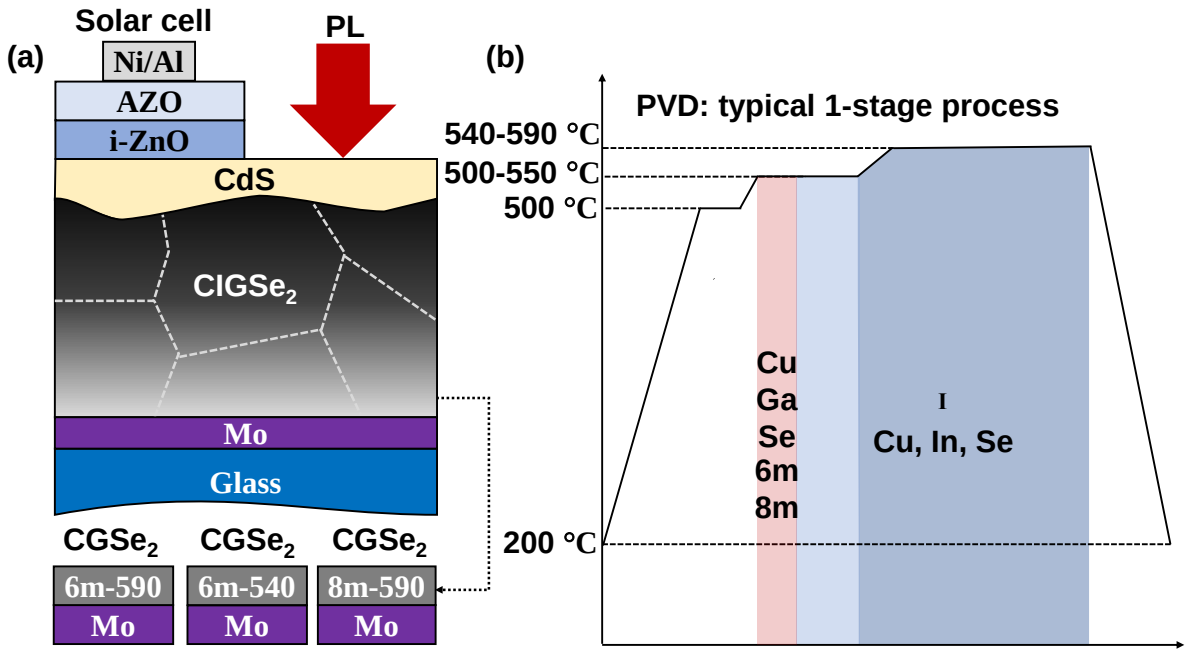

Figure 3.1 (a) The structure of $CuInSe_2$ with a Ga single grading. 6/6/8m-590/540/590: 6/6/8 minutes deposition of $CuGaSe_2$ followed by $CuInSe_2$ growing with substrate temperature of 590/540/590 °C; (b) The preparation process of $CuInSe_2$ with Ga single grading.

3.1.2 Samples with dielectric layers

In addition to the GBG samples, dielectric layers such as Al_2O_3, TiO_2, and glass are used to investigate the effect of backside recombination on the ΔE_F of $CuInSe_2$ solar cells. Dielectric metal oxides have already been widely used in Si solar cells to reduce interface recombination, which shows a decent passivation effect due to the negative fixed charges at the interface, which keeps the carriers away from the metal[109, 110]. For $Cu(In,Ga)Se_2$ solar cells, a high negative fixed charges Q_f of approximately 10^{13} cm^{-2} is experimentally detected between $Cu(In,Ga)Se_2/Al_2O_3$ interface, which lowers the minority carrier density at this interface by roughly 8 orders of magnitude, thus reducing interface recombination[74].

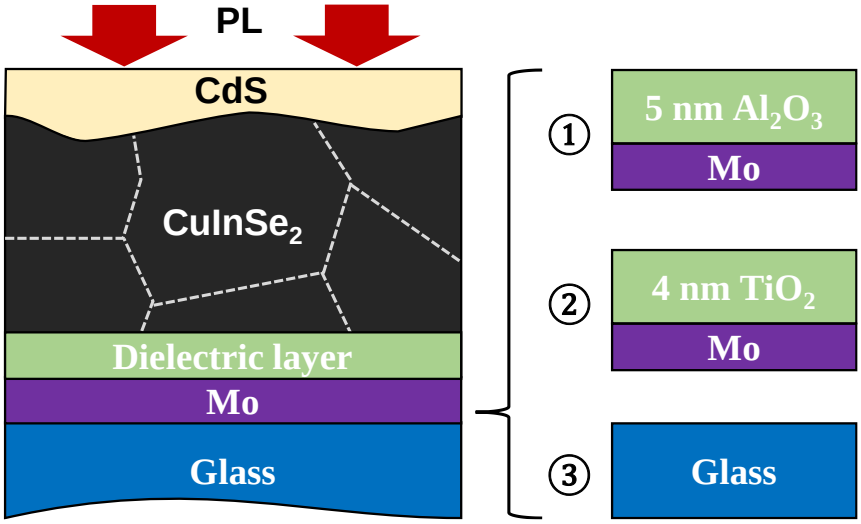

Figure 3.2 The structure of samples passivated by dielectric layers: 5 nm Al_2O_3, 4 nm TiO_2 and soda-lime glass.

To achieve this, a 5 nm layer of Al_2O_3 or a 4 nm layer of TiO_2 is inserted between Mo and $CuInSe_2$, as shown in **Figure 3.2**. Additionally, a sample with $CuInSe_2$ directly grown on soda-lime glass is also prepared, using the same 1-stage process as the GBG samples. To measure PL, all samples are coated with CBD CdS. To improve the V_{oc} (ΔE_F), the same fast annealing process used for the GBG samples is applied to these samples. Because the current blocking effects of thick dielectric layers, no finished solar cells are prepared. The results are discussed in **Chapter 4**.

To make continuous and dense Al_2O_3 or TiO_2 films within thickness of few nanometers, the samples were prepared in Institute for Solar Energy Research in Hamelin (ISFH) by atomic layer

deposition (ALD). The Al_2O_3 layers are deposited via plasma-assisted ALD, with a substrate temperature of 200 °C, using trimethyl aluminum (TMA) as the aluminum precursor and an inductively coupled remote oxygen plasma for oxidation. The applied plasma-assisted ALD process has a growth rate of 1.2 Å per cycle, resulting in an Al_2O_3 layer thickness of 5 nm after 42 cycles.

For the TiO_2 layers, a thermal ALD process is used at the same substrate temperature of 200 °C. The process is carried out using a FlexAl reactor from Oxford Instruments and involves the use of tetrakis (dimethylamino) titanium (TDMAT), H_2O, and N_2 as the titanium precursor, oxidant, and purge gases, respectively. The layer thicknesses are determined by the growth rate of 0.43 Å per cycle, with 100 cycles yielding a thickness of 4 nm.

3.1.3 Samples with hole selective transport layers (HTL)

The primary objective of this study is to identify an effective HTL that can suppress backside recombination and facilitate hole transport. To accomplish this goal, various candidate materials with potential for use as high-quality HTLs are explored, as illustrated in **Figure 3.3**.

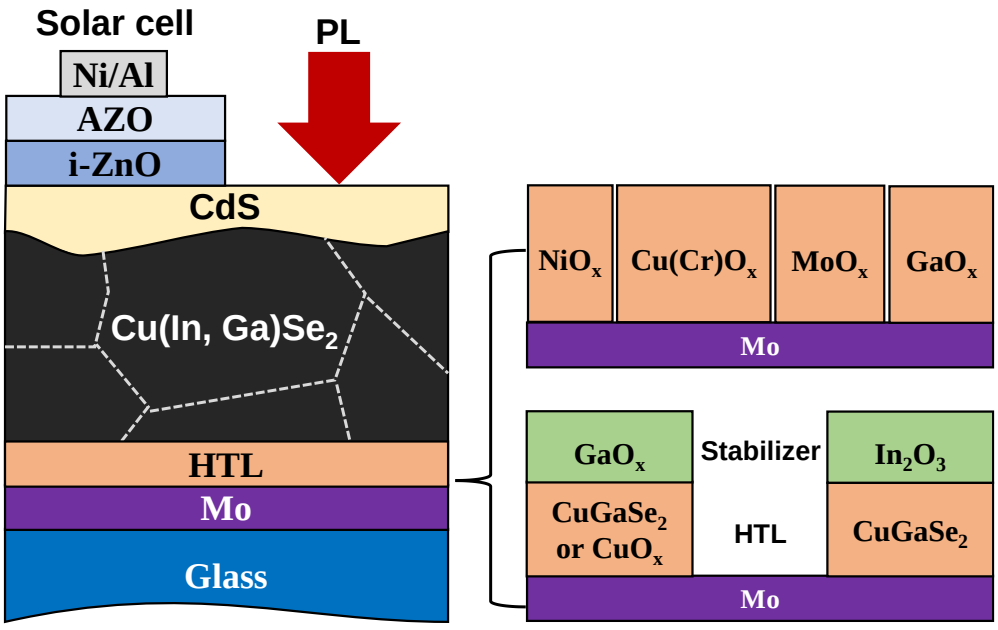

Figure 3.3 The structure of $Cu(In,Ga)Se_2$ solar cells with different HTLs.

NiO_x: Nickel oxide is a p-type semiconductor with a wide bandgap, making it well-suited for use in solar cells due to its favorable band alignment with materials like $Cu(In,Ga)Se_2$[111, 112]. Specifically, the conduction band spike of NiO_x is high enough to minimize backside recombination, while the valence band barrier is not so high as to impede hole transport. This combination of good passivation and transport properties has been observed in various solar cell designs, including those using CdTe[112], Sb_2Se_3[111, 113], and perovskite materials[114, 115]. In this study, a 40 nm-thick layer of NiO_x was deposited onto a Mo substrate using an e-beam evaporator operating at room temperature. The further results are discussed in **A5.1**.

$CuCrO_x$ and CuO_x: They are similar to NiO_x, as both are p-type semiconductors with wide bandgaps. They also has a favorable band alignment with $Cu(In,Ga)Se_2$[116], which makes them potentially useful as working HTLs in solar cells. These material have already demonstrated successful applications as HTL in various types of solar cells, including CdTe[117], perovskites[118-120], and organic solar cells[121]. The further results are discussed in **A5.3**.

MoO_x: While molybdenum oxides do not have an ideal band alignment with $CuInSe_2$, they have been shown to exhibit some passivation effects[122]. In this study, we investigate the passivation effects of thermal evaporated MoO_x thin films at room temperature, and the results are discussed in **A5.4**.

GaO_x: Gallium oxides have been found to have an improper valence band alignment with $Cu(In,Ga)Se_2$, leading to an excessively high transport barrier for holes[123]. This creates additional series resistance, which ultimately reduces the FF[124]. Despite this limitation, it has also been used as an alternative window buffer layer for $Cu(In,Ga)Se_2$ solar cells to mitigate interface recombination[125]. In this thesis, we investigate the passivation and blocking effects of GaO_x, which are presented and discussed in **A5.5**.

During the long-period and high-temperature growth of the absorber, it can be challenging for single layers to remain stable at the backside. In many cases, these layers interact strongly with the absorber by diffusion, leading to damage to either the hole transport layer or the absorber. For example, Cr and Ni have been found to be particularly detrimental to $Cu(In,Ga)Se_2$[126]. To address this issue, we have developed bilayer HTLs in this study. Specifically, oxides such as In_2O_3 or GaO_x are deposited on top of $CuGaSe_2$ or CuO_x to act as stabilizer layers that can prevent the diffusion of the underlying layers. We investigate and compare the blocking ability of In_2O_3

and GaO_x and discuss the transport ability and passivation effect of $CuGaSe_2/In_2O_3$, $CuGaSe_2/GaO_x$, and CuO_x/In_2O_3 individually in **Section 5.2**.

To gain these oxides layers, different technologies are involved:

$CuCrO_x$: They were prepared by chemical vapor transportation (CVD) with help of Luxembourg Institute of Science and Technology (LIST). The films were grown using a MC200 Metal Organic Chemical Vapour Deposition (MOCVD) system, commercially available from Annealsys. Copper bis (2,2,6,6-tetramethyl-3,5-heptanedionate) and Chromium (III) tris(2,2,6,6-tetramethyl-3,5-heptanedionate) (from Sigma Aldrich) were used as precursors while cyclohexane was chosen as solvent for preparing solutions with different concentrations. The solutions were mixed in an equimolar Cu/Cr ratio and then introduced in the canister of the reactor. Nitrogen was used as carrier gas with a flow rate of 350 sccm (standard cubic centimeter per minute) while for the precursor solution a delivery rate of 2 g/min was used. The system uses a tight feedback closed loop which controls the frequency and opening time of injectors/vaporizers in order to ensure a precise quantity of the delivered solution. During the whole deposition process the injectors are kept at 225 °C in order to vaporize the liquid solution coming from the reactor canisters. The substrate temperature for deposition is 400 °C.

In_2O_3 and GaO_x: They were prepared by solution combustion synthesis (SCS) with help of Luxembourg Institute of Science and Technology (LIST). In our case, the solution was prepared by dissolving 1203.2 mg of $In(NO_3)_3 \cdot xH_2O$ in 20 mL of 2-methoxyethanol (2-MOE) to form 0.2 M solutions. 800 µL of acetylacetone ($C_5H_8O_2$) was added as a fuel to the solutions. 90 mL of 14.5 M NH_3 (aqueous) was added to raise the pH and promote the formation of $In(acac)_x$ (acac = $C_5H_7O_2$) complexes of In ions. The solutions were then stirred until they became clear. With this clear solution, the In_2O_3 films were prepared by spin coating the solutions at 3000 rpm for 60 s on the substrates, followed by hot-plate heating at 130 °C for 1 min. The process of spin-coating-drying was repeated four times to achieve 50 nm thickness. Finally, the crystallization of films was performed by placing the samples on hot-plate in air with the setting temperature varying from 200 to 350 °C for 3 min. The GaO_x was prepared by the same method and procedure, the only difference was replacing $In(NO_3)_3 \cdot xH_2O$ by $Ga(NO_3)_3 \cdot xH_2O$

CuO_x: Prepared by SCS with help of Luxembourg Institute of Science and Technology (LIST). For the SCS, the overall preparation process is similar to In_2O_3 or GaO_x, in which the $In(NO_3)_3 \cdot xH_2O$ or $Ca(NO_3)_3 \cdot xH_2O$ is replaced by $Cu(NO_3)_2 \cdot xH_2O$.

3.2 SCAPS simulation setups

SCAPS means Solar Cell Capacitance Simulator which is a one-dimensional solar cell simulator developed at the Department of Electronics and Information Systems of the University of Gent by Prof. Dr. Marc Burgelman and his colleagues[102, 127, 128]. And it is specially optimized for simulating $Cu(In,Ga)Se_2$ and CdTe solar cells. In this work, the SCAPS is widely used to understand or explain the mechanism of solar cells. Basically, there are two sets of parameters are involved in this work for simulation.

In **Chapter 4 and Chapter 6**, the simulation of influence of backside recombination on ΔE_F and the ODF:

Table 3.1 Critical parameters used in SCAPS simulation[90]. The 1 μm $CuInSe_2$ is only applied to simulate the influence of back surface recombination on the ODF.

Parameters		**$CuInSe_2$**
Thickness	**d (μm)**	1 or 3
Band gap	**E_g (eV)**	1.02
Electron affinity	**χ (eV)**	4.5
Dielectric permittivity	**ε (relative)**	13.6
Effective density of states in the conduction band	**N_c (cm^{-3})**	7.78×10^{17}
Effective density of states in the valence band	**N_v (cm^{-3})**	2.1×10^{19}
Electron thermal velocity	**e-V_{th} (cm/s)**	1×10^{7}
Hole thermal velocity	**h-V_{th} (cm/s)**	1×10^{7}

Electron mobility	**e-mobility (cm^2/Vs)**	100			
Hole mobility	**h-mobility (cm^2/Vs)**	25			
Shallow acceptor density	**N_A (cm^{-3})**	8.8×10^{15} – 3×10^{16}			
Shallow donor density	**N_D (cm^{-3})**	/			
Effective radiative recombination coefficient	**B (cm^3/s)**	/	1.4×10^{-13} (1 um)	4.3×10^{-13} (3 um)	
Defect type		/	Single donor(0/+)	Single acceptor(0/-)	neutral
Electron and hole capture cross section	**σ (cm^2)**	/	1×10^{-15}		
Defects density	**N_t (cm^{-3})**	/	8×10^{15} (Metastable defects)		1×10^{15}
Defects position		/	Middle gap	Above E_v 0.2 eV	Middle gap
Defects distribution	**E_t distribution**	/	Uniform		
Surface condition					
Parameters		Back surface	Front surface		
Surface recombination velocity of electron	**S_n (cm/s)**	1×10^0 -1×10^6	1.4×10^3		
Surface recombination velocity of hole	**S_p (cm/s)**	keep the same with S_n	1.4×10^3		
Work function	**W (eV)**	Auto-flat band			

Table 3.2 Metastable defects setting[90]

Name	Individual capture/emission processes	Expression	Energy barrier	Type
'Electron capture'	Electron capture hole emission	$\tau_{\mathrm{EC}}^{-1} = \frac{1}{\nu_{\mathrm{ph}}} c_{\mathrm{n}} c_{\mathrm{p}} n N_{\mathrm{v}} \exp\left(-\frac{\Delta E_{\mathrm{EC}}}{\mathrm{k_b} T}\right)$	$\Delta E_{\mathrm{EC}} = 0.40$ eV	donor-to-acceptor
'Hole emission'	Double hole emission	$\tau_{\mathrm{HE}}^{-1} = \frac{1}{\nu_{\mathrm{ph}}} c_{\mathrm{p}}^2 N_{\mathrm{v}}^2 \exp\left(-\frac{\Delta E_{\mathrm{HE}}}{\mathrm{k_b} T}\right)$	$\Delta E_{\mathrm{HE}} = 0.81$ eV	donor-to-acceptor
'Hole capture'	Double hole capture	$\tau_{\mathrm{HC}}^{-1} = \frac{1}{\nu_{\mathrm{ph}}} c_{\mathrm{p}}^2 p^2 \exp\left(-\frac{\Delta E_{\mathrm{HC}}}{\mathrm{k_B} T}\right)$	$\Delta E_{\mathrm{HC}} = 0.35$ eV	acceptor-to-donor
'Electron emission'	Electron emission hole capture	$\tau_{\mathrm{EE}}^{-1} = \frac{1}{\nu_{\mathrm{ph}}} c_{\mathrm{n}} c_{\mathrm{p}} p N_{\mathrm{C}} \exp\left(-\frac{\Delta E_{\mathrm{EE}}}{\mathrm{k_B} T}\right)$	$\Delta E_{\mathrm{EE}} = 0.94$ eV	acceptor-to-donor

SCAPS is primarily utilized for device simulations, although it is still possible to investigate the ΔE_{F} and ODF of an individual semiconductor layer. The ΔE_{F} can be obtained by computing the difference between the electron and hole quasi-Fermi levels ($\Delta E_{\mathrm{F}} = E_{\mathrm{F}}^{\mathrm{n}} - E_{\mathrm{F}}^{\mathrm{p}}$). To conduct ODF simulations, the neutral density (ND) parameter is changed to realize illumination or generation flux ranging from 10^{12} $\mathrm{cm^{-2}s^{-1}}$ to 10^{21} $\mathrm{cm^{-2}s^{-1}}$.

While SCAPS does not directly provide radiation flux, it is feasible to calculate it by equating the number of photons emitted via radiation with the number of electrons that recombine radiatively. The radiation flux can then be computed using the radiative recombination current density, $\emptyset_{\mathrm{r}} = \frac{J_{\mathrm{r}}}{\mathrm{q}}$, where $\emptyset_{\mathrm{r}}$ is the radiation flux, J_{r} is the integrated radiation recombination current density and q is the elementary charge. All parameters used in these simulations are current state-of-the-art values that are available in studies[90]. It is worth noting some specific settings:

I. The standard thickness of the $CuInSe_2$ layer is 3 μm, while the 1 μm layer is used to simulate the impact of back surface recombination on the ODF, as the thinner $CuInSe_2$ layer exhibits a more pronounced effect.

II. The effective radiative recombination coefficient in this study is determined by equating the radiative recombination flux to the generation flux under one sun, if radiative recombination as the sole recombination pathway (i.e., surface and bulk recombination are set to 0). To achieve this, we set ΔE_F equal to ΔE_F^{SQ}[83]:

$$\emptyset_r = \frac{J_r}{q} = G = d \cdot B n_i^2 \exp\left(\frac{\Delta E_F^{SQ}}{k_B T}\right) \quad \textbf{3.1}$$

Where G is the generation flux, d is the thickness of the absorber, B is the effective radiative recombination coefficient and n_i is the intrinsic charge carrier density. The SCAPS simulator provides us with a thickness-dependent effective radiative recombination coefficient (as shown in **Table 3.1**) that is nearly three orders of magnitude smaller than the actual radiative recombination coefficient[129]. One reason for this is that the model used in this study does not fully satisfy the assumptions of the SQ model, which include a step function of absorptivity, infinite carrier mobility, or zero absorber thickness. Another significant factor is that the radiation flux provided by the SCAPS simulator is an internal radiation flux that does not take into account light outcoupling and photon recycling. Photon recycling occurs because the interface only allows photons within the escape cone to be emitted, while the rest are reflected back into the absorber and absorbed again. As a result, the internal radiation flux obtained from the SCAPS simulator is a factor of $4n^2$ larger than the external radiation flux, where n is the refractive index[24]. To consider both the effects of deviation from the SQ model and the difference between internal and external photon flux, we use this smaller effective B in all simulations.

III: In these simulations, metastable defects with a density of 8×10^{15} cm^{-3} are used, which is comparable to the net doping density that varies from 8.8×10^{15} cm^{-3} to 3×10^{16} cm^{-3}. This is particularly crucial for the metastable transition theory discussed in **Chapter 6** since observing ODF values greater than 1 in the low injection regions is only possible when the number of holes gained from metastable defects conversion is comparable to the net doping density. The donor state of the metastable defects is located in the middle of the band gap, while the acceptor state is positioned 0.2 eV above the valence band edge. Setting both of these states as shallow defects consistently leads to convergence issues in our simulations. It is also essential to note that these metastable configurations are only working when the absorber is considered in equilibrium at each illumination intensity. This implies that the measurement working point and initial working point

of different illumination intensities should be chosen and simulated simultaneously in the "batch" setup of SCAPS.

Devices' simulation in Chapter 5 and Chapter 7:

For the devices' performance simulation, the parameters are based on the Ref[130].

Table 3.3 the parameters for the devices' simulation

Parameters		**AZO**	**i-ZnO**	**CdS/ Zn(OS)**	**CI(G)Se2**	**GaO_x**
Thickness	***d* (μm)**	0.2	0.06	0.04	2/0.9	0.04
Band gap	**E_g (eV)**	3.3	3.3	2.4/3.2	1.0/1.15	4.7
Electron affinity	**χ (eV)**	4.6	4.6	4.2/4.4	4.5	3.2
Dielectric permittivity	**ε (relative)**	9	9	10	13.6	9
Effective density of states in the conduction band	**N_c (cm^{-3})**	2.2×10^{18}				
Effective density of states in the valence band	**N_v (cm^{-3})**	1.8×10^{19}				
Electron thermal velocity	**e-V_{th} (cm/s)**	10^7				
Hole thermal velocity	**h-V_{th} (cm/s)**	10^7				

Electron mobility	**e-mobility (cm^2/Vs)**	100				
Hole mobility	**h-mobility (cm^2/Vs)**	25				
Shallow acceptor density	**N_A (cm^{-3})**	/	/	/	10^{16}	10^{15}
Shallow donor density	**N_D (cm^{-3})**	10^{20}	10^{18}	10^{17}	/	/
Effective radiative recombination coefficient	**B (cm^3/s)**	/	/	/	2.8×10^{-13}	/
Absorption coefficient	α (cm^{-1})	From file			From Model **Equation 7.6**	
		ZnO.abs	ZnO.abs	CdS-base.abs, ZnS.abs	α_0:4×10^4 β_0:1×10^{-12} E_0: 25meV	α_0:4×10^4 β_0:1×10^{-12}
Defect type		D	D	A	Neutral	Neutral
Electron capture cross section	**σ_n(cm^2)**	10^{-15}	10^{-15}	10^{-17}	10^{-15}	10^{-15}
hole capture cross section	**σ_h(cm^2)**	10^{-13}	10^{-13}	10^{-12}	10^{-15}	10^{-15}
Defects density (Neutral)	**N_t (cm^{-3})**	10^{17}	10^{17}	10^{18}	2×10^{14}	10^{17}
Defects position		Middle gap				
Defects distribution	**E_t distribution**	Uniform				

Surface condition			
Parameters		Back surface	Front surface
Surface recombination velocity of electron	**S_n (cm/s)**	10^2 /10^6	1.4×10^3
Surface recombination velocity of hole	**S_p (cm/s)**	10^2 /10^6	1.4×10^3
Work function	**W (eV)**	Auto-flat band	
Front Transmission		0.93/0.99 (wavelength independent)	
Back reflection		0.6/0.95 (wavelength independent)	

Chapter 4 The role of backside recombination

This chapter is based on the published paper[131], in which the influence of backside recombination on the ΔE_F and ODF is discussed. In this chapter, results about influence on ΔE_F are presented. In **Chapter 6**, results about the ODF are discussed.

The interface recombination can dominate the efficiency loss of solar cells, especially when the minority carrier lifetime in the bulk of the absorber is long enough to guarantee a comparable minority carrier diffusion length to the absorber thickness. The backside recombination velocity (S_b) of Cu(In,Ga)Se_2 depends on structure or dopants of the sample, for example, the shape of Ga gradient and Na doping. A literature value of backside recombination velocity of 8×10^4 cm/s was estimated from modeling electron beam induced current (EBIC) characterization[132, 133]. It was also reported that the backside recombination velocity of Cu(In,Ga)Se_2 is related to the amount of NaF supplied during the post-deposition treatment (PDT)[107]. The TRPL simulations were introduced to estimate the backside recombination velocities, which suggest the Na leads to a reduction in backside recombination from $>10^5$ to $<10^2$ cm/s[107]. For the homogeneous absorber, e.g. pure $CuInSe_2$, without the alkalis post-deposition treatment, the backside recombination velocity is believed to be higher than 10^5 cm/s. This was proved by Ref.[101], in which the simulated effective minority carrier lifetime matches well with the experimental results when the backside recombination velocity is higher than 10^5 cm/s. It is noted that the similar results were obtained with backside recombination velocity of 10^5, 10^6 and 10^7 cm/s, meaning the influence of backside recombination is saturated. Other evidence can be found by EBIC modeling, which shows that minority carrier diffusion length is almost the same with backside recombination velocity of 10^5 and 10^7 cm/s[108]. In this chapter, the reasonable value of 10^6 cm/s is implemented to do the simulations and calculations. Therefore, the pure $CuInSe_2$ without Ga lateral gradient suffers a significant $\Delta E_F(V_{oc})$ losses due to the dominant non-radiative recombination taking place at the backside. The development of Ga gradient achieved by a 3-stage process is discussed in **Chapter 2**.

In this chapter, SCAPS simulations and experiments quantitatively show the influence of back surface recombination on the performance of $CuInSe_2$ solar cells. In **section 4.1**, SCAPS

simulation results suggest how much ΔE_F or V_{oc} can be theoretically improved by reducing backside recombination depending on minority carrier lifetime and frontside recombination. In **section 4.2**, the narrow bandgap Cu(In,Ga)Se_2 (E_g = ~1.01 eV) with a Ga back grading (GBG) is discussed, which shows the good passivation effects of GBG. In **section 4.3**, ALD-prepared dielectric thin layers (Al_2O_3 and TiO_2) are introduced to suppress backside recombination, and their effects of reducing backside recombination are discussed. In **section 4.4**, the specific backside recombination velocities of GBG and dielectric layer passivated samples are determined and discussed. The passivation effect of GBG will be shown to be comparable to dielectric layers.

4.1 Overview of ΔE_F loss from SCAPS simulations

The simulation baseline parameters are based on previous studies[90, 130], and they are also summarized in **Table 3.1**. For the typical Cu(In,Ga)Se_2 solar cell without the alkalis PDT, the lifetime is in the range of 25 to 50 ns[134, 135]. With an advanced and optimized growth technology or an alkalis post-deposition treatment, the lifetime longer than 200 ns is achievable[62, 63, 136-138]. Thus, as shown in

Figure 4.1, the ΔE_F as a function of a lifetime (1 to 200 ns) and S_b (1 to 10^6 cm/s) was simulated and plotted.

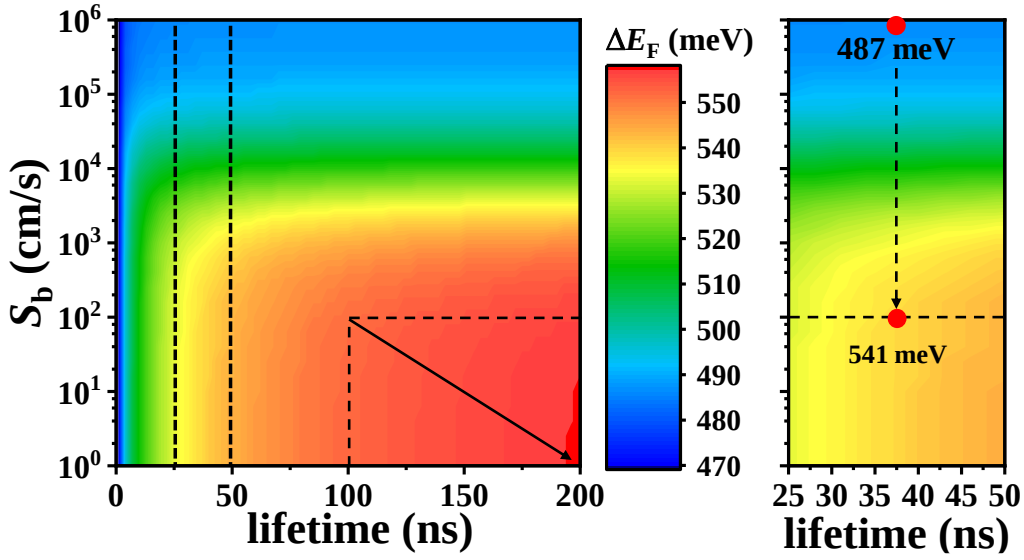

Figure 4.1 SCAPS simulation results of the influence of the backside recombination on ΔE_F depending on minority carrier lifetime: ΔE_F as a function S_b and lifetime. The E_g, N_A and S_f

involved in this simulation are fixed to 1.02 eV, 1×10^{16} cm^{-3} and 1.4×10^{3} cm/s. The second figure is an enlargement of the first figure with a lifetime range from 25 ns to 50 ns. In the right bottom region and along the arrow, ΔE_F barely depends on the bulk lifetime due to the frontside recombination. With an experimental lifetime of 37 ns for Cu poor $CuInSe_2$ grown by 1-stage process, the ΔE_F can be improved from 487 meV to 541 meV by reducing S_b to 10^2 cm/s.

The ΔE_F is simulated because, on the one hand, it is the upper limit of the V_{oc}. On the other hand, it is easier to compare with the experimental ΔE_F determined by transformed absolute PL without need to consider additional non-radiative losses due to the front contact. The ΔE_F in SCAPS simulation is calculated by considering the energy difference between Fermi level of electron and hole at the middle of the absorber ($\Delta E_F = E_{Fn} - E_{Fp}$). In this simulation, the bandgap (E_g), doping density (N_A) and frontside recombination velocity (S_f) are fixed to 1.02 eV, 1×10^{16} cm^{-3} and 1.4×10^{3} cm/s. The E_g of 1.02 eV is close to the value of stoichiometric sample (Cu/In=1). In a realistic case, the E_g of samples, specifically the sample without Ga (~0.99 eV), is slightly lower than 1.02 eV due to the tail states introduced by Cu deficits (Cu/In<1)[139]. The sample with GBG has bandgap of ~1.01 eV that is higher than Ga free samples due to the diffusion of Ga. The higher bandgap contributes to higher ΔE_F in simulations. But it will not change the conclusion because the ΔE_F improvement is considered. The doping density of 10^{16} cm^{-3} is a moderate value that is widely reported[140]. By applying a CdS covering, it is possible to achieve a low frontside recombination velocity at a magnitude level of three (~10^3 cm/s) [101]. The ΔE_F of the absorber is proportional to the logarithm of the effective lifetime, meaning the longer effective lifetime leads to a higher ΔE_F. This lifetime depends on recombination taking place on the surfaces and bulk, the higher recombination leads to a short effective lifetime. As suggested by the simulation results, with a high $S_b>10^4$ cm/s, then increasing the bulk lifetime does not effectively improve ΔE_F. This is because the effective lifetime is primarily affected by backside recombination, meaning that the ΔE_F loss is dominated by the backside recombination. With $S_b<10^3$ cm/s, the dominant recombination shifts from the backside to the bulk, thus the ΔE_F increases obviously from 470 meV to 550 meV with the increase in lifetime until 100 ns. As shown in right bottom region of **Figure 4.1** with the arrow, when the lifetime is beyond 100 ns, ΔE_F barely depends on bulk lifetime because the ΔE_F loss is dominated by the frontside recombination, which will be discussed later in **Figure 4.2**. For the best 1-stage $CuInSe_2$ prepared up to now in this work, the bulk lifetime is

around 37 ns. The estimation of the bulk lifetime will be discussed in **section 4.4**. With this lifetime, the simulation results predict an improvement in ΔE_F of ~50 meV from 487 meV to 541 meV by lowering S_b to 10^2 cm/s.

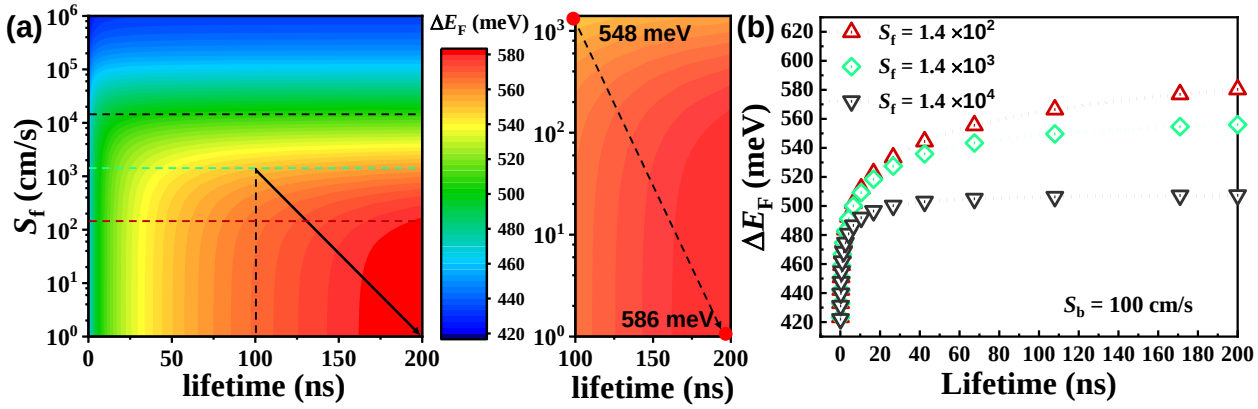

Figure 4.2 The influence of the frontside recombination on ΔE_F depending on minority carrier lifetime, simulation is done by SCAPS: (a) ΔE_F as a function S_f and lifetime. The E_g, N_A and S_b involved in this simulation are fixed to 1.02 eV, 1×10^{16} cm^{-3} and 10^2 cm/s. The second figure is an enlargement of the first figure with a lifetime range from 100 ns to 200 ns and the S_f range from 1.4×10^3 to 10^2 cm/s, which more clearly shows this improvement is from 548 meV to 586 meV (b) The ΔE_F as a function of lifetime corresponding to the dashed lines with same the color in **Figure 4.2 (a)**.

The influence of frontside recombination on ΔE_F is shown in **Figure 4.2**, which has a similar effect as the backside recombination. However, it has an even stronger impact on ΔE_F loss because most of photons are absorbed in the near frontside where the generation of minority carrier is higher and recombination takes place before carriers' diffusion. As a result, the high S_f of 10^6 cm/s can lead to an even lower ΔE_F of 420 meV compared to the situation with S_b of 10^6 cm/s. When the bulk lifetime is extremely short, for example it is lower than 10 ns, changing S_f from 10^0 to 10^4 cm/s only has tiny influence on ΔE_F because the loss due to non-radiative recombination is dominated by the short bulk lifetime. With increase in bulk lifetime, the lower S_f leads to a much higher ΔE_F, which means the front surface recombination starts taking over the main non-radiative losses. **Figure 4.2 (b)** corresponds to the dashed lines in **Figure 4.2 (a)** with the same color, which shows a specific case of front surface recombination. For the case with S_b of 1.4×10^4 cm/s that is 1 order magnitude larger than the value can be achieved by CdS covering, the improvement in ΔE_F is

almost saturated when the bulk lifetime is longer than 30 ns. Meanwhile, reducing S_f can obviously improve ΔE_F, and this improvement is higher with a longer bulk lifetime, meaning the dominant recombination starts shifting from the bulk to the front surface. With the experimental lifetime of 37 ns, the further decrease in S_f by one order of magnitude to 1.4×10^2 cm/s doesn't make much difference as shown between the green and the red curves in **Figure 4.2 (b)**. But when increasing S_f by one order of magnitude, the decrease in ΔE_F is around 25 meV which is not negligible as shown by the black curve.

4.2 Passivation by Ga back grading (GBG)

Even with a thick absorber of 3 μm and a moderate lifetime of 37 ns, the SCAPS simulation results suggest that another ~50 meV improvement in ΔE_F can be achieved by reducing the backside recombination. Then it is interesting to check how much improvement in ΔE_F can be achieved experimentally. The easiest and most accessible strategy to suppress backside recombination is using Ga back grading (GBG) in which the narrow bandgap Cu(In,Ga)Se_2 (E_g = ~1.01 eV) is grown with a high Ga profile towards the backside. To realize such a Ga gradient, thus a conduction band minimum gradient, a $CuGaSe_2$ precursor was introduced before the $CuInSe_2$ deposition. The reference sample is a pure $CuInSe_2$ grown by 1-stage process with substrate setting temperature of 590°C. The other three samples have different Ga profiles as shown in **Figure 4.3**. The different Ga profiles are achieved either by changing the amount of the $CuGaSe_2$ or the $CuInSe_2$ deposition temperature as discussed in **Section 3.1.1**. The notation 6m-540, 6m-590, or 8m-590 refers to the deposition process of a sample consisting of two layers: first, a pre-deposition of $CuGaSe_2$ for either 6 or 8 minutes, followed by deposition of 1-stage $CuInSe_2$. The highest setting temperature for the substrate during the $CuInSe_2$ deposition step is either 540 °C or 590 °C, depending on the case. Notably, the substrate temperature during the $CuGaSe_2$ pre-deposition step is 40 °C lower than the maximum temperature used for the $CuInSe_2$ deposition. Cu/III ratio of these samples are around 0.96 that was determined by EDS. All samples are covered by CBD CdS to minimize frontside recombination. In addition, all the samples had a 2-minutes fast annealing in air on a pre-heated hot plate at the temperature of 200 °C. The details about samples' preparation are discussed in **Section 3.1.1**.

The Ga lateral profile was measured by non-calibrated secondary ion mass spectrometry (SIMS) and then the absolute value of Ga/(Ga+In) (GGI) is calibrated by the corresponding PL, which is discussed in **section 2.3.5**. The calibrated results of GGI and correlated E_g are shown in **Figure 4.3 (b)**. The 8m-590 sample with the thickest $CuGaSe_2$ precursor layer has the highest E_g at the backside. To have a higher Ga at the backside with a thinner $CuGaSe_2$, we can reduce the diffusion of Ga by reducing the substrate temperature from 590 °C to 540 °C. As a result, the 6m-540 sample has a similar but slightly lower E_g even with a thinner $CuGaSe_2$ precursor layer. Among the samples tested, the 6m-590 sample exhibits the flattest Ga profile, resulting in a flatter E_g. This can be attributed to the thinner $CuGaSe_2$ precursor layer and higher $CuInSe_2$ deposition temperature, the thinner $CuGaSe_2$ reduces the total amount of Ga and the higher temperature promotes its diffusion from the backside into the bulk. A higher content of Ga towards the backside results in a higher E_g and a corresponding increase in the conduction band minimum. This leads to a reduction in minority carrier (electron) density, enabling lower backside recombination that is proportional to the minority carrier density. This relation can be described by the simplified **Equation 4.1**:

$$U_s^{gra} \approx S_b \Delta n_{gra} = S_b \Delta n_{flat} \exp\left(\frac{-\Delta E_c}{k_b T}\right) = S_b^{eff} \Delta n_{flat} \qquad \textbf{4.1}$$

Where Δn_{gra} and Δn_{flat} are minority carrier density of GBG and Ga free sample, respectively. S_b is the backside recombination velocity of the Ga free sample, which is 10^6 cm/s[101]. ΔE_c is the conduction band minimum offset when compared to Ga free sample with a flat band. S_b^{eff} is the effective backside recombination velocity that is equal to $S_b \exp\left(\frac{-\Delta E_c}{k_b T}\right)$, which is an equivalent backside recombination velocity by considering the minority carrier density. However, it does not satisfy the definition of the backside recombination velocity that is only determined by defects density and carrier capture cross-section. By doing this, the backside recombination of samples with different passivation can be easily compared. Then according to the E_g depth profile shown in **Figure 4.3 (b)**, the effective backside recombination velocities of samples are determined based on **Equation 4.1**. The 8m-590 sample with the highest E_g has the lowest backside recombination velocity around 6.2×10^3 cm/s. The 6m-590 sample with the flattest E_g has the highest backside recombination velocity of around 4.3×10^4 cm/s. The 6m-540 sample has a moderate value that is around 9.2×10^3 cm/s. The estimated values are based on the assumption that the Fermi level of

electrons is flat. However, this assumption might lead to an overestimation of the effective backside recombination velocity, especially in cases where the electron's diffusion length greatly exceeds the absorber's thickness, which causes the Fermi level bending towards the backside. Nevertheless, for 1-stage process prepared sample with a relatively shorter bulk lifetime and thus a shorter diffusion length, the bending of the Fermi level is not significant. As a result, the error in estimation using this method remains acceptable. This is supported by similar backside recombination velocities determined through alternative approaches. The details of backside recombination velocities' determination and comparison of different samples are discussed in **section 4.4**.

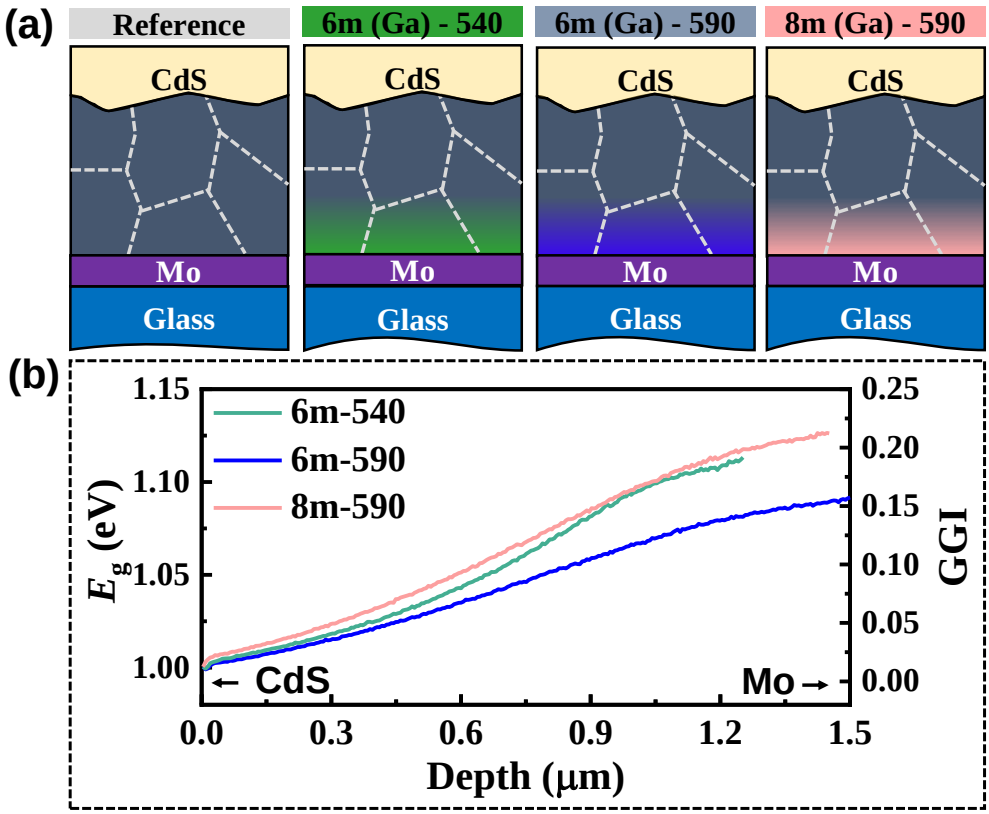

Figure 4.3 (a) The different Ga profiles of studied samples were realized by tuning the thickness of $CuGaSe_2$ or the substrate temperature. The reference sample was produced using a one-stage process in which $CuInSe_2$ was directly grown on Mo. 6m/8m means the deposition duration of $CuGaSe_2$ precursor is 6/8 minutes, because the fluxes of sources are fixed, the longer deposition time means a thicker $CuGaSe_2$ layer. And 540/590 means the highest substrate setting temperature of $CuInSe_2$ grown by 1-stage process is 540/590 °C. It is noted that the setting

temperature of $CuGaSe_2$ is 40 °C below the highest setting temperature of $CuInSe_2$; (b) The Ga lateral depth profile and correlated E_g, which is determined by non-calibrated SIMS and PL The details can be found in method **Section2.3.5**.

Theoretically, the backside recombination is suppressed by a higher conduction band minimum toward the backside. The experimental proof of passivation by GBG is firstly given by the time-resolved photoluminescence (TRPL) that shows the PL counts decay as a function of time. According to the 2-exponential decay function, the lifetime τ_1 and τ_2 with their weight factor A_1 and A_2 can be fitted. Then, the weighted effective lifetime is determined based on **Equation 2.33**. Before the measurements, the samples are covered by CBD CdS and experienced a 2-minute annealing in air at temperature of 200 °C. As shown in **Figure 4.4**, the Ga free sample with a flat band has the fastest decay which leads to the shortest effective lifetime around 3.0 ns. The lifetime of GBG sample depends on the ΔE_c, meaning the higher ΔE_c results in a longer lifetime up to 13.3 ns. For the absorber grown by the same process and covered with the same CdS, the bulk and frontside lifetime among different samples can be assumed to be rather similar, the longer effective lifetime means a longer backside lifetime with less backside recombination. It agrees with the effective backside recombination velocity determined by **Equation 4.1**. The 6m-540 sample has a lower backside recombination velocity than the 6m-590 sample, but because the lower growth temperature gives a lower-quality absorber[141], its effective lifetime is a bit shorter than the 6m-590 sample.

With the same doping density, the longer effective lifetime indicates a higher ΔE_F. The ΔE_F can be determined by absolute PL as shown in **Figure 4.4 (c)**. Based on Planck's Generalized Law, the absolute PL spectra can be transformed according to **Equation 2.27**, by fitting the high photon energy part of the transformed absolute PL spectra where the fitting temperature is fixed to ambient temperature and absorptivity $a(E) = 1$, the ΔE_F is obtained as an intercept. More details about absolute PL and ΔE_F determination are discussed in **Section 2.3.2**. The ΔE_F of different samples are summarized in **Figure 4.4 (d)**. It shows that the Ga free reference sample has the lowest ΔE_F of ~499 meV, and the ΔE_F is obviously improved for samples with GBG. The highest ΔE_F of ~547 meV is achieved by the 8m-590 sample, which suggests an improvement in ΔE_F of ~50 meV compared to the reference sample. This improvement fits very well with the prediction of the

SCAPS simulation, meaning the improvement in ΔE_F by reducing the backside recombination is confirmed by both experiments and simulations.

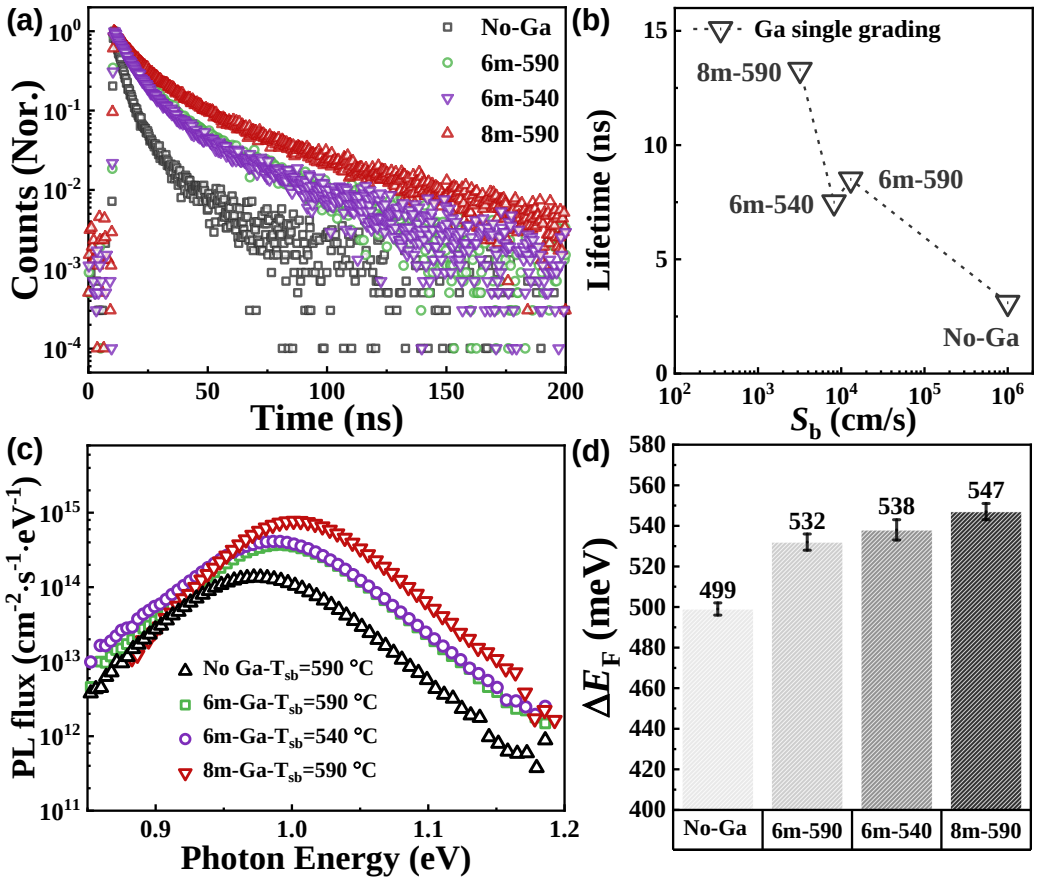

Figure 4.4 (a) TRPL of the samples with or without GBG; (b) The weighted effective lifetime (**Equation 2.33**) of different samples with respect to the S_b that is determined by the SCAPS simulation (**Section 4.4**); (c) The absolute PL spectra of different samples with One-Sun equivalent illumination intensity; (d) The ΔE_F of different samples acquired by fitting high energy part of absolute PL spectra according to the Planck's Generalized Law.

In the case of solar cells, GBG samples underwent a fast-annealing process for 2 minutes at a temperature of 200 °C in air. These samples exhibited a lower V_{oc} of around 20 mV compared to the measured ΔE_F/q. This reduction in V_{oc} can be attributed to additional recombination caused by unoptimized front surface (contacts)[142]. It's worth noting that no fast-annealing treatment was applied to the reference solar cells without GBG, which resulted in significantly lower V_{oc} compared to ΔE_F/q of the reference sample with fast annealing. Assuming that the observed 30

meV improvement in ΔE_F due to fast annealing contributes equally to the V_{oc} improvement of the reference solar cells, the best GBG solar cells (6m-540) show a 45 mV higher V_{oc} than the reference solar cells. This improvement supports the previously discussed enhancement in ΔE_F and validates the effectiveness of GBG's backside passivation.

Because of the unoptimized Ga gradient or contacts, *J-V* curves of 6m-540 and 6m-590 samples show a high series resistance (R_s) which leads to a low FF of ~50%. In an optimized case, e.g. the 8m-590 sample, a high FF up to 75% can be achieved. The high FF is due to a decent low R_s and a rather low diode factor which will be discussed later in **Section 7.3**. Regarding J_{sc}, no obvious differences are found among these samples. With the highest V_{oc} and FF, the 8m-590 sample achieves the highest efficiency of around 15.6%.

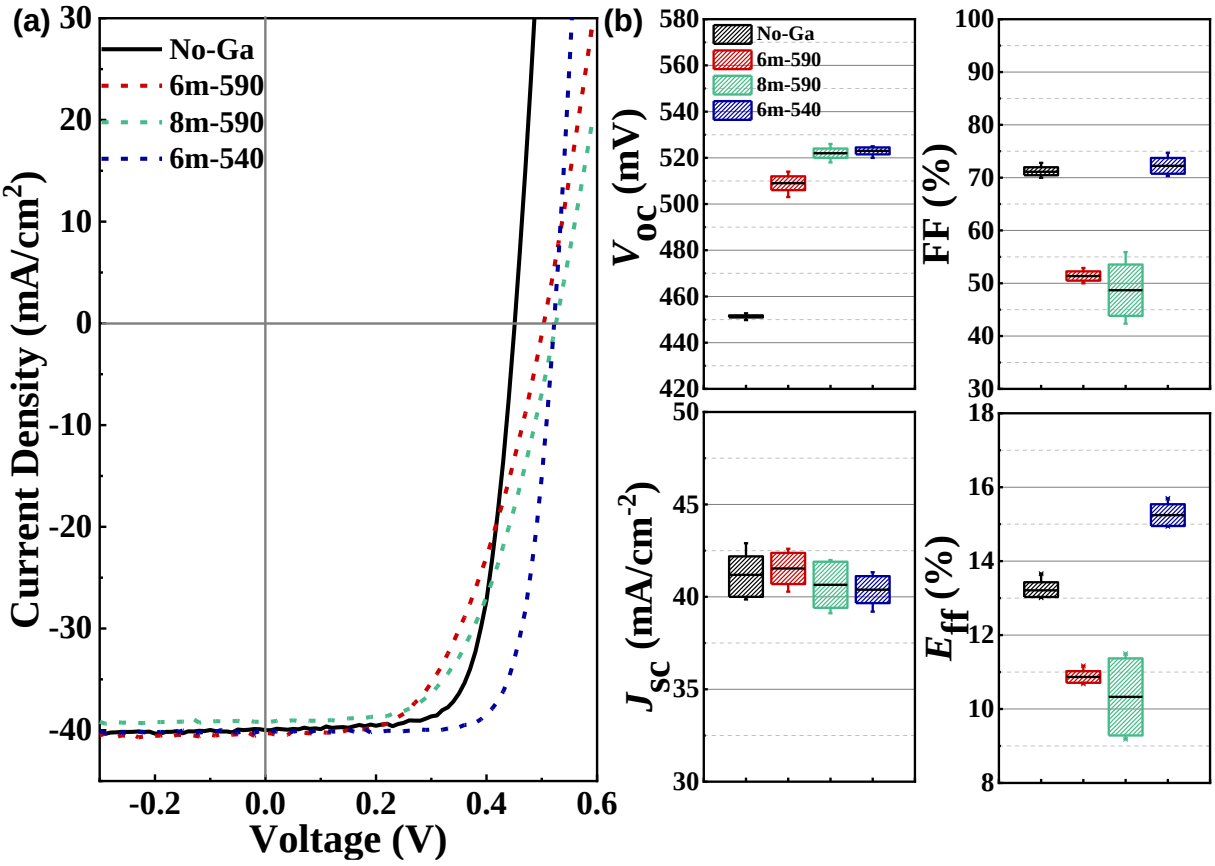

Figure 4.5 (a) Illuminated *J-V* curves of samples with or without GBG; (b) The box plot, in which the box represents the interquartile range (25th to 75th percentile), the line is the mean value and the whisker is based on 1.5 IQR (interquartile range) value: Statistical results of V_{oc}, FF, J_{sc} and E_{ff}.

4.3 Passivation by metal oxides (Al_2O_3 and TiO_2)

Besides introducing a GBG, dielectric metal oxides, e.g. Al_2O_3 and TiO_2, were also used to suppress backside recombination for $CuInSe_2$ solar cells. Passivation effects have already been confirmed in $Cu(In,Ga)Se_2$ devices, as improvements in V_{oc} have been observed with the use of patterned Al_2O_3 or fully covered TiO_2[75, 143, 144].

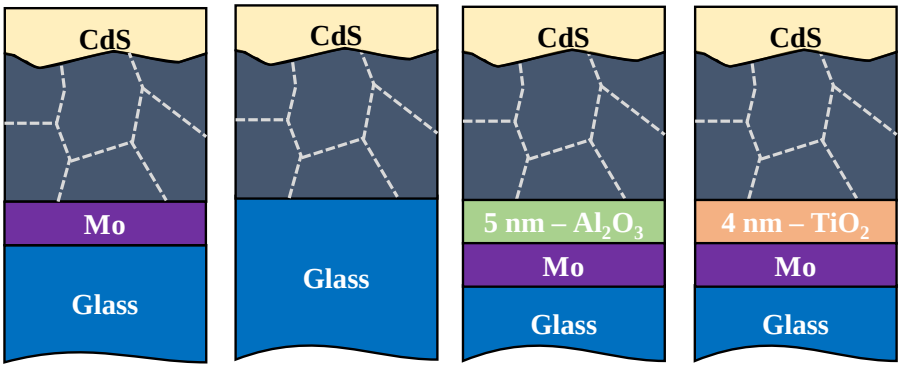

Figure 4.6 The structures of samples that are used to study the passivation effects of Al_2O_3, TiO_2 and SiO_2 (glass).

To verify the passivation effects of dielectric layers for $CuInSe_2$, ALD prepared 5 nm Al_2O_3 and 4 nm TiO_2 are used to suppress the backside recombination of pure $CuInSe_2$. These Al_2O_3 and TiO_2 were prepared by Institute for Solar Energy Research in Hamelin (ISFH). The conditions of preparation are explained in **Section 3.1.2**. The sample structures studied are shown in **Figure 4.6**, three samples are passivated by 5 nm Al_2O_3, 4 nm TiO_2 or sola-lime glass, and the reference sample is directly grown on Mo. The sample grown on soda-lime glass is considered to be passivated by SiO_2. The $CuInSe_2$ is grown by a one-stage process with the Cu/In = 0.87, which is determined by the EDS. The highest substrate setting temperature during the $CuInSe_2$ deposition is 590 °C. All the samples are covered by CBD CdS to minimize the frontside recombination and avoid the degradation because of oxidization. And then the samples are annealed in air at temperature of 200 °C for 2 minutes. The passivation effect is first confirmed by the TRPL measurements shown in **Figure 4.7 (a)**. The Mo reference sample has the fastest PL counts decay with respect to the time, thus the shortest effective lifetime around 6 ns. This lifetime is a bit longer than the lifetime of the reference sample of the GBG series (3 ns), which is likely due to a more Cu-poor absorber[145]. Improvement in lifetime is observed after using different dielectric layers. Among

them, the passivation effect of Al_2O_3 is the best, which leads to the longest lifetime of 29 ns. The TiO_2 and glass are less effective to reduce recombination, but they also have a good capacity to suppress backside recombination that results in a longer lifetime of 16 ns and 20 ns, respectively. The longer lifetime is attributed to the lower backside recombination velocity. **Figure 4.7 (b)** shows that the lower S_b leads to a longer lifetime, which again proves the good passivation of dielectric layers. The backside recombination velocity is estimated by SCAPS simulation, which will be discussed later in **Section 4.4**.

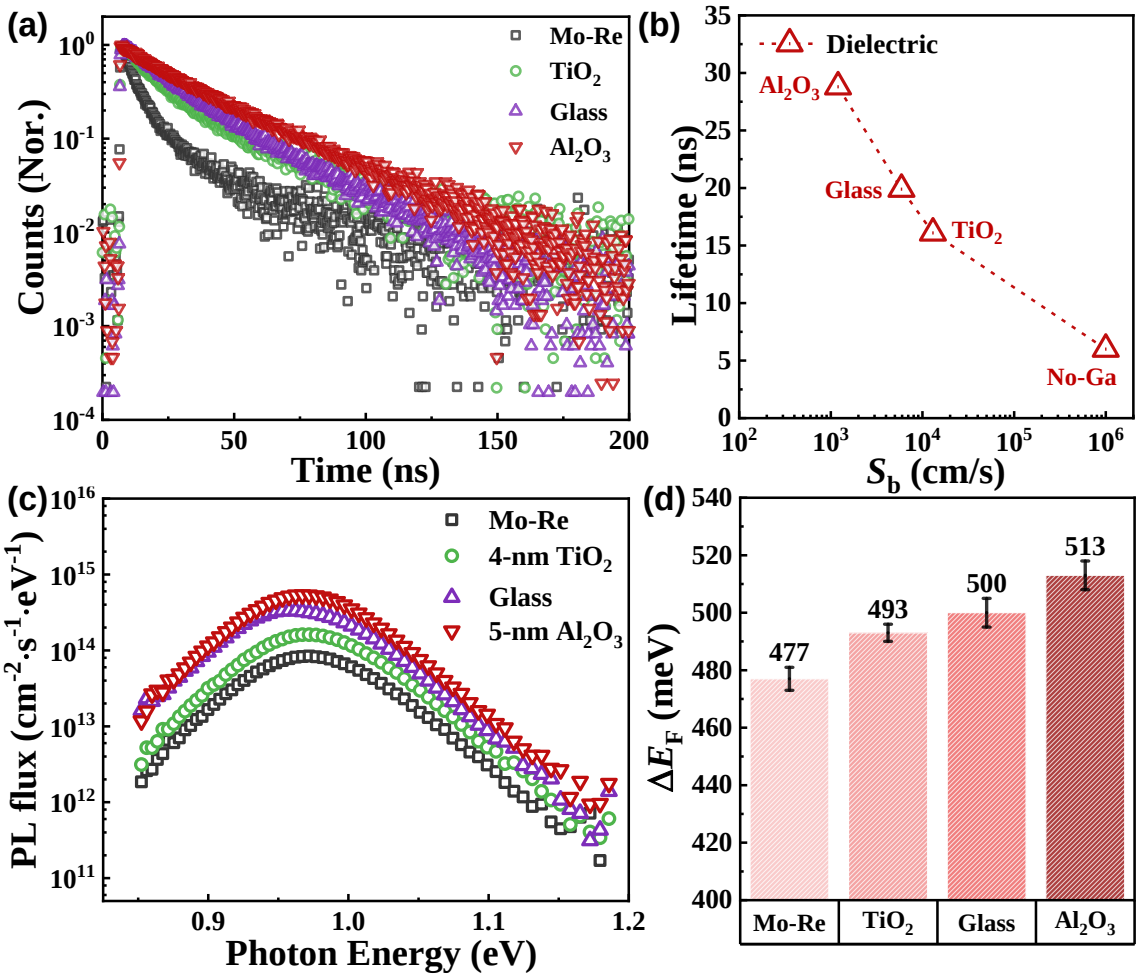

Figure 4.7 (a) TRPL of the different samples with or without dielectric layers (Al_2O_3, TiO_2 or soda-lime glass); (b) The weight effective lifetime of different samples with respect to the corresponding S_b. The S_b is estimated from SCAPS simulation as discussed in **Section 4.4**; (c) The absolute PL spectra of different samples under one-Sun equivalent illumination intensity; (d)

The ΔE_F is calculated by fitting high energy wing of transformed absolute PL spectra according to the Planck's Generalized Law.

Another proof of passivation is the improvement in ΔE_F. As shown in **Figure 4.7 (c)**, the ΔE_F is obtained by fitting the high energy wing of the transformed absolute PL spectra with the fitting temperature fixed to ambient temperature. The results summarized in **Figure 4.7 (b)(d)** show that the increase in ΔE_F relies on the lifetime, the longer lifetime leads to a higher ΔE_F. The highest ΔE_F of ~513 meV can be achieved by using Al_2O_3. Compared to the Mo reference sample without any passivation, the improvement in ΔE_F is around 50 meV which is similar the result of GBG samples. A similar improvement suggests that the passivation effect of GBG is comparable to dielectric metal oxides.

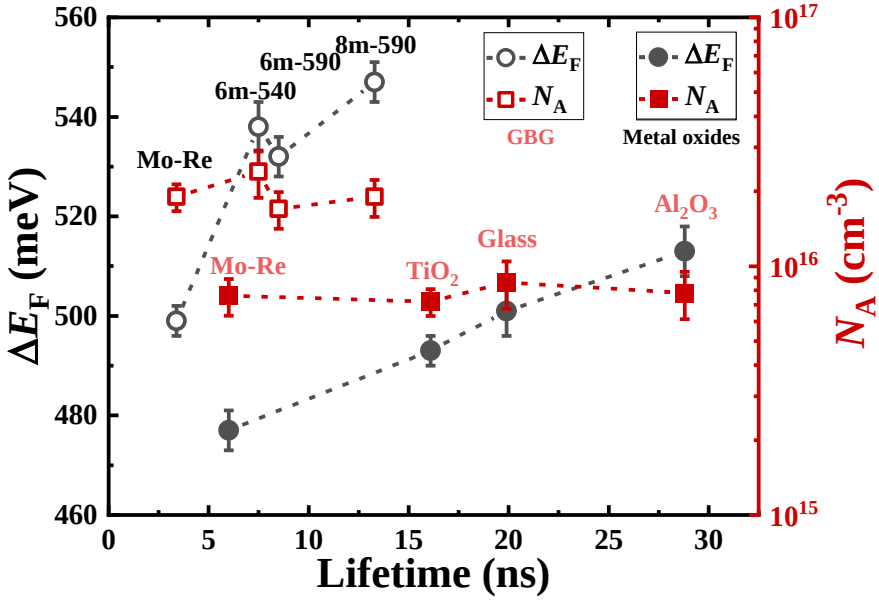

Figure 4.8 The comparison of ΔE_F, effective lifetime and doping density of different samples. The GBG samples have shorter lifetime, but higher doping density compared to the dielectric layer passivated samples. Consequently, the GBG samples have higher ΔE_F compared to dielectric layer passivated samples.

Assuming the Fermi levels of electron and hole are flat across the absorber, with the same doping density, the longer lifetime means a higher ΔE_F. However, as shown in **Figure 4.8,** the metal oxides passivated samples have longer lifetime but lower ΔE_F, indicating they have lower doping density

compared the GBG series. The lower doping density is likely due to the low Cu/In ratio, which results in a higher density of In_{Cu} antisite defect that is a shallow donor[43, 146-148]. To verify this, an optical method based on PL is used to determine the doping density of these samples. According to **Equation 2.46**, the estimated doping density of dielectric series and GBG series are around 8.0×10^{15} cm^{-3} and 1.8×10^{16} cm^{-3}. The doping density of each sample is shown in **Figure 4.8**, which confirms the higher doping density of GBG samples.

4.4 Comparing the passivation of GBG and dielectric layers

Although, the comparable passivation effects of GBG and dielectric oxides are indicated by the similar improvement in ΔE_F. The backside recombination velocity is a better parameter to show the quality of the interface. Unlike GBG samples where the backside recombination velocity can be straightforwardly estimated by **Equation 4.1**, the backside recombination velocity of dielectric layer passivated sample can be solved graphically or numerically by SCAPS simulation. To make the simulations reliable and based on realistic experiments, we need three experimental parameters that are doping density (N_A), thickness (d), and bulk lifetime (τ_b) of the absorber.

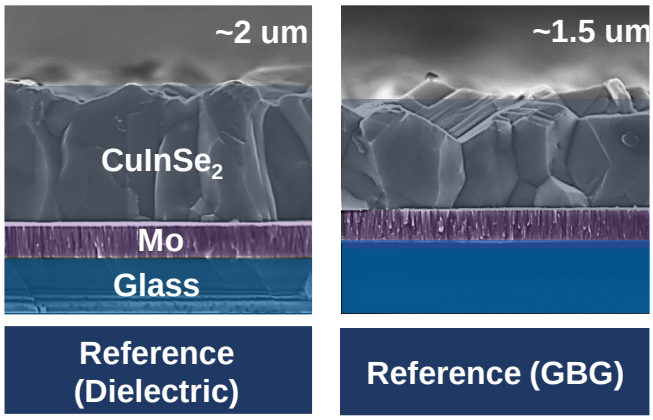

Figure 4.9 SEM cross-section of the reference sample of the dielectric layer and GBG passivated series. From the top to the bottom, there are $CuInSe_2$, Mo and soda-lime glass.

For the doping density, it has been already calculated via PL based methods as discussed in **Section 4.3**. The thickness of the absorber layer is confirmed by an SEM cross-section image as shown in **Figure 4.9**. The absorber thickness of the dielectric layer and GBG series is around 2.0

μm and 1.5 μm. While we did not verify the thickness of every sample using SEM cross-section, we are confident that the thickness is consistent within each series. This is because each series was prepared using the same recipe and within a short time frame. Within this period, the reproducibility of the samples is guaranteed by our stable PVD system.

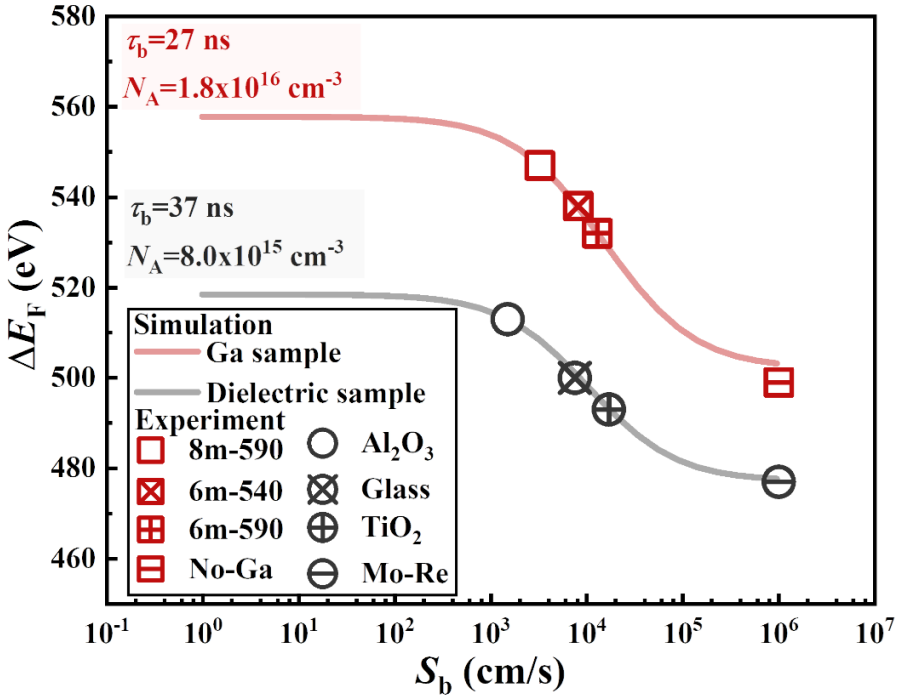

Figure 4.10 The ΔE_F as a function S_b depending on different bulk lifetime and doping density: the solid lines are SCPAS simulated results. The symbols are experimental results. By comparing the experimental ΔE_F to the simulated results, the corresponding S_b of each sample can be determined.

For the bulk lifetime, it can be estimated from the reference sample that has a backside recombination velocity around 3 orders of magnitude higher than the frontside. With the boundary condition $S_{back} >> S_{front}$, the τ_s of the reference sample without backside passivation can be estimated according to **Equation 2.54**. Using τ_s and weighted effective lifetime (τ_e) measured from the TRPL, the bulk lifetime (τ_b) can be determined by the **Equation 2.52**. The τ_b of the reference samples for the GBG and dielectric layer passivated series are estimated to be 27 ns and 37 ns, respectively. It was assumed that the backside passivated samples have the same τ_b as their corresponding reference samples, since they were prepared under similar conditions. Using the

experimentally determined values of N_A, d, and τ_b, we conducted SCAPS simulations to predict the ΔE_F as a function of S_b. The simulation results, represented by solid lines in **Figure 4.10**, are compared to the experimentally determined ΔE_F to estimate the S_b of the backside passivated samples. It should be noted that the assumption of using the same τ_b for all samples may be problematic for the 6m-540 sample, as it was prepared under a lower substrate setting temperature compared to the reference sample. This lower temperature can result in a shorter τ_b for this sample, which would require a lower S_b to achieve the same ΔE_F. Therefore, the higher τ_b involved in the simulation may overestimate the S_b of this sample. However, this error is considered acceptable, as the S_b calculated from **Equation 4.1** is very close to the value estimated from the SCAPS simulation (**Table 4.1**). Additionally, this suggests that decreasing the substrate setting temperature from 590°C to 540°C may not have a significant influence on τ_b. Otherwise, a clear difference in the estimated S_b between the two methods would have been expected.

Considering the S_b estimates obtained from SCAPS simulation, it can be inferred that the GBG samples exhibit S_b values that are of the same order of magnitude as those of the dielectric layer passivated samples. This finding serves to reinforce the notion that both passivation methods have similar levels of effectiveness.

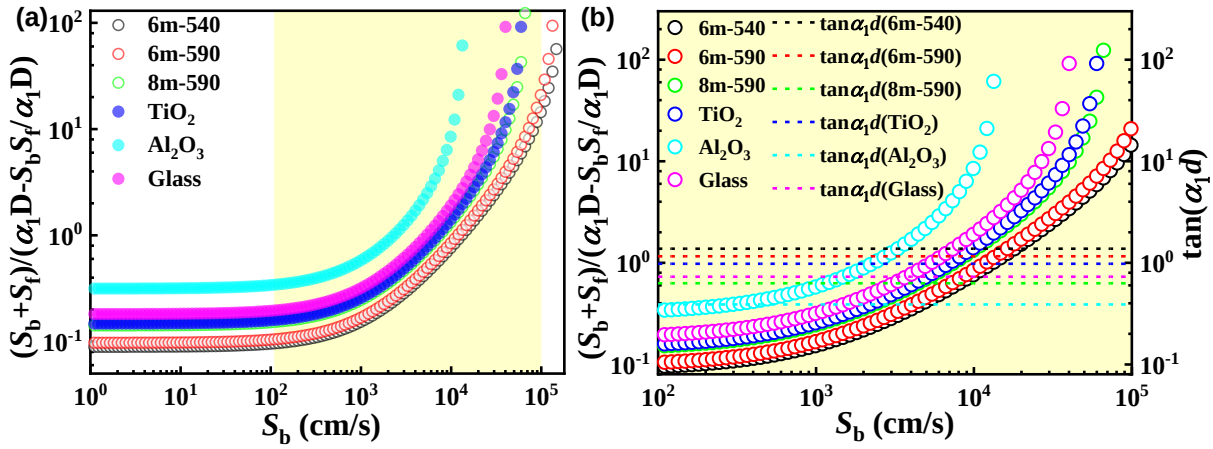

Figure 4.11 (a) The right side termof **Equation 2.51** as a function of S_b. (b) Plot the left and right sides of **Equation 2.51** in the same figure. The intersection of the two curves corresponds to the S_b of the backside passivated sample.

Besides solving the backside recombination velocity by simulation, graphical methods are also used to further prove the accuracy of S_b estimated by SCAPS simulation. For the backside

passivated samples, the boundary condition $S_b >> S_f$ that leads to **Equation 2.54** is no longer valid. In this case, the general solutions can be solved grapicaly based on **Eqation 2.51 and 2.53**. Using the assumption that the bulk lifetime of the backside passivated samples is similar to their unpassivated reference sample, we can use the previously estimited values of τ_b and τ_{eff} to determine the α_1 of different samples using **Equation 2.53**. To determine the S_b of different samples by using **Equation 2.51**, we first plot the left side of this equation as a function of S_b in **Figure 4.11 (a)**. In **Figure 4.11 (b)**, we add the right side of this Equation as dashed lines. The intersection of the dashed line and its corresponding curve (with the same color) represents the solution of **Equation 2.51**, which is the graphically determined value of S_b. By determining the S_b at the different intersection points, we can calculate the S_b of the different samples, which are summarized in **Table 4.1**. The grapitical results are found to be in close agreement with the simulation results, with a maximum difference of a factor of 3. To maintain consistency throughout this work, we refer to S_b values discussed in other chapters as those obtained from SCAPS simulation, unless otherwise specified.

Table 4.1 V_{oc}, ΔE_F, lifetime, doping density and (effective) back surface recombination velocity. The V_{oc} is the highest value obtained among solar cells. The ΔE_F is the mean value with an error.

Sample	V_{oc} (mV)	ΔE_F (meV)	Lifetime (ns)	N_A (cm^{-3})	S_b-graphical (cm/s)	S_b-Eqn.4.1 (cm/s)	S_b-SCAPS (cm/s)
8m-590 Ga	**524**	**547±4**	**13.3**	**1.9×10^{16}**	**$4.5\times10^{3*}$**	**$6.2\times10^{3*}$**	**$3.2\times10^{3*}$**
6m-590 Ga	**503**	**532±4**	**8.5**	**1.7×10^{16}**	**$1.4\times10^{4*}$**	**$4.3\times10^{4*}$**	**$1.3\times10^{4*}$**
6m-540 Ga	**525**	**538±5**	**7.5**	**2.4×10^{16}**	**$1.8\times10^{4*}$**	**$9.2\times10^{3*}$**	**$8.2\times10^{3*}$**
No-Ga Re	**453**	**499±3**	**3.4**	**1.9×10^{16}**		**1.0×10^{6}**	
Al_2O_3	/	**513±5**	**28.8**	**7.8×10^{15}**	**3.0×10^{2}**		**1.2×10^{3}**
Glass		**501±5**	**19.9**	**8.6×10^{15}**	**3.7×10^{3}**		**5.9×10^{3}**
TiO_2		**493±3**	**16.1**	**7.2×10^{15}**	**6.9×10^{4}**		**1.3×10^{4}**
Mo-Re		**477±4**	**6.0**	**7.6×10^{15}**		**1.0×10^{6}**	

**: The S_b of the GBG sample is an effective surface recombination velocity. The S_b of reference sample is assumed to be 1.0×10^6 cm/s. Our simulations and calculations are based on this value.*

4.5 Summary

In this chapter, we investigate the impact of backside recombination on the ΔE_F through SCAPS simulations and experiments. Our findings indicate that reducing backside recombination can enhance ΔE_F by approximately 50 meV, even for a thick absorber of about 2 μm. Furthermore, the higher improvement in ΔE_F can be achieved by employing a higher quality absorber with an extended lifetime and by minimizing frontside recombination. For the GBG samples, we observe that the 8m-590 sample, with the highest E_g at the backside, yields the highest ΔE_F of ~547 meV. Similarly, for the dielectric layer passivated samples, the Al_2O_3 passivated sample exhibits the best passivation effect among the various dielectric layers, with the highest ΔE_F of ~513 meV. The superior ΔE_F of GBG samples compared to the dielectric layer passivated samples is primarily attributed to the higher doping density. When comparing the improvement in ΔE_F relative to their corresponding reference sample, both GBG and dielectric layer passivated samples show a comparable enhancement of ~50 meV, indicating similar passivation effects. We also quantify the surface S_b of different samples using both simulation and graphical methods, which yield values in close proximity with each other, providing evidence for the reliability of the estimated S_b values. Both GBG and dielectric layer passivated samples exhibit the lowest S_b around 10^3 cm/s, suggesting a similar passivation effect, as implied by the improvement in ΔE_F.

Chapter 5 $Cu(In,Ga)Se_2$ solar cells with HTLs

As previously discussed in **Chapter 4**, $Cu(In,Ga)Se_2$ solar cells suffer from significant losses in $\Delta E_F(V_{oc})$ due to severe backside recombination. This problem can be mitigated by introducing a higher Ga gradient towards the backside that creates a conduction band gradient. However, the inhomogeneity of the Ga profile can introduce additional radiative and non-radiative recombination, which limits the efficiency of the solar cell beyond current records. To address these challenges, a new structure with a homogeneous absorber and hole selective transport layers is highly desirable to remove Ga gradient and mitigate the backside recombination at the same time. In this chapter, we have investigated the impact of various HTL candidates on the performance of $Cu(In,Ga)Se_2$ solar cells.

In our pursuit of identifying a suitable material or structure to function effectively as a hole selective transport layer, we conducted a series of screening experiments. However, it is important to note that we encountered numerous challenges and several setbacks during this process. In **Section 5.1**, the study focuses on investigating the stability and passivation effects of various single layers such as NiO_x, $CuCrO_x$, CuO_x, MoO_x, and GaO_x. It is crucial to ensure the thermal stability of HTLs during the growth of $Cu(In,Ga)Se_2$ in order to achieve functional efficiency. In **Section 5.2**, HTLs with metal oxide stabilizers are examined, as they show promise in enhancing stability and reducing backside recombination. Specifically, the blocking effect of In_2O_3 on the diffusion of Ga has been found. **Section 5.3** further investigates the application of dual-layer HTLs in submicron $Cu(In,Ga)Se_2$ solar cells. In such cells, backside recombination plays a critical role, as the diffusion length of minority carriers is often longer than the thickness of the absorber. The use of stable HTLs with metal oxide stabilizers is essential to reduce backside recombination and improve efficiency. And in this section, it is found that the excess Cu is critical for the presented HTL to realize a good hole transportation, which ensures the high FF. Finally, **Section 5.4** summarizes the main findings and conclusions of the study on HTLs.

5.1 Single layer HTL: Stability VS Passivation

This section explores the use of single layers as potential HTLs for enhancing the efficiency of solar cells. Single layers, referring to a single layer deposited onto the Mo substrate, are investigated in detail. Specifically, the thermal stability of the single layers is assessed, followed by an evaluation of its impact on solar cell performance. The single layer is deposited prior to the $CuInSe_2$ layer, and its thermal stability to function as an effective HTL is examined. By studying the photoelectric performance of different samples, this study aims to provide insights into the feasibility of using single layers as HTLs and their potential for enhancing solar cell efficiency.

Unfortunately, the extensive investigation of single layers, including NiO_x, $CuCrO_x$, CuO_x, MoO_x, and GaO_x, as HTLs has proven to be unsuccessful. In most cases, during the initial stages of the investigation, it becomes evident that these layers are either thermally unstable or exhibit very weak passivation effects. As a result, further investigations are terminated once it becomes clear that good passivation cannot be achieved. Consequently, the results obtained are limited, as the underlying reasons for these failures have not been thoroughly investigated. These findings are presented in **A5 Annex of Chapter 5.**

Nevertheless, these failures serve as crucial steppingstones toward success. They highlight the significance of improving the thermal stability of HTLs in order to achieve functional HTLs. Additionally, they demonstrate the excellent thermal stability exhibited by metal oxides, such as GaO_x. This observation triggers the idea of utilizing GaO_x or In_2O_3 as thermal stabilizers to prevent the diffusion of underlying layers, which may consist of a p-type wide bandgap semiconductor. The results of dual-layer HTLs incorporating these concepts will be discussed in the following sections.

5.2 HTL with a metal oxide stabilizer

As demonstrated in the previous **Section 5.1**, certain HTL candidates such as NiO_x, $CuCrO_x$, CuO_x and $CuGaSe_2$ exhibit inadequate thermal stability, leading to diffusion of these layers during absorber deposition that may degrade the absorber layer due to the introduction of impurities like Ni and Cr. And the diffusion may destroy the HTL layer, rendering the passivation ineffective. Conversely, metal oxides such as GaO_x demonstrate good thermal stability, maintaining a relatively constant thickness before and after absorber deposition. However, despite its thermal

stability, GaO_x does not show a clear passivation effect, rather resulting in a higher loss of ΔE_F due to the introduction of additional non-radiative recombination. Moreover, from previous studies[149-152], it was reported that the GaO_x between the back contact and the absorber results in a roll-over of *J-V* curve, contributing to higher V_{oc} loss and lower FF. This is because the improper band alignment between the absorber and GaO_x hinders hole transport[149, 152, 153]. Meanwhile, the n-type GaO_x may also form a reversed junction compared to the main junction, which limits the current density of the diode[154]. Therefore, further research is required to address these issues and find more suitable HTL candidates for enhancing device performance.

Taking advantage of the thermal stability of metal oxide such as GaO_x, we propose to use GaO_x and the similar In_2O_3 as stabilizers to prevent the diffusion of the underlying HTL layer. Our initial speculation is that $CuGaSe_2$ can be kept at the backside with help of the oxide capping layers, which is expected to improve the thermal stability and passivation of the HTL layer. But the results go beyond our expectation, especially in term of the sample with In_2O_3 capping layer. In this section, we will investigate different combinations of HTL candidates with GaO_x or In_2O_3. Among these combinations, the $CuGaSe_2/In_2O_3$ combination demonstrates effective passivation and hole transport property.

5.2.1 CuO_x/GaO_x

As discovered in previous works[126], the presence of impurities such as Cr and Ni in $Cu(In,Ga)Se_2$ can lead to a significant reduction in the quality of absorbers due to high non-radiative recombination. Therefore, it is preferable to implement HTLs that are free of poisonous impurities to avoid compromising the absorber's performance. CuO_x and $CuGaSe_2$ are promising candidates for HTL materials as their diffusion into $Cu(In,Ga)Se_2$ does not significantly alter its optoelectronic properties. Moreover, these materials are reported to be p-type semiconductors and exhibit good band alignment with $Cu(In,Ga)Se_2$[123]. In this section, we investigated the use of GaO_x as a stabilizer for CuO_x to improve its thermal stability. The thickness of CuO_x is ~40 nm, which was prepared by SCS with annealing temperature of 300 °C in air. The thickness of GaO_x layers are 40 nm, 60 nm, and 80 nm, respectively, which were prepared by SCS and annealed at 300 °C in air. The thickness of the oxides is estimated from the preparing process, details are

discussed in **Section 3.1.3**. **Figure 5.1** shows the SEM cross-section image of the structure with HTL (40 nm CuO_x/80 nm GaO_x) and ~1.5 µm $CuInSe_2$. The $CuInSe_2$ was prepared by a 3-stage process with the maximum substrate setting temperature of 580 °C. While the interface between the HTL and $CuInSe_2$ is not very clear in the image, an inter-layer around 100 nm is visible between the Mo and $CuInSe_2$ layers. The thermal stability of GaO_x ensures that it can maintain its thickness before and after the absorber deposition **(Figure A5.8)**. However, we are unable to clearly identify individual CuO_x and GaO_x layers, implying a diffusion of CuO_x or its interaction with GaO_x. This suggests that GaO_x may not be a sufficient diffusion-blocking layer to keep the HTL at the backside, at least not for CuO_x.

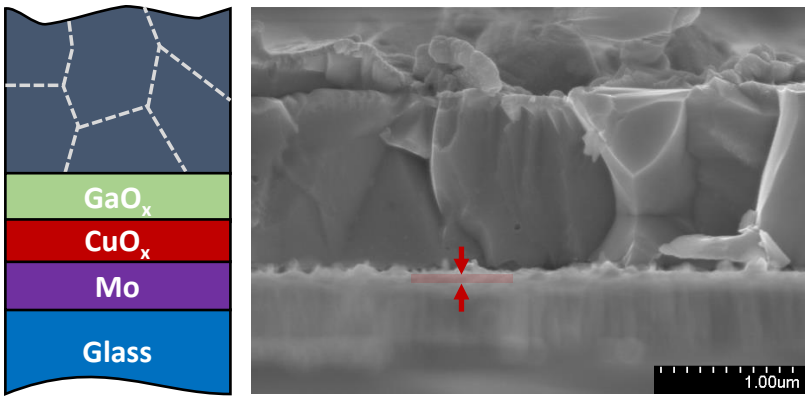

Figure 5.1 The sketch of sample structure and its corresponding SEM cross-section image. From the SEM cross-section image, a thin layer around 100 nm is between $CuInSe_2$ and Molybdenum.

Further evidence of CuO_x diffusion is observed in the PL spectrum, as depicted in **Figure 5.2 (a)**. In comparison to the reference sample, the PL bandgap of the sample with CuO_x/GaO_x exhibits a slight blue shift, indicating that the sample is closer to stoichiometric due to Cu diffusion. Previous studies have reported that the bandgap of Cu poor $Cu(In,Ga)Se_2$ increases with increasing Cu content [155]. While Ga diffusion can also increase the bandgap of the material, as discussed in **Section A5.5 (Figure A5.9)**, the presented results show that SCS prepared GaO_x is quite thermally stable and no blue shift of bandgap of $CuInSe_2$ was observed due to adding GaO_x at the backside. In addition to the PL bandgap shift, the absolute PL intensity of the samples with CuO_x/GaO_x is lower, and this effect becomes more pronounced with increasing GaO_x layer thickness, indicating higher non-radiative recombination. This leads to lower ΔE_F and higher ΔE_F deficits, one of the possible reasons is likely due to a degraded back contact. But we can not exclude this layer may

also result in a lower quality absorber. These results are actually similar to the impact of a single GaO_x layer on the performance of $CuInSe_2$ as discussed in **Section A5.5**, indicating adding a CuO_x layer in this case will not improve the passivation effects compared to the case only with single GaO_x layer. Nevertheless, it is essential to acknowledge that the potential for enhanced passivation of this structure cannot be ruled out, as further optimization of the properties of the CuO_x and GaO_x layers may yield improved results. The discussions and conclusions drawn in this thesis are bounded by the observations made within this research and the existing knowledge available in the literature. Although it has been shown in **Section A5.5** that amorphous GaO_x does not likely block Na diffusion from the soda-lime glass to the absorber, the same NaF PDT (5 nm NaF, annealed at T_{sb} = 350 °C for 10 minutes in a Se atmosphere) is applied to these samples. The ΔE_F difference between the samples before and after the NaF PDT is illustrated in **Figure 5.2 (c)**, where no significant improvement in ΔE_F is observed. The ΔE_F remains almost unchanged or decreases up to 20 meV. But it is worth to mention that the ineffectiveness of NaF PDT may also be a result of the unoptimized PDT process.

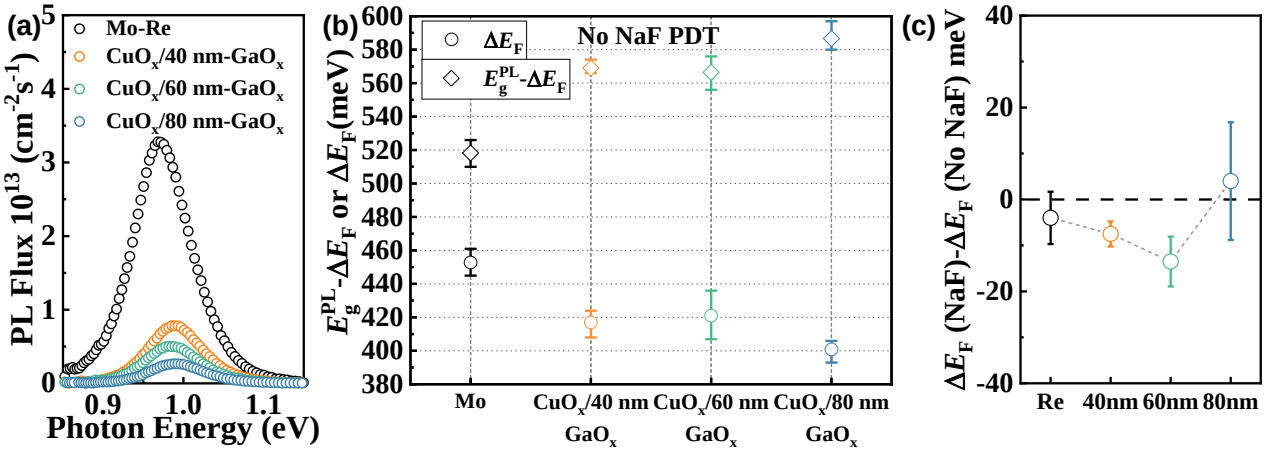

Figure 5.2 (a) The absolute PL spectra of samples with different thickness combination of CuO_x and GaO_x. The slight blue shift of the PL maximum peak of samples with HTL compared to the reference sample may indicate the diffusion of Cu. The lower PL intensity of samples with HTL suggests a higher non-radiative recombination; (b) ΔE_F and ΔE_F deficits: the samples with CuO_x/GaO_x show a lower ΔE_F that deceases with the thicker GaO_x. The ΔE_F is acquired by fitting the high energy wing of transformed absolute PL spectra with fixing the fitting temperature to the ambient temperature. E_g^{PL} is the PL band gap which is the energy

corresponding to the PL flux maximum; (c) After the NaF PDT, no improvement in ΔE_F is observed.

In conclusion, the GaO_x layer shows a good thermal stability in harsh environments with Se and high temperature. However, it may be insufficient in blocking the diffusion of CuO_x underneath, leading to inefficient passivation of the CuO_x/GaO_x combination. The effects of CuO_x/GaO_x on the performance of $CuInSe_2$ are similar to those of GaO_x, with both demonstrating inadequate passivation and causing a reduction in the ΔE_F, due to additional non-radiative losses.

5.2.2 $CuGaSe_2/GaO_x$

As discussed in **Section 5.2.1**, it is likely that the passivation efficiency of GaO_x is limited due to its inability to block the diffusion of CuO_x layers. To address this limitation, we have investigated the thermal stability and passivation effect of $CuGaSe_2/GaO_x$ in this section.

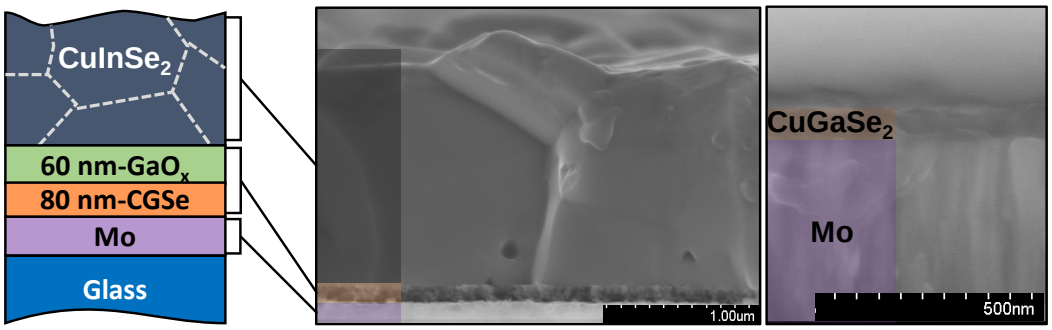

Figure 5.3 The structure sketch of the $CuInSe_2$ with $CuGaSe_2/GaO_x$. SEM cross-section image on the right side shows 80 nm $CuGaSe_2$ on top of Mo before GaO_x deposition. SEM cross-section image on the left side shows ~120 nm layer between Mo and $CuInSe_2$

Specifically, 80 nm of $CuGaSe_2$ was thermally evaporated onto a Mo substrate at substrate setting temperature of 356 °C, followed by deposition of GaO_x synthesized by SCS with the annealing temperature of 300 °C in air. The thicknesses of these films are 40 nm, 60 nm, and 80 nm. The $CuInSe_2$ was prepared by a standard 3-stage process at maximum substrate setting temperature of 580 °C. The sketch shows a sample structure of 80 nm $CuGaSe_2$ and 60 nm GaO_x. The thickness of $CuGaSe_2$ was checked by the SEM cross-section image as shown in right side **Figure 5.3**. The thickness of the GaO_x is an empirical value based our preparation process. These empirical values

agree well with our measured thickness by SEM as discussed in **Section 3.1.3**. The SEM cross-section image after the absorber deposition shows an inter-layer of ~120 nm between Mo and $CuInSe_2$ with very fine grains. However, similar to the situation with CuO_x/GaO_x, no distinct layers can be identified, implying diffusion and interaction between the two materials.

The PL spectra in **Figure 5.4 (a)** provide evidence of the unfavorable diffusion of Ga through the $CuGaSe_2/GaO_x$ interface. Specifically, the bandgap of the sample with $CuGaSe_2/GaO_x$ shifts to a higher energy compared to the reference sample, indicating an increase in the bandgap of the absorber due to Ga diffusion. While the increase in Cu content can also slightly shift the bandgap to a higher energy, in this case, the shift of 30 meV is more pronounced and likely due to Ga diffusion. Furthermore, increasing the thickness of GaO_x does not effectively block $CuGaSe_2$, as the bandgap of samples with different thicknesses of GaO_x is almost the same. The absolute PL intensity shown in **Figure 5.4 (a)** decreases with an increase in thickness of GaO_x, which is likely related to this unfavorable diffusion. Meanwhile, ineffectiveness of passivation may be also related to the optoelectronic properties of SCS synthesized GaO_x, which are not optimized. Consequently, the ΔE_F deficit of samples with $CuGaSe_2/GaO_x$ increases with an increase in GaO_x thickness, as shown in **Figure 5.4 (c)**. To rule out the influence of Na on ΔE_F, the NaF PDT treatment, as applied to the samples with CuO_x/GaO_x and GaO_x, was performed on these samples. However, no significant improvement in ΔE_F is observed after the NaF PDT, implying that GaO_x does not significantly block Na diffusion from the soda-lime glass, or other non-radiative losses just overcompensate any improvement due to doping.

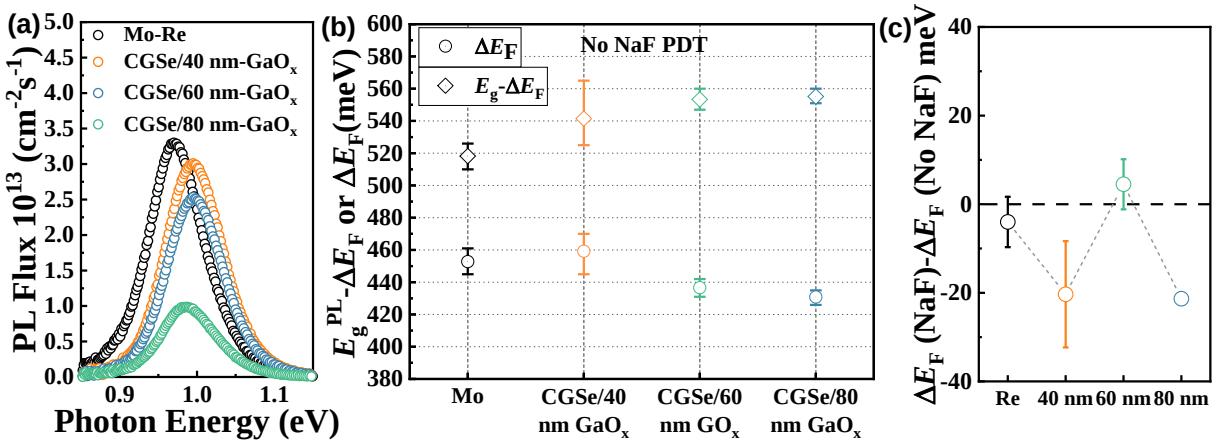

Figure 5.4 (a) The absolute PL of sample with different thickness combination of $CuGaSe_2/GaO_x$. The thickness of $CuGaSe_2$ is the same of 80 nm. The thickness of GaO_x is 40, 60

and 80 nm, respectively; (b) The ΔE_F and ΔE_F deficits of different samples. The ΔE_F is acquired by fitting the high energy wing of transformed absolute PL spectra with fixing the fitting temperature to the ambient temperature. E_g^{PL} is the PL band gap which is the energy corresponding to the PL flux maximum. (c) The difference of ΔE_F of samples before and after the NaF PDT.

In conclusion, the SCS synthesized amorphous GaO_x is not a proper stabilizer that can block the diffusion of Cu or Ga. No passivation effect is observed for $CuGaSe_2/GaO_x$, inversely, it increases non-radiative recombination with an increase in GaO_x thickness, which leads to the higher ΔE_F deficits.

5.2.3 $CuGaSe_2/In_2O_3$

The previous sections have explored the thermal stability and passivation effects of the CuO_x/GaO_x and $CuGaSe_2/GaO_x$ combinations. It was found that GaO_x exhibits high thermal stability with minimal thickness changes (**Annex Figure A5.8**) observed before and after absorber deposition. However, the blocking effect of GaO_x for both CuO_x and $CuGaSe_2$, more specifically the blocking of Ga and Cu, was found to be inefficient. As a result, no passivation was observed, and instead, there was an increase in ΔE_F loss due to additional non-radiative recombination as the GaO_x thickness increased.

Given the unsatisfactory blocking and passivation effects of GaO_x, this section focuses on using In_2O_3 as a blocking layer for $CuGaSe_2$. The presented results in this thesis show that In_2O_3 has a good blocking effect to Ga, resulting in comparable passivation to Ga grading. Furthermore, solar cells with the $CuGaSe_2/In_2O_3$ combination show good FF because of the good hole transport property of the HTL. Therefore, the use of In_2O_3 as a stabilizer for $CuGaSe_2$ is a promising alternative to Ga gradient, providing improved backside passivation and hole transport for the development of high-efficiency solar cells.

The preparation of the HTL, $CuGaSe_2$ covered by a thin In_2O_3 layer, is discussed first. **Figure 5.5 (a)** shows the sample preparation procedure, in which a 100 nm $CuGaSe_2$ was co-evaporated onto Mo-covered soda-lime glass substrates at a substrate setting temperature T_{sb} of 356 °C in a

PVD system. Subsequently, the sample was removed from the vacuum system, and a 50 nm In_2O_3 layer was deposited onto the $CuGaSe_2$ layer in ambient atmosphere using the SCS method with three different annealing temperatures (200 °C, 250 °C, and 300 °C). Following this, a ~1.8 µm homogeneous $CuInSe_2$ was grown in the PVD system using a three-stage process, with the substrate setting temperature in the second and third stages set to T_{sb} = 570 °C. The samples for PL measurements were covered with CBD CdS to prevent surface degradation and reduce front surface recombination. To finish the devices, an i-ZnO/Al-ZnO double window layer and Ni/Al grids were deposited sequentially using sputtering and electron beam evaporation techniques. Further details of the sample preparation procedure can be found in the **Chapter 2**.

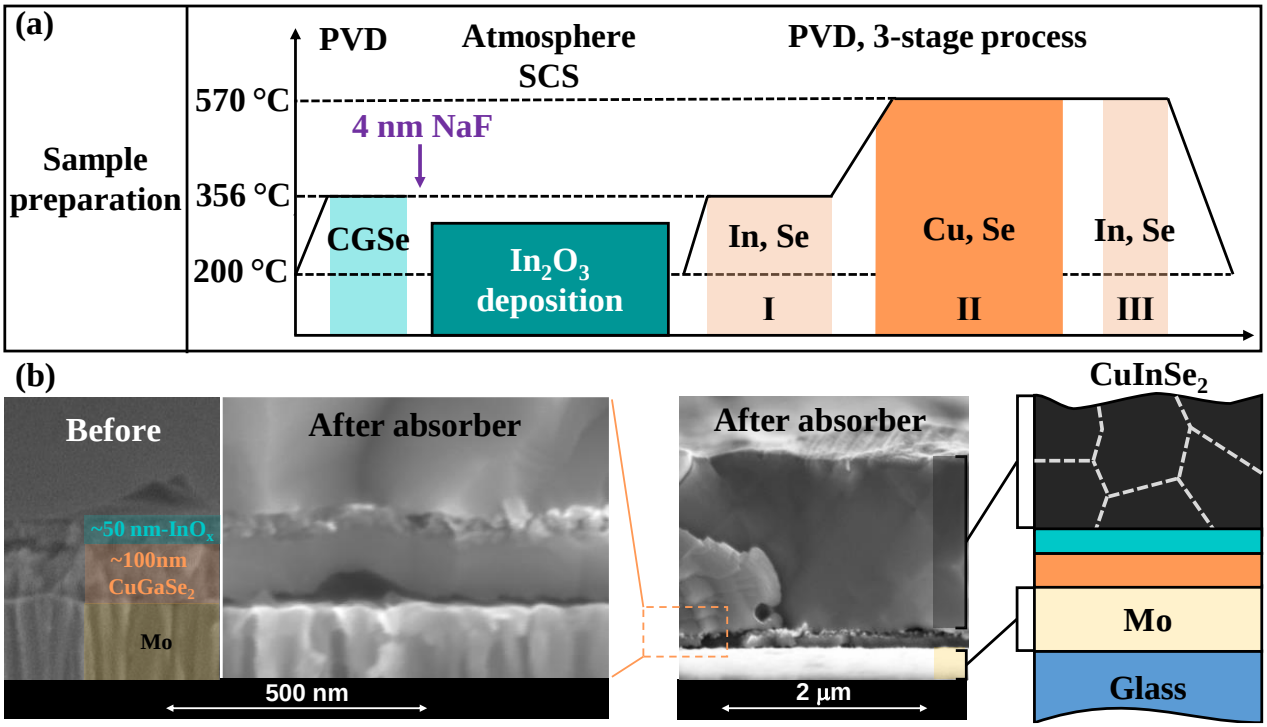

Figure 5.5 (a) The sample preparation procedure: 100 nm $CuGaSe_2$ was thermally evaporated onto Mo substrate with setting temperature of 356 °C in the PVD system. Then the sample was taken out to be covered by 50 nm SCS synthesized In_2O_3 in ambient with annealing temperature of 200 °C, 250 °C and 300 °C. Subsequently, PVD was used to grow a $CuInSe_2$ absorber with a three-stage process; (b) The structure of sample with $CuGaSe_2/In_2O_3$ and its corresponding SEM cross-section, which shows that the thickness of the $CuGaSe_2/In_2O_3$ layer does not change after the $CuInSe_2$ deposition, which demonstrates the good thermal stability of the HTL ($CuGaSe_2/In_2O_3$).

Prior to applying In_2O_3 as a stabilizer on the surface of $CuGaSe_2$, we investigated the properties of the layers synthesized by SCS with different annealing temperatures on Si substrates. We performed Differential Scanning Calorimetry (DSC) and Grazing Incidence X-ray Diffraction (GIXRD) analyses to characterize these layers, and the results are presented in **Figure 5.6**. The thermal behavior of an oxidizer (NO_3^-) and fuel (acetylacetone) mixture precursor during In_2O_3 formation was investigated using DSC (**Figure 5.6 (a)**). The DSC results show an intense and sharp exothermic signal at 190 °C, attributed to the onset of the combustion reaction between NO_3^- and acetylacetone, leading to the formation of an In-O-In framework[156, 157]. A small and broad exothermic peak in the range of 250-300 °C is also observed, likely due to further decomposition of residual organic components[158]. The heat flow signal remains constant beyond 300 °C, indicating complete removal of organic components.

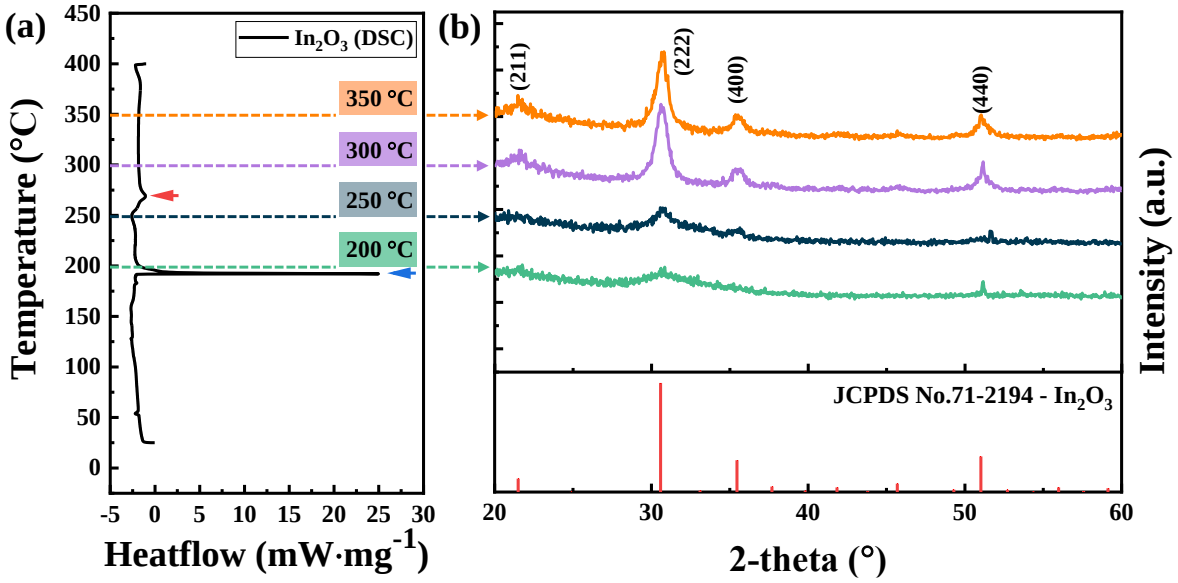

Figure 5.6 (a) Differential Scanning Calorimetry analysis was performed to investigate the thermal behavior of the In_2O_3 precursor deposited on a Si substrate. The DSC results showed that the first combustion reaction occurred at approximately 190 °C, indicating the formation of In-O-In bonds, while the second reaction took place in the temperature range of 250 °C-300 °C, suggesting a further decomposition of organic components; (b) Grazing incidence X-ray diffraction measurements were conducted for samples with different annealing temperatures. The GIXRD patterns revealed that the width of the (222) reflection peak in the low temperature (200 °C and 250 °C) annealed samples was indicative of the formation of cubic In_2O_3

nanograins. As the annealing temperature increased, the intensity of the (222) reflection peak became more pronounced, meaning the better crystallization of In_2O_3 which is likely due to further decomposition of organic components.

Grazing Incidence X-Ray Diffraction (GIXRD) was used to gain insight into In_2O_3 formation, as shown in **Figure 5.6 (b)**. The GIXRD patterns of the films prepared with different annealing temperatures reveal the formation of cubic In_2O_3 nanograins at 200 °C, indicated by the broad signal of the (222) planes of In_2O_3, which is identified by PDF card No. 71-2194 at 31°. The intensity of the peaks improve significantly as the crystallization temperature increases to 300 °C, which is unlike the situation of GaO_x that has an amorphous structure with the same annealing temperature (**Figure A5.8**). The diffractogram of the 350 °C-heated film stays comparable with that of the 300 °C-heated film, supporting the complete decomposition of organic components as previously observed in the DSC results[156]. Therefore, annealing temperature of 300°C is chosen as the highest annealing temperature for the In_2O_3 stabilizer films. These findings provide valuable insights into the thermal behavior and structural evolution of In_2O_3 formation, which are essential for the development of efficient In_2O_3-based devices.

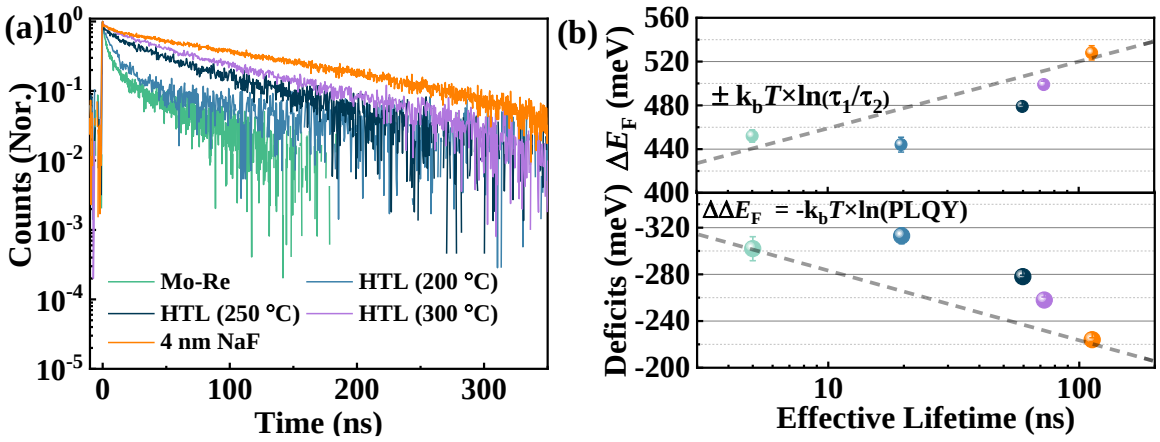

Figure 5.7 (a) The TPRL was measured for reference samples on Mo in comparison to samples with a $CuGaSe_2$ layer (100 nm) and an In_2O_3 layer (50 nm). The In_2O_3 layer was subjected to annealing at three different temperatures, namely, 200°C, 250°C, and 300 °C. In order to enhance Na doping, a 4 nm NaF precursor was added to one of the samples with In_2O_3 annealed at a temperature of 300 °C; (b) The ΔE_F and $\Delta\Delta E_F$ (ΔE_F deficits) of the samples were determined based on the absolute PL spectra. The ΔE_F is acquired by fitting the high energy wing of

transformed absolute PL spectra with fixing the fitting temperature to the ambient temperature. The ΔE_F deficits are calculated based on PLQY, which accounts for the non-radiative losses in the samples. The gray dashed lines in the figures represent the expected ΔE_F and ΔE_F deficits based on the TRPL measured lifetimes of the HTL ($CuGaSe_2/In_2O_3$) passivated samples compared to the reference sample.

One of the critical issues that need to be addressed is the thermal stability of the $CuGaSe_2/In_2O_3$ combination. To investigate this, we used SEM to obtain cross-section images of the $CuGaSe_2/In_2O_3$ before and after the absorber deposition, as shown in **Figure 5.5 (b)**. The images reveal that the initial thickness of the In_2O_3 and $CuGaSe_2$ layers before the deposition of $CuInSe_2$ is approximately 50 nm and 100 nm, respectively. Upon deposition of $CuInSe_2$, we observed that the individual stack of two layers remained intact and their thickness remained unchanged, which is completely different with the case of using GaO_x where only one single layer can be observed. Having established the thermal stability of the HTL, we proceeded to investigate its optoelectronic properties because a proper HTL is more than thermal stability as we discussed previously.

Effective passivation of the HTL is crucial to mitigate backside recombination in solar cells, which is expected to lead higher ΔE_F by reducing non-radiative recombination. To evaluate the passivation effect of the HTL, time-resolved photoluminescence (TRPL) measurements of the absorbers were performed to determine the effective lifetime of the reference sample and samples with HTL. The results in **Figure 5.7 (a)** demonstrate that the PL transients of the HTL passivated samples are slower than those of the reference sample, indicating longer effective lifetimes. **Figure 5.7 (b)** shows the ΔE_F and ΔE_F deficits of samples with respect to their corresponding lifetime values, obtained from the weighted average of the two-exponential fits to the PL transients (**Equation 2.33**). The ΔE_F deficits are determined by photoluminescence quantum yield (PLQY, **Equation 2.28**), which refers to the non-radiative losses[69, 84, 159]. For the sample with In_2O_3 annealed at a low temperature (200°C), the lifetime improved from 5 ns to 20 ns. Further increasing the In_2O_3 annealing temperature (300°C) improves the lifetime to 73 ns. The shorter lifetime of the sample annealed at a lower temperature may be attributed to the presence of organic residues in the In_2O_3, as indicated by the differential scanning calorimetry (DSC) measurements. Organic residues have been shown previously to diminish the quality of the absorbers[160]. Since the absorbers in all samples were prepared using the same process and covered with the same CdS

layer, it is reasonable to assume that these samples have similar bulk lifetimes (τ_b) and front surface recombination velocities (S_f). Therefore, the longer effective lifetime measured by the TRPL indicates a lower backside recombination velocity (S_b), thus a lower backside recombination.

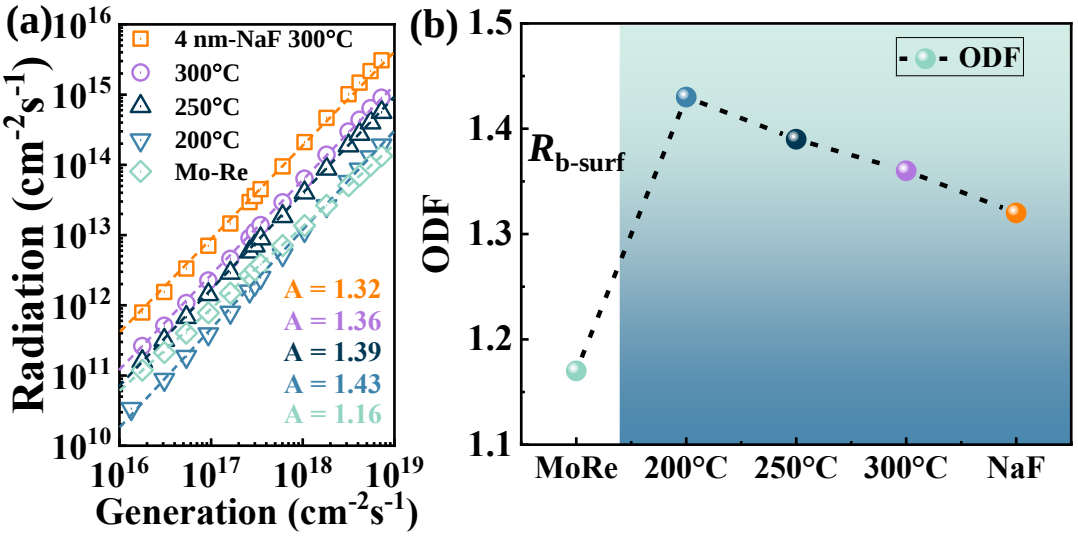

Figure 5.8 (a) Illumination intensity dependent PL is used to determine the ODF of different samples: Reference sample without HTL and samples with HTL ($CuGaSe_2/In_2O_3$). The annealing temperature of In_2O_3 changes from 200 °C to 300 °C. Another 4 nm NaF precursor was added to one HTL passivated sample, and In_2O_3 annealing temperature for this sample is 300 °C; (b) The ODF of Mo reference sample is lower due to the serious backside recombination. The radiation is the integrated PL flux over photon energy. The higher ODF of HTL passivated samples suggest a reduction in backside recombination. The decreasing trend observed in the ODF with an increase in In_2O_3 annealing temperature or the addition of extra NaF is attributed to the improvement in doping density.

The passivation effect is also confirmed by measuring the optical diode factor, which is determined by the illumination intensity dependent PL measurements, as shown in **Figure 5.8 (a)**. In this study, the ODF theory based on metastable defects transition, which is discussed in **Chapter 6**, is used to interpret the results. The methodology for measuring ODF is described in **Section 2.3.3**. According to the theory, both serious backside recombination and low doping density of the absorber can result in low ODF values. The Mo reference sample exhibits a low ODF (1.16), indicating that backside recombination dominates its non-radiative recombination loss. The

introduction of the HTL results in an increased ODF value of 1.43, suggesting that the HTL provides decent passivation that shifts the dominant non-radiative recombination from the backside to the bulk of the absorber. These findings support the conclusion that the passivation effect of the HTL improves the performance of the absorber. The ODF then gets lower with increasing annealing temperature of In_2O_3 and adding NaF precursor. The lower ODF in this case is due to higher doping density, as discussed in following, improving annealing temperature of In_2O_3 and adding NaF precursor can improve the doping density of the absorber. The higher doping density of the absorber improves the hole reservoir, which flattens the influence of extra holes converting from metastable defects transition (e.g. from donors to acceptors), thus results in a lower ODF. The more details about the influence of backside recombination and doping density on the ODF will be discussed in **Chapter 6**.

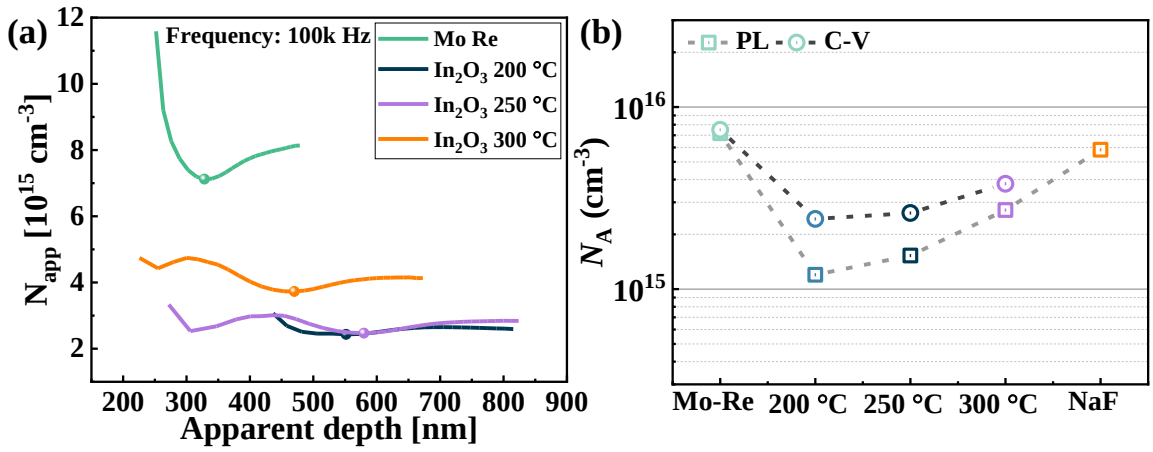

Figure 5.9 (a) *C-V* measurements: the depth profile of apparent doping density. The doping density presented in **(b)** refers to the value observed at zero bias, as highlighted in the figure with a sphere. The measurements were carried out at low temperature with a high frequency of 100 kHz to remove the capacitance contributed by deep defects in the material; (b) The doping densities are determined by methodology based on PL and *C-V*. The doping density estimated by PL is a bit lower than that estimated by the *C-V*. But the presented trend is the same. Both show lower doping density in HTL ($CuGaSe_2/In_2O_3$) passivated sample, which can be improved by increasing the In_2O_3 annealing temperature or adding additional NaF precursor.

Although the HTL offers reasonable passivation effects, which lead to a longer lifetime compared to the Mo reference sample, the improvement in ΔE_F is lower than expected. According to the theoretical prediction, assuming a homogeneous carrier distribution and a flat Fermi level, an order

of magnitude longer lifetime should result in an increase in ΔE_F of 59 meV at room temperature (**Equation 2.34**), as depicted by the grey dashed line in **Figure 5.7 (b)**. However, the ΔE_F of samples with the HTL is below this grey dashed line, indicating that the improvement in ΔE_F is less than expected. This deficit in ΔE_F is most likely due to insufficient doping. To assess the doping density of the samples, both PL and *C-V* methodologies were used. The doping density obtained from *C-V* measurements is determined by the value at zero bias and was carried out at low temperature to minimize the influence of deep defects on capacitance. The PL method assumes that quasi-Fermi levels are flat throughout the absorber depth, and doping density is determined from the lifetime and ΔE_F (**Equation 2.46**). The details of these characterization methods are discussed in **Section 2.5.1**. As shown in **Figure 5.9 (b)**, both methods yield similar doping densities within an error range, confirming lower doping density of the HTL-passivated samples. This lower doping density is likely due to residues of organic compounds in In_2O_3 containing carbon and nitrogen, as previously discussed. This also explains the increase in doping density for the samples with the higher annealing temperature of In_2O_3 since the higher annealing temperature promotes the decomposition of organics, which reduces the amount of carbon and nitrogen.

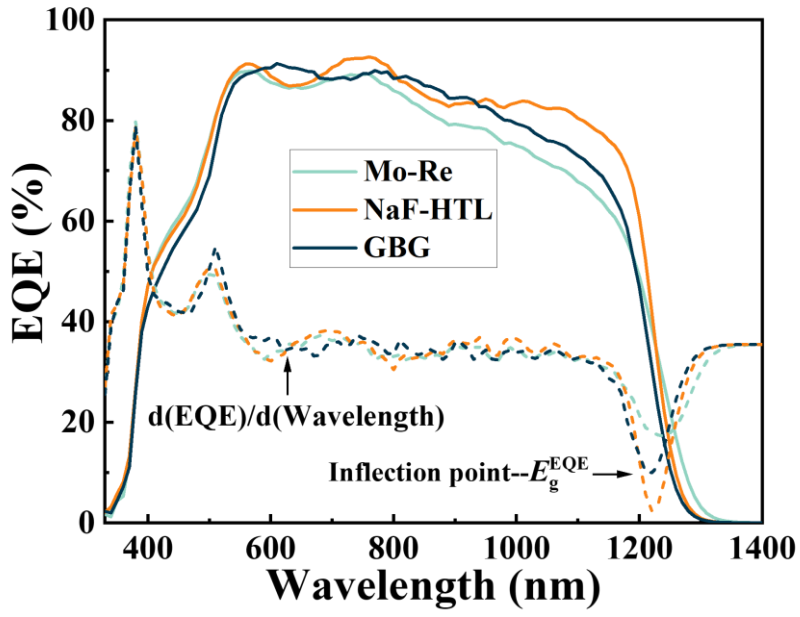

Figure 5.10 The EQE of Mo reference sample, HTL ($CuGaSe_2/In_2O_3$) passivated sample with NaF precursor and Ga single grading sample from our previous work (**Chapter 4**). The HTL passivated sample has the best EQE response to long wavelength photons, indicating the best collection of long wavelength photon generated carriers, thus the best backside passivation.

The other reason is that the In_2O_3 is not only a barrier for Ga but also a barrier for Na diffusing from soda-lime glass. The introduction of a 4 nm NaF precursor between $CuGaSe_2$ and In_2O_3 further enhances the doping density of the sample, as shown in **Figure 5.9 (b)**, bringing it to a level comparable to that of the Mo reference sample. This improvement in doping density results in a higher ΔE_F, while also reducing the ODF, as illustrated in **Figure 5.8 (b)**, which is beneficial for obtaining a higher FF[23, 90, 91]. However, even with an ODF of 1.32 for the best sample with the highest V_{oc}, it remains too high to achieve a high FF. In addition, adding NaF precursor leads to a longer lifetime of the sample, up to 113 ns. Overall, the sample with NaF precursor achieves the highest value of ΔE_F, reaching 530 meV, due to the combined improvements in doping density and lifetime.

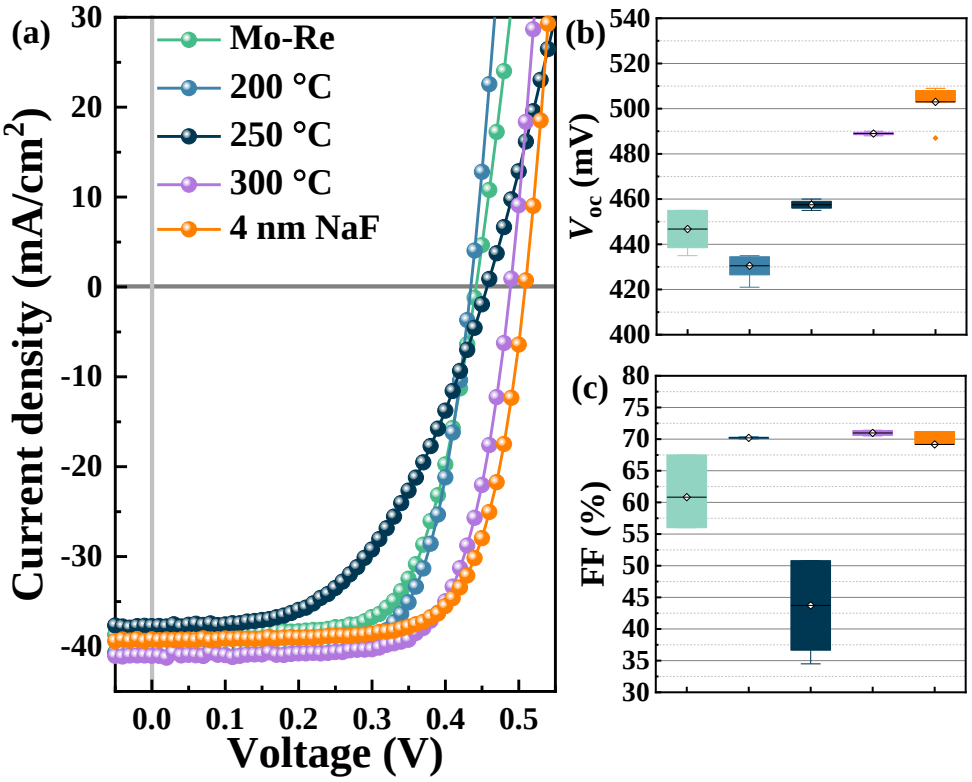

Figure 5.11 (a) The *J-V* curves of different samples; The box plot, in which the box represents the interquartile range (25^{th} to 75^{th} percentile), the black line with a circle is the mean value and the whisker is based on 1.5 IQR (interquartile range) value: (b) The V_{oc} of different samples: the increase in V_{oc} is consistent with the improvement in ΔE_F; (c) The FF of different samples: except the sample with In_2O_3 annealed at the temperature of 250 °C, other HTL ($CuGaSe_2/In_2O_3$) passivated samples show the FF more than 70%, indicating good hole transport abilities.

So far, the passivation effects of the HTL are demonstrated by the higher ΔE_F and longer lifetime of unfinished devices. Additionally, the passivation effects are confirmed by finished devices, as shown in **Figure 5.10**, which presents the EQE of the Mo reference and HTL passivated samples in comparison to the GBG sample discussed in **Chapter 4**. The reference sample with the Mo back contact exhibits a more gradual EQE edge due to the lower chance of carriers generated near the back contact to be collected, resulting in an overall lower EQE. In contrast, the sample with backside gradient has lower absorption for long wavelength irradiation due to the low bandgap region is considerably thinner than the whole film thickness, and the steepest onset of absorption and collection is observed for the HTL sample, indicating the best passivation of the back contact, which is comparable and even better than the GBG. Furthermore, the passivation effect of the HTL is also supported by *J-V* characterization of solar cells. As shown in **Figure 5.11 (b)**, the improvement in V_{oc} is consistent with the improvement of ΔE_F. As shown in **Figure 5.12**, all other samples exhibit a lower V_{oc} than the measured ΔE_F/q[69]. Around 10 meV higher (ΔE_F-qV_{oc}) deficit of the solar cells with additional NaF compared to, for example, the reference solar cells, is most likely due to slightly higher front surface recombination[142], suggesting that the front interface with the buffer layer requires further optimization, despite the reduction in backside recombination.

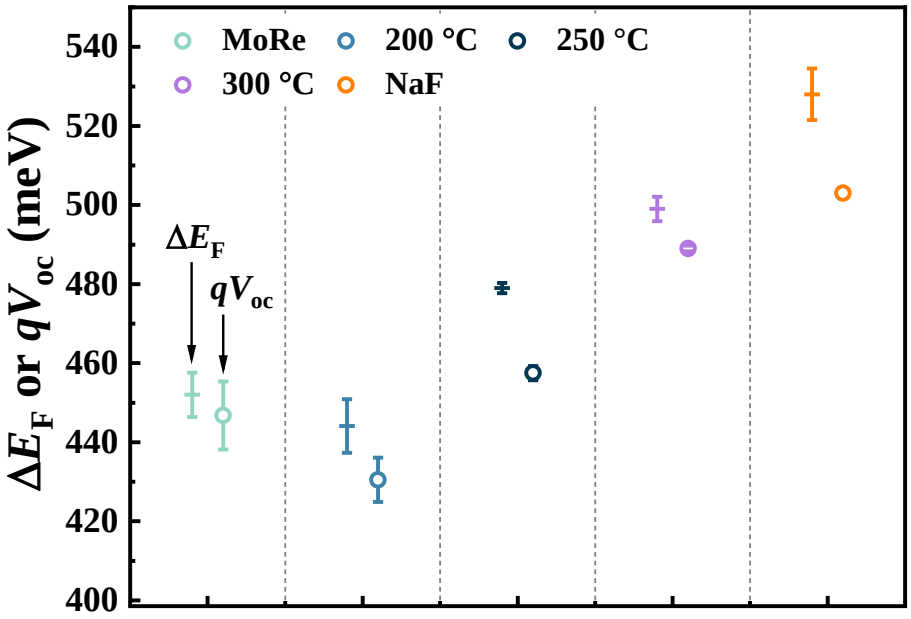

Figure 5.12 Comparison of ΔE_F and qV_{oc}. Around 10 meV higher (ΔE_F - qV_{oc}) of some solar cells compared to others is most likely due to slightly higher front surface recombination.

The good passivation effects of $CuGaSe_2/In_2O_3$ combination are demonstrated by multiple characterizations. However, to achieve high-performance solar cells, a functioning HTL must not only have good passivation properties that improve the V_{oc} but also demonstrate good hole transport properties, which ensures a high FF. Fortunately, all $CuGaSe_2/In_2O_3$ samples, except for the sample with In_2O_3 annealed at 250 °C, exhibit smooth *J-V* curves with an exponential shape, resulting in FF values greater than 70%. These findings provide evidence for the good hole transport ability of this HTL structure.

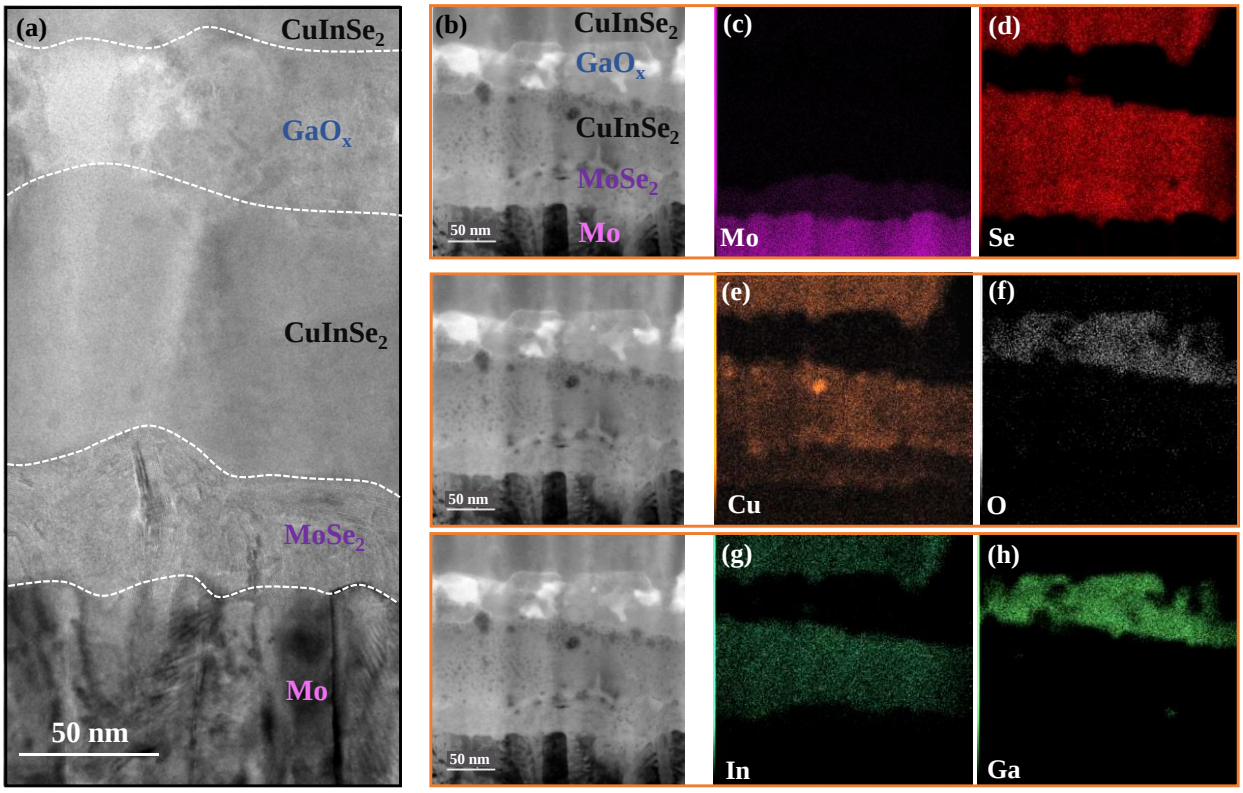

Figure 5.13 (a) Cross-section High-resolution TEM (HRTEM) image taken from Mo (bottom) to $CuInSe_2$ (Top); (b) The bright filed scanning TEM (STEM) image from the same cross-section, in which the corresponding element mapping was measured by EDS; (c),(d),(e),(f),(g) and (h) shows the distribution of Mo, Se, Cu, O, In and Ga, respectively.

From the SEM cross-section, it clearly shows that there are two individual layers staying at the backside after the absorber deposition. This observation proves the thermal stability of the HTL which can potentially mitigate the backside recombination and transport holes. The good passivation of this HTL is confirmed by the improvement in ΔE_F as well as V_{oc} when comparing

HTL involved samples to the reference samples. Meanwhile, it also gives good FF of solar cells, which indicates a good transport property of holes. However, there is still a lack of clarity regarding the subsequent processes occurring in these two layers during the absorber deposition, as well as the mechanisms behind their effective functioning as a HTL with good passivation and hole transport properties. To address these concerns, a transmission electron microscopy (TEM) measurement was conducted to investigate the processes occurring at the near backside interface.

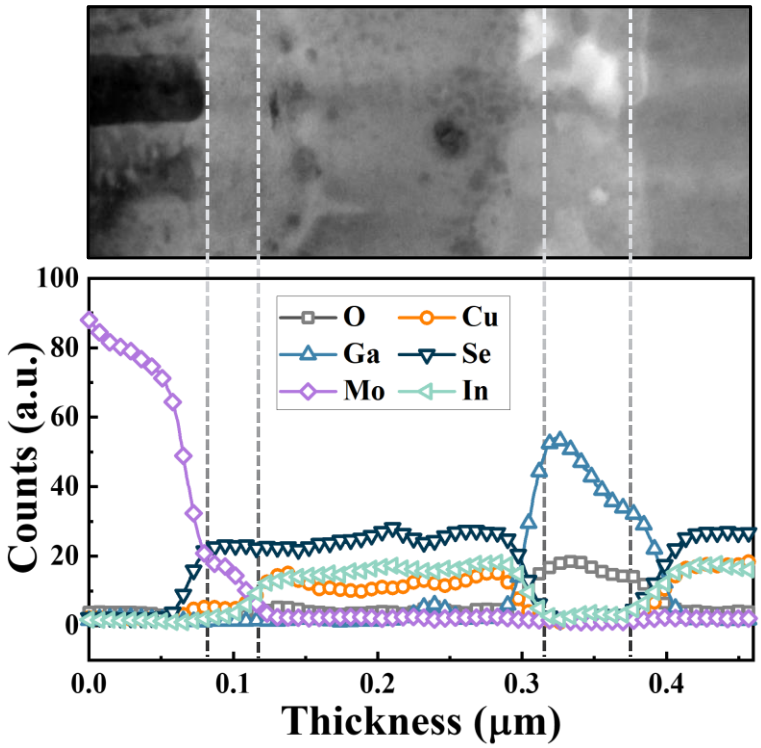

Figure 5.14 The element distribution along the cross-section measured by the EDS line scanning.

Figure 5.13 (a) (b) is the TEM cross-section image taken from near backside interface, Mo (bottom) to $CuInSe_2$ (Top). **Figure 5.13 (a)** is the high-resolution TEM (HRTEM) image and **Figure 5.13 (b)** is the bright filed scanning TEM (STEM) image, these are three same images. The checked sample is the same sample in **Figure 5.5 (b)**, which shows two layers between Mo and $CuInSe_2$ in SEM cross-section image. The corelated elemental distributions of **Figure 5.13 (b)** were also determined by EDS and results are shown in **Figure 5.5 (c), (d), (e), (f), (g) and (h)** corresponding to Mo, Se, Cu, O, In and Ga, respectively. From the bottom to top, the TEM image firstly shows a Mo layer, which is responsible for the highest sign of Mo as shown in **Figure**

***5.13* (c)**. The second layer on the top of the Mo is not very clear in **Figure 5.13 (b)**, in which the corresponding element mapping was measured. But this layer is shown very clear in **Figure 5.13 (a)**, which is most likely a $MoSe_2$ layer that has been widely observed in previous studies[161-163]. This speculation is supported by **Figure 5.13 (c) and (d)**, which shows this layer is Mo and Se rich. In addition, **Figure 5.14** shows a DES line scan of **Figure 5.13 (b)** from the bottom to the top, it also shows a clear accumulation of Mo and Se in this region (at thickness of ~0.1 μm), which confirms the formation of $MoSe_2$.

Above the $MoSe_2$ layer, there are two layers in sequence from the bottom to top corresponding to the two layers shown in **Figure 5.5 (b)**. Depending on the position, the thickness of these two layers could be a bit thicker than the thickness determined from the SEM cross-section image. The thickness difference is most likely due to the inhomogeneity. In Annex **Figure A5.12**, the TEM image gained from another position shows a very close thickness of these layers compared to the values obtained from SEM image. Meanwhile, we can not exclude the possibility that the thickness of these layers could change due to inter-diffusion during the absorber deposition. From the element mapping, it shows a strong inter-diffuse did take place, leading to an exchange of In in In_2O_3 by Ga. It is notable that we had $CuGaSe_2$ covered by In_2O_3 before the absorber deposition. The oxygen rich region in **Figure 5.13 (f)** should represent the In_2O_3 if there is no massive interdiffusion taking place. However, the metal element in this specific region is no longer In but Ga, because no significant amount of In can be found in this region as shown in **Figure 5.13 (g)**, but a large amount of Ga is detected in this region as shown in **Figure 5.13 (h)**. Meanwhile, in the region where it should be $CuGaSe_2$ before the absorber deposition, **Figure 5.13 (h)** shows that no Ga can be detected. Inversely, a significant amount of In can be detected in this region as shown in **Figure 5.13 (g)**. The clearer element depth profile is shown in **Figure 5.14**, the comparison of different elements shows that the oxide layer is Ga rich and other elements, e.g. Cu, In and Se can be barely detected. The layer under the oxide layer is an accumulation of Cu, In and Se, inversely, no significant Ga can be found. This element distribution indicates a strong exchange of In and Ga taking place during the absorber layer deposition, which likely results in formation of $CuInSe_2/GaO_x$ which changes the combination of $CuGaSe_2/In_2O_3$ before the absorber deposition. The exchange of In and Ga may be explained by the free energy differences of involved compounds. The following chemical reaction can be used to describe the process of exchange taking place between In and Ga:

$$2CuGaSe_2 + In_2O_3 = 2CuInSe_2 + Ga_2O_3$$

According to the free energy values reported by Guillemoles[164], the free energy difference of this reaction is around -125 kJ/mol, which is a rather high driving force to promote the exchange of In and Ga. With other free energy values reported by David Cahen et.al.[165], this value is a bit lower. However, it still gives a free energy difference of -91 kJ/mol, which is enough to drive the exchange of In and Ga.

These results suggest that the In_2O_3 does block Ga diffusing into the absorber, but with a strong exchange of In by Ga, which changes the composition of these layers, leading to a formation of $CuInSe_2$ and GaO_x. Despite the exchange of In and Ga, the oxide is a good block layer to stop Ga diffusing into the absorber. As shown in **Figure 5.13 (h)** (top region of the figure) and **Figure 5.14** (within distance above 0.4 μm), almost no Ga can be detected in the absorber layer, meaning the Ga is well blocked by the oxide layer. As we discussed before, a homogeneous absorber is favorable to reduce the non-absorption of longwave-length photons and the radiative loss of V_{oc}, thus the blocking effect of the oxide to the diffusion of Ga is very important to avoid forming Ga lateral profile. No diffusion of Ga into the absorber means the bandgap of the absorber will not be shifted to a higher value. And this blocking effect depends on the thickness of the original In_2O_3. In **Section 5.3.2**, the influence of reducing thickness of In_2O_3 will be discussed.

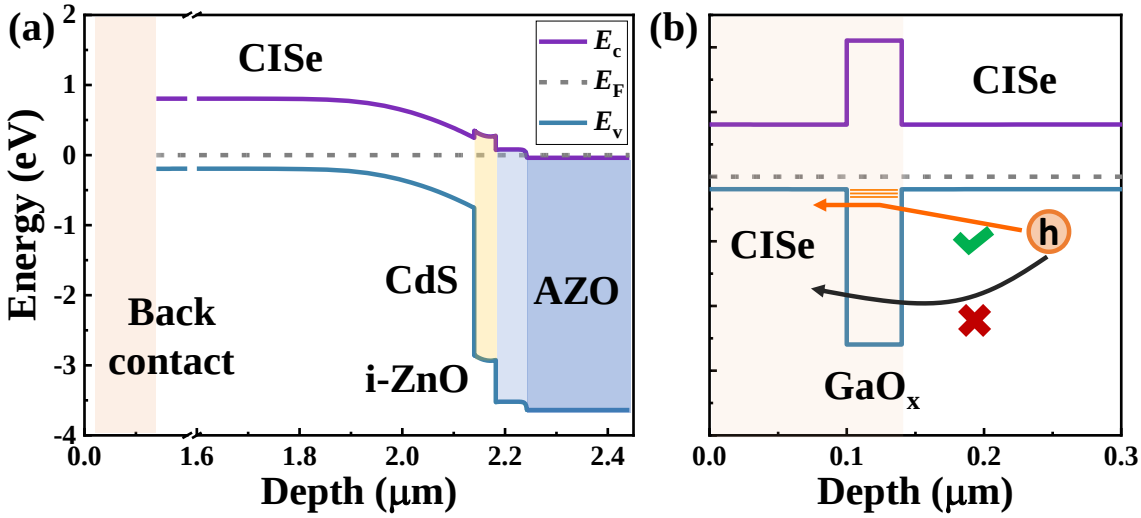

Figure 5.15 (a) The simulated band structure of $CuInSe_2$ solar cell; (b) The magnification of the back contact part. Theoretically, the high valance band valley is a hole transport barrier that

blocks the transport of holes. The Cu-related deep defects levels of GaO_x are close to the valance band maximum of $CuInSe_2$, which may assist the transport of holes.

The good passivation and hole transport ability of the HTL has been demonstrated experimentally. However, the formation of GaO_x due to exchange between In and Ga is not beneficial for transport of holes in principle. The GaO_x has a wide bandgap with a large electron affinity, which results in deep valance band barrier with energy above 2 eV compared to the $Cu(In,Ga)Se_2$. According to previous works, the bandgap and electron affinity of GaO_x was found to be around 4.7 eV[123, 166-169] and 3.2 eV[167-169], respectively. These values can be a little different depending on the different methods of preparing and measuring samples. But not matter in which case, it will not significantly change the band alignment between GaO_x and $Cu(In,Ga)Se_2$, thus will not change the following discussion. Based on bandgap of 4.7 eV and electron affinity of 3.2 eV, the potential band diagram of our solar cell is plotted as shown in **Figure 5.15**. It is clearly shows that the high hole transport barrier above 2 eV will not allow holes going through, thus limiting the diode current density and thus lowering the FF.

Meanwhile, experimentally, the GaO_x has been widely believed as a hole transport blocking layer, which seriously limits the diode current density and results in a low FF. The formation of GaO_x is well-known issue for high temperature growth of $Cu(In,Ga)Se_2$ on TCO contact. With substrate temperature above 450 °C[152, 170, 171], it was found thermodynamically favorable for Ga to react with TCO leading to formation of GaO_x at the interface between TCO and $Cu(In,Ga)Se_2$. It is believed that the existence of this GaO_x is typically amorphous with a high bandgap and resistance, which forms a serious barrier for extracting holes[149, 152, 170, 172]. As a result, the *J-V* curves show a S-shape or roll-over behavior due to the hole transport blocking caused by GaO_x. Actually, the similar hole transport blocking was observed in our experiments. An obvious hole transport blocking effect of GaO_x was found for submicron $Cu(In,Ga)Se_2$ solar cells (**Figure 5.19 (d)**), which leads to a very limited current density and FF. The details will be discussed in **Section 5.3.1**. To solve the problem of hole transport blocking due to GaO_x, adding NaF or Ag precursor before the $Cu(In,Ga)Se_2$ deposition is an effective way. It is very likely that the hole transport ability depends on the compensation of GaO_x, for example the Na[150, 173] or Ag[149] doping.

However, the Na or Ag doping is not very likely the explanation for our case because the samples without NaF precursor, e.g. the samples with In_2O_3 annealed at temperature of 200 °C and 300 °C, show a good FF, and we did not introduce any Ag precursor in our experiments. Thus, there must be some other mechanisms improving its hole transport property. And we believe the hole transport property of GaO_x is related to excess Cu doping. Some works reported that the Cu can introduce deep acceptor states that are close to the valance band maximum of $Cu(In,Ga)Se_2$ as shown in **Figure 5.15 (b)**. In this figure, the valance band alignment will not change significantly by varying GGI, because the increasing Ga can barely change the position of valence band maximum[39, 40, 43], meaning the valance band alignment in this figure can represent case of $Cu(In,Ga)Se_2$ with GGI form 0 to 1. From reported literatures, two Cu-related deep acceptor states were predicted by DFT calculation[174, 175]. And these deep acceptors states were also observed from PL and photoinduced absorption. Jiejing Zhang et.al. reported two Cu introduced deep acceptors in hydrothermal method synthesized GaO_x:Cu nanocrystals by PL measurements, and the emitted photons from these defects have an energy of 2.34 eV and 2.43 eV [176]. Yijun Zhang et.al. reported a Cu related deep acceptor state in sputtering prepared GaO_x:Cu thin film. This defect level was observed by room temperature PL measurements, which contributes to a PL emission with corresponding photon energy of 2.6 eV[177]. In addition, two Cu related deep acceptor states were reported in Cu-doped GaO_x crystal that was prepared by Czochralski (CZ) and vertical gradient freeze (VGF) methods. These two defect levels were observed by photoinduced absorption, in which the corresponding absorption energy was found to be 2.1 eV and 2.6 eV[178]. Therefore, as shown in **Figure 5.15 (b)**, it is possible that the Cu-related defect levels near the valance band maximum of the $Cu(In,Ga)Se_2$ supply an additional hole transport channel that helps the transport of holes. The defect levels assisted carrier transport was reported previously, the transport of holes is most likely helped by the Cu-related defects in GaO_x [176] and $In_xGa_{2-x}O_3$ [179]for perovskite solar cells. Additional evidence for the hole transport property depending on Cu doping is discussed in **Section 5.3.3**, the presented results show that the extra Cu annealing of oxides layer before the $Cu(In,Ga)Se_2$ deposition can effective remove hole blocking effect, leading to a high FF of 77%. More details will be discussed in **Section 5.3.3**.

On one hand, the presence of defects may play a significant role in facilitating hole transport, offering a plausible explanation for the observed good hole transport property. On the other hand, both DFT calculations and experimental findings indicate that Cu doping can enhance the p-type

conductivity of GaO_x. This suggests that the improved p-type conductivity could be another contributing factor to the favorable hole transport ability. However, it is important to note that a definitive conclusion regarding the exact mechanism responsible for the enhanced hole transport property remains elusive at this stage. Further in-depth investigations are necessary to unravel the precise underlying mechanism. But we can conclude that the hole transport ability is very likely depending on the excess Cu or Cu doping, this will also be proved in **Section 5.3.3**.

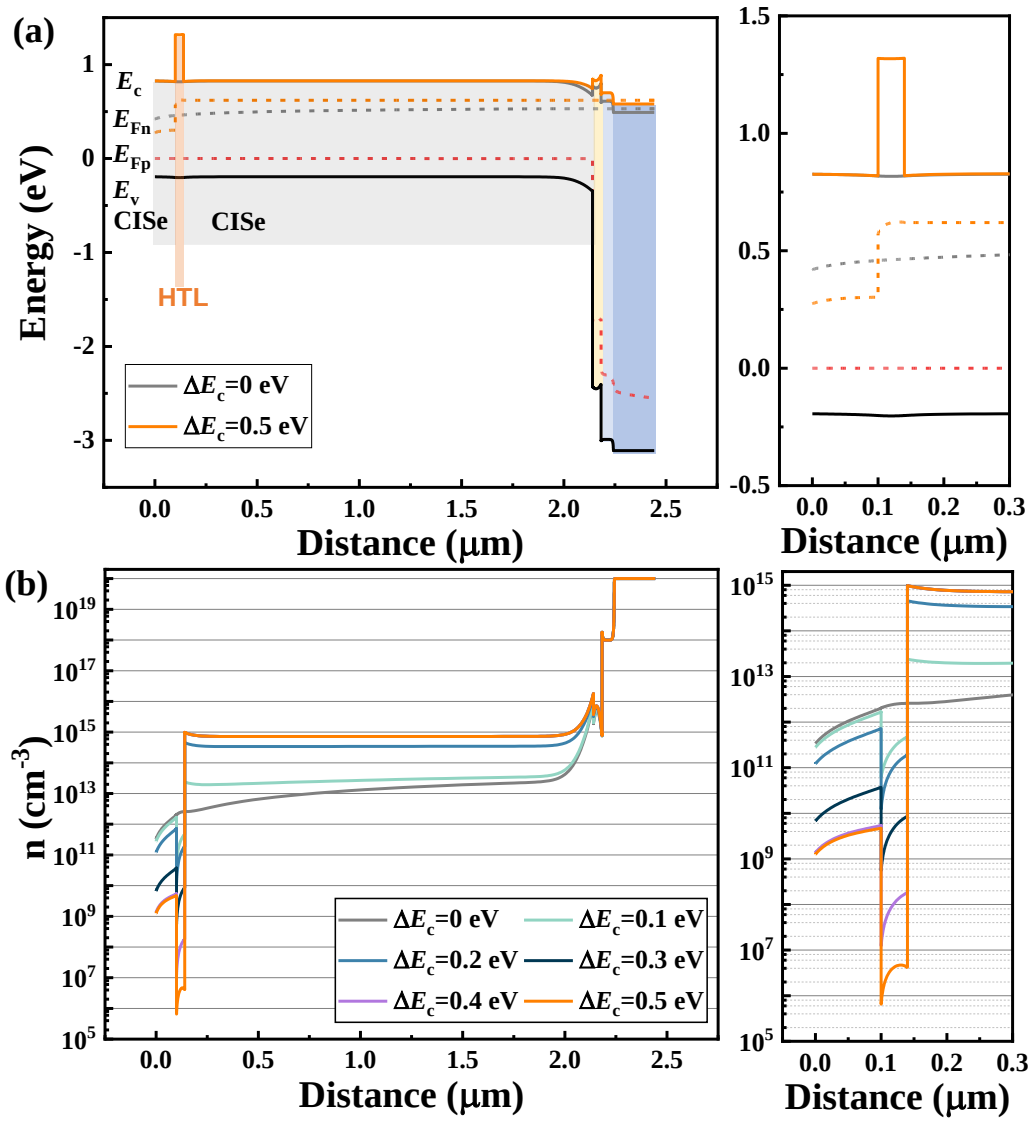

Figure 5.16 (a) The simulated band diagram under open-circuit condition, which shows the influence of conduction band spike on the electron Fermi level; (b) The electron density as a function of distance under open-circuit condition.

The effective passivation observed in our study can be attributed to the presence of a high conduction band spike between GaO_x and $Cu(In,Ga)Se_2$, leading to a reduction in the density of minority carriers at the backside and subsequently minimizing backside recombination, which is directly proportional to the minority carrier density. Previous research has demonstrated that the introduction of a conduction band spike by a hole transport layer (HTL) significantly reduces interface recombination[180]. However, our case differs slightly due to the presence of an additional $CuInSe_2$ layer beneath the wide bandgap GaO_x layer. Consequently, the device with the HTL exhibits the same $CuInSe_2$/Mo interface as the reference sample. To investigate the passivation mechanism potentially contributed by the conduction band spike, we conducted SCAPS simulations. To clearly observe the influence of backside recombination on the V_{oc}, the absorber's bulk lifetime was set to 500 ns, ensuring a sufficiently long minority carrier diffusion length of 11 μm compared to the 2 μm thickness (μ_e = 100 $cm^2/V{\cdot}s$, T = 300 K). The recombination velocities of electrons and holes at the back and front contacts were set to 10^6 cm/s and 10^3 cm/s, respectively, while no additional interface defects were considered. Other general parameters are summarized in **Table 3.3**. To simplify the simulation and avoid the complexity of introducing valence band barrier, the valence band is kept flat artificially by tuning the electron affinity of the HTL. In this case, only the influence of conduction band spike is considered.

Figure 5.16 (a) shows the band diagram of the simulated devices under illumination and open-circuit condition. The right figure is the magnification of the left figure within distance (film thickness) between 0 and 0.3 μm. It includes two different situations: one has no conduction band spike (ΔE_c = 0 eV) and another has conduction band spike of 0.5 eV (ΔE_c = 0.5 eV). For the simulated device with HTL (ΔE_c = 0.5 eV), the electron Fermi-level (E_{Fn}) of $CuInSe_2$ thin layer contacting with metal contact (contacting layer) is lower compared to that of simulated device without HTL (the orange dashed line is lower than the gray dashed line). The conditions with ΔE_c between 0 and 0.5 eV do not show in the **Figure 5.16 (a)**, because it is too hard to compare with too many curves. But E_{Fn} increasingly getting lower with increase of ΔE_c, meaning minority carrier (electron) density in this contacting layer depending on the ΔE_c. The higher ΔE_c leads to a lower electron carrier density. And this can be verified by **Figure 5.16 (a)** that shows the electron density with respect to the film thickness. The magnified figure (right) clearly shows that the electron density in this contacting layer is lower with higher ΔE_c. The reduction in electron density starts

getting saturated when ΔE_c = 0.3 eV, and it keeps almost same when ΔE_c = 0.4 eV and 0.5 eV. Because the serious backside recombination velocity of 10^6 cm/s, the electron density depth profile bends downward to the contact. The conduction band spike can reduce the electron density in this contacting layer because it is an electron transport barrier which blocks the electron current. This blocking effect is proportional to the exponential of $\Delta E_c/k_bT$ [23], which explains the lower electron density in the contacting layer. The small amount of electron in this layer is mostly from generation.

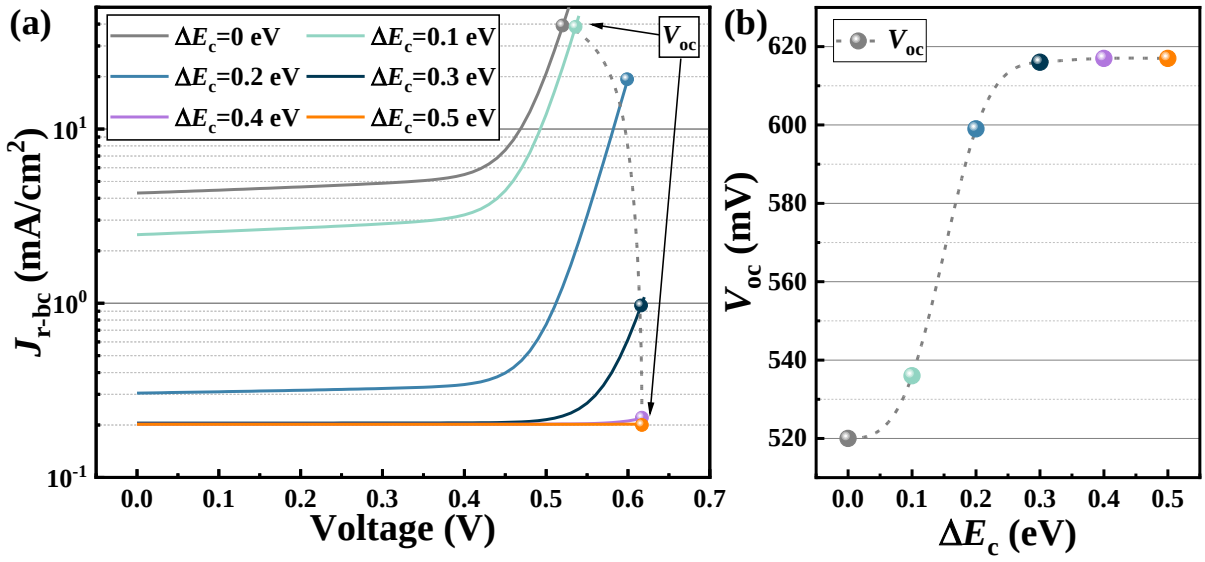

Figure 5.17 (a) The simulated back contact recombination current density ($J_{r\text{-}bc}$) as a function of voltage. In this simulation, the backside recombination velocity is set to be 10^6 cm/s. The conduction band spike (ΔE_c) reduces the back contact recombination current density, and it starts to saturate when this spike is higher than 0.3 eV. The sphere represents the back contact recombination current density at V_{oc}; (b) The influence of ΔE_c on V_{oc}.

Since the backside recombination is proportional to the electron density, **Equation 2.13**, the lower electron density at the backside lowers the backside recombination between metal contact and contacting layer. **Figure 5.17 (b)** shows the back contact recombination current density ($J_{r\text{-}bc}$) as a function of voltage in situations with different ΔE_c. The sphere on each curve represents the $J_{r\text{-}bc}$ at V_{oc} for each case with different ΔE_c. In low voltage region (Voltage<0.4 V), the $J_{r\text{-}bc}$ of simulated device is significantly reduced by increasing ΔE_c. With a higher voltage, the $J_{r\text{-}bc}$ of the case with high ΔE_c increases much slower compared to the case without ΔE_c or with low ΔE_c. Consequently,

$J_{r\text{-}bc}$ of the case with high ΔE_c at the V_{oc} is much lower compared to that of the case without ΔE_c or the low ΔE_c. The lower $J_{r\text{-}bc}$ means lower backside recombination which leads to a higher V_{oc}. As shown in **Figure 5.17 (a)**, the V_{oc} can be improved by around 100 mV by increasing ΔE_c from 0 to 0.4 eV. Because the $J_{r\text{-}bc}$ is low enough when ΔE_c reaching beyond 0.3 eV, the impact of backside recombination on V_{oc} becomes very small, thus the improvement in V_{oc} by reducing back contact recombination starts getting saturated when ΔE_c = 0.3 eV.

In summary, the conduction band spike reduces the back contact recombination because it is an electron transport barrier that lowers the electron density at metal contact interface. However, it is notable that this HTL with a conduction band spike can only reduce the interface recombination between metal contact and $CuInSe_2$. The new interface between the HTL and the absorber can be another problematic interface that introduces an extra recombination channel. In other simulations (not shown in here), even with ΔE_c of 0.5 eV, introducing interface recombination between HTL and absorber with recombination velocity of 10^6 cm/s can lead to low V_{oc} of 520 mV, which is the same low V_{oc} due to serious backside recombination taking place at metal contact interface. This may potentially be the reason for that GaO_x layers introduced by different methods show different passivation effects since they may have different interfaces with the absorbers. This will be discussed in the following.

There are still two things which are not very clear and can be argued. Firstly, if the excess Cu doping in GaO_x is critical to improve the hole transport property, it is expected that some Cu should accumulate in GaO_x then can be detected by the element mapping. However, **Figure 5.14** shows that it is hard to find Cu accumulating in GaO_x layer. High amount of Cu can be detected at the two interfaces of GaO_x, but simultaneously with high amount of In and Se. Because the resolution of the EDS measurement in this case is around 10 nm, it is most likely that the Cu is from $CuInSe_2$ rather than the doped Cu in GaO_x. However, we can not exclude the possibility of Cu doping from EDS measurements because the sensitivity may be insufficient to detect the small amount of doped Cu. Therefore, it is interesting to have a SIMS measurement on this sample, which gives us a higher sensitivity. Secondly, the TEM results imply the formation of GaO_x due to element exchange between In and Ga. The backside passivation effect of GaO_x may attribute to the conduction band spike as shown in **Figure 5.15 (b)**. But, in **Section 5.2.2**, GaO_x prepared directly by SCS does not show significant passivation effect. Perhaps, the passivation effect of GaO_x relies

on the morphology, composition (e.g. Ga/O ration, the amount of Cu doping) and crystallization. Indeed, we peeled the absorber from the substrate and measured the XRD from the backside, it shows a broad diffraction peak at 2θ of 19.3° which seems correlated to the (201) orientation of β-GaO_x (**Annex Figure A5.13**). These properties may have an impact on interface recombination between GaO_x and absorber, which can not be suppressed by the conduction band spike. Unfortunately, so far, the evidence is not enough to explain the different passivation effect between the GaO_x formed by element exchange and the one prepared directly by SCS. But it is interesting to have a further experiment in which adding excess Cu to SCS prepared GaO_x and check the passivation and hole transport property.

The $CuGaSe_2$ with an In_2O_3 stabilizer forms a stable and efficient hole selective transport structure with promising passivation and transport properties. This HTL structure withstands the harsh growth conditions of the chalcopyrite. However, due to element exchange between In and Ga taking place during the growth of absorber, the two layers at the backside are converted from $CuGaSe_2/In_2O_3$ to $CuInSe_2/GaO_x$. The good passivation effects can attribute to the conduction band spike between GaO_x and $CuInSe_2$. And good hole transport ability is most likely related to Cu introduced defects in GaO_x, which assists the transport of holes. However, the further works and evidence are required to support the proposed speculations. Despite the not exactly clear working mechanism of the HTL, it does improve the performance of our solar cells. The HTL enhances the lifetime of $CuInSe_2$ samples from 5 ns to 113 ns, with an associated increase in ΔE_F of ~80 meV, demonstrating the passivating effect of this novel HTL. The device built with this HTL exhibits a high FF of >71%, indicating good hole transport property without obvious current blocking effects.

5.3 Application of dual-layer HTL to submicron $Cu(In,Ga)Se_2$ solar cells

5.3.1 Passivation VS hole transportation

In **Section 5.2**, we demonstrate how the $CuGaSe_2/In_2O_3$ combination acts as a functional HTL with good properties of passivating and transporting holes. In this Section, we will focus on submicron $Cu(In,Ga)Se_2$ (with thickness less than 1 μm), because the HTL developed in previous

section has potential applications in submicron $Cu(In,Ga)Se_2$ solar cells which offers cost savings by reducing material consumption. Furthermore, submicron solar cells with thickness less than 100 nm on TCO glass can make semi-transparent modules that are well-suited for building-integrated photovoltaic (BIPV) and agrivoltaic applications. For example, they could be used to create energy-efficient windows or to power agricultural greenhouses.

To produce high-efficiency submicron solar cells, mitigating backside recombination is essential[181-183]. For submicron $Cu(In,Ga)Se_2$ films with a thickness of less than 1.0 µm, backside recombination is a more significant issue as more charge carriers are generated in the near backside region and can easily diffuse to the backside. In thick $Cu(In,Ga)Se_2$, a higher Ga gradient towards the backside can typically suppress backside recombination. However, optimizing the growth process to build such a gradient in a limited thickness is a major challenge that researchers are currently facing in the production of high-efficiency submicron solar cells[184].

Fortunately, the HTL structure developed in this work provides a solution for mitigating backside recombination without the need to optimize the Ga gradient. By utilizing the passivation and hole transport ability of the HTL developed in this thesis, the backside recombination of submicron $Cu(In,Ga)Se_2$ can be effectively suppressed. This approach provides a practical solution for producing high-efficiency submicron $Cu(In,Ga)Se_2$ solar cells.

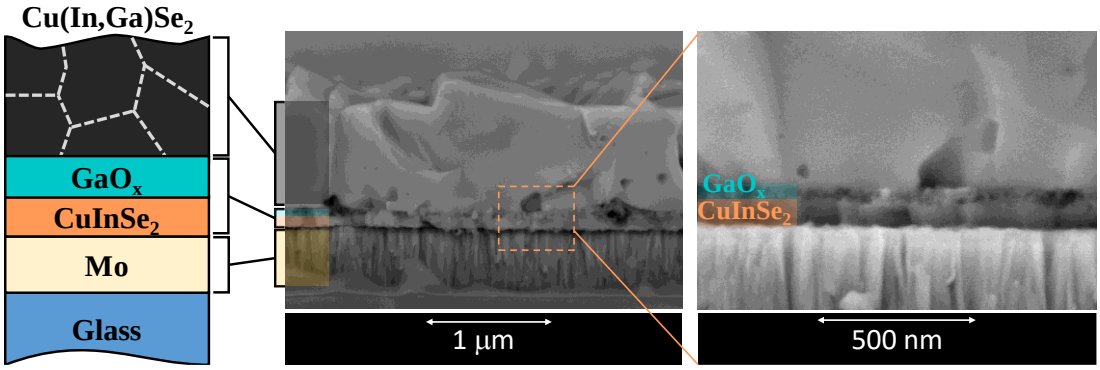

Figure 5.18 The sample structure and its corresponding SEM cross-section image: The SEM image shows the thickness of $Cu(In,Ga)Se_2$ is around 800 nm. Additionally, two distinct layers of GaO_x (~40 nm) and $CuInSe_2$ (~100 nm) are located beneath of $Cu(In,Ga)Se_2$. The element exchange taking place in $CuInSe_2$ samples implies the formation a $CuInSe_2/GaO_x$ stack, which is likely happening to $Cu(In,Ga)Se_2$ as well because of the similar preparing process.

$Cu(In,Ga)Se_2$ with a thickness of approximately 800 nm is prepared using a 3-stage process (maximum T_{sb} = 580 °C) that results in a Ga gradient. However, the growth process of the absorber is suboptimal, leading to significant ΔE_F losses due to the backside recombination. To mitigate this issue for submicron $Cu(In,Ga)Se_2$, a layer of 100 nm $CuGaSe_2$ covered with 40 nm In_2O_3 is used. The $CuGaSe_2$ was deposited onto the Mo coated soda-lime glass at substrate temperature of 356 °C and the In_2O_3 was synthesized by SCS with an annealing temperature of 300 °C in air. The reference sample means the submicron $Cu(In,Ga)Se_2$ directly grown on Mo substrate.

The structure of the sample, along with its corresponding SEM cross-section image are shown in **Figure 5.18**. The growth duration of the submicron absorber is only one-third of that required for a standard absorber. Reducing the growth duration reduces the Cu-rich growth duration, which can, in turn, may reduce absorber quality by decreasing the grain sizes. However, the SEM cross-section image shows a film with grain sizes of 1-2 μm. This suggests that reducing the growth duration will not decrease the crystal quality, ensuring a long minority carrier lifetime of the bulk and the potential to create an efficient solar cell. Additionally, the SEM image reveals two distinct layers of GaO_x (~40 nm) and $CuInSe_2$ (~100 nm). The EDS mapping results in **Section 5.2.3** imply the formation of a $CuInSe_2/GaO_x$ stack in $CuInSe_2$ due to element exchange during the sample preparation. Due to the similar preparation process of $CuInSe_2$ and $Cu(In,Ga)Se_2$, it is highly probable that this element exchange also occurs during the preparation of $Cu(In,Ga)Se_2$.

The presence of a good HTL underneath is indicative of a favorable passivation effect that can result in longer minority carrier lifetime and higher ΔE_F. To investigate this passivation effect, TRPL was employed to determine the minority carrier lifetime. As shown in **Figure 5.19 (a)**, the sample with the HTL exhibits a much slower decay of PL counts compared to the reference sample, indicating a longer weight effective lifetime of 125 ns compared to that of reference sample of 11 ns. This passivation effect is further corroborated by the reduction in ΔE_F deficits ($- k_b T \ln[PLQY]$) as shown in **Figure 5.19 (b)**, the samples with the HTL displaying a significantly higher ΔE_F and lower ΔE_F deficit by around 80 meV compared to the reference sample.

Furthermore, the passivation effect is also demonstrated through the ODF in **Figure 5.19 (d)**. The ODF of the sample with the HTL (1.35) is higher than that of the reference sample (1.17), confirming effective mitigation of backside recombination, which shifts the loss of ΔE_F to the bulk recombination. Further discussion of the ODF is presented in **Chapter 6.** The high ODF value of

1.35 also suggests that the doping density of the sample is low. The doping density of the absorber can be estimated using **Equation 2.46**, based on the PL measurements. The estimated doping density is approximately 1-2×10^{15} cm^{-3}, which is one order of magnitude lower than the highest doping density measured from the GBG samples (**Table 4.1**), which is around 1.8×10^{16} cm^{-3}. This significant difference in doping density results in a lower ΔE_F of approximately 60 meV, indicating that the doping density must be improved with an aim to gain solar cells with higher efficiency. Additionally, the higher ODF value leads to a lower FF, which limits the efficiency of the solar cells. Therefore, improving the doping density is crucial to optimize the performance of the solar cells. One way to achieve this is introducing alkalis PDT[185-187]. Further details about the efficiency loss of solar cells are discussed in **Chapter 7**.

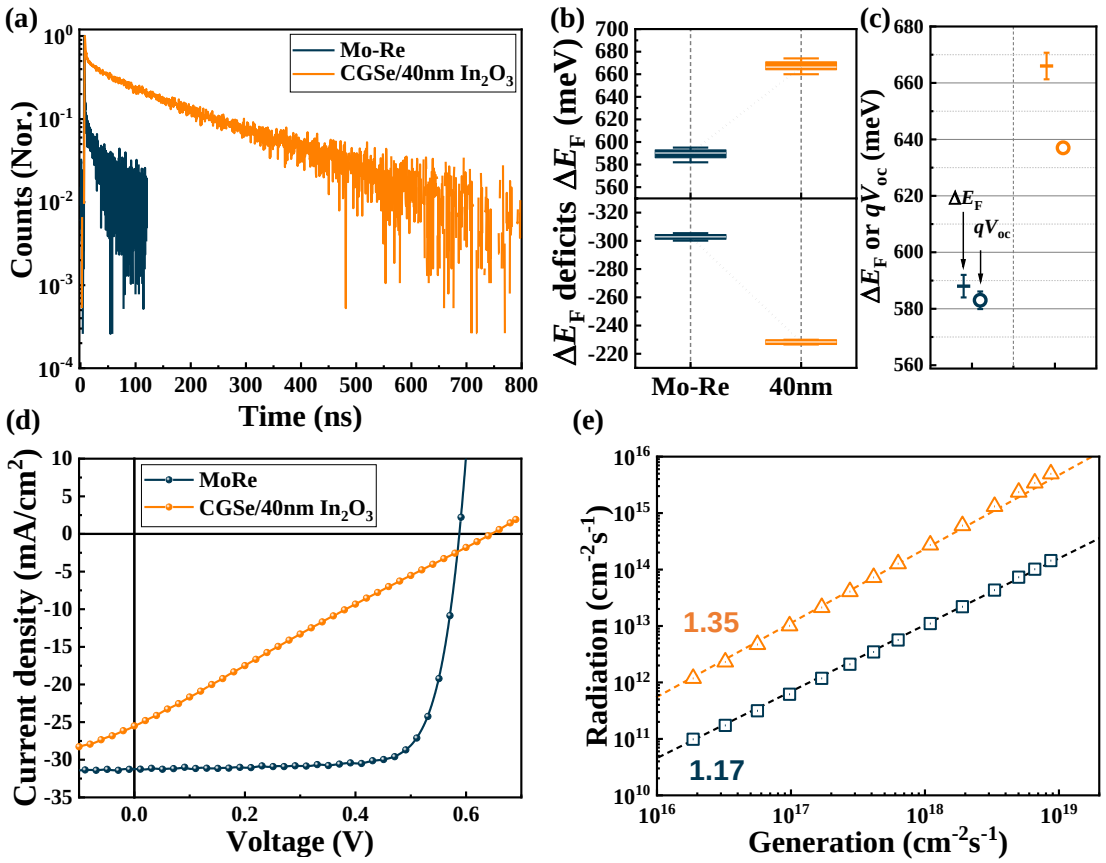

Figure 5.19 (a) To identify the samples, the HTL passivated sample is named by the deposition sequence of the HTL ($CuGaSe_2/In_2O_3$), but it is worth to mention that the exchange of In an Ga may convert the $CuGaSe_2/In_2O_3$ to $CuInSe_2/GaO_x$. The TRPL measurement of the reference sample and the sample with HTL revealed a significantly slower decay rate in the latter, indicating a longer lifetime as a result of backside passivation; The box plot, in which the box

represents the interquartile range (25^{th} to 75^{th} percentile), the inside the box is the mean value and the whisker is based on 1.5 IQR (interquartile range) value: (b) Compared to the reference samples, the good passivation provided by the HTL leads to significantly higher ΔE_F and lower ΔE_F deficits; (d) The 40 nm GaO_x leads to a hole transport blocking effect which results in loss of J_{sc}, V_{oc} and extremely low FF; (e) The higher ODF observed in samples with HTL compared to the reference sample provides further evidence of backside passivation achieved by implementing HTL.

The longer effective lifetime and thus higher ΔE_F demonstrate the effectiveness of HTL in passivating the backside recombination. However, as previously discussed, a functional HTL is not only required for its passivation capabilities but also for its ability to transport holes smoothly. The smooth transportation of holes is crucial to prevent current blocking effects and achieve a good FF and J_{sc}, which determine the efficiency of solar cells. Unfortunately, the strong blocking effects of holes due to the 40 nm GaO_x layer are observed in the submicron $Cu(In,Ga)Se_2$ solar cells. **Figure 5.19 (d)** shows a typical illumination *J-V* characteristic of a reference sample and a sample with HTL. The best reference solar cell (best FF) exhibits FF of ~77%. This good FF suggests a smooth transport of carrier without obvious barriers of transportation. Inversely, the *J-V* curve for the sample with HTL shows a linear rather than an exponential relation, indicating that GaO_x generates a significant hole transport barrier that behaves like a resistor in series. As a result, this leads to an extremely low FF and a reduction in J_{sc}. In addition, this hole transport barrier saturates the forward diode current, leading to a higher V_{oc} deficits compared to the $\Delta E_F/q$ as shown in **Figure 5.19 (c)**.

To ensure proper functioning of the HTL, it is crucial to improve its hole transport property. When having even thicker GaO_x for $CuInSe_2$ in **Section 5.2.3**, no apparent hole transport blocking effect was observed. Two hypotheses are proposed to explain the blocking effect observed in the submicron $Cu(In,Ga)Se_2$ cells. The thickness of the In_2O_3 layer may be excessive for the submicron absorber due to the shorter growth duration, which limits its interaction with other layers, for example the element exchange between In and Ga shown by EDS mapping. This suggests that a thinner In_2O_3 layer may be more suitable for optimizing the performance of the submicron absorber. To investigate this, the optimization of the In_2O_3 thickness was carried out, and its impact on the solar cells' performance is studied in **Section 5.3.2**. Secondly, the presence

Cu doping in GaO_x is very likely important for enhancing the hole transport. It is possible that the insufficient interaction between the oxides and Cu may result in current blocking. This insufficient interaction may be caused by the short absorber deposition duration or low amount of Cu in $CuGaSe_2$ layer. To address this issue, we introduced an extra Cu annealing step before the absorber deposition, allowing sufficient interaction of oxides with Cu to modify the properties of GaO_x. The details of the Cu post-annealing are discussed in **Sections 5.3.3**.

5.3.2 Thickness optimization of In_2O_3

Section 5.3.1 presents the implementation of 100 nm $CuGaSe_2$ and 40 nm In_2O_3, exhibiting good passivation effects that reduce ΔE_F loss by approximately 80 meV. However, it also shows a strong hole transport blocking effect which leads to a very low FF. Because of the short preparation duration of submicron Cu(In,Ga)S**e**$_2$ compared to the thick absorber, it is possible that the interaction duration for these layers is insufficient, especially in case of a thick oxide layer, to form a properly Cu doped GaO_x layer. Consequently, it introduces high hole transport barrier, leading to a very low FF. To address this issue, thinner In_2O_3 layers of 20 nm and 10 nm were introduced and their effects of passivation and hole transport were investigated.

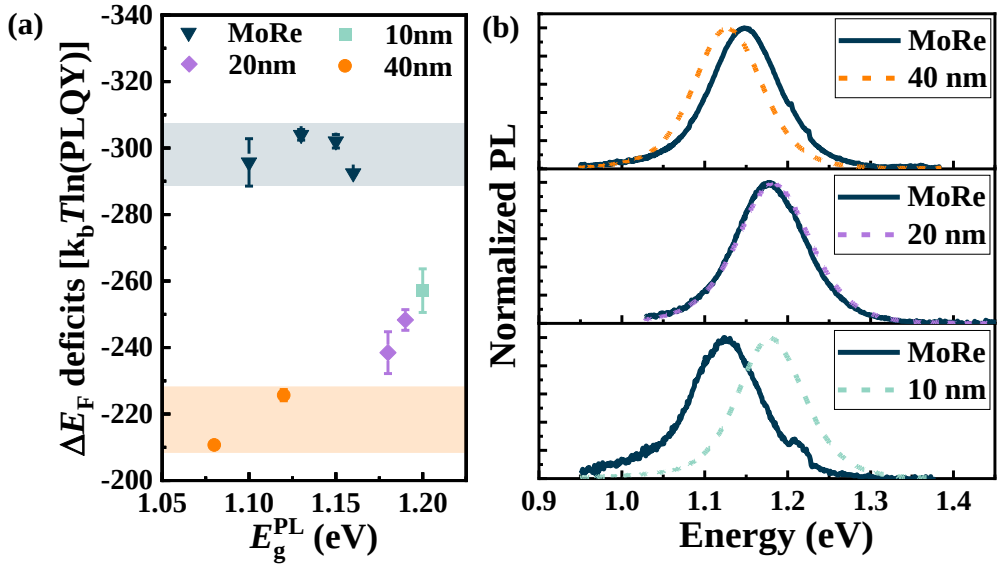

Figure 5.20 (a) Influence of In_2O_3 thickness on ΔE_F deficits compared to the reference samples (without backside passivation). Three samples with a combination of ~100 nm $CuGaSe_2$ and

40/20/10 nm In_2O_3 were tested. The presented bandgap corresponds to the PL flux maximum, and ΔE_F was obtained by fitting the high energy wing of transformed absolute PL spectra while fixing the fitting temperature to ambient temperature; (b) The blue shift of the PL maximum indicates the diffusion of Ga from backside to the bulk, which increases the GGI of the bulk, thus leading to a higher bandgap.

Figure 5.20 (a) shows submicron Cu(In,Ga)Se_2 prepared using a three-stage process at maximum substrate setting temperature of 580 °C. The absorber preparation process is the same as the one used in previous section, thus the thickness of these samples is estimated to be around 800 nm according to SEM cross-section image shown in **Figure 5.18**. The PL bandgap of these samples are different from 1.08 eV to 1.2 eV due to the different GGI. In_2O_3 capping layers were prepared using SCS with an annealing temperature of 300°C in air, and the studied thicknesses were 40, 20, and 10 nm. The reference samples were not passivated by HTL. All samples with HTL exhibit lower ΔE_F deficits than the reference sample, indicating a mitigation of backside recombination and reduction in non-radiative recombination. The ΔE_F deficits were calculated based on PLQY, which represents the non-radiative losses. With 40 nm In_2O_3, the lowest ΔE_F deficit of -210 meV was achieved. However, thinning In_2O_3 layer to 10 nm results in an increase in ΔE_F deficit by approximately 50 meV, from 210 meV to 260 meV, suggesting a degradation of passivation effects. This degradation of backside passivation is very likely related to the diffusion of Ga in $CuGaSe_2$, which can not be fully blocked by the oxide layer. Since the In_2O_3 layer is thinner, it can be expected that the GaO_x formed by element exchange is thinner. It is possible that, in this case, the GaO_x is not thick enough to have a good enough passivation.

Figure 5.20 (b) shows shift of the PL bandgap depending on the thickness of In_2O_3. For samples with 40 nm In_2O_3, the bandgap is slightly lower than the reference sample, likely due to slight diffusion of In from In_2O_3. As discussed before, the EDS line scanning (**Figure 5.14**) shows that 50 nm In_2O_3 is thick enough to block the diffusion of Ga to $CuInSe_2$ absorber. In case of submicron Cu(In,Ga)Se_2, a thinner In_2O_3 of 40 nm is used, but considering the short deposition time of the absorber, it is reasonable to believe that 40 nm In_2O_3 is thick enough to block the diffusion of Ga. If it is not exact the case (meaning the Ga may be not fully blocked), the amount of Ga diffusion should be very tiny compared to the potential diffusion of In from In_2O_3. Consequently, it results in a red shift of the PL bandgap of samples with 40 nm In_2O_3. When reducing In_2O_3 to 20 nm, the

PL bandgap of samples with HTL is roughly the same as the reference sample. This is most likely because reducing In_2O_3 to 20 nm allows more Ga diffusing to the absorber, which compensates the diffusion of In. The only significant blue shift of the PL bandgap was observed in samples with 10 nm In_2O_3, indicating more diffusion of Ga from the backside to the bulk compared to the case with 20 nm In_2O_3. The degradation of backside passivation is probably related to the diffusion of Ga, and more importantly, the thinner oxide layer may be not enough to effectively block the electrons reaching back contact, thus increasing the backside recombination.

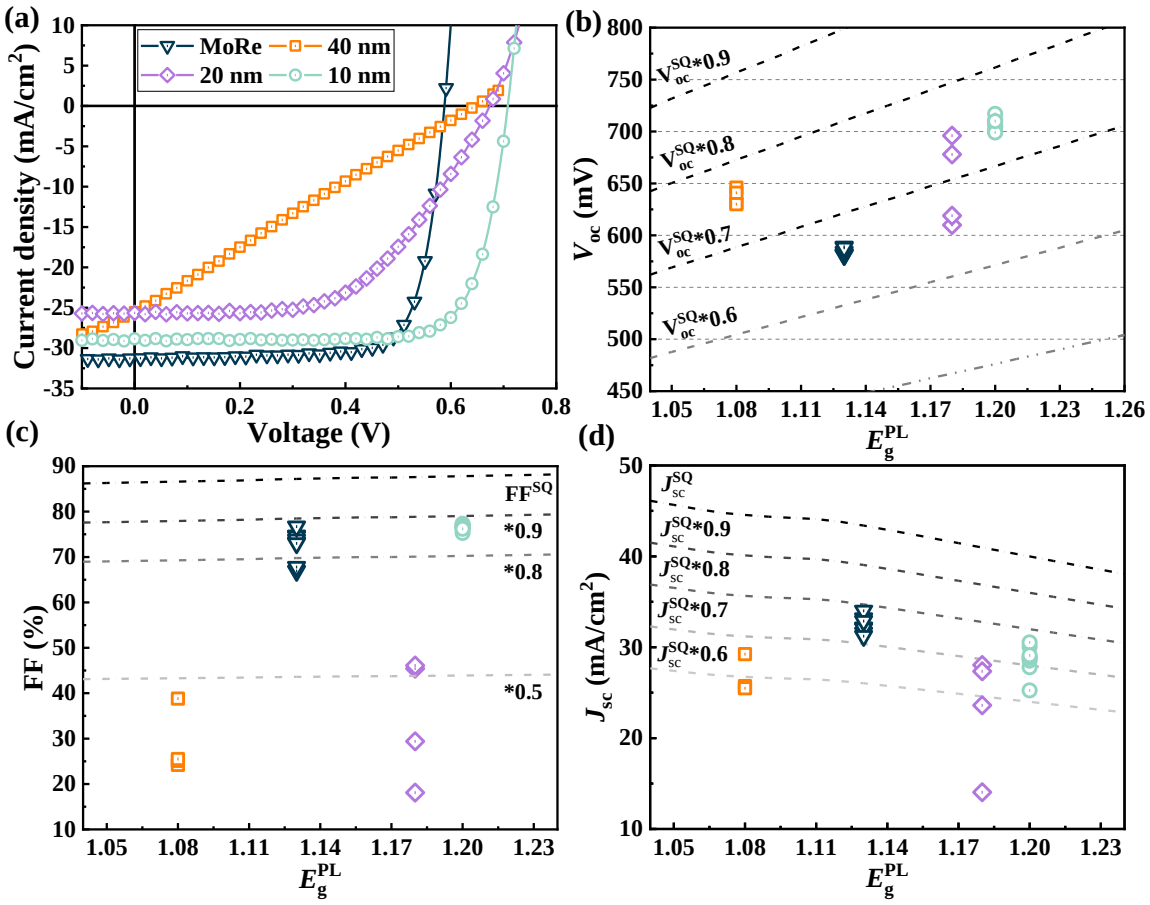

Figure 5.21 (a) The *J-V* characteristics of different samples (the one with best FF) are shown: the reference sample grown directly on Molybdenum and samples with HTL ($CuGaSe_2/In_2O_3$), where 100 nm $CuGaSe_2$ is covere by In_2O_3 with three different thicknesses (40, 20, and 10 nm). Reducing the thickness of In_2O_3 layer results in a reduction of R_s and an improvement in FF, indicating enhanced hole transport property. The V_{oc}, FF and J_{sc} as a function of E_g^{PL}: (b) The V_{oc} of the samples with different thickness of In_2O_3; (c) Samples with 40 and 20 nm In_2O_3 have poor hole transport, leading to low FF. Reducing the thickness of In_2O_3 layer improves hole transport,

resulting in an improvement in FF. The highest FF of 77.3%, close to 90% of the SQ value, is achieved by reducing the thickness of In_2O_3 layer to 10 nm; (d) The hole transport is blocked by thick oxides, which results in a decrease in J_{sc}. In the worst case, the current is entirely blocked, leading to an extremely low current density.

To clearly indicate which sample will be discussed, the thickness of In_2O_3 (according to deposition sequence) will be literally used in the following discussion. However, it is notable that the In_2O_3 was most likely converted to GaO_x after the absorber deposition due to element exchange as we discussed before. The effectiveness of using a HTL to mitigate backside recombination is also demonstrated by the improved performance of solar cells, as depicted in **Figure 5.21 (b)**. The V_{oc} of samples with HTL aligns well with the discoveries observed in ΔE_F, which again proves a significant reduction in backside recombination. The solar cells with 40 nm In_2O_3 ($E_g^{PL} = 1.08$ eV) exhibit a V_{oc} that is approximately 77% of the SQ V_{oc}. And solar cells passivated by 20 nm In_2O_3 exhibit higher V_{oc} losses, which are roughly similar to those of the samples with 10 nm In_2O_3. Solar cells with 20 nm In_2O_3 have low FF and J_{sc} compared to the reference samples, which implies a hole transport blocking. The higher deficits of V_{oc} may be a result of the hole transport blocking since it saturates the forward bias current. Besides, small V_{oc} variations can also take place due to different runs of solar cell fabrication, owing to differences in frontside recombination resulting from issues of reproducibility. Despite these variations, the behavior of V_{oc} does not contradict the ΔE_F trend with respect to thickness of In_2O_3.

The mitigation of backside recombination by introducing a HTL has been demonstrated by improvements in both ΔE_F and V_{oc}. However, the thickness of In_2O_3 needed for passivation affects the performance of the solar cells. In terms of hole transport, the results show an improvement in FF with a thinner In_2O_3, as indicated by the "squareness" of the *J-V* curve in **Figure 5.21 (a)**. For instance, the FF of the sample with 20 nm In_2O_3 is improved compared to the sample with 40 nm In_2O_3. However, it seems that the hole blocking of the 20 nm In_2O_3 is still worse than the reference sample, resulting in FF loss. To fully eliminate the FF loss due to hole transport blocking, a thinner In_2O_3 of 10 nm is investigated. The transportation of holes is clearly improved, resulting in the highest FF of 77.3%. However, this improvement in hole transport comes at the cost of losing ΔE_F and V_{oc}, which creates a trade-off between FF and V_{oc}. Achieving high efficiency solar cells requires both high FF and V_{oc}. For instance, with FF of 77.3%, to achieve an efficiency higher than

20%, both J_{sc} and V_{oc} must be higher than 82% of the SQ value (e.g., $0.82 \cdot J_{sc}^{SQ}(E_g = 1.21\ \text{eV}) = 32.3\ \text{mA/cm}^2$, $0.82 \cdot V_{oc}^{SQ}(E_g = 1.21\ \text{eV}) = 788\ \text{mV}$), as suggested by **Figure 5.21 (c) (d)**. This requires improving V_{oc} by at least 80 mV, which is challenging without a fully passivated backside. In addition, J_{sc} should be improved by about 3 mA/cm^2, which could be potentially realized by introducing photon recycling (in terms of submicron absorbers), reducing the parasitic absorption of CdS, and adding an anti-reflection coating, as discussed in **Chapter 7**.

To achieve high-efficiency solar cells, it is crucial to find a way to keep both good passivation and hole transport properties of the HTL. As previously discussed, a thick In_2O_3 layer (40 nm) effectively blocks the diffusion Ga from $CuGaSe_2$, leading to the best passivation of the backside recombination, thus the lowest deficits in ΔE_F. However, this thickness strongly inhibits hole transport, resulting in low FF and reduced J_{sc}. Conversely, reducing the thickness of In_2O_3 improves hole transport but compromises the backside passivation. These trade-offs limit the maximum achievable efficiency of the solar cell.

Therefore, optimizing the thickness of In_2O_3 alone may not provide a comprehensive solution. To achieve high efficiency, it is necessary to modify the electrical properties of the HTL while maintaining a fully passivated backside and decent hole transport property simultaneously. One approach to achieve this is by introducing an excess Cu post-annealing on the In_2O_3 layer, as discussed in the next section.

5.3.3 Cu annealed In_2O_3

In the previous section, it is shown that tuning the thickness of In_2O_3 results in a trade-off between backside passivation and hole transport. A thick In_2O_3 provides good backside passivation but blocks hole transport, while a thin In_2O_3 improves hole transport but sacrifices backside passivation. Achieving both high V_{oc} and FF simultaneously is critical for achieving high-efficiency solar cells. Thus, a thick In_2O_3 with modified electrical properties is required to guarantee both good backside passivation (V_{oc}) and hole transport (FF).

In **Section 5.2.3**, **Figure 5.15 (b)** shows a high valence band barrier between $CuInSe_2$ and GaO_x, which should block the transport of holes in principle. And we did see this blocking effect for

submicron Cu(In,Ga)Se_2 solar cells in **Section 5.3.1**, but not for $CuInSe_2$ solar cells discussed in **Section 5.2.3**. Based on the indication from literatures[176, 179], we speculate that the Cu doping for GaO_x plays an important role on hole transport. The different behavior of GaO_x may be related to the excess amount Cu, e.g. the amount of Cu in $CuGaSe_2$ under layers, which leads to a different amount of Cu doping in GaO_x. Unfortunately, due to lack of understanding at beginning, the amount of Cu in $CuGaSe_2$ was not carefully controlled and checked. To address the question of whether Cu matters, in this section, the effects of Cu annealing on In_2O_3 are investigated.

Four different samples were prepared, the reference sample without HTL and the other three samples with $CuGaSe_2/In_2O_3$. 100 nm $CuGaSe_2$ was deposited onto Molybdenum-coated soda-lime glass at a substrate setting temperature of 356 °C, which were prepared by the same conditions as the one used for solar cells discussed in **Section 5.3.1**. The three samples were then covered by In_2O_3 with thicknesses of 20 nm, 30 nm, and 40 nm, respectively. They were synthesized by SCS with an annealing temperature of 300 °C in air. To carry out the Cu annealing process, around 30-40 nm Cu was deposited onto the surface of the In_2O_3 by thermal evaporation in PVD, and the thin film stacks of $Mo/CuGaSe_2/In_2O_3/Cu$ were heated from 200 °C to 500 °C in 6 minutes, followed by another 20 minutes of annealing at 500 °C in vacuum. After the Cu annealing of In_2O_3, the substrates were cooled down to 356 °C and a submicron Cu(In,Ga)Se_2 was grown by a 3-stage process at maximum substrate setting temperature of 580 °C.

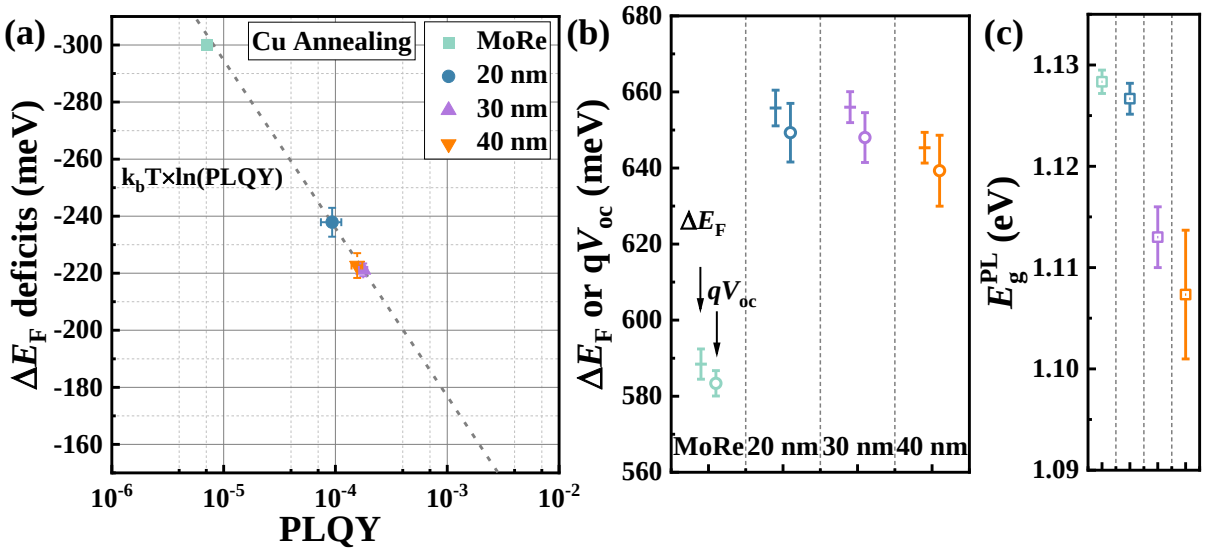

Figure 5.22 (a) The ΔE_F deficits of the samples are plotted as a function of PLQY, with the reference sample having the absorber directly grown on Mo, and the backside of the other three

samples is passivated by Cu-annealed HTLs ($CuGaSe_2/In_2O_3$), with a $CuGaSe_2$ thickness of approximately 100 nm and In_2O_3 stabilizer thicknesses of 20 nm, 30 nm, and 40 nm, respectively; (b) The ΔE_F and V_{oc} of the different samples are shown. The ΔE_F was obtained by fitting the high-energy wing of transformed absolute PL spectra while fixing the fitting temperature to ambient temperature; (c) E_g^{PL} of the samples is presented, which is the energy corresponding to the maximum PL flux.

Figure 5.22 (a) depicts the relationship between the ΔE_F deficit and PLQY of the samples. The ΔE_F deficit represents the non-radiative losses calculated by $k_bT \times \ln(PLQY)$. The reference sample, without an HTL, exhibits the worst PLQY of approximately 7×10^{-6}, resulting in the highest ΔE_F deficit of around 300 meV. This high ΔE_F deficit indicates a substantial backside recombination, which causes high non-radiative loss at the backside. Upon adding the HTL, i.e., 100 nm $CuGaSe_2$/20 nm In_2O_3, the PLQY is improved significantly by over one order of magnitude, leading to a reduction in ΔE_F deficit of around 60 meV. This significant reduction in non-radiative recombination is comparable to the passivation effect of the HTL without Cu annealing, as discussed in **Section 5.3.2**. This demonstrates the good passivation effect of the Cu-annealed HTL, and more importantly, suggests that Cu annealing does not compromise the passivation effect. Otherwise, the unwanted trade-off between passivation and hole transport would need to be reevaluated, which cannot result in high-efficiency solar cells.

Furthermore, by increasing the thickness of In_2O_3 to 30 nm, an additional ΔE_F deficit reduction of approximately 15 meV is achieved, indicating better passivation of the backside. This better passivation is very likely related to the better block of Ga diffusion from $CuGaSe_2$, and thus formation of thicker GaO_x layer. However, this plausible passivation effect is not confirmed by the TRPL characteristics, which will be discussed later. Increasing the thickness of In_2O_3 to 40 nm does not further improve the ΔE_F deficit, implying that 30 nm of In_2O_3 is sufficiently thick to passivate the backside. Therefore, further optimization of the solar cells' performance should be based on the 30 nm In_2O_3.

In summary, the HTL can reduce the ΔE_F deficit by approximately 80 meV compared to the reference sample without passivation. **Figure 5.22 (b)** illustrates that the improvement in ΔE_F is around 65 meV, where ΔE_F is determined by fitting the high energy wing of the transformed

absolute PL spectra using Planck's generalized law, assuming $a(E) = 1$ and fixing the fitting temperature to the measured ambient temperature. This improvement in ΔE_F is slightly lower than the reduction in ΔE_F deficit, which is due to the slightly lower bandgap of the samples with thicker In_2O_3 (30 nm and 40 nm), as shown in **Figure 5.22 (c)**. The bandgap presented in **Figure 5.22 (c)** corresponds to the PL bandgap, i.e., the energy corresponds to the PL flux maximum. The lower bandgap is most likely due to the slight diffusion of In in In_2O_3, which slightly lowers the GGI value of the absorber. The thicker In_2O_3 leading to a lower bandgap implies this diffusion.

The passivation effect of Cu-annealed HTL is supported not only by the reduction in ΔE_F deficit, but also by the results of TRPL and ODF. **Figure 5.23 (a)** shows the TRPL characteristic, which shows that the normalized PL counts decay more slowly in the HTL passivated samples than in the reference sample, indicating a longer effective lifetime. Since the $Cu(In,Ga)Se_2$ and CdS were prepared using the same process, the bulk lifetime and front surface lifetime should be essentially the same within an error due to inhomogeneity. Therefore, the longer effective lifetime of the HTL passivated samples suggests a longer back surface lifetime with less non-radiative recombination at the backside. By fitting the PL counts decay with a 2-exponential decay function and considering the weighted lifetime according to **Equation 2.33**, the estimated weighted effective lifetime of the HTL passivated samples is around 115 ns. The PL counts decays among samples passivated by HTL with different thicknesses of In_2O_3 are very similar, indicating that the difference in weighted effective lifetime is less than 5 ns. Therefore, the 15 meV difference in ΔE_F deficit between these samples cannot be attributed to backside passivation, but rather to doping density. However, beyond attributing the difference in doping densities to inhomogeneity, it is unclear why samples prepared under identical conditions would have distinct doping densities. In contrast, the reference sample exhibits a much faster PL counts decay and a much shorter weighted effective lifetime of 8 ns, which is around 15 times lower than that of the HTL passivated samples. Assuming a uniform distribution of free carriers (flat Fermi levels across the depth of the film), this difference in weighted effective lifetime leads to a higher ΔE_F of around 70 meV according to the relation of $k_b T \times \ln(\tau_1/\tau_2)$ (**Equation 2.34**), where τ_1 and τ_2 are the weighted effective lifetimes of the HTL passivated and reference samples, respectively. 70 meV improvement in ΔE_F estimated from weighted effective lifetime is similar to measured results from the absolute PL, which confirms the good passivation effect of Cu-annealed HTL.

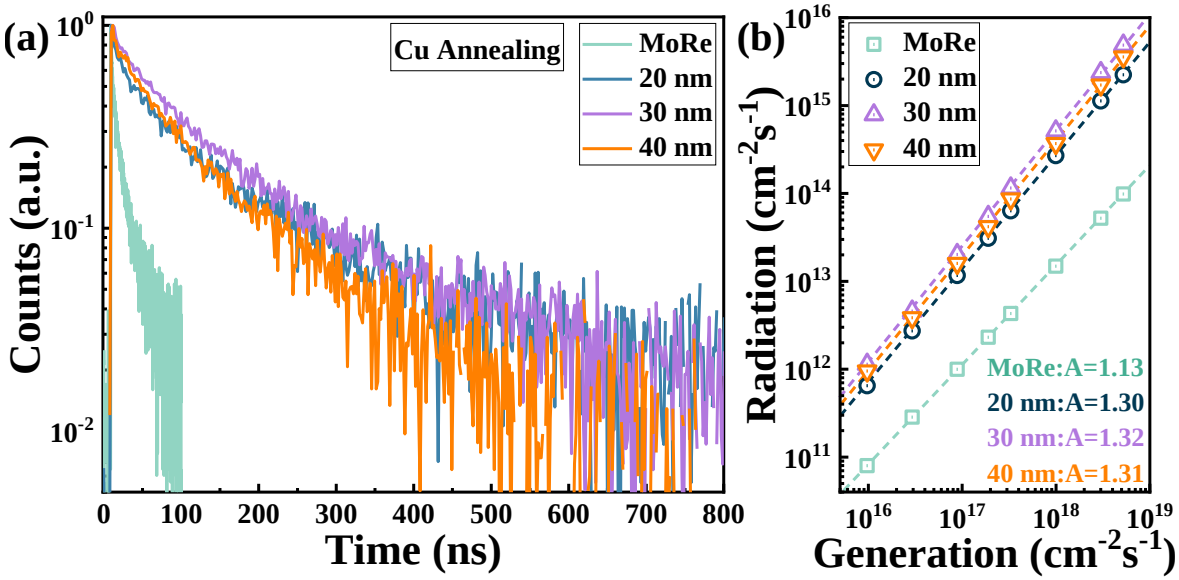

Figure 5.23 (a) TRPL decay curves of the reference sample and samples with Cu-annealed HTL ($CuGaSe_2/In_2O_3$). The TRPL curves show the decay of PL counts as a function of time, indicating the carrier lifetime. The reference sample is not passivated by Cu-annealed HTL, while the other three samples are passivated by Cu-annealed HTL with different thicknesses of In_2O_3 (20 nm, 30 nm, and 40 nm) on top of a 100 nm $CuGaSe_2$ layer. The slower decay of PL counts in the HTL-passivated samples suggests a longer carrier lifetime due to reduced non-radiative recombination at the backside of the absorber; (b) PL intensity or radiation as a function of illumination intensity for the reference sample and samples with Cu-annealed HTL. The PL intensity or radiation is the integrated PL flux over photon energy. The higher ODF of the HTL-passivated samples indicates a reduction in backside recombination.

The passivation effect of Cu-annealed HTL is further supported by the ODF values. The reference sample exhibits the lowest ODF of 1.13, which is attributed to the high backside recombination. Adding HTL reduces backside recombination and shifts the dominant non-radiative recombination from the backside to the bulk, resulting in a higher ODF of around 1.31. It is important to note that the low ODF may also be a consequence of the high doping density. However, the doping density of these samples are rather low, which can not be the reason for the low ODF. Based on the PL characteristics and **Equation 2.46**, the estimated doping density is around $1\sim2\times10^{15}$ cm^{-3}, which is relatively low compared to the optimal doping density of our solar cell that is $\sim1.8\times10^{16}$ cm^{-3}. Furthermore, due to the low doping density, the backside passivated samples exhibit relatively

high ODF, thereby limiting the FF of solar cells. These observations emphasize the necessity of enhancing the doping density of solar cells by adding additional alkali PDT to achieve highly efficient solar cells.

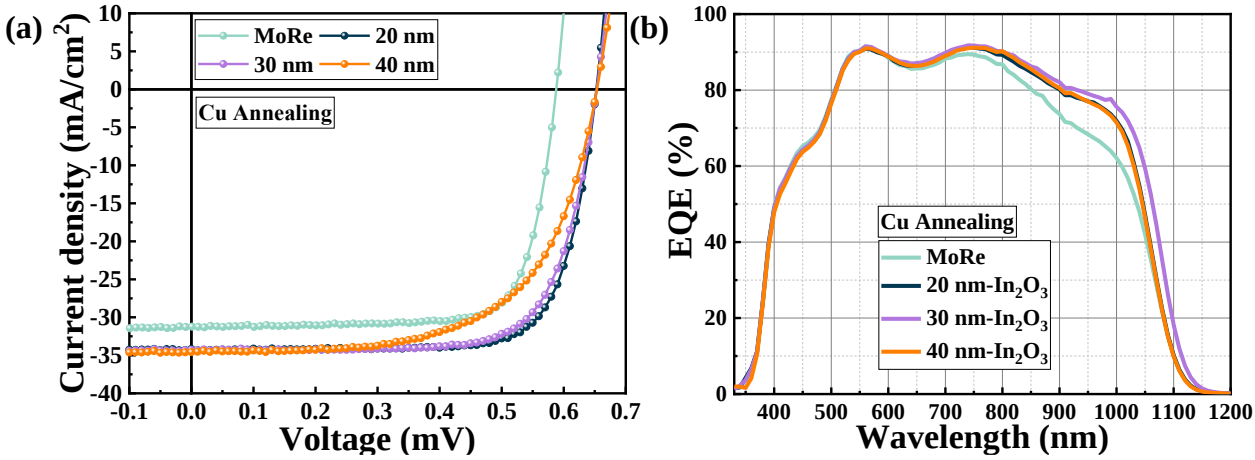

Figure 5.24 (a) Illumination *J-V* characteristics of the best reference solar cell and solar cell passivated by Cu-annealed HTL ($CuGaSe_2/In_2O_3$). The reference solar cell is without passivation of Cu-annealed HTL, and the other solar cells are passivated by the Cu-annealed HTL. The HTL is combination of 100 nm $CuGaSe_2$ covered by In_2O_3 with different thickness of 20 nm, 30 nm and 40 nm; (b) EQE characteristics of solar cells with and without HTL passivation. The backside passivation provided by the HTL improves the collection efficiency of long-wavelength photons generated carriers.

The passivation effect of Cu-annealed HTL is demonstrated to be effective without any reduction after annealing, which is crucial for solar cells to overcome the trade-off between V_{oc} and FF. **Figure 5.24 (a)** illustrates the illumination *J-V* characteristic of solar cells prepared by standard solar cell fabrication processes discussed in **Section 2.2.5**. It is evident that the V_{oc} of HTL passivated samples is approximately 65 mV higher than the reference sample, which is consistent with the improvement in ΔE_F. **Figure 5.26 (a)** summarizes the statistical results of V_{oc} improvement, confirming the significant 65 mV enhancement by passivation of Cu-annealed HTL. Additionally, the difference between $\Delta E_F/q$ and V_{oc} in **Figure 5.22 (b)** suggests that the front surface passivation is well-maintained with a V_{oc} loss of less than 10 mV.

Moreover, the HTL passivated solar cells exhibit a higher J_{sc} of around 1.5 mA/cm^2, as shown by the *J-V* curves in **Figure 5.24 (a)** and the statistical results in **Figure 5.26 (c)**. The improvement

in J_{sc} is attributed to the effective backside passivation, which enhances the collection of long wavelength photons generated free carriers. The EQE results in **Figure 5.24 (b)** provide evidence for the improved response to long wavelength photons ranging from 750 nm to 1050 nm for HTL passivated samples. Although the sample with 30 nm In_2O_3 shows a slightly lower bandgap, which slightly shifts the EQE absorption edge to a longer wavelength, all HTL passivated samples with different thicknesses of In_2O_3 display similar EQE responses. This observation indicates that either these solar cells have similar backside recombination or the difference in backside recombination is insufficient to have a discernible effect on EQE.

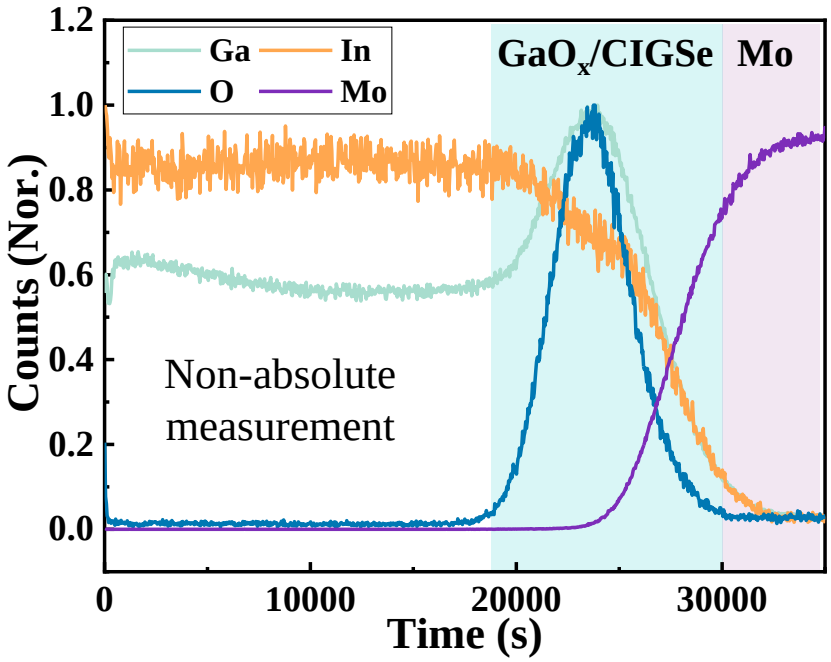

Figure 5.25 SMIS measurement: the normalized counts of Ga, In, Mo and oxygen (O) distribution with respect to sputtering time. This is non-absolute measurement, which means the normalized counts ratio does not represent the accurate compensation. The samples with Cu annealed HTL ($CuGaSe_2/In_2O_3$) show a very flat Ga and In towards the back contact, meaning the observed backside passivation effect is due to HTL rather than Ga gradient.

The good passivation effect of HTL compared to the reference sample has been conclusively verified. We attribute this favorable passivation to the HTL, although the potential influence of the Ga gradient formed during the absorber preparation through 3-stage processes may have been overlooked. Nevertheless, the reference sample exhibits unfavorable ΔE_F (**Figure 5.22**) and short lifetime (**Figure 5.23**), suggesting an unoptimized Ga gradient that possibly does not contribute

significantly to the backside passivation. To further substantiate this hypothesis, we conducted SIMS analysis on the sample with Cu-annealed HTL, and the results are depicted in **Figure 5.25**. The resolution limitations of SIMS made it challenging to distinguish between the oxide layer and $CuInSe_2$ layer at the backside. However, the oxygen-accumulated region displays higher Ga, indicating that Ga from the $CuGaSe_2$ layer is primarily confined within the oxide layer, consistent with TEM measurements (**Figure 5.13**). The most crucial finding from this SIMS measurement is the uniform Ga and In of the absorber, with only a slight elevation in Ga grading towards the frontside. This result suggests that there is no significant backside passivation contributed by Ga grading towards the backside. The observed backside passivation can be attributed to the introduced HTL.

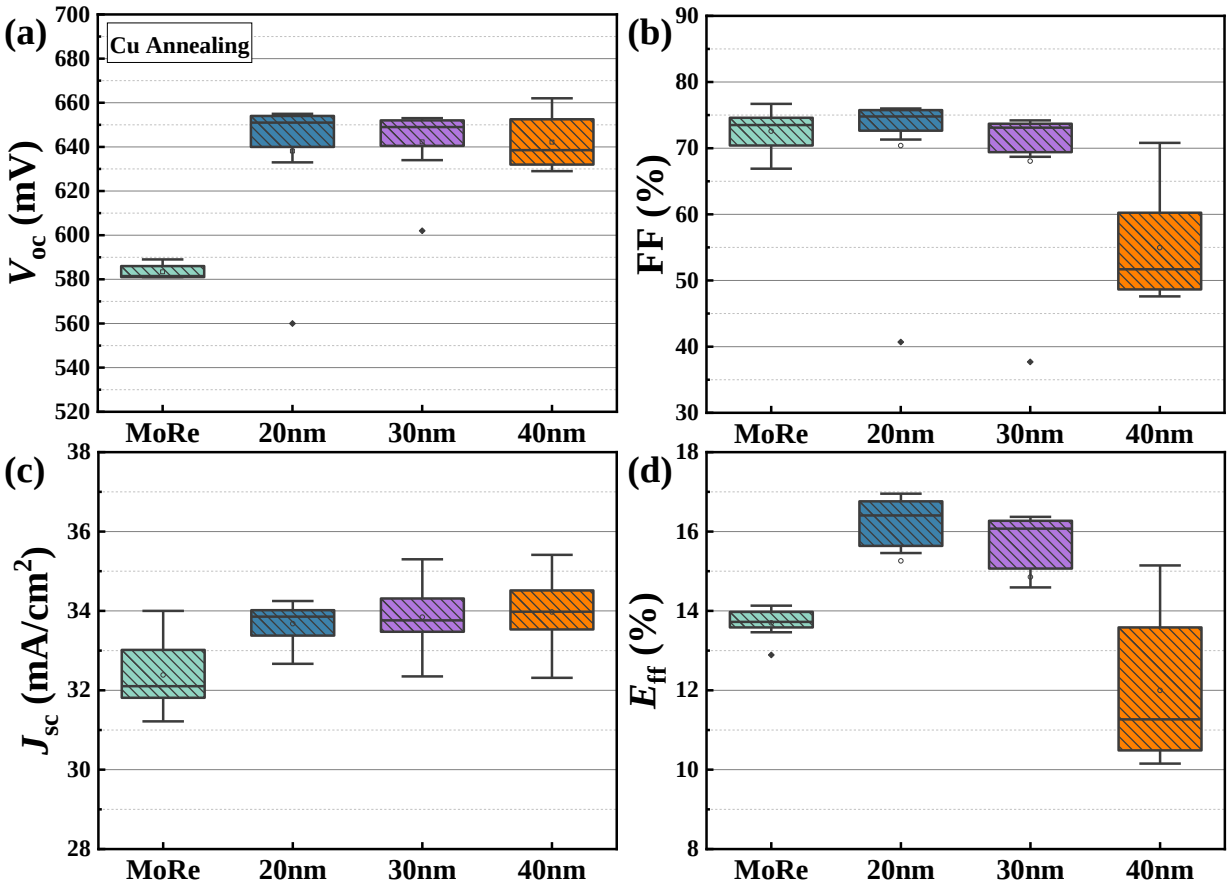

Figure 5.26 The figure presents a box plot with a clear depiction of the statistical distribution of the illumination *J-V* characteristics of the solar cells. The box represents the interquartile range (25^{th} to 75^{th} percentile), while the black line inside the box indicates the median value. The small circle denotes the mean value. The whisker extends up to 1.5 times the interquartile range (IQR)

and identifies the maximum and minimum values. The statistical parameters of the illumination *J-V* characteristics are as follows: (a) V_{oc} (b) FF, (c) J_{sc} and (d).

In addition to achieving high V_{oc} through sufficient passivation, good HTL must also provide sufficient hole transport to ensure high FF. In this study, the Cu-annealed HTL demonstrated good hole transport, leading to improved FF of the solar cells. As shown in **Figure 5.24 (a)**, the *J-V* curves of solar cells with Cu-annealed HTL exhibit better FF. Among the solar cells with HTL, the best FF of around 76% was achieved with 20 nm In_2O_3, which is similar to the reference solar cells and much higher than that of solar cells without Cu annealing (**Figure 5.21 (a)**). However, increasing the thickness of In_2O_3 leads to higher R_s, resulting in increased hole transport blocking and reduced FF. As shown in **Figure 5.26 (b)**, the FF reduction for solar cells with 30 nm In_2O_3 is only 1%~2%, leading to a slightly lower efficiency than the solar cells with 20 nm In_2O_3 (**Figure 5.26 (d)**). A more significant loss of FF (>20%) is observed for the solar cells with 40 nm In_2O_3, resulting in the lowest efficiency among the different series of solar cells. Optimization of the Cu annealing process is required to improve FF for solar cells with thicker In_2O_3. Nonetheless, our results demonstrate that Cu annealing efficiently improves hole transport without compromising backside passivation compared to HTL without Cu annealing. By implementing the Cu-annealed HTL with 20 nm In_2O_3, we achieved the highest efficiency of ~17%. We anticipate that further optimization of the Cu annealing process for solar cells with thicker In_2O_3 could result in even higher efficiency.

5.4 Summary

In this chapter, we investigate the passivation effects and hole transport properties of various HTLs for solar cells. We begin by exploring single layers such as NiO_x, $CuCrO_x$, and CuO_x, which are found to be thermally unstable due to their strong interaction with the absorber during absorber deposition at high substrate temperatures. This interaction disrupts the integrity of these layers, leading to a loss of their passivation effects. Furthermore, the diffusion of impurities like Ni and Cr from these layers into the absorbers negatively impacts the quality of the absorbers, resulting in extremely poor solar cell performance. Another monolayer, GaO_x, shows a higher level of thermal stability with minor diffusion. However, it provides only weak passivation effects, which

increases the ΔE_F of the absorber by less than 15 meV. This level of passivation is insufficient to achieve high efficiency solar cells. Moreover, GaO_x exhibits low hole transport property, leading to a decrease in FF when compared to reference samples without GaO_x. Additionally, our studies on MoO_x suggest that thin MoO_x layers with thicknesses less than 6 nm provide weak passivation effects, resulting in an improvement in ΔE_F of less than 10 meV. Thicker MoO_x layers with thicknesses larger than 10 nm, on the other hand, cause a decrease in ΔE_F of around 20 meV. However, in both cases, there is no clear indication that MoO_x can function effectively as an HTL. This lack of improvement in ΔE_F could be attributed to the absence of Na, as oxides are known to block Na diffusion from the soda-lime glass to the absorbers. However, NaF PDT for samples with GaO_x and MoO_x did not significantly improve their ΔE_F, indicating that Na blocking is not the primary issue.

It has been found so far that single layers investigated in this thesis do not function properly as HTLs due to either their thermal instability or their insufficient passivation effect. To overcome these shortages, a dual-layer structure of HTL covered by thermal stable oxides, such as GaO_x and In_2O_3, has been proposed. The goal is to use thermal stable oxides as stabilizers to stabilize the single layers that have the potential to work as a good HTL. Initially, the combinations of CuO_x/GaO_x and $CuGaSe_2/GaO_x$ were investigated. However, the presented results imply a significant diffusion of the underlying layer (CuO_x or $CuGaSe_2$), indicating that GaO_x prepared by SCS is ineffective in blocking the diffusion of the underlying layers. And these layers do not improve the ΔE_F of absorbers, indicating that the passivation effects of these layers are too low to achieve high-efficiency solar cells. The successful HTL structure was developed by combining 100 nm $CuGaSe_2$ with 50 nm In_2O_3. However, after the absorber deposition, the element exchange between In and Ga was observed, which results in formation of $CuInSe_2/GaO_x$ from $CuGaSe_2/In_2O_3$. With $CuInSe_2/GaO_x$, it improvs the ΔE_F of $CuInSe_2$ by approximately 80 meV compared to the reference without backside passivation. Moreover, this combination showed good hole transport ability, which maintains a good FF of 71%. The passivation effect of HTL may attribute to the GaO_x introduced conduction band spike, which reduces the minority carrier density at backside, thus reducing the backside recombination. But the passivation effects may also reply on the morphology, composition (e.g. Ga/O ration, the amount of Cu doping) and crystallization of GaO_x, which could be the reason why SCS prepared GaO_x does not work properly. The good

hole transport may be related to Cu doing of GaO_x since it can improve the p-type conductivity of GaO_x and introduce defects levels close the valence band maximum of the absorber, which assists the transport of holes.

Beside $CuInSe_2$ solar cells, the introduction of a 100 nm $CuGaSe_2$/ 40 nm In_2O_3 structure reduces backside recombination in submicron $Cu(In,Ga)Se_2$ with a thickness of approximately 800 nm. This structure shows an improvement in ΔE_F of 80 meV compared to the reference without backside passivation, indicating its good passivation effects. However, this structure also experiences hole transport blocking, resulting in a reduction in J_{sc} and an extremely low FF of approximately 30%. Reducing the thickness of In_2O_3 helps to remove the hole transport barrier and maintain a high FF of solar cells. The highest FF of approximately 77% is achieved by reducing the thickness of In_2O_3 to 10 nm, but this improvement comes with a compromise of backside passivation, leading to an increase in V_{oc} deficit of around 30 mV. The degradation of backside passivation is likely due to the inability of the thinner In_2O_3 to efficiently block the diffusion of Ga and thus formation of a thinner GaO_x. These observations suggest an unwanted trade-off between FF and V_{oc}, which is unfavorable to making high-efficiency solar cells. Therefore, reducing the thickness of In_2O_3 is not an ultimate solution for achieving high efficiency solar cells. Additionally, the excess Cu in this structure is found to be crucial to obtaining good enough hole transport property. Introducing Cu annealing to this HTL is a promising approach to improving the hole transport property without degrading the backside passivation. This approach allows solar cells with 20 nm In_2O_3 to achieve an FF of approximately 76% and V_{oc} of approximately 656 meV (E_g^{PL}=1.13 eV). Increasing the thickness of In_2O_3 to 30 nm or 40 nm results in approximately 15 meV lower ΔE_F deficits but with a price of losing FF. The FF of solar cells with 30 nm In_2O_3 is slightly reduced by 1% to 2%, while the loss of FF of more than 20% occurs in solar cells with 40 nm In_2O_3. This reduction in FF indicates that optimizing the Cu annealing process is necessary for thicker In_2O_3. Finally, with Cu annealed HTL, the submicron $Cu(In,Ga)Se_2$ with a thickness of approximately 800 nm achieves an efficiency of approximately 17%.

Chapter 6 ODF: the influence of backside recombination and doping density

This chapter is based on the diode factor model, which considers the effects of metastable defects transition[90]. In **section 6.1**, we investigate the impact of backside recombination on the ODF. Through a combination of experimental measurements and simulation analysis, we demonstrate that significant backside recombination results in a decrease in the ODF. To understand the underlying mechanism behind this reduction, we employ SCAPS simulations, which provide valuable insights into the process. Furthermore, in **section 6.2**, we focus on the influence of doping density on the ODF. This examination explores how variations in doping density affect the ODF. To consolidate our findings, **section 6.3** presents a comprehensive summary that encompasses both the impacts of backside recombination and doping density on the ODF.

6.1 Influence of backside recombination on the ODF

In **Chapter 4**, we extensively discussed the issue of serious backside recombination in $CuInSe_2$ solar cells, primarily caused by poor semiconductor and metal (Mo) contact interfaces. However, we explored several strategies to mitigate this problem, such as incorporating Ga to induce a conduction band gradient, implementing metal oxide dielectric layers, or employing the hole transport layer (HTL) described in **Chapter 5**.

Regarding the dielectric layers, we found that the lowest backside recombination velocity was achieved by Al_2O_3, followed by bare soda-lime glass (SiO_2) and TiO_2. The S_b values shown in **Figure 6.1 (c)** were estimated through SCAPS simulations, as discussed in **Chapter 4 (Table 4.1)**. It is important to note that the samples investigated in this chapter are the same ones analyzed in **Chapter 4**. To determine the ODF, we employed the illumination intensity-dependent photoluminescence technique, which is thoroughly detailed in **Section 2.3.3**. Empirically, we observed that the radiation emitted from the sample exhibited a linear relationship with respect to generation over a logarithmic scale spanning two orders of magnitude. Based on **Equation 2.39**, the fitted ODF represents the average value within the studied generation range.

The experimental findings demonstrate that the Mo reference sample exhibits the lowest ODF of 1.10. However, after the introduction of dielectric layers, the ODF increases, accompanied by a decrease in backside recombination, as depicted in **Figure 6.1 (c)**. Among the various dielectric layers tested, Al_2O_3 proves to be the most effective in passivation, resulting in the highest ΔE_F of 513 meV, as discussed in **Section 4.3**. With the significant reduction in backside recombination achieved by Al_2O_3, the ODF increases from 1.10 to 1.28. The SCAPS simulation also shows a similar influence of backside recombination on the ODF. In the simulation, the setting doping density (N_A) is 8.8×10^{15} cm^{-3}, which closely aligns with the experimental results presented in **Table 4.1**. Other simulation parameters are listed and discussed in **Section 3.2 (Table 3.1 and Table 3.2)**.

The density of metastable defects considered in the simulation is 8×10^{15} cm^{-3}, which is comparable to the doping density. Only a sufficient transition of metastable defects can shift the Fermi level of the holes downwards, consequently increasing the ODF. The specific value of 8.8×10^{15} cm^{-3} is chosen because it yields ODF values consistent with our experimental results. However, the precise density of metastable defects in our samples remains uncertain. Nonetheless, the SCAPS simulation exhibits the same trend as observed in the experiments. As discussed in **Section 3.2**, the radiation flux can be determined in SCAPS by considering the radiation recombination current density (J_r) divided by the elementary charge (q). By adjusting the ND filter setting in SCAPS, the generation can be controlled. Consequently, the radiation-generation curves obtained from the SCAPS simulation can be plotted, as shown in **Figure 6.1 (b)**. Through linear fitting of these curves on a logarithmic scale, the average ODF from the SCAPS simulation is determined. Besides fitting the average ODF from the radiation-generation curves, the local ODF, as depicted in **Figure 6.2 (a)**, can be derived from the d lnR_r to d ln$G$ ratio ($A = d\ln R_r/d\ln G$) obtained from SCAPS simulation. This derivative reveal that the ODF is not a constant value across the studied generation range, which aligns with our expectation due to the generation-dependent metastable defects transition. Nevertheless, the change in the ODF is relatively moderate, as evidenced by the flat and broad peak, allowing for a reasonable linear fitting within a logarithmic scale, as shown in **Figure 6.1 (b)**.

Among different backside recombination velocities considered in simulations, the highest velocity of 10^6 cm/s results in the lowest ODF of 1.12. Although only the results for a backside recombination velocity of 10^6 cm/s are presented, similar ODF values are obtained for backside

recombination velocities of 10^5 or 10^7 cm/s. When the backside recombination velocity (S_b) is below 10^3 cm/s, the highest ODF of 1.26 is achieved. Further reduction in S_b does not significantly influence the ODF, suggesting that S_b below 10^3 cm/s has a negligible impact. The influence of S_b on the experimental and simulated ODF is compared and summarized in **Figure 6.1 (c)**. Both show a similar trend, confirming that high backside recombination leads to a lower ODF. Having a low diode factor is beneficial for achieving a higher fill factor (FF) [90, 91], which ultimately leads to improved efficiency. However, the low ODF resulting from backside recombination is unfavorable due to high non-radiative recombination occurring at the backside reduces the V_{oc}, which, in turn, reduces the FF. The influence of diode factor and V_{oc} on the FF of solar cells will be discussed in **Chapter 7**.

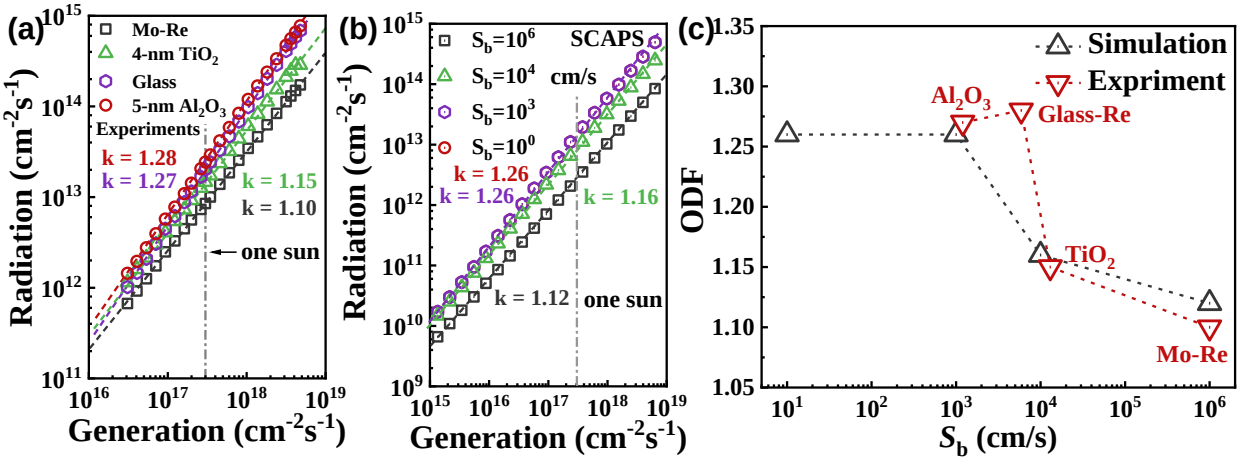

Figure 6.1 Logarithmic plot of radiation flux as a function of generation flux. The slope of the linear fitting provides the average ODF of the sample across the measured generation range. (a) Experimental results of the ODF for the Mo reference sample and dielectric layer passivated samples; (b) SCAPS simulation results of the ODF with different backside recombination velocities. The front surface recombination velocity is set to be 1.4×10^3 cm/s; (c) Comparison of simulated and experimental ODF values in relation to the backside recombination velocity. The backside recombination velocity of the dielectric layer passivated sample is estimated from the SCAPS simulation, as discussed in **Chapter 4**.

Based on the comprehensive analysis of experimental and simulated results, it becomes evident that high backside recombination leads to a decrease in the ODF. The simulation provides further insights into the underlying reasons for this reduction. **Figure 6.2 (a)** shows a simulated local ODF as a function of generation flux with backside recombination velocity changing from 10^6 cm/s to

10^0 cm/s. Local ODF is the first order derivative of logarithm of radiation flux over generation flux (d ln$R$/d ln$G$). In this simulation, the front surface recombination velocity is set to be 1.4×10^3 cm/s and doping density of 8.8×10^{15} cm^{-3}. Other parameters for the simulation can be found in **Table 3.1**. It is observed that increasing the backside recombination velocity results in a flatter change in the local ODF with respect to generation, thereby reducing the average ODF under low injection conditions. One plausible explanation suggests that the significant backside recombination lowers the ODF by diminishing the free electron density through non-radiative recombination via interface defects. Consequently, there is an insufficient number of electrons available to be captured by metastable donors, which is a crucial step for the transition from donors to acceptors. As a result, this reduces the value of "d ln$p$/d ln$G$" and, subsequently, the ODF, which is dependent on the additional change in hole concentration.

However, **Figure 6.2 (b)** presents an interesting observation. In this figure, it shows the change of electron density (n) and hole density (p) with respect to the generation flux at the middle of the absorber. It demonstrates that while serious backside recombination can shift the peak of "d ln$p$/d ln$G$" to higher injection levels, it does not lower the maximum value of "d ln$p$/d ln$G$". If we assume that the lifetime is independent of generation ("d ln τ_n/d ln$G$" can be ignored), **Equation 2.45** suggests that backside recombination should not decrease the ODF. In fact, it implies that similar ODF values could be achieved even with high backside recombination. As long as the generation is sufficiently high, the same maximum of "d ln$p$/d ln$G$" can be achieved. However, this result contradicts our experimental and simulation results regarding the lower ODF.

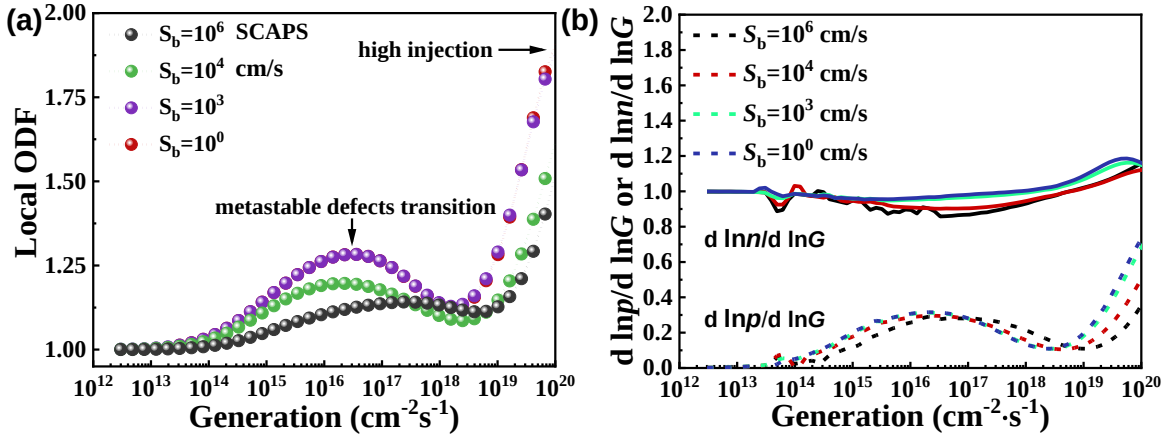

Figure 6.2 (a) Simulated results of the local ODF as a function of generation for various backside recombination velocities. Local ODF is the first order derivative of logarithm of

radiation flux over generation flux (d ln$R$/d ln$G$). In this simulation, the front surface recombination velocity is set to be 1.4×10^3 cm/s and doping density of 8.8×10^{15} cm^{-3}. High backside recombination results in a lower local ODF, leading to a lower average value under low injection conditions; (b) Solid lines are "d ln$n$/d ln$G$" and dashed lines are "d ln$p$/d ln$G$" with respect to generation flux with different backside recombination velocities.

As discussed earlier, it has been observed that high backside recombination does not significantly reduce the "d ln$p$/d ln$G$" (change in hole density with respect to generation flux), indicating that the absolute amount of metastable transition remains the same as long as the generation flux is sufficiently high. This observation is further supported by the electron occupation on donor states. The occupation of a metastable donor state by an electron signifies a transformation to an acceptor state and the release of a hole ([Metastable donor]$^+$ + e^- $\rightarrow$[Metastable acceptor]$^-$ + h^+).

Figure 6.3 (a) presents simulated results of the electron occupation on metastable defects, with the y-axis representing generation and the x-axis representing the position of the absorber layer within the film. The color scale indicates the level of electron occupation. In both cases of low and high backside recombination velocities, the backside region consistently exhibits lower electron occupation due to band bending caused by the higher work function of the back contact (**Figure 6.4 (a) (b)**). This band bending reduces electron density at the backside. When comparing the situation with low S_b (S_b=10^0 cm/s) to the high S_b situation (S_b=10^6 cm/s), it is observed that the high S_b situation shifts the same level of electron occupation to a higher generation flux by approximately one order of magnitude. However, this shift does not result in a flattening of the change(derivative) in occupation with respect to generation flux. For instance, at the middle of the film, **Figure 6.3 (b)** displays the change in electron occupation and its corresponding derivative with respect to generation flux. The solid and dashed lines represent electron occupation as a function of generation flux with S_b values of 10^0 cm/s and 10^6 cm/s, respectively. The lines with symbols represent the derivatives of occupation with respect to generation flux. With a high backside recombination velocity of 10^6 cm/s, the curve depicting the increase in electron occupation is shifted to higher generation flux compared to the situation with a low backside recombination velocity of 10^0 cm/s. This shift results in a shift of their derivative curves with respect to generation flux, but without lowering the maximum value. This is confirmed by the derivative curves with symbols in **Figure 6.3 (b)**. As mentioned previously, the occupation of

electrons on metastable defects corresponds to the transition from donors to acceptors, and thus the derivative of electron occupation with respect to generation flux dominates the "d ln*p*/d ln*G*" (change in acceptor concentration with respect to generation). Therefore, this shift observed in the derivative of electron occupation with respect to generation flux supports the shift in "d ln*p*/d ln*G*" as shown in **Figure 6.2 (b)**. It should be noted that although the derivative curve of high backside recombination is slightly lower than that of the low backside recombination case, this small change does not significantly reduce the ODF, especially considering that the studied ODF represents the average local ODF over a range of two orders of magnitude in generation flux.

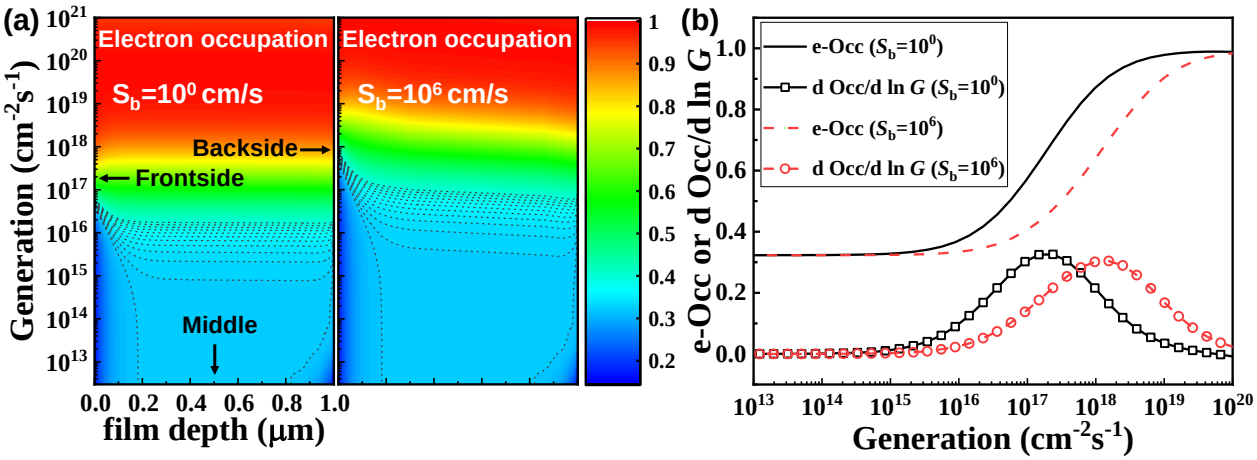

Figure 6.3 (a) The electron occupation on the metastable donor states increases with generation flux. The comparison between low S_b (left side, S_b=10^0 cm/s) and high S_b (right side, S_b=10^6 cm/s) shows that the high S_b shifts the occupation level to higher generation flux. The lower occupation at the backside is attributed to band bending caused by the fixed work function; (b) The electron occupation changes with generation at the middle of the film, as indicated in the figure. High back surface recombination causes a shift in the maximum of the derivative curve to the higher generation flux, but there is no significant reduction in the maximum value.

Therefore, there are additional factors contributing to the lower ODF in samples with significant backside recombination. So far, our discussion has been based on the assumption that the influence of effective lifetime in **Equation 2.44** is negligible. However, the dashed lines in **Figure 6.2 (b)** reveal that serious backside recombination leads to a sublinear increase in minority carrier density with generation, resulting in "d ln*n*/d ln*G*<1" and consequently lowering the ODF. This behavior

indicates that the effective lifetime of minority carriers is generation-dependent due to the pronounced back surface recombination.

Previous studies on silicon solar cells have shown that the effective lifetime can exhibit generation dependence, attributed to the asymmetry in electron and hole capture cross-sections at interfaces such as the Si-SiO_2 interface[188]. In our simulation, we have assumed equal electron and hole capture cross-sections (**Table 3.1**), thus ruling out the introduction of generation-dependent effective lifetime through this asymmetry. However, for Cu(In,Ga)Se_2 solar cells with the model discussed in this work, this dependence can be explained by changes in the transport of minority carriers towards the back contact, which become generation-dependent due to band bending influenced by metastable defects transitions

The band bending observed in the simulation is a result of the high work function of the contact, which increases the hole density and reduces the electron density at the backside of the Cu(In,Ga)Se_2. In SCAPS simulation, the "auto-flat bands" function was utilized to maintain a flat band structure at the two contacts. The work function of the contacts is calculated based on the presence of shallow uniform acceptor density, which represents a natural defect. However, the impact of charged metastable donors on the doping density is not taken into account. Consequently, the automatically calculated work function, determined by the shallow uniform acceptor density, results in a higher work function compared to the scenario where the doping density is reduced by the presence of metastable donors. This discrepancy leads to band bending in low injection conditions. However, as the generation flux increases, this band bending is alleviated due to the transition of metastable defects, which enhances the hole density. Further elaboration on this phenomenon will be provided in the subsequent discussion. In actual Cu(In,Ga)Se_2 solar cells, it is believed that the formation of $MoSe_2$ at the interface between Cu(In,Ga)Se_2 and Mo contributes to an ohmic contact with an upward bended band structure[189]. To investigate this issue, the sketch of the band diagrams are presented in **Figure 6.4 (a)** and **(b)**, illustrating the cases with and without metastable defects, respectively. In both cases, the backside recombination velocity is low, for example, 10^0 cm/s.

It is important to note that the terms "low generation" and "high generation" in **Figure 6.4 (a)** and **(b)** refer to relative values within the context of low injection conditions. Both cases correspond to low injection, but the high generation condition results in a higher population of free

carriers. In the case without metastable defects (**Figure 6.4 (b)**), compared to the low generation flux, the high generation flux shifts up the Fermi level of electrons while the Fermi level of holes remains unchanged. This is because, in low injection conditions, the density of excited holes is significantly lower than the doping density of the absorber. As a result, the band bending remains unchanged since the hole density remains nearly constant. In contrast, in the case with metastable defects (**Figure 6.4 (a)**), the high generation not only shifts up the Fermi level of electrons but also shifts down the Fermi level of holes due to metastable defects transitions that enhance the hole density. This increase in hole density leads to a reduction in band bending. With the same generation level, the Fermi level of electrons in both cases remains at the same level within the bulk. However, the less pronounced band bending of the conduction band at the backside reduces the distance between the conduction band minimum and the Fermi level of electrons, indicating an increase in electron density at the backside. Even with a higher backside recombination velocity, the downward bending of the Fermi level of electrons towards the back contact does not change the conclusion. This is because a similar metastable defects transition introduces analogous band bending relaxation, depending on the generation level.

Figure 6.4 (c) provides evidence for the increase in electron density at the backside. For instance, with $S_b = 10^0$ cm/s, the dashed blue line illustrates an extra increase in electron density with respect to generation in a logarithmic scale. Notably, at generation levels below 10^{16} $cm^{-2}s^{-1}$, the electron density in the case with metastable defects is lower than that in the case without metastable defects. This disparity arises because, at low generation levels, the metastable defects reside in donor states, resulting in a reduction in hole density. Consequently, the conduction band experiences a significant bending, leading to a lower electron density compared to the case without metastable defects. The extra increase in electron density, caused by metastable defects transition, corresponds to the variation observed in "d ln$n$/d ln$G$" with respect to generation, as depicted in **Figure 6.4 (d)**. Moreover, this variation aligns with the values calculated for the ODF using "d lnR_r/d ln$G$," implying that the change in electron density at the back interface dominates the ODF. Because the electron density is generation-dependent, the backside recombination that is proportional to it will be generation-dependent as well.

One might raise a concern regarding the ODF model discussed in this thesis, which pertains to the additional hole contribution from metastable defects transitions leading to a downward shift of the Fermi level of holes, resulting in ODF>1. However, at the backside interface, the ODF is

determined by the change in electron density, which appears inconsistent with the discussed model. This discrepancy can be attributed to two factors. Firstly, the hole density at this interface remains fixed due to the work function of the contact in low injection conditions, resulting in "d ln$p$/d ln$G$ = 0" (as shown by the black lines in **Figure 6.4 (d)**). Secondly, the extra increase in electron density at the backside interface is caused by metastable defects transitions, which increase the hole density in the bulk and reduce the band bending at the backside. Therefore, the model based on metastable defects transitions remains valid. Consequently, the ODF>1 arises from the effects of metastable defects transitions rather than band bending. This is evident from the case without metastable defects. Even with the similar band bending as shown in **Figure 6.4 (c)**, a linear increase in electron density is observed under low injection conditions. And this linear increase leads to a constant "d ln$n$/d ln$G$" value of 1 under low injection conditions, as depicted in **Figure 6.4 (d)**. Additionally, "d ln$n$/d ln$G$" and "d ln$p$/d ln$G$" may vary at different depths within the film. However, according to the definition of the ODF presented in **Equation 2.43**, the ODF is the sum of these two derivative terms. Due to carrier continuity, regardless of the position within the film, the sum of "d ln$n$/d ln$G$" and "d ln$p$/d ln$G$" must be constant, indicating the same ODF value.

With a high backside recombination velocity, such as 10^6 cm/s, the electron density is generally reduced due to increased backside recombination, as depicted in **Figure 6.4 (c)**. Additionally, the extra increase in electron density diminishes as a consequence of the high backside recombination, which is proportional to the backside recombination velocity and electron density. This implies that the high backside recombination velocity can suppress the extra increase in electron density until reaching a balance between higher recombination and the extra increase in electron density. As a result, the high backside recombination flattens the "d ln$n$/d ln$G$" curve, as shown in **Figure 6.4 (d)**. It is now evident that the backside recombination is generation-dependent due to metastable defects transition. More specifically, it exhibits an extra increase with an increase in generation. In terms of electrons within bulk, e.g. at the middle of the absorber, more electrons diffuse towards the backside compensating for the higher recombination. Consequently, it results in an extra reduction in electrons in the bulk (middle) as shown in **Figure 6.2 (b)**. And this diffusion or extra reduction of electrons is higher with a higher backside recombination velocity.

In terms of the ODF, as discussed earlier, it is the sum of "d ln$n$/d ln$G$" and "d ln$p$/d ln$G$". In the middle of the film, the hole density is not fixed and changes depending on the metastable defects transition. Furthermore, it has been established that backside recombination does not reduce

"d ln$p$/d ln$G$" in the middle of the film. As long as a sufficient number of electrons are excited, the same number of metastable defects can convert, resulting in "d ln$p$/d ln$G$" reaching nearly the same maximum value. However, due to the sublinear increase in "d ln$n$/d ln$G$" explained earlier, the ODF decreases due to higher backside recombination.

The conclusion of a low ODF resulting from generation-dependent backside recombination is drawn based on the findings from SCAPS simulation. It should be noted that there may be additional mechanisms in reality that contribute to lowering the ODF, which are presently beyond our current understanding. Nevertheless, we would like to emphasize that the presented model is capable of explaining our experimental and simulation results.

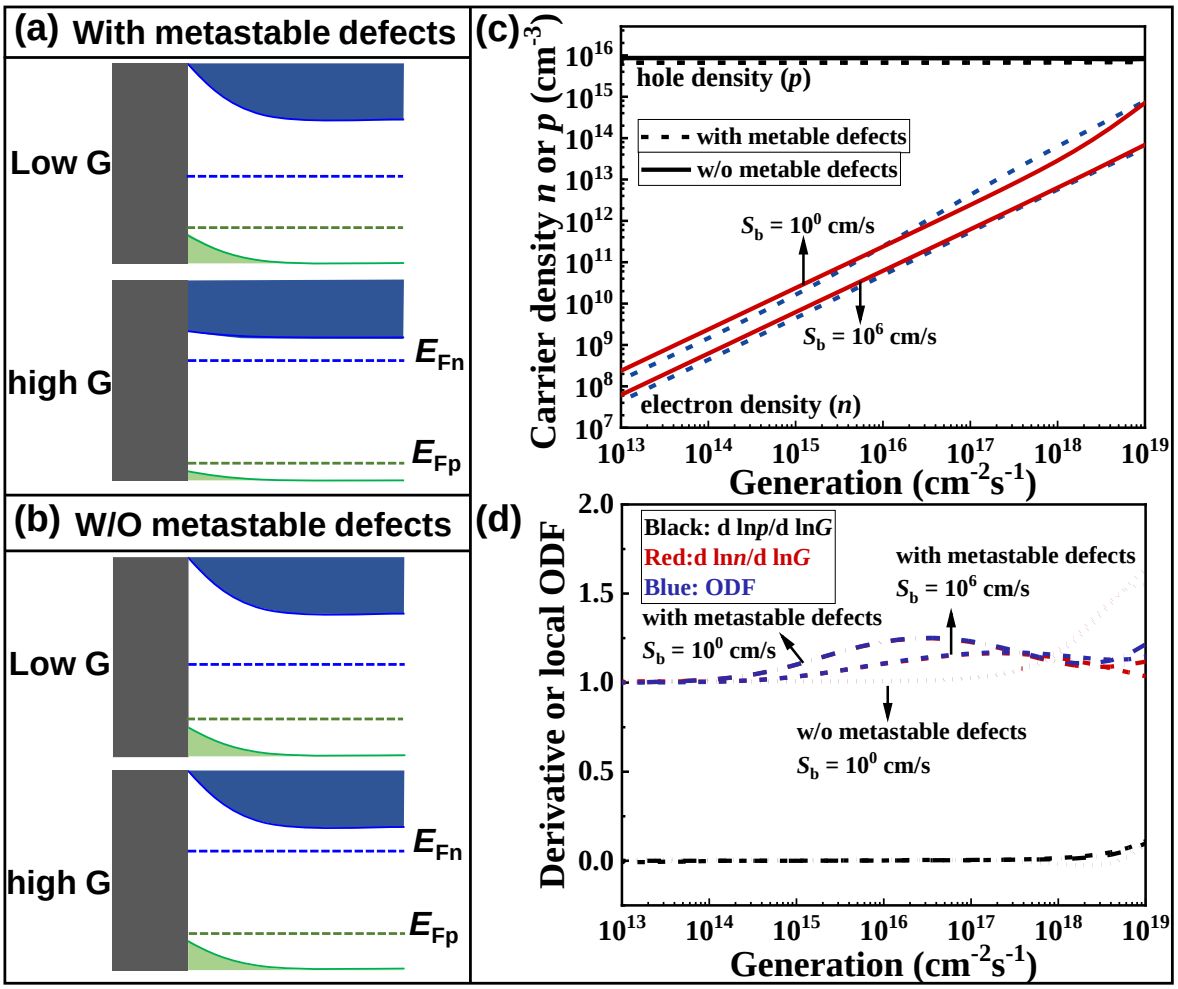

Figure 6.4 The band structure sketch illustrates a p-type absorber with a high work function contact. It should be noted that the low generation and high generation shown in (a) and (b) are relative values, both indicating a low injection condition. These results are specifically discussed

in the context of a low injection condition. Importantly, the same generation corresponds to the same electron density in the bulk. (a) In the presence of metastable defects, the band bending becomes generation-dependent. Higher generation levels result in reduced band bending due to metastable defects transition, which increases the doping density of the absorber; (b) Conversely, in the absence of metastable defects, the doping density remains generation-independent; (c) It presents the carrier density at the back interface as a function of generation. In the low injection condition, the hole density at the backside is fixed by the work function of the metal, rendering it generation-independent. Without metastable defects, the electron density exhibits a linear increase in a logarithmic scale. However, in the presence of metastable defects, the electron density increases first super-linearly and then sub-linearly in a logarithmic scale. Notably, serious backside recombination hampers the increase in electron density; (d) It displays the derivatives "d ln$n$/d ln$G$" and "d ln$p$/dln$G$," as well as the local ODF, which is calculated using "d lnR_r/d ln$G$." These quantities are plotted as functions of generation.

In summary, the ODF is reduced by the serious backside recombination, which is influenced by the generation-dependent backside recombination associated with metastable defects transition related band bending. It is essential to emphasize that this discussion relies on the model of metastable defects transition, which attributes generation-dependent backside recombination to such transitions. However, it is worth noting that other explanations or factors may also contribute to this phenomenon. For instance, a significant asymmetry in the capture cross-sections of electrons and holes could also play a role in generation-dependent recombination[190]. With the model of metastable defects transition, the simulation results indicate a significant decrease in the ODF when the backside recombination velocity (S_b) exceeds 10^3 cm/s, suggesting that the ODF may not be sensitive to S_b values below 10^3 cm/s. While achieving a low ODF is generally desirable, it becomes problematic when it arises from backside recombination. This situation can lead to substantial V_{oc} deficits and a loss of solar cell efficiency. Therefore, it is crucial not only to attain a low ODF but also to identify the specific recombination mechanism responsible for driving the low ODF. In the next section, we will further explore the impact of doping density on the ODF and propose a specific approach to discern the dominant recombination process governing the ODF.

6.2 Influence of doping density on the ODF

In this section, we explore the influence of the doping density of the absorber on the ODF, in addition to the backside recombination discussed in the previous section. Previous studies in **Chapter 4** (**Table 4.1**) have shown that the samples with GBG passivation exhibit similar backside recombination velocities compared to the samples with dielectric layer passivation. According to the findings presented in **Section 6.1**, a low backside recombination velocity corresponds to a higher ODF. However, **Figure 6.5 (a)** reveals that the GBG samples have slightly higher ODFs compared to the reference sample without Ga grading, contrary to what was expected based solely on their lower backside recombination.

Therefore, it can be inferred that factors other than backside recombination also play a role in influencing the ODF. As discussed earlier, the ODF>1 in low injection is explained by the additional shift downwards of the Fermi level of holes due to metastable defects transition. The magnitude of this shift determines the value of the ODF, with a larger shift resulting in a higher ODF. Since the samples were consistently prepared under the same Se over flux (pressure), it suggests that the samples have a similar density of V_{Se}, which is responsible for the metastability[23, 97]. Assuming that the density of metastable defects is relatively constant, the doping density of the sample should influence the shift of the Fermi level of holes. In the presence of the same amount of metastable defects transition, a higher doping density makes it more difficult to shift the Fermi level of holes downwards, resulting in a lower ODF. Conversely, a lower doping density leads to a higher ODF.

To address this, the doping density of the samples was calculated using **Equation 2.46**, and the results are summarized in **Chapter 4 (Table 4.1)**. It is observed that the GBG samples have a doping density of approximately 1.8×10^{16} cm^{-3}, which is higher than that of the dielectric layer passivated samples (8.0×10^{15} cm^{-3}). This experimental result confirms our earlier discussion that a higher doping density reduces the ODF. In addition to the experimental results, SCAPS simulations provide further evidence supporting the decrease in ODF with an increase in doping density. This is illustrated in **Figure 6.5 (b)**, where the results of the SCAPS simulation show a similar trend. In the simulation, the backside recombination velocity is set to 10^3 cm/s, which has a negligible influence on the ODF as discussed in **Section 6.1**. Starting with the lowest setting of

doping density at 8.8×10^{15} cm^{-3}, the simulation yields the highest ODF of 1.26. This value is close to that of the Al_2O_3 passivated sample, which has a similar doping density and backside recombination velocity. As the setting doping density increases, the ODF consistently decreases, reaching 1.03 when the doping density is raised to 3.0×10^{16} cm^{-3}. Notably, when the setting doping density is close to that of the GBG samples (1.4×10^{16} cm^{-3}), the ODF obtained from the SCAPS simulation aligns well with the experimental result of 1.1. **Figure 6.5 (c)** summarizes the correlation between the ODF and doping density for both simulations and experiments, demonstrating good agreement between the two. Thus, the results from both simulations and experiments consistently indicate that a higher doping density leads to a lower ODF.

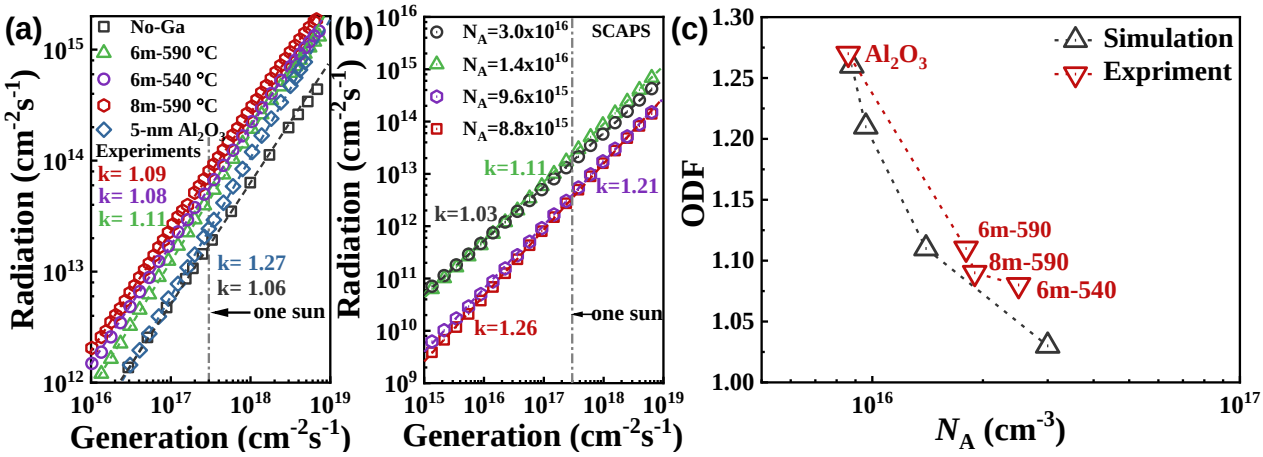

Figure 6.5 Logarithmic plot of radiation as a function of generation: (a) Experimental results demonstrate that GBG samples exhibit low ODFs despite their low backside recombination. The lower ODF compared to the dielectric layer passivated sample, such as Al_2O_3, can be attributed to the higher doping density; (b) SCAPS simulation results align with the experimental findings, confirming that a higher doping density corresponds to a lower ODF; (c) Summary of simulated and experimental ODFs with backside passivation, illustrating the correlation between ODF and doping density. Both simulations and experiments consistently show a decreasing trend in ODF with an increase in doping density.

In addition to the GBG samples, the HTL passivated samples exhibit similar trends. As discussed in **Section 5.2.3**, the implementation of a $CuGaSe_2/In_2O_3$ HTL effectively reduces the backside recombination in $CuInSe_2$ solar cells. However, the doping density of the absorber is compromised by organic residues in the SCS-synthesized In_2O_3 layer and the insufficient presence of Na caused by the blocking effect of the oxide layer. To improve the absorber's doping density, the annealing

temperature of In_2O_3 is increased, and additional NaF precursors is introduced. **Figure 6.6** shows the ODF results for different samples. The Mo reference sample, characterized by significant backside recombination, exhibits the lowest ODF. This low ODF is primarily influenced by non-radiative recombination occurring at the backside, which is unwanted as the high backside recombination leads to high V_{oc} deficits. Upon insertion of the HTL layer, the ODF significantly increases from 1.16 to 1.42, indicating a shift in the dominating recombination from the backside to the bulk of the absorber. With a higher doping density of the absorber, the ODF further decreases to 1.32, providing further evidence that both serious backside recombination and doping density contribute to a lower ODF. Despite these observations, it is important to note that the HTL passivated samples still exhibit higher ODF values compared to GBG or dielectric layer passivated samples, which is likely attributed to their lower doping density. The higher ODF values in these samples lead to lower fill factors (FF). The impact of ODF on FF will be further discussed in **Chapter 7**.

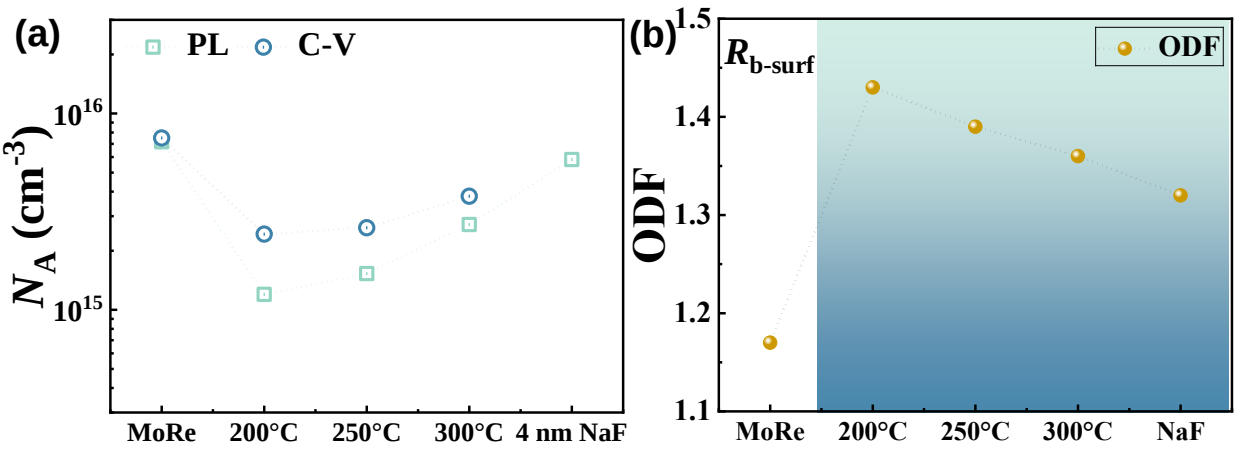

Figure 6.6 (a) The doping density of different samples determined through *C-V* and PL measurements. $CuGaSe_2/In_2O_3$ passivated samples exhibit lower doping density attributed to the presence of organic residues in the In_2O_3 layer and the Na blocking effect caused by the oxide layer. Increasing the annealing temperature of In_2O_3 can mitigate the impact of organic residues and enhance the doping density. Additionally, the addition of NaF precursor aids in supplementing Na that is a p-type dopant; (b) The ODFs of various samples and their correlation with doping density. The Mo reference sample exhibits the lowest ODF due to severe backside recombination. As the doping density increases, the ODF decreases.

Based on the experimental and simulation findings, it has been observed that higher doping density leads to a lower ODF. In cases where the backside recombination velocity is relatively low, around 10^3 cm/s, the impact of backside recombination on the ODF can be disregarded. In such cases, the lifetime is independent of generation, and the ODF is solely determined by "d ln$p$/d ln$G$." Considering that the density of metastable defects is assumed to be the same (set value in simulations), a higher initial doping density hinders the downward shift of the Fermi level of holes. This reduced shift results in a smaller "d ln$p$/d ln$G$," leading to a lower ODF. **Figure 6.7** provides evidence supporting this explanation. In **Figure 6.7 (a)**, the solid lines represent the change in hole density as simulated by SCAPS concerning generation. With a higher initial doping density, a higher generation is required to generate a sufficient number of additional holes that can significantly impact the hole density. This shift in the peak of "d ln$p$(N_A)/d ln$G$" to higher generation is due to the increased hole reservoir. Moreover, the maximum achievable "d ln$p$(N_A)/d ln$G$" is reduced. Consequently, the local ODF shown in **Figure 6.7 (a)** is shifted to a higher generation and flattened due to the higher doping density. Additionally, **Figure 6.7 (a)** displays the hole density of two backside passivated samples as a function of generation with spherical markers, the hole density is determined by **Equation 2.46**. The hole density shows an additional increase with generation, confirming the experimental occurrence of metastable defects transition. When compared to simulation results, the experimental results exhibit a similar trend. The sample with higher doping density (8m-590, 1.9×10^{16} cm^{-3}) displays a flatter increase in hole density compared to the less doped sample (5nm-Al_2O_3, 8.6×10^{15} cm^{-3}), indicating a reduction in "d ln$p$/d ln$G$" and consequently resulting in a lower ODF. It is worth mentioning that, even with a similar initial doping density (e.g., 8.8×10^{15} cm^{-3} in simulation compared to 8.6×10^{15} cm^{-3} in the experiment), the hole density in simulation shown in **Figure 6.7 (a)** is lower. This disparity is attributed to the presence of metastable defects in the donor configuration in SCAPS simulation, which reduces the hole density.

As previously discussed, both serious backside recombination and higher doping density can contribute to a low ODF. It is crucial to determine which recombination mechanism is responsible for the low ODF. While low ODF caused by backside recombination is undesirable due to its negative impact on V_{oc}, low ODF resulting from higher doping density is preferred as it can improve V_{oc}. Besides, the behavior of the Radiation-Generation curves provides valuable insights for identifying the origin of the low ODF. In the case where backside recombination dominates

the low ODF, the Radiation-Generation curves exhibit divergent behavior. **Figure 6.1 (b)** demonstrates that as backside recombination velocity (S_b) increases, the differences among radiation fluxes are small under very low injection conditions, but these differences progressively increase with higher generation. This phenomenon arises because backside recombination for samples with high S_b is generation-dependent, leading to sub-linear increase in radiation flux.

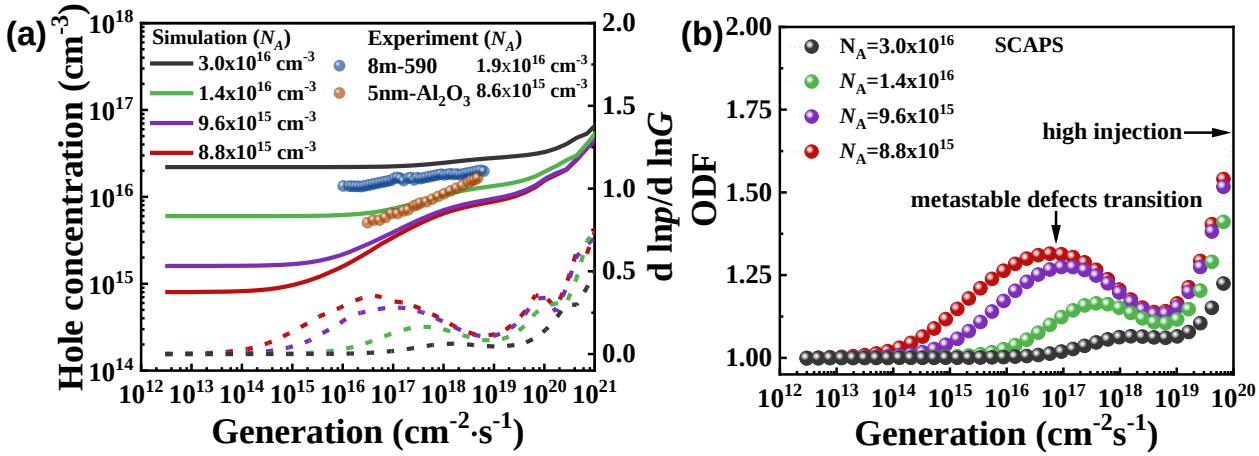

Figure 6.7 (a) The plot shows the variation of hole density and "d ln*p*/d ln*G*" as a function of generation. The solid lines represent SCAPS simulated hole density for different doping densities, while the spheres depict experimental results obtained using **Equation 2.46**. The lifetime, measured through time-resolved photoluminescence (TRPL), is assumed to be independent of generation. The dashed lines correspond to SCAPS simulated "d ln*p*/d ln*G*" values for different doping densities; (b) The plot illustrates the influence of doping density on the local ODF with respect to generation, as simulated by SCAPS.

On the other hand, when the low ODF is attributed to higher doping density, the Radiation-Generation curves exhibit a convergent behavior, opposite to the backside recombination-dominated case. As depicted in **Figure 6.5 (b)**, the convergence implies that the differences among the curves are significant at very low generation, but these differences gradually diminish as generation increases. At extremely low generation, where most metastable defects reside in donor states, the variation in doping density among samples is substantial, resulting in notable discrepancies in radiation flux. However, as generation increases, the holes originating from metastable defects transition mitigate the differences in doping density, leading to reduced discrepancies in radiation flux.

In conclusion, both the ODF itself and the behavior of the Radiation-Generation curves provide valuable indications of the dominant recombination mechanism. This section highlights that higher doping density can contribute to a lower ODF by flattening the additional increase in hole density caused by metastable defects transition. Unlike the low ODF resulting from serious backside recombination, the lower ODF due to higher doping density is favorable as the high doping density improves V_{oc}. While achieving a lower ODF is desirable for enhancing FF, it remains crucial to determine the dominant recombination mechanism at play.

6.3 Summary

In this chapter, we extensively discuss the influence of backside recombination and doping density on the optical diode factor (ODF), utilizing a model based on metastable defects transition. Even under low injection conditions, the presence of illumination intensity-dependent metastable defects transition from donors to acceptors leads to an ODF greater than 1. The additional holes resulting from the metastable defects transition further shift down the quasi-Fermi level of holes, contributing to an extra increase in ODF (ΔODF). The ODF serves as a reliable indicator for identifying the dominant efficiency loss mechanism in solar cells, as it varies depending on the prevailing recombination mechanism.

Both serious backside recombination and high doping density can contribute to a low ODF. Backside recombination diminishes the ODF due to generation dependent backside recombination, which results in generation dependent lifetime. The resulting low ODF associated with serious backside recombination is undesirable due to high backside recombination results in substantial V_{oc} loss. On the other hand, high doping density facilitates a lower ODF by enlarging the hole reservoir, thereby reducing the impact of extra holes resulting from metastable defects transition. The lower ODF achieved through increased doping density is favorable, as higher doping density improves V_{oc}. While a low ODF is generally preferred to ensure a high fill factor (FF), it is crucial to avoid low ODF caused by non-radiative recombination.

Besides, the behavior of radiation-generation curves provides valuable insights into the dominant recombination mechanism at play. In the case where the low ODF arises from serious backside

recombination, the radiation-generation curves of different samples exhibit divergent behavior. Conversely, when the low ODF is attributed to high doping density, the radiation-generation curves demonstrate convergent behavior. These distinctive behaviors of the Radiation-Generation curves serve as indicative signals of the underlying dominant recombination mechanism.

Chapter 7 Efficiency loss analysis

This chapter mainly focuses on discussing efficiency loss of submicron $Cu(In,Ga)Se_2$ solar cell with the HTL structure as discussed in **Section 5.3.3**. The best solar cell currently we made has a efficiency around 17%, which is far below the record efficiency of 23.35% of $Cu(In,Ga)Se_2$ [1]. To improve the efficiency of our solar cells, it is important to figure out where do we loss the efficiency. These analyses of efficiency loss are based on the existing results that are either from us or from the literatures. We are not going to discuss how to go beyond the current record efficiency but rather practically discussing how to get close to record efficiency with an aim of achieving efficiency beyond 20%.

Section 7.1 gives an overview of efficiency loss of our best solar cell compared to the SQ limit. From this comparison, it shows the weakness of solar cell, and thus figuring out a path to improve efficiency of solar cells. **Section 7.2** will concentrate on discussing the V_{oc} loss based on radiative and non-radiative loss[68, 84, 191, 192]. Meanwhile, some practical methods are mentioned to further improve V_{oc} according to the literature results, which allows us predicting an improvement in V_{oc} around 100 mV attributing to longer effective lifetime and higher doping density. **Section 7.3** will discuss improving of FF based on the diode factor and V_{oc}. **Section 7.4** shows the potential improvement in J_{sc} by optimizing the reflection, e.g. implementing anti-reflection coating (ACR), reducing parasitic absorption from the CdS and using backside reflector (BR).

7.1 The overview of efficiency losses

To address the issue about efficiency loss and figure out the weakness of the solar cells, it is necessary to compare the efficiency of real solar cells to their SQ limit. The comparison shows it clear how much losses the solar cells have for each parameter, e.g. V_{oc}, FF and J_{sc}, which determines the efficiency of solar cells. **Figure 7.1** shows the comparing results between our current best solar cell and its SQ limit. The values of SQ limit are based on the calculation by considering the radiative emission from front side due to a prefect backside reflector[83]. The bandgap of the absorber involved in this calculation is 1.15 eV that is the corresponding energy of the inflection point of the derivative of EQE over energy of photons [dEQE(E)/dE]. The absorption

edge of EQE, normalized PL and dEQE(E)/dE are shown in **Figure 7.2**. The band gap form the PL is slightly lower (30 meV) than the bandgap from the inflection point of dEQE(E)/dE (**Figure *7.2* (b)**), which is due to radiative losses and will be discussed in details in **Section 7.2**. The previous study proposed to use the weighted average bandgap to represent the bandgap of the absorber[68], particularly in case with an obvious radiative loss. This weight average bandgap is considered based on the probability function of the bandgap distribution, which gives a statistical bandgap. In case of Cu(In,Ga)Se_2, the difference between weighted average bandgap and bandgap form the inflection of dEQE(E)/dE is very tiny about 1 meV[68], which is tiny enough to allow us directly using the bandgap from the inflection point of dEQE(E)/dE.

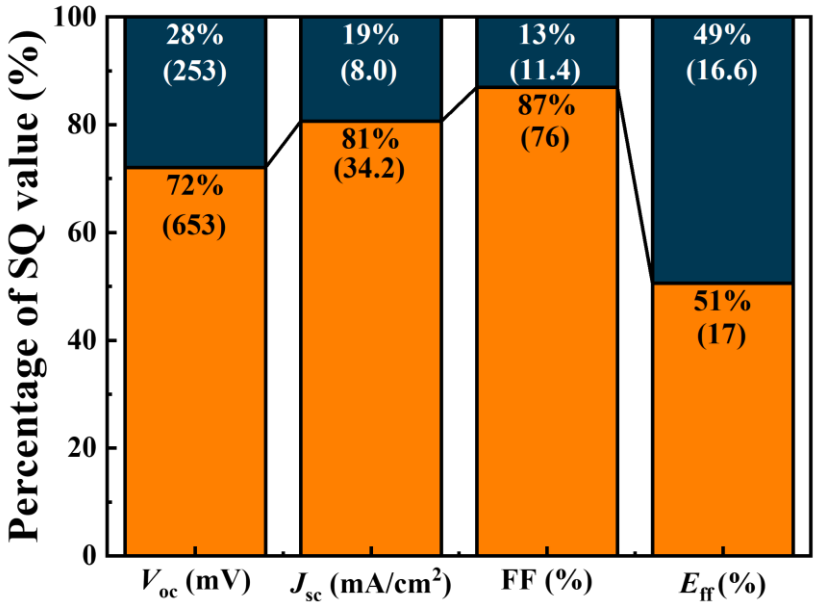

Figure 7.1 The overview of efficiency loss compared to the SQ limit. The SQ values are based on the calculation of considering radiative emission only from the front side due to a prefect backside reflector[*83*].The bandgap involved in this analysis is 1.15 eV, which is the corresponding energy of the inflection point of dEQE(E)/dE. The orange parts are the values from our best solar cell and the blue parts are the losses compared to the SQ values.

As shown in **Figure 7.1**, our measured best V_{oc} (653 mV) is only 72% of the SQ value (906 mV), which contributes to the most severe loss in efficiency. Then followed by J_{sc} (34.2 mA/cm^2) that is 81% and FF (76%) that is 87%. In **Section 7.3**, we will show that the FF can be further improved

by reducing the diode factor and improving V_{oc}. Despite the further improvement can be made, 87% of FF compared to the SQ value is indeed a rather good value when compared to the record solar cell (93% of SQ value[FF=80.4%])[1]. Assuming the further optimization will not improve our FF, to achieve our goal of having efficiency more than 20%, the V_{oc} and J_{sc} must be equivalently improved to more than 83% of its SQ value (V_{oc} = 752 mV and J_{sc} = 35 mA/cm^2). This means we must gain another 100 mV and 0.8 mA/cm^2 in V_{oc} and J_{sc}, respectively. The severe loss in V_{oc} indicates a high non-radiative recombination that our solar cells are still facing. We believe this non-radiative recombination loss can be overcame by introducing alkalis PDT, e.g. NaF, KF and RbF PDT, which will improve effective lifetime and doping density of the Cu(In,Ga)Se_2 solar cells[63, 185, 186, 193, 194]. The details about V_{oc} loss and its further optimization will be discussed in **Section 7.2**. In terms of J_{sc}, SCAPS simulation is used to predict how much J_{sc} can be gain by using ARC and reducing parasitic absorption of CdS. These results will be discussed in **Section 7.4**.

7.2 V_{oc} loss analysis

The V_{oc} loss analysis is based on the previous work[68], in which the V_{oc} loss is considered by detailed-balance analysis. The V_{oc} of a solar cell can be regarded as the radiative recombination limited V_{oc} of a real solar cell subtracts the non-radiative loss:

$$V_{\mathrm{oc}} = \frac{\mathrm{k_b}T}{\mathrm{q}}\ln\left(\frac{J_{\mathrm{SC}}^{\mathrm{REL}}}{J_0^{\mathrm{REL}}}\right) = \frac{\mathrm{k_b}T}{\mathrm{q}}\ln\left(\frac{J_{\mathrm{SC}}^{\mathrm{REL}}}{J_{0,\mathrm{rad}}^{\mathrm{REL}}} \times \frac{J_{0,\mathrm{rad}}^{\mathrm{REL}}}{J_0^{\mathrm{REL}}}\right) = \frac{\mathrm{k_b}T}{\mathrm{q}}\ln\left(\frac{J_{\mathrm{SC}}^{\mathrm{SQ}}}{J_0^{\mathrm{SQ}}} \times \frac{J_{\mathrm{SC}}^{\mathrm{REL}}}{J_{\mathrm{SC}}^{\mathrm{SQ}}} \times \frac{J_0^{\mathrm{SQ}}}{J_{0,\mathrm{rad}}^{\mathrm{REL}}} \times \frac{J_{0,\mathrm{rad}}^{\mathrm{REL}}}{J_0^{\mathrm{REL}}}\right) \quad \textbf{7.1}$$
$$= V_{\mathrm{oc}}^{\mathrm{SQ}} - \Delta V_{\mathrm{oc}}^{\mathrm{SC}} - \Delta V_{\mathrm{oc}}^{\mathrm{rad}} - \Delta V_{\mathrm{oc}}^{\mathrm{nrad}}$$

The $J_{\mathrm{SC}}^{\mathrm{REL}}$, J_0^{REL} and $J_{0,\mathrm{rad}}^{\mathrm{REL}}$ are the short-circuit current density, recombination current density and radiative recombination current density form a real solar cell, respectively. The recombination term (J_0^{REL}) contains radiative recombination and non-radiative recombination. $J_{\mathrm{SC}}^{\mathrm{SQ}}$ and J_0^{SQ} is short-circuit current density and recombination current density of SQ values, respectively. The J_0^{SQ} only contains the radiative recombination with a step-like absorption function, which is the assumption of SQ model. $V_{\mathrm{oc}}^{\mathrm{SQ}}$ is the V_{oc} of SQ limit. $\Delta V_{\mathrm{oc}}^{\mathrm{SC}}$ is the V_{oc} loss due to difference in real

short-circuit current density and SQ-approach value. $\Delta V_{\mathrm{oc}}^{\mathrm{rad}}$ is the radiative loss of V_{oc}, which results from the absorptivity ($a(E)$) of a real solar cell deviating from the step function like absorptivity of SQ model. The further $a(E)$ of a real solar cell deviates from a step function like absorptivity, meaning the less steep absorption and more sub-bandgap absorption. Consequently, the solar cell will have higher radiative loss of V_{oc}. $\Delta V_{\mathrm{oc}}^{\mathrm{nrad}}$ is the non-radiative recombination which includes SRH and Auger recombination. In case of Cu(In,Ga)Se_2 solar cell, the SRH recombination dominates the non-radiative loss.

A solar cell is a diode which can work only when there is recombination taking place. In a SQ model, the only and minimal recombination is radiative recombination that is determined by the black body radiation. Thus, the J_0^{SQ} of an ideal solar cell in SQ model is given by:

$$J_0^{\mathrm{SQ}} = \mathrm{q}\int_{E_{\mathrm{g}}}^{\infty} \emptyset_{\mathrm{bb}}(E)\mathrm{d}E \qquad \textbf{7.2}$$

Where $\emptyset_{\mathrm{bb}}(E)$ is the black body radiation. In a well performed solar cell, the external quantum efficiency (EQE(E)) approximately equals to the absorptivity, meaning EQE(E)≈$a(E)$. This is valid with an assumption that the solar cell does not have a serious transport loss of carriers. Meanwhile, for the backside passivated samples, the backside recombination is small enough to allow us to ignore the influence of recombination loss due to backside recombination[191, 192]. With this approximation, the $J_{0,\mathrm{rad}}^{\mathrm{REL}}$ from the sample is given by:

$$J_{0,\mathrm{rad}}^{\mathrm{REL}} = \mathrm{q}\int_{0}^{\infty} a(E)\emptyset_{\mathrm{bb}}(E)\mathrm{d}E \approx \mathrm{q}\int_{0}^{\infty} \mathrm{EQE}(E)\emptyset_{\mathrm{bb}}(E)\mathrm{d}E \qquad \textbf{7.3}$$

Thus, the radiative loss of V_{oc} is determined by the ratio between Equation **7.2** and **7.3**:

$$\Delta V_{\mathrm{oc}}^{\mathrm{rad}} = \frac{\mathrm{k_b}T}{\mathrm{q}}\ln\left(\frac{\int_0^{\infty} a(E)\emptyset_{\mathrm{bb}}(E)\mathrm{d}E}{\int_{E_{\mathrm{g}}}^{\infty} \emptyset_{\mathrm{bb}}(E)\mathrm{d}E}\right) \approx \frac{\mathrm{k_b}T}{\mathrm{q}}\ln\left(\frac{\int_0^{\infty} \mathrm{EQE}(E)\emptyset_{\mathrm{bb}}(E)\mathrm{d}E}{\int_{E_{\mathrm{g}}}^{\infty} \emptyset_{\mathrm{bb}}(E)\mathrm{d}E}\right) \qquad \textbf{7.4}$$

Equation 7.4 shows clear that the radiative loss of V_{oc} is due to $a(E)$ of a real solar cell is not a step like function. To minimize the radiative loss of V_{oc}, it requires a steep absorption edge that is close to step like function as much as possible. For Cu(In,Ga)Se_2 solar cells, the non-ideal $a(E)$ is about sub-bandgap absorption and non-absorption of long wavelength photons. The sub-bandgap absorption is mainly contributed by the bandgap fluctuation[195] due to inhomogeneities in

composition, stress distribution and stoichiometry, and electrostatic fluctuation due to charged defects[129, 196]. Meanwhile, for a gradient Cu(In,Ga)Se_2, the narrow notch position with the lowest bandgap has insufficient thickness to absorb all of low energy photons, contributing to the nonideal absorptivity. In case of submicron Cu(In,Ga)Se_2, the limited thickness also contributes to the nonideal absorptivity. Regarding non-radiative loss of V_{oc}, it can be determined from PLQY, **Equation 2.28**.

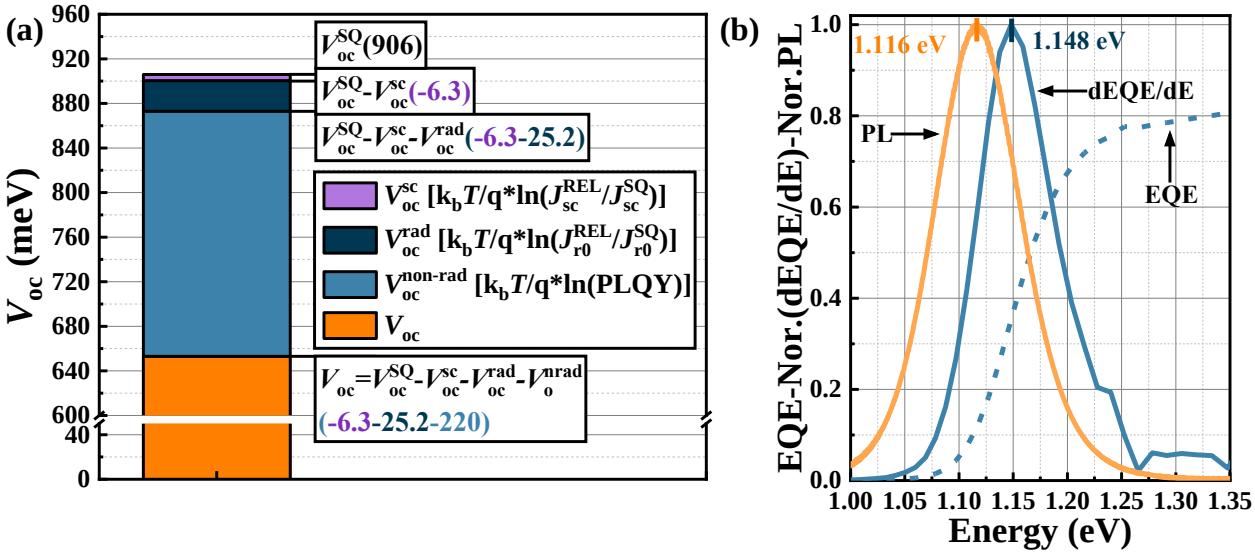

Figure 7.2 (a) V_{oc} loss analysis based on the **Equation 7.1** for the best submicron Cu(In,Ga)Se_2 solar cell we prepared so far; (b) The red shift of PL bandgap compared to the inflection point of EQE(E), which is related to the radiative loss of solar cell.

With this V_{oc} loss analysis model discussed above, the specific V_{oc} loss of our solar cells can be calculated and shown in **Figure 7.2 (a)**. The V_{oc} loss due to the difference in short-circuit current density is as small as 6.3 mV. In this calculation, the J_{sc} from the solar cell is calculated from the integration of the product of sun spectrum (ϕ_{sun}) and EQE(E) spectrum over the energy of photons:

$$J_{sc} = q\int_0^{\infty} \emptyset_{sun}(E)\mathrm{EQE}(E)\mathrm{d}E \qquad \textbf{7.5}$$

The J_{sc} of SQ-approach is based on the bandgap of 1.15 eV that is the corresponding energy of the inflection point of dEQE(E)/dE. There is a very tiny V_{oc} of ~2 mV can be potentially improved by increasing the J_{sc} from 33.2 to 36.8 mA/cm^2 as discussed in **Section 7.4**.

Compared to the tiny loss in V_{oc} due to J_{sc}, we have much higher V_{oc} loss due to non-radiative and radiative recombination. Regarding radiative loss of V_{oc}, **Equation 7.4** is implemented for calculation. The results in **Figure 7.2 (a)** shows a loss in V_{oc} of 25.2 mV. This is a moderate radiative loss of V_{oc} because a value around 20-50 mV was observed for Cu(In,Ga)Se_2 solar cells[68, 197]. And this radiative loss of V_{oc} is consistent with the red shift of PL bandgap compared to EQE bandgap, which is 32 meV. The radiative loss theoretically can be reduced by growing a homogeneous thick absorber that is close to stoichiometry. The homogeneous absorber reduces the Ga profile introduced band fluctuation, and it improves the absorption of long-wavelength photons. And stoichiometry sample reduces the tail states because of Cu deficits[155, 198]. In addition, the higher growth temperature and alkalis (Na and Rb) PDT can also reduce the tail states[199]. However, considering this practical case, the radiative loss may not be reduced significantly, because we are working on submicron absorber which is not thick enough to absorber longwave-length photons. Thus, the contribution of reducing radiative loss to improvement of V_{oc} is not included in **Figure 7.3**. But we want to emphasize that it does not mean eliminating the radiative loss is not important. It can be a very important improvement in V_{oc} when we consider a homogeneous thick absorber or a thin absorber with a good backside reflector (BR).

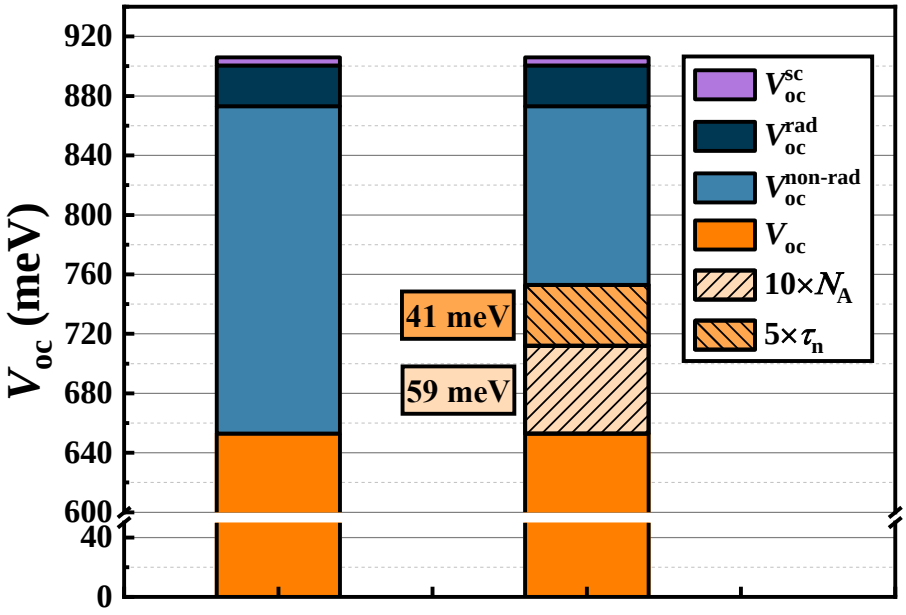

Figure 7.3 The potential improvement of V_{oc} by improving effective lifetime and doping density of our solar cell to state-of-art values.

In term of non-radiative recombination, it is the main V_{oc} loss channel, which leads to a V_{oc} loss of around 220 mV. This loss is attributed to the fact that our solar cells do not have sufficient long effective lifetime and high doping density. Since compared to the Mo reference samples, introducing HTL at the backside improves V_{oc} by 80 mV and effective lifetime from 8 ns to 115 ns, it indicates that the backside is well passivated. Therefore, we believe that the dominant non-radiative channel shifts from the backside to the bulk and front surface. To improve quality our absorber and front surface, it is necessary to introduce proper alkalis PDT, e.g. NaF, KF and RbF PDT, which has been shown to improve effective lifetime and doping density of the $Cu(In,Ga)Se_2$ solar cells[63, 186, 193, 198, 200]. By considering the state-of-art values of effective lifetime and doping density, we can estimate the potential improvement in V_{oc} for our solar cells. The best effective lifetime in our case is around 115 ns that is roughly 5 times shorter than the reported effective lifetime of the state-of-art $Cu(In,Ga)Se_2$ which is around 500 ns[62, 63]. Meanwhile, the doping density of our solar cells is around 1×10^{15} cm^{-3}, compared to the state-of-art value of around 1×10^{16} cm^{-3}, the doping density of our solar cells is around 1 order of magnitude lower[62, 200]. Assuming Fermi-levels are flat and doping are homogeneous, the improvement in V_{oc} due to longer effective lifetime and higher doping density can be estimated by **Equation 2.34** and **Equation 2.47**. With this estimation, **Figure 7.3** shows that the V_{oc} can be improved by 41 mV with a 5 times longer effective lifetime and 59 mV with 1 order of magnitude higher doping density. The total V_{oc} can be potentially improved by 100 mV, leading to V_{oc} of 753 mV that is 83% of the SQ-approach value. The 83% of the SQ-approach value guarantees that it is possible to achieve an efficiency higher than 20% as we discussed in **Section 7.1**.

7.3 FF loss analysis

The FF loss analysis is based on considering the influence of V_{oc} and diode factor on FF according to the one diode equation with influence of R_{sh} and R_s, as shown by **Equation 2.6**. To do this simulation, the "2-3 diode Fit" tool developed by Suckow et.al[201] is used. This tool is based on a 2-diode model; however, the saturation current density of the second diode (J_{02}) is set as small as 10^{-16} mA/cm^2, which means the effect of the second diode is negligible, and thus it can be treated as a 1-diode model. The R_s, R_{sh} and J_{sc} used in simulation is fixed to 0.4 $\Omega\cdot cm^2$, 1000 $\Omega\cdot cm^2$ and

34.2 mA/cm^2 that are from our experimental results. The different V_{oc} with specific diode factor is manipulated by adapting J_{01}, then the corresponding FF is given.

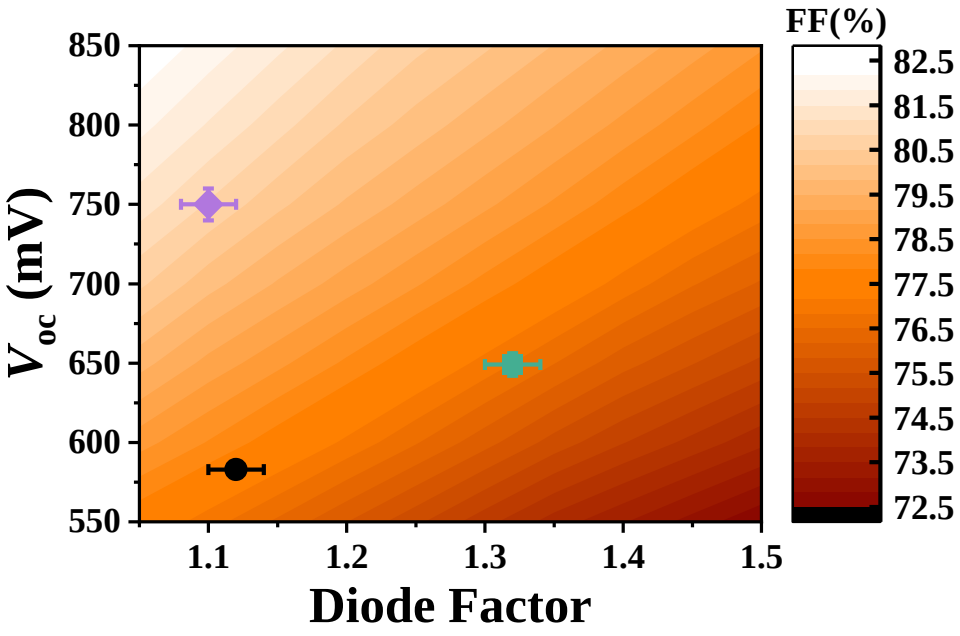

Figure 7.4 The color map is the dependence of FF on V_{oc} and diode factor. The green sphere is our best submicron Cu(In,Ga)Se_2 solar cells so far. The black sphere is the reference sample (on Mo without backside passivation) of the best submicron Cu(In,Ga)Se_2 solar cells. The purple sphere is the higher FF can be potentially achieved by lowering diode factor and improving V_{oc}.

Figure 7.4 is simulated influence of V_{oc} and diode factor on FF. The black sphere is the experimental result of Mo reference sample with V_{oc} of ~580 mV and diode factor of 1.12, and the green dot is the experimental result of HTL (20 nm In_2O_3 with Cu annealing) passivated sample with V_{oc} of ~650 mV and diode factor of 1.33 (**Section 5.3.3**). The diode factors of solar cells plotted in **Figure 7.4** are ODFs, in which we assume the recombination taking place in SCR is limited, which will not impact significantly on the EDF. Because of this, the ODF is believed to be close to EDF. The results show that the higher V_{oc} and lower diode factor lead to a higher FF. And the influence of V_{oc} and diode factor on FF can compensate each other, which means the same FF can be achieved either by low V_{oc} and diode factor or high V_{oc} and diode factor. When comparing the experimental results of V_{oc} and diode factor to the simulation, the simulation indicates the FF of Mo reference sample and HTL passivated sample is around 77.5% and 76.5%, respectively. These results agree well with the experimental FF of Mo reference sample and HTL

passivated sample, which are around 77% and 76% for the best sample. The FF of the Mo reference sample and HTL passivated sample is close because their V_{oc} and diode factor compensate with each other. To gain a higher FF, it is necessary to have high V_{oc} and low diode factor simultaneously. As we discussed in **Section 7.2**, by introducing alkalis PDT, it is very likely that another 100 mV of V_{oc} can be improved by having longer effective lifetime and higher doping density, resulting in a V_{oc} of 753 mV. Additionally, as we showed in **Section 6.2**, with doing density higher than 10^{16} cm^{-3}, it is possible to have a lower diode factor of around 1.1. By considering both contribution of the higher V_{oc} and the lower diode factor to FF, the purple sephere in **Figure 7.4** suggests a potential achievable FF of ~81%, which is ~93% of the SQ-approach limit.

7.4 J_{sc} loss analysis

To evaluate how much current density can be potentially improved for the submicron solar cell with a thickness 800-900 nm, we did EQE simulation by using SCAPS. The basic device structure for simulation is Cu(In,Ga)Se_2/CdS/i-ZnO/AZO. The general parameters for the simulation are summarized in **Table 3.3**. Particularly, a homogeneous Cu(In,Ga)Se_2 with a thickness of 900 nm and setting bandgap of 1.15 eV is used. It is notable that the absorption coefficients of AZO, i-ZnO and CdS are default values from the SCAPS database. The experimentally measured EQE has a bit higher response from 350 nm to 390 nm, this is likely due to our AZO/i-ZnO has a bit higher transmission for photons with energy close to its bandgap. Despite this small difference, the simulated parasitic absorption loss for high energy photons as shown in **Figure 7.5 (a)**, between black dashed line and light green solid line, from the wavelength of 350 nm to 550 nm agrees well with our experimental results.

To make the absorption edge of the simulation EQE match with our experimental results, the absorption coefficient of the absorber is given by a model which contains two terms[202]:

$$\alpha = \begin{cases} (\alpha_0 + \frac{\beta_0 E_g}{E})\sqrt{\frac{E - E_g}{E_g}}, E \geq E_g \\ \gamma_0 \exp(\frac{E - E_g}{E_0}), E < E_g \end{cases} \quad \textbf{7.6}$$

Where E is energy of photons and E_g is setting bandgap. α_0 and β_0 are model parameters that can tune α. γ_0 is proportionality constant that is chosen to make α is smooth and continuous at point where $E=E_g$. E_0 is the tail decay energy. The first term of **Equation 7.6** describes the approximation of absorption coefficient with photon energy higher than E_g, which is proportional to $(E-E_g)^{1/2}$. The second exponential term is a tail states correlated term which determines how much sub-bandgap absorption will be involved. By setting proper values of these parameters as shown in **Table 3.3**, we make the simulation EQE absorption edge matches well with the experimental result.

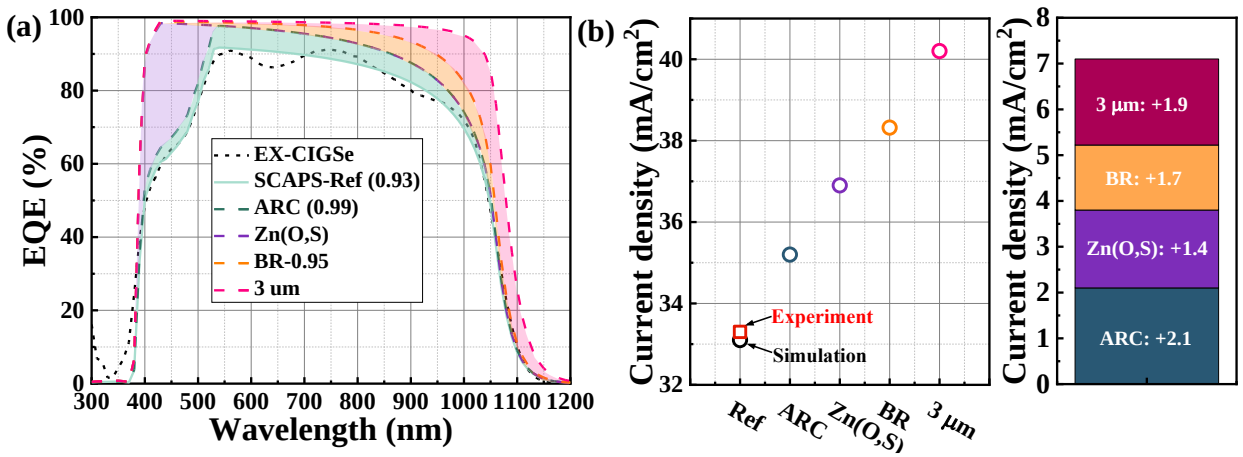

Figure 7.5 (a) Experimental and simulated EQE spectra: black dashed line is form one of our best submicron Cu(In,Ga)Se_2 solar cells; The light green solid line is the simulated EQE which gives the integrated current density closed to experimental result. The dark green dashes line is optimized by reducing front surface reflection, increasing front surface transmittance from 93% to 99%. The purple dashed line is optimized by eliminating the parasitic absorption of CdS, replacing CdS by Zn(O,S). The orange dashed line is optimized by increasing the backside reflection from 60% to 95%. The pink dashed line is the case with using 3 μm absorber; (b) The simulated results of current density that may be potentially improved by doing each optimization.

A front surface transmission of 0.93 (constant value, wavelength independent) is used in simulation to make simulated EQE roughly agrees with the experimental result from wavelength 550 nm to 1000 nm. Because the limited options for optical simulation, the simulated EQE can not reproduce the interference observed in real solar cells. But it will not change our general conclusion

about J_{sc} optimization, because the simulated J_{sc} is very close to the experimental result as shown in **Figure 7.5 (b)**.

First, to simulate how much refection loss can be potentially reduced by adding an anti-reflection coating (ARC), we increase the front surface transmission from 0.93 to 0.99. The light green area in **Figure 7.5 (a)** corresponds to the gain in EQE by reducing front surface reflection, which contributes to an increase in J_{sc} about 2.1 mA/cm^2 as shown in **Figure 7.5 (b)**.

Second, by replacing CdS buff by a higher bandgap buffer, e.g. Zn(O,S), it reduces the parasitic absorption loss due to CdS as shown in **Figure 7.5 (a)** with the purple area. The improvement in this arear leads to an increase in J_{sc} about 1.4 mA/cm^2 as summarized in **Figure 7.5 (b)**.

Third, because we are working with a thin Cu(In,Ga)Se_2 with thickness around 800-900 nm, this thickness is insufficient to absorb, especially, longwave-length photons. Using a good backside reflector (BR) can improve the equivalent absorption length, thus reducing the transmission loss. The Mo back contact used in experiments is not a good enough reflector which can only reflect 60% photons with wavelength between 300 nm-1100 nm[203]. But by using a better reflector like Cu or Ag, the reflectivity can be improved to more than 95% with wavelength between 500 nm to 1100 nm[203]. To estimate how much J_{sc} can be improved by using a good BR, the backside reflectivity is improved from 0.6 to 0.95, which results in a better collection of photons as shown in **Figure 7.5 (a)** with orange area. The correlated increase in J_{sc} is about 1.7 mA/cm^2 as shown in **Figure 7.5 (b)**.

In addition, we checked the effect of using a rather thick absorber with all optimizations discussed above. In this simulation, the thickness of absorber is set to 3 μm. The EQE in **Figure 7.5 (a)** shows an improvement in pink area, suggesting a better collection of long-wavelength photons. This better collection leads to an increase in J_{sc} of 1.9 mA/cm^2 as shown in **Figure 7.5 (b)**. It means, at least with the absorption coefficient modeled by **Equation 7.6**, the 900 nm absorber plus a backside reflector with reflectivity of 0.95 is still insufficient to absorber all the photons. But we could use light trapping structure as is usually applied in other solar cells to improve absorption.

In practice, adding ARC and using Zn(O,S) to replace CdS are more handleable for us, because we have correlated technologies and knowledges in storage. Considering the J_{sc} improvement based on using ARC and Zn(O,S), the J_{sc} of 36.7 mA/cm^2 (E_g^{EQE}1.15 eV) seems achievable. In

terms of BR[183, 204], it is more complicated because this structure requires developing $Cu(In,Ga)Se_2$ on transparent contact. But we will not exclude the possibility of implementing a better BR in the future with $Cu(In,Ga)Se_2$ on transparent contact. Some previous works have shown its possibility, the key issue is about taking time to optimize the fabricating processes[183, 204, 205].

7.5 Summary

This chapter starts with efficiency loss analysis by comparing our best solar cell to its SQ-approach limit. The weakest part of our solar cell is V_{oc} that is only 72% of the SQ value. Then followed by J_{sc} that is 81% of the SQ value. The FF is 87% of the SQ value, which is best among these three parameters. The high loss in V_{oc} indicates a dominant non-radiative recombination. The V_{oc} loss analyses according to the detailed balance model suggest that the V_{oc} loss due to lower J_{sc} compared to the SQ value is 6.3 mV, the V_{oc} loss due to radiative recombination is 25.2 mV and non-radiative loss is 220 mV. We predict that the optimized alkalis PDT will likely reduce the non-radiative loss by up to 100 mV, leading to a V_{oc} of 753 mV (E_g^{EQE}=1.15 eV). In terms of FF, from the results of one-diode model-based simulation, FF can be potentially improved by keeping high V_{oc} and low diode factor. With V_{oc} of 750 mV and diode factor of 1.1, it shows a higher FF of 81%. Additionally, the potentially improved in J_{sc} is estimated by applying EQE simulations. The presented results suggest that current density of 2.1 mA/cm^2 can be improved by adding an ARC and 1.4 mA/cm^2 can be improved by using Zn(O,S) to replace CdS. Considering implementation of both strategies, it leads a predictable J_{sc} of 36.7 mA/cm^2. Finally, with these predicted improvements in V_{oc}, FF and J_{sc}, the efficiency of 22.4% is predicted.

Summary and outlook

This thesis aims to investigate and address the issue of backside recombination in $Cu(In,Ga)Se_2$ solar cells. The focus is on understanding the extent of V_{oc} improvement achievable by reducing backside recombination through a combination of experimental and simulation approaches. By implementing classical backside passivation strategies such as Ga single gradient and dielectric layers, significant improvements of at least 40 meV ΔE_F are observed in $CuInSe_2$ solar cells due to reduced backside recombination. These findings are supported by simulation results, which also show similar enhancements. Furthermore, simulations predict that by improving the bulk lifetime of the absorber from 37 ns to 200 ns and reducing the backside recombination velocity from 10^6 cm/s to 10^2 cm/s, a remarkable ΔE_F improvement of approximately 80 meV can be achieved. These results underscore the significance of mitigating backside recombination for the attainment of high-efficiency solar cells.

Traditionally, backside recombination in high-efficiency $Cu(In,Ga)Se_2$ solar cells has been addressed by passivating the backside with a Ga gradient, which introduces a higher conduction band gradient towards the backside. This conduction band gradient facilitates the migration of minority carriers away from the back contact, thereby reducing backside recombination. However, this approach has limitations such as inhomogeneous distribution of Ga, leading to radiative and non-radiative losses that hinder further efficiency improvements. To overcome these limitations, the integration of a homogeneous absorber with a hole selective transport layer between Mo and the absorber is proposed. This structure enables simultaneous mitigation of backside recombination and efficient hole transport. Overall, this research highlights the importance of mitigating backside recombination for the development of high-efficiency $Cu(In,Ga)Se_2$ solar cells, and presents a novel approach involving a homogeneous absorber and a hole selective transport layer to address the limitations of previous methods

In the context of a hole selective transport structure, the primary challenge lies in developing a layer that can effectively mitigate backside recombination while facilitating efficient hole transport. One of the difficulties is finding a suitable layer that can withstand the harsh deposition conditions of the absorber, as these conditions often lead to the destruction of the hole selective transport layer through high-temperature-induced diffusion. In this study, we have successfully developed

a novel hole selective transport layer with good thermal stability, allowing it to withstand the challenging growth conditions of the absorber. This layer combines $CuGaSe_2$ and In_2O_3 and exhibits promising passivation effects and hole transport properties. Our findings reveal a significant elemental exchange between In and Ga during the absorber preparation, resulting in the conversion of $CuGaSe_2/In_2O_3$ to $CuInSe_2/GaO_x$. Additionally, the 50 nm oxide layer serves as an effective barrier, preventing Ga diffusion into the absorber layer. This is crucial for achieving a homogeneous absorber without a Ga gradient. The improved backside passivation significantly enhances the $\Delta E_F/q(V_{oc})$ of $CuInSe_2$ and submicron $Cu(In,Ga)Se_2$ solar cells, leading to an improvement of V_{oc} up to approximately 80 mV. However, the presence of a thick layer also introduces notable hole-blocking effects, resulting in a significantly reduced FF. Although reducing the thickness of In_2O_3 layer can improve hole transport, it compromises the passivation effect. This reduction in backside passivation is likely attributed to Ga diffusion into the absorber, as the thin oxide layer cannot entirely impede Ga diffusion. Furthermore, a thin In_2O_3 layer results in the formation of a thin GaO_x layer, which may not provide sufficient passivation. Therefore, the efficiency improvement of solar cells by reducing the thickness of In_2O_3 is constrained by the trade-off between backside passivation (V_{oc}) and hole transport (FF). The introduction of an additional Cu annealing for $CuGaSe_2/In_2O_3$ before absorber deposition shows that the hole transport properties of HTL depend largely on the Cu doping within the GaO_x layer. This Cu-assisted annealing process effectively enhances hole transport while maintaining passivation. Through the incorporation of the Cu annealing process, we have achieved a submicron $Cu(In,Ga)Se_2$ solar cell with an efficiency of approximately 17% (E_g^{EQE}=1.15 eV, V_{oc} = 656 mV, FF = 76%, and J_{sc} = 34.1 mA/cm^2).

Furthermore, our investigation also encompasses the analysis of the impact of backside recombination and doping density on the ODF. The ODF discussed in this thesis is based on the metastable defect transitions, such as the transition from donors to acceptors, which contribute to a high ODF. However, it is preferable to achieve a low ODF as it leads to a high FF. Both experimental and simulated results consistently demonstrate that high backside recombination and high doping density result in a low ODF. The decrease in ODF caused by backside recombination leads to a loss in V_{oc}, which should be mitigated. Conversely, the reduction in ODF due to high doping density can enhance V_{oc}, offering a direction for future optimization to achieve higher efficiency with improved FF and V_{oc}.

Within the scope of this work, we have substantiated a crucial concept that demonstrates the viability of a hole selective transport structure for $Cu(In,Ga)Se_2$ solar cells. This structure exhibits a comparable passivation effect and hole transport property to the conventional Ga gradient approach. This finding represents a significant milestone of this research, providing a conclusive answer to the question of whether a hole selective transport layer can effectively replace the Ga gradient in $Cu(In,Ga)Se_2$ solar cells. This breakthrough opens the door to a new structural paradigm for $Cu(In,Ga)Se_2$ solar cells, but it also raises further important questions that warrant exploration. While the successful implementation of the hole selective transport structure represents a major advancement, there are still open questions and avenues for future investigation. Continued research is necessary to explore and optimize the novel structure further, including understanding the passivation mechanism of this HTL. This work serves as a foundation, stimulating further inquiry and paving the way for continued advancements in the field of $Cu(In,Ga)Se_2$ solar cells.

As discussed in **Section 5.2.3**, the hole transport property is likely influenced by Cu doping. We have proposed several hypotheses, such as the ability of Cu to enhance p-type conductivity and introduce defect states near the valence band maximum, thereby improving hole transport. However, direct evidence is still required to confirm changes in conductivity and the formation of Cu-related deep defects. Investigating the properties of the hole selective transport layer through specific experiments would be intriguing. For instance, growing thick oxide layers and incorporating different Cu annealing processes could be explored. Measuring photoluminescence to evaluate defects and performing current-voltage measurements to assess conductivity could provide valuable insights.

The integration of a hole selective transport structure alleviates the need for extensive optimization of the Ga gradient, thus simplifying the fabrication process of the absorber. If given the opportunity to continue this research, my focus would be on transferring the fabrication of solar cells onto transparent conductive oxide contacts using the HTL developed in this study. This HTL offers the advantage of enabling reducing the thickness of absorber, which has potential applications in semitransparent solar cells, bifacial solar cells, and thin solar cells with photon recycling. The utilization of the HTL may not only simplify the fabrication process but also opens up new possibilities for advanced solar cell designs and applications.

List of publications

1. **Taowen Wang**, Florian Ehre, Thomas Paul Weiss, Boris Veith-Wolf, Valeriya Titova, Nathalie Valle, Michele Melchiorre, Omar Ramírez, Jan Schmidt, and Susanne Siebentritt. (2022). Diode Factor in Solar Cells with Metastable Defects and Back Contact Recombination. Advanced Energy Materials, 2202076.

2. Susanne Siebentritt, Uwe Rau, Sevan Gharabeiki, Thomas P. Weiss a, Aubin Prot, **Taowen Wang**, Damilola Adeleye, Marwan Drahem and Ajay Singh. (2022). Photoluminescence assessment of materials for solar cell absorbers. Faraday Discussions, 239, 112-129.

3. Thomas Paul Weiss, Florian Ehre, Valentina Serrano-Escalante, **Taowen Wang**, and Susanne Siebentritt. (2021). Understanding performance limitations of Cu(In,Ga)Se_2 solar cells due to metastable defects—a route toward higher efficiencies. Solar RRL, 5(7), 2100063.

4. S. Levcenko, R. Biller, T. Pfeiffelmann, K. Ritter, H. H. Falk, **T. Wang**, S. Siebentritt, E. Welter and C. S. Schnohr. (2022). High-resolution XEOL spectroscopy setup at the X-ray absorption spectroscopy beamline P65 of PETRA III. Journal of Synchrotron Radiation, 29(5).

5. Omar Ramírez, Jiro Nishinaga, Felix Dingwell, **Taowen Wang**, Aubin Prot, Max Hilaire Wolter, Vibha Ranjan and Susanne Siebentritt. (2023). On the Origin of Tail States and Open Circuit Voltage Losses in Cu(In,Ga)Se_2. Solar RRL, 7(13), 2300054.

Acknowledgements

The long journey of my doctoral training has finally reached its culmination as I sit down to write this acknowledgement. Throughout this process, I have found great joy in conducting research, exploring new ideas, and overcoming challenges. However, it is important to acknowledge that the path to earning a doctorate is not without its difficulties and moments of stress. Fortunately, I did not have to navigate this journey alone. As a foreign researcher, I have been fortunate to receive tremendous support from the kind-hearted individuals in my immediate surroundings. Their unwavering assistance has been instrumental in my achievements and the progress I have made. I am deeply grateful for their contributions. I would like to take this opportunity to express my sincere appreciation to all those who have extended their help and support to me along the way. Without their guidance, encouragement, and generosity, I would not have been able to accomplish what I have today. Their belief in me and their willingness to lend a helping hand have made a significant impact on my success. I am truly grateful to have had such a supportive network of people who have played a role in shaping my journey. To my supervisor, collaborators, colleagues, friends, and family, thank you for your invaluable assistance, understanding, and patience throughout this process. Your presence in my life has made all the difference.

First and foremost, I would like to express my deep appreciation to my supervisor, Prof. Dr. Susanne Siebentritt. Four years ago, when I faced numerous rejections in my search for a PhD position, Susanne had faith in me and provided me with the opportunity to work at LPV. At that time, I had limited knowledge about Susanne and LPV, and I had no idea what my PhD journey would entail. However, I can proudly say that LPV is a great team created by Susanne. I am incredibly grateful for the joyful and supportive working environment at LPV, which has allowed me to work efficiently and without excessive stress. I have also greatly cherished my relationship with Susanne. As a PhD candidate, I firmly believe in the importance of independence. I believe that PhD researchers should take the initiative to propose research directions and develop solutions to the challenges they face. This requires a supervisor who is open-minded and, more importantly, trusts their students. Susanne exemplifies this type of supervisor who has placed great trust in me and provided me with the means to realize my ideas. This trust has been one of the key factors in the successful development of the HTL in our research project. In the beginning, the concept of

using thick oxides at the backside for hole transport seemed unconventional. However, with my explanation, Susanne decided to support me and allowed me to pursue this approach. She provided me with the freedom to explore and implement my proposed ideas, while also providing valuable guidance through our personal meetings. These discussions have been instrumental in my growth and development as a researcher. During my master's studies, I was primarily focused on experimental work in solar cell fabrication, with limited understanding of the underlying physics. Susanne, being not only an expert in solar cell fabrication but also possessing extensive knowledge of solar cell physics, has been an invaluable mentor. I have learned a great deal from her, which has enhanced my understanding of solar cell operation and enabled me to identify optimization strategies for improving their efficiency. There are many more aspects I could express my gratitude for, but in summary, if someone were to ask me where I earned my PhD degree, I would proudly tell them that I had the privilege of working at LPV under the guidance of Prof. Dr. Susanne Siebentritt. Her support, trust, and expertise have been instrumental in shaping my research journey, and I am truly grateful for the opportunity to have worked alongside her.

Undoubtedly, the success of our research project cannot be attributed solely to the efforts of my supervisor and me. I would like to extend my gratitude to Prof. Dr. Phillip Dale, who played a pivotal role in the PACE project, which provided the foundation for my research. Your dedication and hard work have given PhD candidates in the PACE project the opportunity to engage in diverse lectures and training sessions that expand our knowledge beyond our respective areas of expertise. This exposure is crucial for our professional growth and will undoubtedly benefit our future career development. Thank you for your invaluable contribution. I would also like to express my appreciation to Prof. Dr. Alex Redinger. During the most challenging phase of developing the HTLs, we had a meeting where you provided insightful advice on backside passivation. Although the specific approach did not yield the desired results, your guidance and suggestions served as a catalyst for my own creative thinking and inspired me to explore alternative solutions. Your contribution had a lasting impact on my research journey, and I am grateful for your support.

I would like to express my heartfelt appreciation to all of my collaborators who have contributed to the success of this research. First, I want to acknowledge my dear friend and invaluable collaborator, Longfei Song. His expertise in wide bandgap oxide semiconductors and his meticulous work in the preparation and characterization of oxides using SCS were instrumental to

the development of the HTLs discussed in this thesis. Through many personal meetings and discussions, we worked together tirelessly to ensure the proper functioning of the oxide-based HTLs. His deep insights and unwavering dedication cannot be overlooked when attributing the achievements of this research. Moreover, I am truly grateful for his exceptional responsibility and commitment to meeting all experimental deadlines without any postponement. Longfei, you are the research peer I always dreamt of having. Thank you, buddy. I would also like to express my gratitude to Dr. Boris Veith-wolf, Dr. Valeriya Titova, and Prof. Dr. Jan Schmidt from the Institute for Solar Energy Research Hamelin (ISFH) for their assistance in preparing the ALD Al_2O_3 and TiO_2 films. Their expertise and collaboration were vital in achieving the desired material properties. Additionally, I appreciate the support of Dr. Nathalie Valle and Adrian-Marie Philippe from the Luxembourg Institute of Science and Technology (LIST) for their contributions in performing TEM and SIMS measurements, which provided crucial insights into the structural and compositional aspects of the samples. I appreciate Dr. Hasan Arif Yetkin from LEM and Dr. Petru Lunca Popa from LIST for their invaluable help, discussions, and assistance in the preparation of $CuCrO_x$. I would also like to express my gratitude to Farooq Muhammad Uzair from SPM for his contributions in preparing MoO_x. I am grateful to Prof. Dr. Claudia Schnohr and Dr. Sergiu Levcenco from the University of Leipzig for inviting me to participate in the XEOL experiments. Through this collaboration, I gained valuable knowledge about the setup and execution of synchrotron measurements in Hamburg. Furthermore, I would like to extend my appreciation to Dr. Christian Kaufmann from the Institut Kompetenz-Zentrum Photovoltaik Berlin (PVcomB) for providing me with the opportunity to learn the techniques for growing smooth $Cu(In,Ga)Se_2$ layers at PVcomB. To all of my collaborators, I am truly grateful for your support, expertise, and willingness to collaborate. Your contributions have been instrumental in the success of this research project, and I am honored to have had the opportunity to work with each of you.

I would like to extend my heartfelt gratitude to my CET members, Prof. Dr. Thomas Kirchartz and Dr. Tom Wirtz. Thank you both for generously dedicating your valuable time to join the CET meetings and provide me with insightful advice, which has greatly enhanced the quality of my research. I also want to express my sincere appreciation to my jury members, Prof. Dr. Thomas Kirchartz, Prof. Dr. Susanne Siebentritt, Prof. Dr. Phillip Dale, Dr. Romain Carron, and Prof. Dr. Eva Unger. I am truly grateful for you accepting the invitation to be part of my defense committee. Special thanks to Pill for serving as my chair.

Furthermore, I would like to acknowledge and thank all my dear colleagues and friends in LPV, LEM, and SPM, with a special mention to Florian Ehre, Omar Ramirez Sanchez, Aubin Prot (AKA: JC, AKA: 奥宾, and AKA: Dr. aB), Ricardo Poeira, Thomas Weiss, Mohit Sood and Sevan Gharabeiki. Your guidance and expertise in various experimental setups, such as PVD (Florian) and measurements (PL: Florian and Omar, EQE and J-V: Mohit), have been invaluable. I am truly grateful for our engaging discussions on solar cells, scientific ideas, problem-solving approaches, and the memorable moments we shared over beers and board games. I would also like to extend my special thanks to Patricia Ramoa, Thomas Schuler, and Michele Melchiorre. Patricia, your kindness and gracefulness have been greatly appreciated, from handling daily administrative tasks such as room bookings, orders, and travel plans. Your support has allowed us to dedicate more time to our research, and I cannot imagine achieving what we have without your assistance. Thomas, your expertise as a highly skilled engineer has been indispensable in ensuring the proper functioning of our equipment. Thank you, professors. Michele, as one of the best chemists I have had the privilege to work with, your responsibility and patience have been truly remarkable. Thanks to your outstanding work, we have established reproducible standard processes to fabricate high-quality solar cells.

I am also deeply grateful to my Chinese cousins (friends), especially Xin He, Juntong Chen, and Longfei Song. Thank you for your constant encouragement during times when I felt discouraged. I particularly appreciate your efforts in keeping me occupied with cooking, allowing me to explore various dishes. Perhaps I may be granted the honorary title of "Doctorate of Chief (Cooking)"?

Special thanks go to my family, especially my parents. Your unwavering support, respect for my choices, and encouragement have played an instrumental role in my personal and academic development. I am profoundly grateful for being raised in such a nurturing environment, even though I am working 8000 km away from home.

Lastly, I would like to give a special acknowledgment to OpenAI, specifically ChatGPT, for its assistance in editing and improving the clarity of this thesis.

At the end, I would like to express appreciation for my own personal journey. I have faced numerous challenges and overcome adversities that many cannot imagine or comprehend. While

I have experienced moments of sorrow and hardship, I am not one to dwell on sadness. Instead, I choose to express myself through an ancient Chinese prose:

“天将降大任于是人也，必先苦其心志，饿其体肤，空乏其身，行拂乱其所为，所以动心忍性，增益其所不能——《孟子·告子下》”

My journey of overcoming difficulties is far from over; the completion of my doctoral training marks the beginning of new challenges and endeavors to conquer.

A5 Annex of Chapter 5

A5.1 NiOx

NiO_x is a p-type wide bandgap semiconductor that has demonstrated promising results as an effective material for integration into various solar cells, including CdTe[112], Sb_2Se_3[111, 113], and perovskites[114, 115]. NiO_x has been found to exhibit excellent passivation and hole transportation properties in these applications. Theoretical studies of its band structure have revealed that NiO_x possesses favorable band alignment with $Cu(In,Ga)Se_2$, which enables it to mitigate backside recombination without impeding the transport of holes[111, 112]. Consequently, the use of NiO_x as a HTL seems a promising strategy for improving the performance of $Cu(In,Ga)Se_2$-based solar cells.

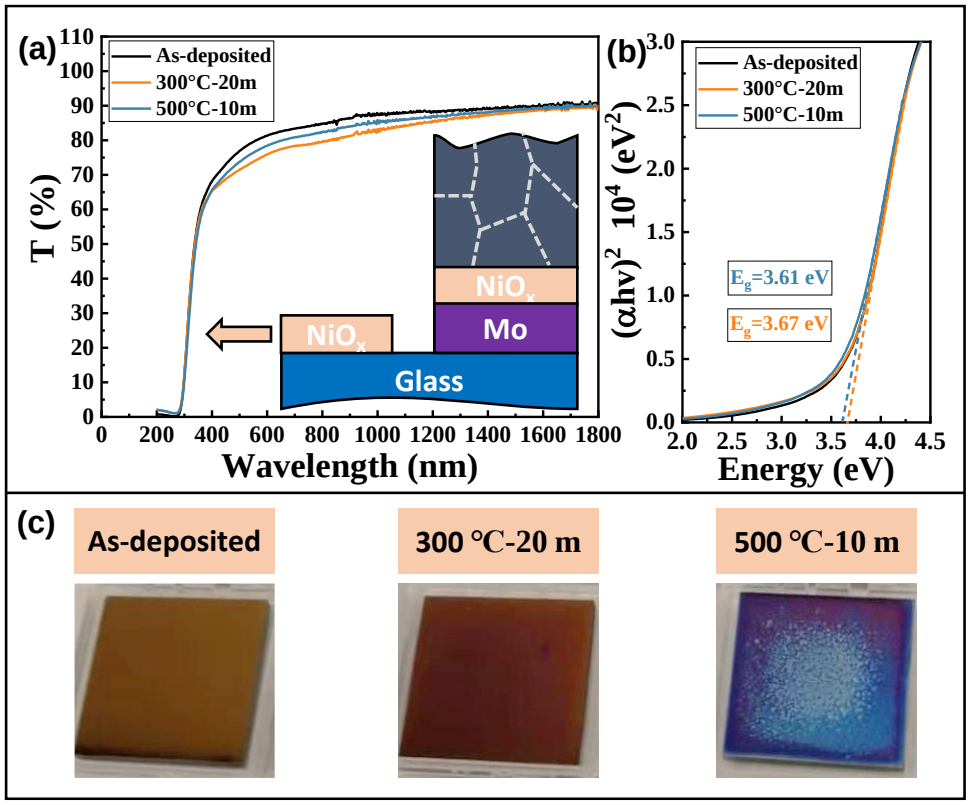

Figure A5.1 (a) The transmission spectra of NiO_x deposited on soda-lime glass with different annealing processes; (b) The tauc-plots of NiO_x converted from the transmission spectra; (c) The appearance of NiO_x/Mo before and after annealing in the air.

In this study, a 40 nm layer of electron beam evaporated NiO_x was deposited on Mo and soda-lime glass, followed by two different post-deposition annealing processes in air. The reason for introducing post annealing is that previous studies have shown that annealing can enhance the solar cell efficiency by improving its conductivity[206] or band alignment via changing its work function[207]. The annealing was performed at temperatures of 300 °C and 500 °C for 20 and 10 minutes, respectively, by placing the samples on a pre-heated hot plate and then allowing them to cool down naturally in air on a 2 mm thick soda-lime glass. The transparency of the annealed samples slightly decreases compared to the as-deposited sample, as shown **Figure A5.1 (a)** with transmission spectra. The Tauc-plot is converted from the transmission spectra and shown in Error! Reference source not found. **(b)**. By fitting the linear part of the tauc-plot, the intercept shows that the bandgap of NiO_x with different annealing is around 3.65 eV, which is consistent with the reported values[208, 209]. This suggests that the bandgap of thermally evaporated NiO_x is likely independent of post annealing in air.

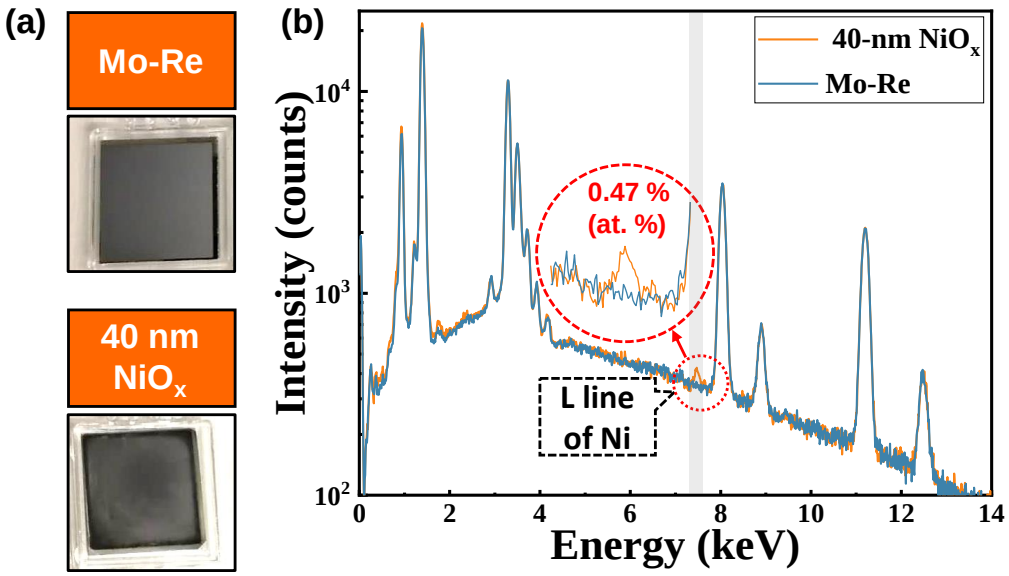

Figure A5.2 (a) The surface appearance of $CuInSe_2$ with and without NiO_x. The Mo reference (Mo-Re) sample does not contain NiO_x. The other sample has a 40 nm e-beam evaporated NiO_x on the Mo; (b) The EDS measurement of sample with and without NiO_x. To obtain the information without disturbance of NiO_x layer, the low energy electron beam with accelerating voltage of 5 kV is used. The L-line of Ni is detected in NiO_x involved sample, which represents Ni content of 0.47% (at%).

NiO_x on Mo substrates is also annealed with the same process, but the appearance of the samples changes significantly, as shown in **Figure A5.1 (c)**. Without any annealing, the sample has a light brown color. With 300 °C annealing for 20 minutes, the color becomes darker, and with 500 °C annealing for 10 minutes, the sample shows a rather bluish color. The change in appearance suggests that annealing NiO_x with Mo in air results in a strong interaction between Mo and NiO_x or O_2, likely leading to the formation of MoO_x. This observation indicates a negative influence on solar cell performance because oxidation can destroy the Mo back contact and lead to lower conductivity and a lower fill factor (FF) due to higher series resistance. Thus, annealing NiO_x in air with Mo is an unwanted issue for making efficient solar cells. However, the critical issue of using NiO_x is not oxidation of Mo since it can be easily avoided by annealing NiO_x in a vacuum or N_2 atmosphere. The real problem is the thermal instability of NiO_x, which causes Ni to diffuse into $Cu(In,Ga)Se_2$ during the growth process. Ni with a concentration above 0.26% (at%) is enough to result in very low efficiency of $Cu(In,Ga)Se_2$ solar cells[126].

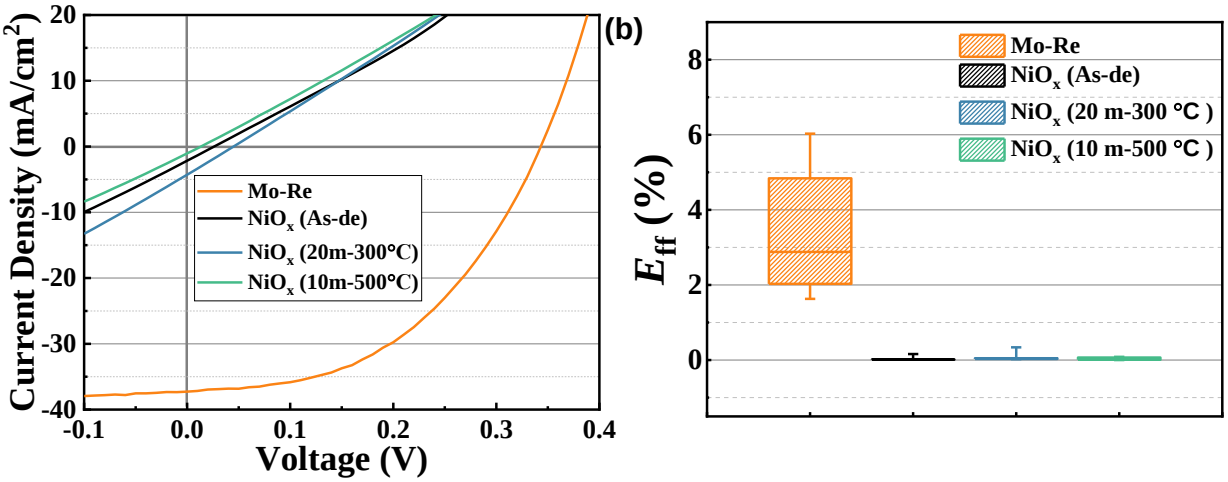

Figure A5.3 (a) The *J-V* characteristics of solar cells with and without NiO_x; The box plot, in which the box represents the interquartile range (25^{th} to 75^{th} percentile), the line inside the box is the mean value and the whisker is based on 1.5 IQR (interquartile range) value: (b) The statistical efficiency of solar cells with and without NiO_x.

Figure A5.2 (a) shows the surface appearance of $CuInSe_2$ with and without a NiO_x layer. The Mo reference sample appears homogeneous with a greyish color, whereas the sample grown with the NiO_x layer exhibits an inhomogeneous color distribution over the film. Since these $CuInSe_2$ were prepared at the same condition by a typical 1-stage process at the substrate setting temperature of

580 °C, meaning the absorbers are essential same if there is no influence of NiO_x. However, the black and greyish parts alternate on the surface of the sample with NiO_x, indicating that the NiO_x or the diffusion of Ni has a significant influence on the growth of $CuInSe_2$. Further evidence for the diffusion of Ni comes from EDS measurements shown in **Figure A5.2 (b)**. These measurements were taken using a low-energy electron beam with an accelerating voltage of 5 kV, which only detects information from the few hundred nanometers at the front surface, and thus cannot reach the NiO_x layer beneath the ~1.5 µm film. Despite this limitation, the measurements still detect around 0.47% (at%) of Ni in the sample involving NiO_x, which is sufficient to completely destroy the absorber and the solar cell[126].

The photovoltaic effects and efficiency of solar cells with and without a NiO_x layer are shown in **Figure A5.3**. The results reveal that solar cells with NiO_x exhibit weak photovoltaic effects and low efficiency, whereas the reference sample, which is Cu-rich, has lower efficiency due to excess Cu but still significantly outperforms the NiO_x involved samples. Therefore, it is essential to solve the thermal instability of these layers to make them work properly as HTLs. Additionally, the similar consequences of using $CuCrO_x$ are found and presented in the next section.

A5.2 $CuCrO_x$

As reported previously, $CuCrO_x$ is a promising candidate as a wide bandgap p-type semiconductor for use as an HTL layer in $Cu(In,Ga)Se_2$ solar cells due to its good band alignment with the absorber material[116]. Previous studies has demonstrated excellent hole selective transport properties of $CuCrO_x$ in other solar cells, such as CdTe[210] and perovskites[118]. However, as discussed earlier, the thermal instability of HTLs is a critical issue that can lead to diffusion and degradation of the layer during the absorber growth process. To evaluate the thermal stability of $CuCrO_x$ films grown by chemical vapor deposition (CVD), a 130 nm thick layer was deposited on a Mo substrate, followed by the standard 3-stage process to deposit ~2 µm of $CuInSe_2$ at the maximum substrate setting temperature of 580 °C.

The cross-sectional SEM image presented in **Figure A5.4 (a)** reveals that inter-diffusion occurs between $CuCrO_x$ and $CuInSe_2$, resulting in morphological changes at the interface. Although the $CuCrO_x$ layer is not completely destroyed, its interaction with the Mo surface appears to be strong

and non-uniform, as evidenced by the winding morphology of the Mo layer (thickness change). Furthermore, the formation of extremely small grains is observed at the interface between $CuInSe_2$ and $CuCrO_x$, indicating that Cr diffusion into the absorber may have a detrimental impact on solar cell performance, similar to the previously observed effects of Ni diffusion. To confirm this, the ΔE_F of samples covered by CBD CdS is determined by fitting the high energy wing of transformed absolute PL spectra with fixing the fitting temperature to the ambient temperature. The results depicted in **Figure A5.4 (b)** reveal that the introduction of $CuCrO_x$ causes a significant reduction in ΔE_F, amounting to approximately 60 meV when compared to the reference sample without $CuCrO_x$. Because the absorbers were prepared under identical conditions, it was expected that they would be identical regardless of the presence of $CuCrO_x$. The substantial decrease in ΔE_F indicates the increase in non-radiative recombination, which is likely due to diffusion of Cr. Consequently, it can be inferred that $CuCrO_x$ is not thermally stable enough to prevent the diffusion of Cr, which adversely affects the performance of both the absorber and thus the solar cells.

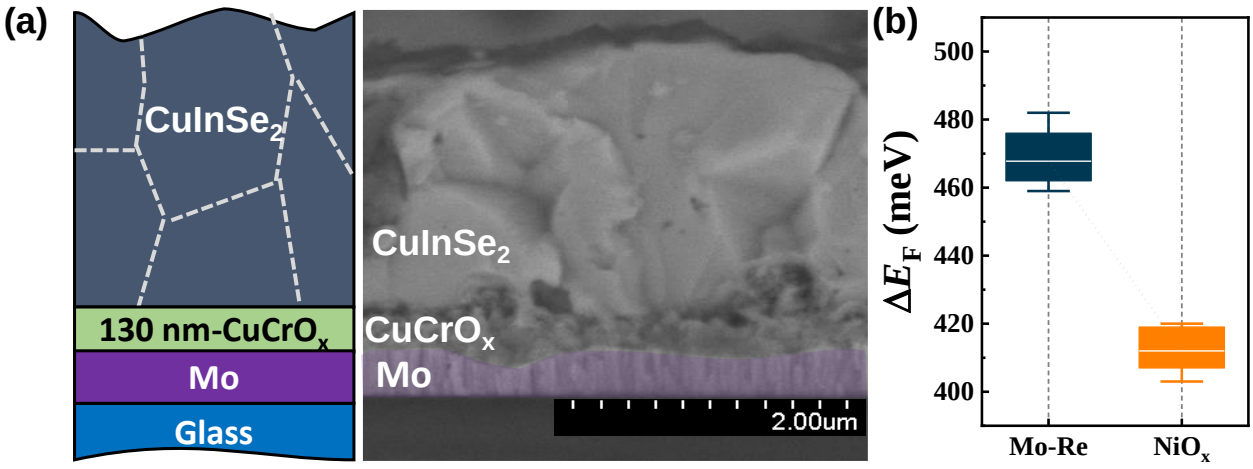

Figure A5.4 (a) The sample structure with $CuCrO_x$ and the corresponding SEM cross-section; (b) The ΔE_F of samples with and without $CuCrO_x$: the ΔE_F of the sample with $CuCrO_x$ is around 60 meV lower than that of the Mo reference sample without $CuCrO_x$, indicating a strong non-radiative recombination due to diffusion of Cr. The ΔE_F is acquired by fitting the high energy wing of transformed absolute PL spectra with fixing the fitting temperature to the ambient temperature.

A5.3 CuO_x

CuO_x is another promising candidate for an effective hole transport layer that can meet the criteria of efficient passivation and transport of charge carriers. Its successful application in other types of solar cells has been demonstrated to result in higher V_{oc} and FF[119, 121, 211]. In this section, a 50 nm layer of CuO_x was deposited on the surface of the Mo substrate by SCS, followed by a deposition of ~1.5 μm $CuInSe_2$ using the standard 3-stage process.

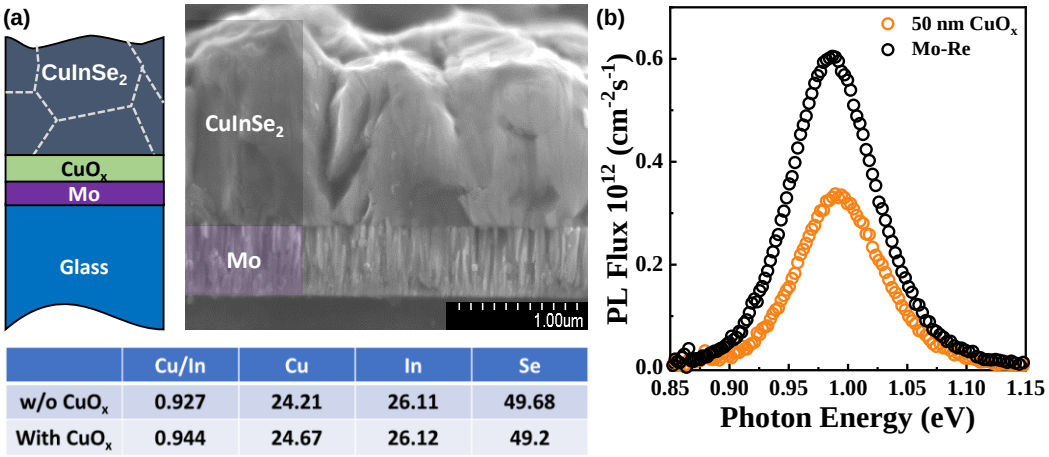

	Cu/In	Cu	In	Se
w/o CuO_x	0.927	24.21	26.11	49.68
With CuO_x	0.944	24.67	26.12	49.2

Figure A5.5 (a) The sketch of the sample structure with CuO_x and its corresponding SEM cross-section after the $CuInSe_2$ deposition. There is no individual layer between Mo and $CuInSe_2$, which suggests the strong diffusion of CuO_x during the growth of the absorber. The component of the samples determined by EDS shows the higher Cu content of sample with CuO_x, indicating the diffusion of the CuO_x; (b) The absolute PL of samples with and without $CuCrO_x$. The lower PL of sample with $CuCrO_x$ suggests that there is no passivation effect. All the measured samples were covered by CdS.

The SEM cross-section image in **Figure A5.5 (a)** shows no obvious interlayer existing between Mo and $CuInSe_2$, indicating that the CuO_x is extremely thermally unstable. The higher Cu/In ratio of the sample with CuO_x compared to the reference sample suggests the diffusion of CuO_x, which increases the amount of Cu in the bulk. The dissolution of CuO_x results in no expected passivation effect, which is confirmed by the absolute PL spectra in **Figure A5.5 (b)**. The PL intensity of the sample with CuO_x is slightly lower than that of the reference sample, resulting in a lower ΔE_F of around 420 meV compared to the reference sample's ΔE_F of 435 meV. These observations further emphasize that the critical issue in making HTLs work effectively is to ensure their stability during

the absorber growth process. Therefore, it is crucial to develop HTL materials that can withstand the harsh conditions of the absorber growth, e.g., high substrate temperature and Se vapor pressure, while maintaining their intended properties.

A5.4 MoO_x

Compared to the candidates are discussed above, previous researches have indicated that MoO_x may not have good band alignment with $Cu(In,Ga)Se_2$ when used as a hole transport layer[122, 212]. However, MoO_x has demonstrated passivation effects in solar cells such as $Cu(In,Ga)Se_2$[122], CdTe[213]and Si[214-216].

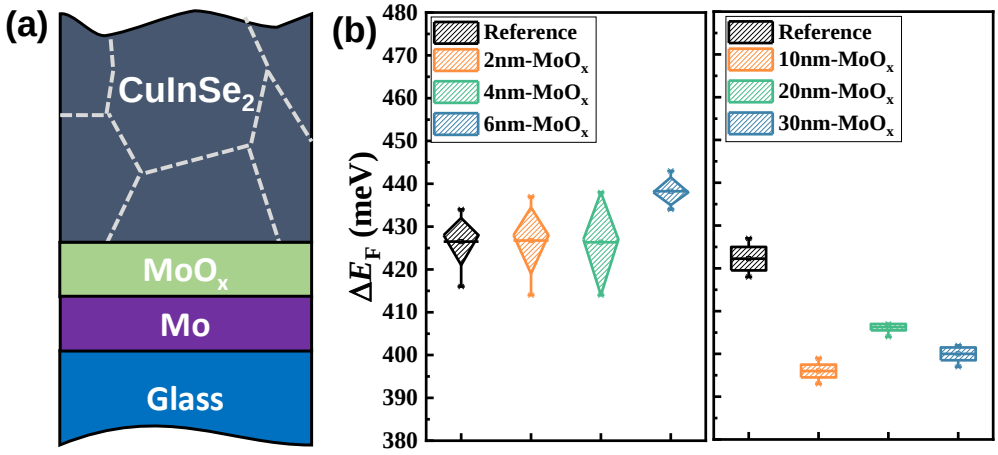

Figure A5.6 (a) The sketch of the sample structure; The box plot, in which the box represents the interquartile range (25^{th} to 75^{th} percentile), the line with a circle is the mean value and the whisker is based on 1.5 IQR (interquartile range) value: (b) The ΔE_F of samples with difference thickness of the MoO_x. The ΔE_F is acquired by fitting the high energy wing of transformed absolute PL spectra with fixing the fitting temperature to the ambient temperature.

In order to investigate the passivation of MoO_x for $CuInSe_2$, thermal evaporated MoO_x layers with thicknesses ranging from 2 nm to 30 nm were introduced onto Mo substrates. Then ~1.5 µm $CuInSe_2$ was deposited on the substrates that are covered by MoO_x with different thickness. The $CuInSe_2$ was prepared by a standard 1-stage process at the substrate setting temperature of 580 °C. The reference sample was prepared with the identical conditions but without MoO_x. **Figure A5.6 (b)** shows the ΔE_F of samples with varying MoO_x thicknesses and CdS covering, which is

determined by fitting the high energy wing of transformed absolute PL spectra with fixing the fitting temperature to the ambient temperature. Samples with 2 nm and 4 nm MoO_x exhibit roughly the same ΔE_F as the reference sample, suggesting no significant passivation effect from very thin MoO_x layers. A slight improvement in ΔE_F of ~10 meV is observed with 6 nm thickness, but thicker MoO_x layers above 10 nm result in a reduction in ΔE_F by 20-30 meV. The reason for this sudden decrease in ΔE_F is not clear, but it is possible that thick MoO_x may block the diffusion of Na from the soda-lime glass, resulting in lower doping density. Overall, the minimal improvement in ΔE_F appears that thermal evaporated MoO_x does not provide significant passivation, thus it can not work as a proper HTL.

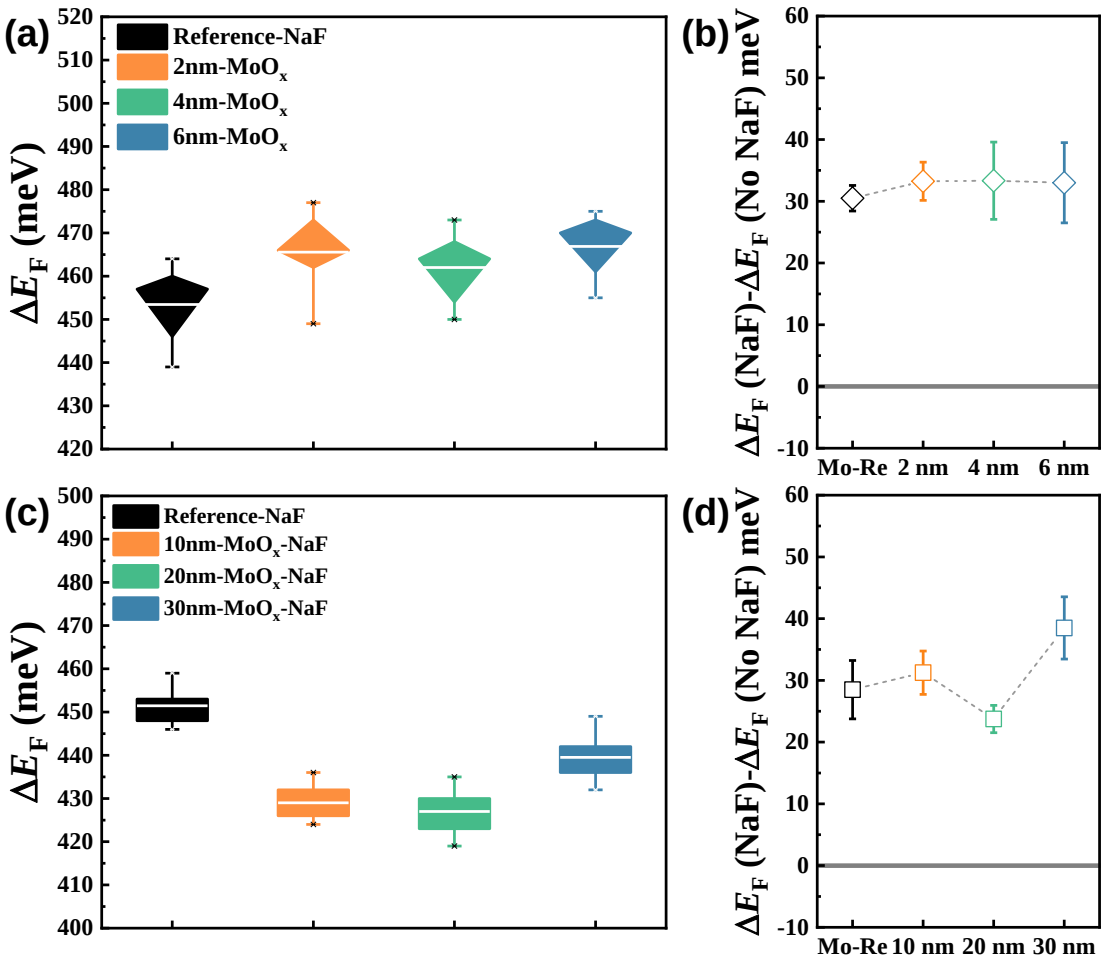

Figure A5.7 The box plot, in which the box represents the interquartile range (25th to 75th percentile), the white line inside the box is the mean value and the whisker is based on 1.5 IQR (interquartile range) value: (a) (c) ΔE_F of samples with thin/thick MoO_x after the NaF PDT. The ΔE_F is acquired by fitting the high energy wing of transformed absolute PL spectra with fixing

the fitting temperature to the ambient temperature. (b) (d) The improvement in ΔE_F after the NaF PDT.

To investigate the doping effect of Na, we performed NaF PDT on all the samples. Firstly, the sample surfaces were refreshed by immersing them in a 5% KCN aqueous solution for 30 seconds, followed by DI water rinsing and compressed N_2 drying. Next, the samples were covered with a 10 nm NaF layer by E-beam evaporation at ambient temperature. The samples were then annealed at 350 °C in the Se atmosphere for 10 minutes in the PVD system. The influence of the NaF PDT on the samples are shown in **Figure A5.7 (b)(d)**, which displays the change in ΔE_F for each sample after treatment. The reference sample showed an increase in ΔE_F of around 30 meV, whereas the improvement for samples with thin MoO_x was only slightly higher than the reference sample at less than 10 meV. However, this small difference may be due to sample inhomogeneity, so it is difficult to draw any conclusion that thin MoO_x can passivate the backside recombination. Even if this small improvement is attributed to thin MoO_x, the passivation effect is too low to yield an efficient solar cell. For samples with thick MoO_x, the improvement in ΔE_F was very similar to the reference sample, indicating a general lack of Na in these samples. Moreover, the thick MoO_x layers do not specifically reduce the Na content; otherwise, a much higher ΔE_F improvement would have been observed for these samples. In fact, the ΔE_F of the sample with thick MoO_x was still lower than the reference sample after the NaF PDT, suggesting that the lower ΔE_F was not due to lack of Na, but rather to an increase in non-radiative recombination.

In summary, we have investigated the passivation effect of MoO_x for $CuInSe_2$ and its relationship with Na doping. The presented results indicate that the thin MoO_x layers with a thickness lower than 6 nm have negligible influence on the ΔE_F compared to the reference sample, implying no significant passivation effect. On the other hand, thicker MoO_x layers with a thickness higher than 10 nm not only fail to passivate the backside recombination, but also result in a decrease in ΔE_F due to increased non-radiative recombination. Furthermore, the observed increase in the ΔE_F by approximately 30 meV following the NaF PDT across all samples suggests a general deficiency of Na in these samples. Therefore, based on these findings, we conclude that MoO_x is not an effective passivation layer for $CuInSe_2$ solar cells, and further research is required to explore alternative passivation materials.

A5.5 GaO_x

Besides MoO_x, GaO_x is also investigated in this work to study its thermal stability and passivation. Sputtered GaO_x is studied as an alternative buffer for the CdS to reduce the parasitic absorption of blue photons because has wider bandgap than the CdS. However, the V_{oc} and FF of the optimized sample is still much lower than CdS covered reference sample, which leads to a lower efficiency[125]. It suggests that the surface passivation of GaO_x is not as efficient as CdS, because of the potential surface damage from the sputtering. However, putting GaO_x at the backside could be another scenario. It is motived to check how stable they are and how much passivation they can provide. If they were stable, it can be probably used as a stabilizer to block the diffusion of unstable HTLs underneath as discussed in **session 5.2**. Another important reason of trying GaO_x is that it does not contain pernicious impurities to $Cu(In,Ga)Se_2$. Even in the worst case that the whole layer disappears due to diffusion, it will not change so much the optoelectronic properties of the absorbers, which can completely destroy the solar cells.

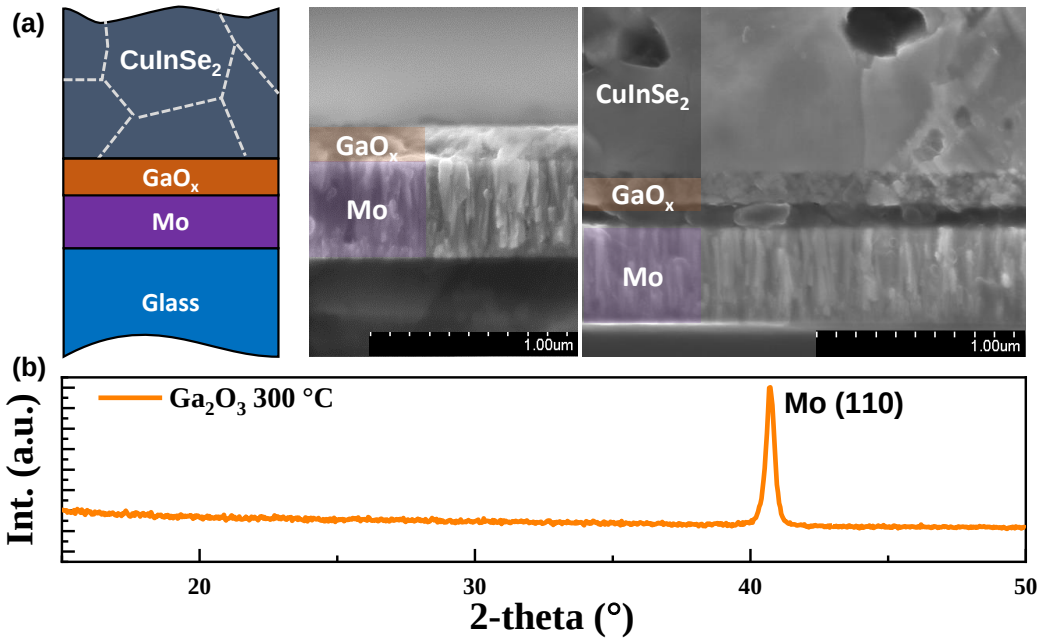

Figure A5.8 (a) The sketch of sample structure with GaO_x layer and its corresponding SEM cross-section of the sample. The SEM image on the left side is Mo/GaO_x before the deposition of $CuInSe_2$. The SEM image on the right side is image after the deposition of $CuInSe_2$; (b) The XRD of the GaO_x prepared by SCS with an annealing temperature of 300 °C.

As shown in **Figure A5.8 (a)**, SEM cross-section image on the left side, a thick GaO_x layer around 150 nm is firstly deposited on the surface of the Mo substrate by SCS with annealing temperature of 300 °C in air. The thick layer is favorable to clarify the thermal stability of GaO_x by comparing the change of the thickness before and after the absorber deposition. As suggested by the SEM cross-section image on the right side of **Figure A5.8 (a)**, there is clearly a GaO_x interlayer with fine grains between Mo and $CuInSe_2$. The as-deposited GaO_x by SCS with an annealing temperature of 300 °C is an amorphous film because no diffraction peaks can be detected by XRD as shown in **Figure A5.8 (b)**. The thickness of this layer is almost unchanged compared to as-deposited GaO_x layer, which means the thermal stability of GaO_x is good that almost no diffusion happens during the growth of the $CuInSe_2$. Another evidence is that the PL bandgap of the absorbers with different thickness of GaO_x stays almost the same as shown in **Figure A5.9 (a)**. The PL band gap is the energy corresponding to the maximum of PL flux. If Ga diffused during the growth of the $CuInSe_2$, the bandgap of the absorber is expected to continuously shift to the higher energy with increase in the thickness of GaO_x. The roughly constant PL bandgaps among different samples demonstrate again the good thermal stability of GaO_x.

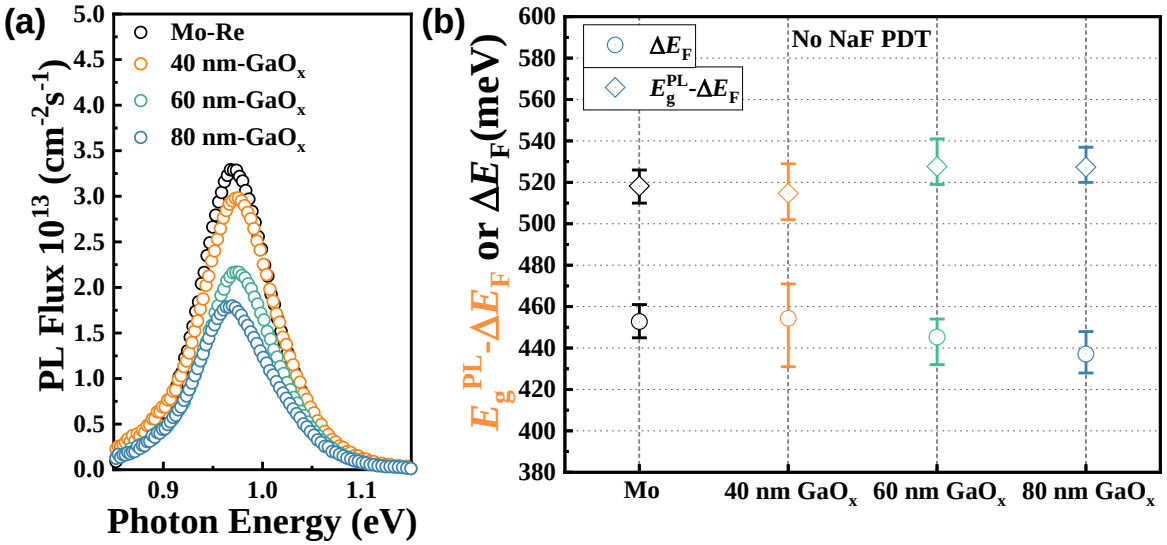

Figure A5.9 (a) The absolute PL of samples with different thickness of GaO_x; (b) The ΔE_F and ΔE_F deficits for samples with different thickness of GaO_x without the NaF PDT. The ΔE_F is acquired by fitting the high energy wing of transformed absolute PL spectra with fixing the fitting temperature to the ambient temperature. E_g^{PL} is the PL band gap which is the energy corresponding to the PL flux maximum.

Currently, the good enough thermal stability of GaO_x is confirmed and a GaO_x layer stays between Mo and $CuInSe_2$. But good HTLs are not only thermal stable but also should have good passivation effects that can reduce the backside recombination, thus improving the ΔE_F. Unfortunately, as shown in **Figure A5.9 (a)**, the absolute PL intensity of samples continue deceasing with increase in thickness of GaO_x, which suggests a higher non-radiative recombination of samples with GaO_x. As a result, the ΔE_F of sample increasingly decreases with the thicker GaO_x layer as shown in **Figure A5.9 (b)**. Because of this unwanted non-radiative recombination, the efficiency of solar cells is getting worse with the increase in thickness of GaO_x as shown in **Figure A5.10 (a)**. The V_{oc} of the reference sample is slightly (~10 meV) lower than its $\Delta E_F/q$, which means the front surface recombination of the finished devices is rather low. However, for the samples with GaO_x, the V_{oc} deficit compared to $\Delta E_F/q$ is higher than the reference sample and getting higher from 30 mV to 40 mV with increase in the thickness of the GaO_x. It was reported that serious front surface recombination bends down the electron Fermi-level of the absorber towards the front contact, which results in high V_{oc} deficit compared to $\Delta E_F/q$[142]. However, it is not likely the case because these samples are prepared with the same procedure at the same time, meaning they should have a very similar front surface recombination. Additionally, the V_{oc} deficit is higher for samples with a thicker GaO_x, which is basically not relevant to the front surface. The current evidence indicates that the issue is most likely caused by an improper band alignment between the GaO_x layer and the absorber[123], which makes the hole Fermi-level bend upwards to the back contact and thus increasing the V_{oc} deficits. It could explain the observation that the thicker GaO_x leads to higher V_{oc} deficits due a larger hole Fermi-level bending introduced by the thicker layer. This can also be proved by the shape of the J-V curves of solar cells. The solar cells were prepared by the standard procedures discussed in **Section 2.2.5**. To fabricate the solar cells, the bare absorbers were initially treated with a 5% KCN solution for 30 seconds to remove any impurities on the surface. The absorbers were then rinsed with DI water to prepare them for the subsequent deposition processes. The CBD method was employed to deposit a layer of CdS on the surface of the absorber. Subsequently, an i-ZnO/AZO window layer was deposited onto the CdS layer by sputtering. Finally, the electron beam evaporation method was used to deposit Ni/Al grids, which act as the electrical contacts for the solar cell. The finished solar cells had a surface area of approximately 0.25 cm^2. For the reference sample, the J-V curve is smooth and gives the FF ~65%. However, in the samples with GaO_x, an increase in GaO_x thickness results in a decrease in the

squareness of the *J-V* curve and thus a decrease in FF as shown in **Figure A5.10 (a)(c)**. The decrease in FF proves again an inappropriate band alignment between GaO_x and absorber, which is a hole transport barrier that blocks the transportation of holes. Regarding the current density, it is roughly the same among different samples, indicating that the barrier does not completely block the hole transport. The reduction in FF and V_{oc} leads to a decrease in the power conversion efficiency of solar cells, which drops from 11% to 6% as the thickness of GaO_x is increased to 80 nm.

In summary, the observation of minimal change in GaO_x thickness before and after absorber deposition confirms the thermal stability of GaO_x, which is crucial for ensuring an effective HTL. However, no passivation of GaO_x is observed, resulting in increased non-radiative losses and a corresponding decrease in ΔE_F. The observed higher V_{oc} deficits compared to ΔE_F are likely due to an improper band alignment between the GaO_x layer and the absorber, which also acts as a barrier to hole transport and reduces FF of the solar cells. Because of loss in FF and V_{oc}, the efficiency of solar cell drops obviously with an increase in GaO_x thickness.

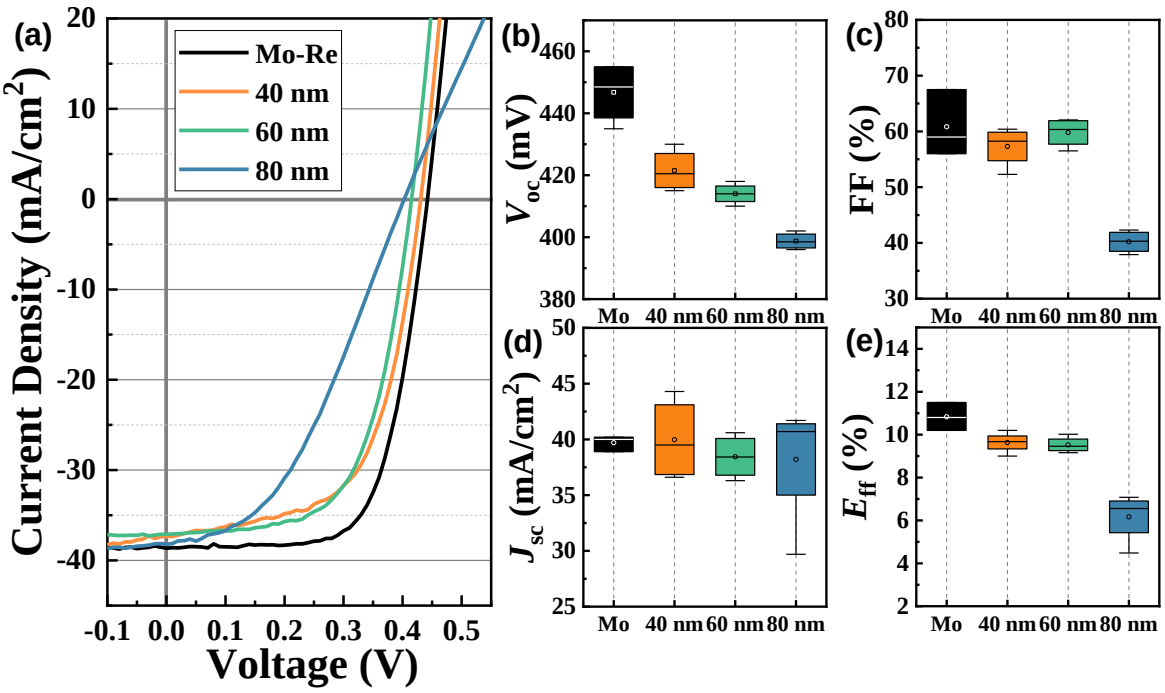

Figure A5.10 (a) Illumination *J-V* characterization of devices with GaO_x: the efficiency decreases with the increase in thickness of GaO_x; The box plot, in which the box represents the interquartile range (25^{th} to 75^{th} percentile), the line inside the box is the median value, the small

circle is the mean value and the whisker is based on 1.5 IQR (interquartile range) value: (b) The V_{oc} of devices decreases with the thicker GaO_x; (c) The loss of FF is possibly due to improper band alignment between GaO_x and $CuInSe_2$, which blocks the hole transport; (d) The current density among different samples stays roughly the same; (d) The thicker GaO_x results in a lower efficiency.

The observed decrease in ΔE_F and V_{oc} in the samples with GaO_x can be attributed to additional non-radiative recombination and improper band alignment at the backside. Additionally, the GaO_x layer may act as a barrier to the diffusion of Na from the soda-lime glass substrate, leading to a reduction in the p-type doping of the absorber and further contributing to higher ΔE_F and V_{oc} losses. To check this, The NaF PDT is done by thermal evaporating 5 nm NaF to the surface of the bare absorbers, then annealed them in a Se atmosphere at the setting substrate temperature of 350 °C for 10 minutes and finally cooled down in the same Se atmosphere. The ΔE_F and its deficits compared to the E_g^{PL} are summarized in **Figure A5.11**, which does not show clear improvement in ΔE_F after the NaF PDT. A marginal increase of approximately 10 meV in the ΔE_F is observed for samples containing 40 nm GaO_x, while the ΔE_F of the remaining samples remains relatively constant, indicating that they already contained sufficient amounts of Na. However, it should be noted that the NaF PDT may not have been optimized in this particular case, and its inefficacy cannot be ruled out as a contributing factor to the lack of significant improvement. Further investigation is required to determine the precise cause of the observed results.

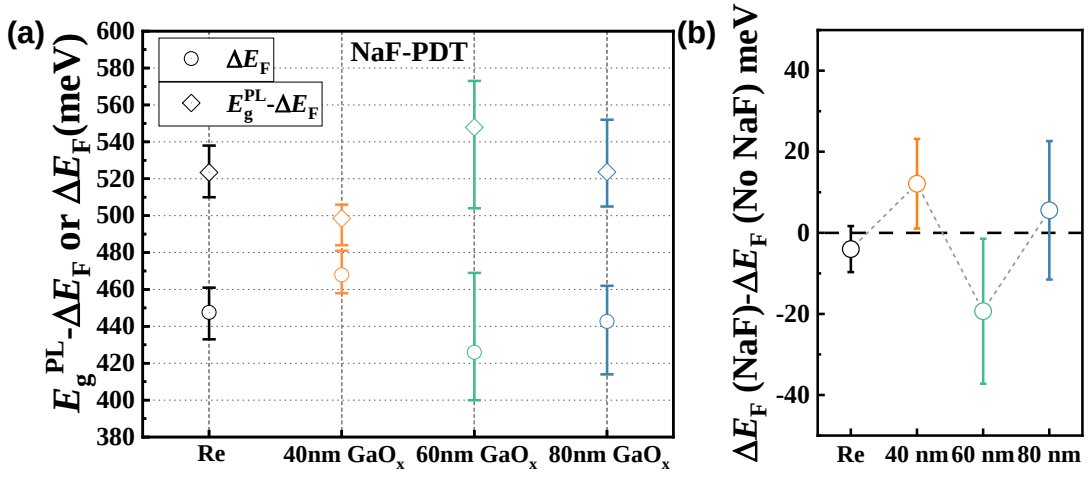

Figure A5.11 (a) The ΔE_F and its deficits compared to the E_g^{PL} of sample before and after the NaF PDT. The ΔE_F is acquired by fitting the high energy wing of transformed absolute PL

spectra with fixing the fitting temperature to the ambient temperature. E_g^{PL} is the PL band gap which is the energy corresponding to the PL flux maximum; (b) The ΔE_F difference of samples before and after the NaF PDT. The ΔE_F of samples remains relatively constant.

A5.6 Thickness of HTL from TEM

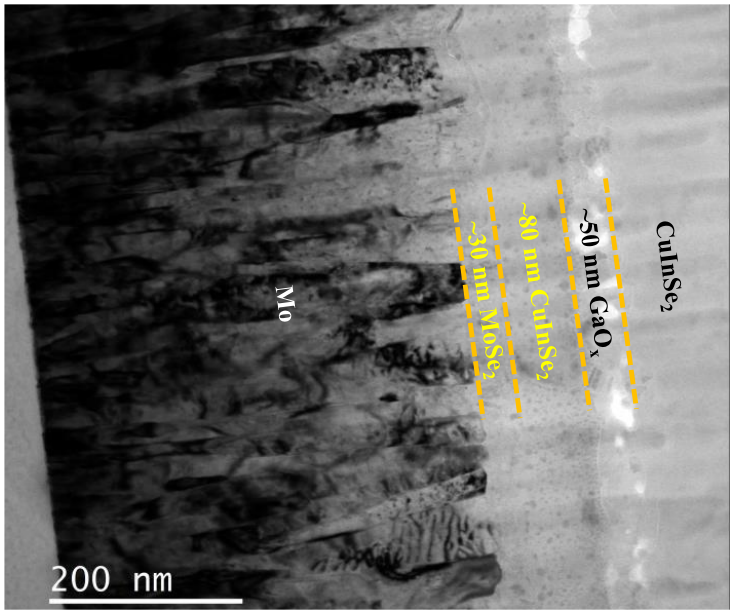

A5.12 TEM cross-section image from the sample discussed in **Section 5.2.3**. It shows the almost the same thickness of interlayers ($CuInSe_2$ and GaO_x) as suggested by the SEM cross-section image. Thus, the thicker layers shown in **Section 5.2.3** by other TEM image may be due to the inhomogeneity of the sample.

A5.7 XRD measured from the backside

The sample discussed in **Section 5.2.3** was peeled off from the substrate, then the XRD was measured from the backside. The result in **Figure A5.13** shows a broad peak around 2θ of 19.3°, which may be related to the (201) orientation of β-Ga_2O_3. It likely that the β-Ga_2O_3 was formed after the element exchange. However, more evidence is required to proof the formation of β-Ga_2O_3.

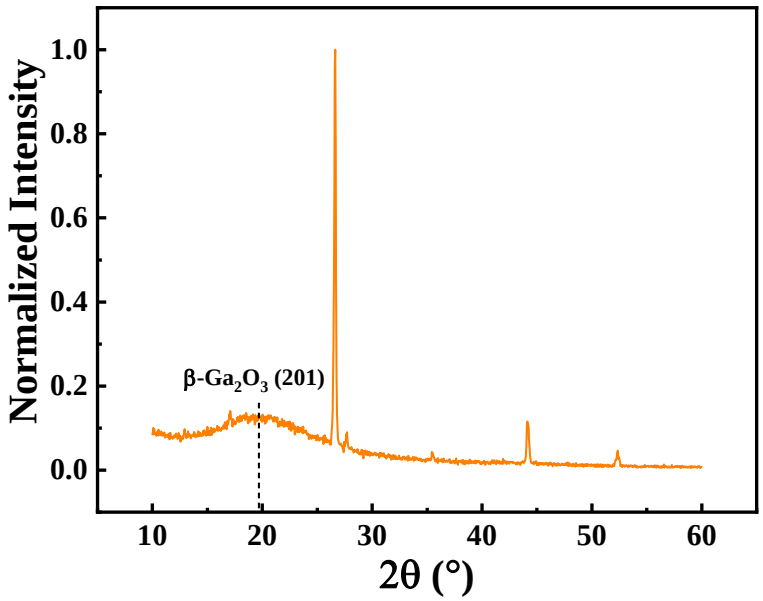

Figure A5.13 The XRD measured from backside of the film. The film stack was peeled off from the Mo. It shows a broad peak around 2θ of 19.3°, which may be related to (201) orientation of β-Ga_2O_3.

Bibliography

[1] M. Nakamura, K. Yamaguchi, Y. Kimoto, Y. Yasaki, T. Kato, H. Sugimoto, Cd-free Cu (In, Ga)(Se, S)$_2$ thin-film solar cell with record efficiency of 23.35%, IEEE Journal of Photovoltaics, 9 (2019) 1863-1867.

[2] Global Temperature and Carbon Dioxide, https://www.globalchange.gov/browse/multimedia/global-temperature-and-carbon-dioxide.

[3] A. Stips, D. Macias, C. Coughlan, E. Garcia-Gorriz, X.S. Liang, On the causal structure between CO_2 and global temperature, 6 (2016) 21691.

[4] B. Earth, Carbon Dioxide and Global Temperature Visualization, https://www.youtube.com/watch?v=IXHOc2rmSPM.

[5] IPCC, AR6 Synthesis Report-Headline Statement-A.4: Current Mitigation Progress, Gaps and Challenges, https://www.ipcc.ch/report/ar6/syr/resources/spm-headline-statements.

[6] BBC, China, Europe and US drought: Is 2022 the driest year recorded?, https://www.bbc.com/news/62751110.

[7] GDP, 2022 International Wildfire, https://disasterphilanthropy.org/disasters/2022-international-wildfires/, (2022).

[8] Danielle Filbig, S. Pauly, Can Luxembourg prevent future flooding?, RTL.lu https://today.rtl.lu/news/luxembourg/a/1940401.html.

[9] UNEP, Green Energy Choices:the benefits, risks and trade-offs of low-carbon technologies for electricity production, https://www.resourcepanel.org/reports/green-energy-choices-benefits-risks-and-trade-offs-low-carbon-technologies-electricity.

[10] B.J. Stanbery, D. Abou-Ras, A. Yamada, L. Mansfield, CIGS photovoltaics: reviewing an evolving paradigm, J. Phys. D: Appl. Phys., 55 (2021) 173001.

[11] M. Ochoa, S. Buecheler, A.N. Tiwari, R. Carron, Challenges and opportunities for an efficiency boost of next generation Cu(In, Ga)Se_2 solar cells: prospects for a paradigm shift, Energy Environ. Sci., 13 (2020) 2047-2055.

[12] L.C. Hirst, N. Ekins‐Daukes, Fundamental losses in solar cells, Prog. Photovolt: Res. Appl., 19 (2011) 286-293.

[13] W. Shockley, H.J. Queisser, Detailed balance limit of efficiency of p‐n junction solar cells, J. Appl. Phys., 32 (1961) 510-519.
[14] P. Würfel, Physics of Solar Cells, Wiley-VCH Verlag GmbH, Weinheim, 2005.
[15] J.A. Nelson, The physics of solar cells, World Scientific Publishing Company, 2003.
[16] J.L. Gray, The physics of the solar cell, Handbook of photovoltaic science, 2 (2003) 82-128.
[17] NREL, https://www.nrel.gov/grid/solar-resource/spectra-am1.5.html.
[18] J. Jaffe, A. Zunger, Theory of the band-gap anomaly in ABC_2 chalcopyrite semiconductors, Physical Review B, 29 (1984) 1882.
[19] U. Würfel, A. Cuevas, P. Würfel, Charge carrier separation in solar cells, IEEE Journal of Photovoltaics, 5 (2014) 461-469.
[20] A. Onno, C. Chen, P. Koswatta, M. Boccard, Z.C. Holman, Passivation, conductivity, and selectivity in solar cell contacts: Concepts and simulations based on a unified partial-resistances framework, J. Appl. Phys., 126 (2019) 183103.
[21] R. Brendel, R. Peibst, Contact selectivity and efficiency in crystalline silicon photovoltaics, IEEE Journal of photovoltaics, 6 (2016) 1413-1420.
[22] M. Green, F. King, J. Shewchun, Minority carrier MIS tunnel diodes and their application to electron-and photo-voltaic energy conversion—I. Theory, Solid·State Electron., 17 (1974) 551-561.
[23] R. Scheer, H.-W. Schock, Chalcogenide photovoltaics: physics, technologies, and thin film devices, John Wiley & Sons, 2011.
[24] P. Wurfel, The chemical potential of radiation, J. Phys. C: Solid State Phys., 15 (1982) 3967.
[25] A. Onno, C. Reich, S. Li, A. Danielson, W. Weigand, A. Bothwell, S. Grover, J. Bailey, G. Xiong, D. Kuciauskas, Understanding what limits the voltage of polycrystalline CdSeTe solar cells, Nature Energy, 7 (2022) 400-408.
[26] D. Kuciauskas, J. Moseley, P. Ščajev, D. Albin, Radiative efficiency and charge‐carrier lifetimes and diffusion length in polycrystalline CdSeTe heterostructures, physica status solidi – Rapid Research Letters, 14 (2020) 1900606.
[27] D. Kuciauskas, J.M. Kephart, J. Moseley, W.K. Metzger, W.S. Sampath, P. Dippo, Recombination velocity less than 100 cm/s at polycrystalline Al_2O_3/CdSeTe interfaces, Appl. Phys. Lett., 112 (2018) 263901.

[28] A. Chirilă, S. Buecheler, F. Pianezzi, P. Bloesch, C. Gretener, A.R. Uhl, C. Fella, L. Kranz, J. Perrenoud, S. Seyrling, Highly efficient Cu(In, Ga)Se_2 solar cells grown on flexible polymer films, Nature materials, 10 (2011) 857-861.

[29] A.M. Gabor, J.R. Tuttle, D.S. Albin, M.A. Contreras, R. Noufi, A.M. Hermann, High-efficiency $CuIn_xGa_{1-x}Se_2$ solar cells made from (In_x, Ga_{1-x})$_2Se_3$ precursor films, Appl. Phys. Lett., 65 (1994) 198-200.

[30] T. Dullweber, O. Lundberg, J. Malmström, M. Bodegård, L. Stolt, U. Rau, H.-W. Schock, J.H. Werner, Back surface band gap gradings in Cu(In, Ga)Se_2 solar cells, Thin Solid Films, 387 (2001) 11-13.

[31] M.A. Green, E.D. Dunlop, J. Hohl-Ebinger, M. Yoshita, N. Kopidakis, X. Hao, Solar cell efficiency tables (Version 58), Prog. Photovolt: Res. Appl., 29 (2021).

[32] H.W. Spiess, U. Haeberlen, G. Brandt, A. Räuber, J. Schneider, Nuclear magnetic resonance in IB–III–VI2 semiconductors, Physica Status Solidi B: Basic Research, 62 (1974) 183-192.

[33] J. Keller, L. Stolt, K.V. Sopiha, J.K. Larsen, L. Riekehr, M. Edoff, On the Paramount Role of Absorber Stoichiometry in (Ag, Cu)(In, Ga)Se_2 Wide‐Gap Solar Cells, Sol. RRL, 4 (2020) 2000508.

[34] S. Shukla, M. Sood, D. Adeleye, S. Peedle, G. Kusch, D. Dahliah, M. Melchiorre, G.-M. Rignanese, G. Hautier, R. Oliver, Over 15% efficient wide-band-gap Cu(In, Ga)S_2 solar cell: Suppressing bulk and interface recombination through composition engineering, Joule, 5 (2021) 1816-1831.

[35] W. Feng, D. Xiao, J. Ding, Y. Yao, Three-Dimensional Topological Insulators in I−III−VI_2 and II−IV−V_2 Chalcopyrite Semiconductors, Phys. Rev. Lett., 106 (2011) 016402.

[36] A. Mudryi, V. Gremenok, A. Karotki, V. Zalesski, M. Yakushev, F. Luckert, R. Martin, Structural and optical properties of thin films of Cu(In, Ga)Se_2 semiconductor compounds, J. Appl. Spectrosc., 77 (2010) 371-377.

[37] R. Carron, E. Avancini, T. Feurer, B. Bissig, P.A. Losio, R. Figi, C. Schreiner, M. Bürki, E. Bourgeois, Z. Remes, Refractive indices of layers and optical simulations of Cu(In, Ga)Se_2 solar cells, STAM, 19 (2018) 396-410.

[38] P. Paulson, R. Birkmire, W. Shafarman, Optical characterization of $CuIn_{1-x}Ga_xSe_2$ alloy thin films by spectroscopic ellipsometry, J. Appl. Phys., 94 (2003) 879-888.

[39] A. Klein, Energy band alignment in chalcogenide thin film solar cells from photoelectron spectroscopy, J. Phys.: Condens. Matter, 27 (2015) 134201.
[40] R. Scheer, Interface and surface properties of ternary semiconductors, Jpn. J. Appl. Phys., 39 (2000) 371.
[41] S. Siebentritt, L. Gütay, D. Regesch, Y. Aida, V.J.S.E.M. Deprédurand, S. Cells, Why do we make Cu(In, Ga)Se_2 solar cells non-stoichiometric?, Sol. Energy Mater. Sol. Cells, 119 (2013) 18-25.
[42] T. Bertram, V. Depredurand, S. Siebentritt, In-Se surface treatment of Cu-rich grown $CuInSe_2$, in: 2014 IEEE 40th Photovoltaic Specialist Conference (PVSC), IEEE, 2014, pp. 3633-3636.
[43] C. Spindler, F. Babbe, M.H. Wolter, F. Ehré, K. Santhosh, P. Hilgert, F. Werner, S. Siebentritt, Electronic defects in Cu(In, Ga)Se_2: Towards a comprehensive model, Physical Review Materials, 3 (2019) 090302.
[44] J. Mikkelsen, Ternary phase relations of the chalcopyrite compound $CuGaSe_2$, J. Electron. Mater., 10 (1981) 541-558.
[45] T. Godecke, T. Haalboom, F. Ernst, Phase equilibria of Cu-In-Se. III. The In_2Se_3-Se-Cu_2Se subsystem, Z. Metallk., 91 (2000) 651-662.
[46] A.M. Gabor, J.R. Tuttle, D.S. Albin, M.A. Contreras, R. Noufi, A.M. Hermann, High‐efficiency $CuIn_xGa_{1-x}Se_2$ solar cells made from $(In_x, Ga_{1-x})_2Se_3$ precursor films, Appl. Phys. Lett., 65 (1994) 198-200.
[47] K. Sakurai, R. Hunger, R. Scheer, C.A. Kaufmann, A. Yamada, T. Baba, Y. Kimura, K. Matsubara, P. Fons, H. Nakanishi, In situ diagnostic methods for thin‐film fabrication: utilization of heat radiation and light scattering, Prog. Photovolt: Res. Appl., 12 (2004) 219-234.
[48] T. Bertram, PhD thesis: Doping, Defects And Solar Cell Performance Of Cu-rich Grown $CuInSe_2$, in: FSTM, University of Luxembourg 2016, pp. 42, https://orbilu.uni.lu/handle/10993/28325.
[49] A.M. Gabor, J.R. Tuttle, M.H. Bode, A. Franz, A.L. Tennant, M.A. Contreras, R. Noufi, D.G. Jensen, A.M. Hermann, Band-gap engineering in Cu(In, Ga)Se_2 thin films grown from $(In, Ga)_2Se_3$ precursors, Sol. Energy Mater. Sol. Cells, 41 (1996) 247-260.
[50] W. Witte, R. Kniese, M. Powalla, Raman investigations of Cu(In, Ga)Se_2 thin films with various copper contents, Thin Solid Films, 517 (2008) 867-869.

[51] N. Barreau, T. Painchaud, F. Couzinié-Devy, L. Arzel, J. Kessler, Recrystallization of CIGSe layers grown by three-step processes: A model based on grain boundary migration, Acta Materialia, 58 (2010) 5572-5577.
[52] D.J. Schroeder, G.D. Berry, A.A. Rockett, Gallium diffusion and diffusivity in $CuInSe_2$ epitaxial layers, Appl. Phys. Lett., 69 (1996) 4068-4070.
[53] D.W. Niles, K. Ramanathan, F. Hasoon, R. Noufi, B.J. Tielsch, J.E. Fulghum, Na impurity chemistry in photovoltaic CIGS thin films: Investigation with x-ray photoelectron spectroscopy, Journal of Vacuum Science Technology A: Vacuum, Surfaces, Films, 15 (1997) 3044-3049.
[54] H. Wang, Y. Zhang, X. Kou, Y. Cai, W. Liu, T. Yu, J. Pang, C. Li, Y. Sun, Effect of substrate temperature on the structural and electrical properties of CIGS films based on the one-stage co-evaporation process, Semicond. Sci. Technol., 25 (2010) 055007.
[55] A. Rockett, J. Britt, T. Gillespie, C. Marshall, M. Al Jassim, F. Hasoon, R. Matson, B. Basol, Na in selenized Cu (In, Ga) Se_2 on Na-containing and Na-free glasses: distribution, grain structure, and device performances, Thin Solid Films, 372 (2000) 212-217.
[56] P.M. Salomé, A. Hultqvist, V. Fjällström, M. Edoff, B. Aitken, K. Vaidyanathan, K. Zhang, K. Fuller, C.K. Williams, Cu(In, Ga)Se_2 Solar Cells With Varying Na Content Prepared on Nominally Alkali-Free Glass Substrates, IEEE Journal of Photovoltaics, 3 (2013) 852-858.
[57] K. Granath, M. Bodegård, L. Stolt, The effect of NaF on Cu(In, Ga)Se_2 thin film solar cells, Sol. Energy Mater. Sol. Cells, 60 (2000) 279-293.
[58] F. Pianezzi, P. Reinhard, A. Chirilă, B. Bissig, S. Nishiwaki, S. Buecheler, A.N. Tiwari, Unveiling the effects of post-deposition treatment with different alkaline elements on the electronic properties of CIGS thin film solar cells, PCCP, 16 (2014) 8843-8851.
[59] M. Powalla, S. Paetel, D. Hariskos, R. Wuerz, F. Kessler, P. Lechner, W. Wischmann, T.M. Friedlmeier, Advances in cost-efficient thin-film photovoltaics based on Cu(In, Ga)Se_2, Engineering, 3 (2017) 445-451.
[60] M. Marudachalam, R. Birkmire, H. Hichri, J. Schultz, A. Swartzlander, M. Al-Jassim, Phases, morphology, and diffusion in $CuIn_xGa_{1-x}Se_2$ thin films, J. Appl. Phys., 82 (1997) 2896-2905.
[61] P. Jackson, D. Hariskos, R. Wuerz, O. Kiowski, A. Bauer, T.M. Friedlmeier, M. Powalla, Properties of Cu(In, Ga)Se_2 solar cells with new record efficiencies up to 21.7%, physica status solidi –Rapid Research Letters, 9 (2015) 28-31.

[62] Y. Kamikawa, J. Nishinaga, H. Shibata, S. Ishizuka, Efficient Narrow Band Gap Cu(In, Ga)Se_2 Solar Cells with Flat Surface, ACS Appl. Mater. Interfaces, 12 (2020) 45485-45492.
[63] T. Feurer, F. Fu, T.P. Weiss, E. Avancini, J. Löckinger, S. Buecheler, A.N. Tiwari, RbF post deposition treatment for narrow bandgap Cu(In, Ga)Se_2 solar cells, Thin Solid Films, 670 (2019) 34-40.
[64] A. Niemegeers, M. Burgelman, R. Herberholz, U. Rau, D. Hariskos, H.W. Schock, Model for electronic transport in C (In, Ga)Se_2 solar cells, Prog. Photovolt: Res. Appl., 6 (1998) 407-421.
[65] G. Sozzi, F. Troni, R. Menozzi, On the combined effects of window/buffer and buffer/absorber conduction-band offsets, buffer thickness and doping on thin-film solar cell performance, Sol. Energy Mater. Sol. Cells, 121 (2014) 126-136.
[66] T. Kodalle, M.D. Heinemann, D. Greiner, H.A. Yetkin, M. Klupsch, C. Li, P.A. van Aken, I. Lauermann, R. Schlatmann, C.A. Kaufmann, Elucidating the mechanism of an RbF post deposition treatment in CIGS thin film solar cells, Sol. RRL, 2 (2018) 1800156.
[67] T. Dullweber, U. Rau, H. Schock, A new approach to high-efficiency solar cells by band gap grading in Cu(In, Ga)Se_2 chalcopyrite semiconductors, Sol. Energy Mater. Sol. Cells, 67 (2001) 145-150.
[68] U. Rau, B. Blank, T.C. Müller, T. Kirchartz, Efficiency potential of photovoltaic materials and devices unveiled by detailed-balance analysis, Phys. Rev. Appl., 7 (2017) 044016.
[69] S. Siebentritt, U. Rau, S. Gharabeiki, T.P. Weiss, A. Prot, T. Wang, D. Adeleye, M. Drahem, A. Singh, Photoluminescence assessment of materials for solar cell absorbers, Faraday Discuss., 239 (2022) 112-129.
[70] Y.H. Chang, R. Carron, M. Ochoa, C. Bozal‐Ginesta, A.N. Tiwari, J.R. Durrant, L. Steier, Insights from Transient Absorption Spectroscopy into Electron Dynamics Along the Ga‐Gradient in Cu(In, Ga)Se_2 Solar Cells, Adv. Energy. Mater., 11 (2021) 2003446.
[71] S. Siebentritt, A. Lomuscio, D. Adeleye, M. Sood, A. Dwivedi, Sulfide Chalcopyrite Solar Cells—Are They the Same as Selenides with a Wider Bandgap?, physica status solidi –Rapid Research Letters, 16 (2022) 2200126.
[72] T. Feurer, R. Carron, G. Torres Sevilla, F. Fu, S. Pisoni, Y.E. Romanyuk, S. Buecheler, A.N.J.A.E.M. Tiwari, Efficiency Improvement of Near‐Stoichiometric $CuInSe_2$ Solar Cells for Application in Tandem Devices, Adv. Energy. Mater., 9 (2019) 1901428.

[73] T. Feurer, B. Bissig, T.P. Weiss, R. Carron, E. Avancini, J. Löckinger, S. Buecheler, A.N. Tiwari, Single-graded CIGS with narrow bandgap for tandem solar cells, STAM, 19 (2018) 263-270.

[74] R. Kotipalli, B. Vermang, J. Joel, R. Rajkumar, M. Edoff, D. Flandre, Investigating the electronic properties of Al_2O_3/Cu(In, Ga)Se_2 interface, AIP Adv., 5 (2015) 107101.

[75] G. Birant, J. de Wild, M. Meuris, J. Poortmans, B. Vermang, Dielectric-based rear surface passivation approaches for Cu(In, Ga)Se_2 solar cells—A review, Appl. Sci., 9 (2019) 677.

[76] T. Umehara, S. Iinuma, A. Yamada, Investigation of the effects of rear surface recombination on the Cu(In, Ga)Se_2 solar cell performances, Electronic Materials Letters, 12 (2016) 479-483.

[77] W. Sharaman, R. Birkmire, S. Marsillac, M. Marudachalam, N. Orbey, T. Russell, Effect of reduced deposition temperature, time, and thickness on Cu(InGa)Se_2 films and devices, in: Conference Record of the Twenty Sixth IEEE Photovoltaic Specialists Conference-1997, IEEE, 1997, pp. 331-334.

[78] T. Negami, S. Nishiwaki, Y. Hashimoto, N. Kohara, T. Wada, Effect of absorber thickness on performance of Cu(In,Ga)Se_2 solar cells, in: 2nd World Conference and Exhibition on Photovoltaic Solar Energy Conversion, Vienna, Austria, 1998, pp. 1181-1184.

[79] Z. Jehl, F. Erfurth, N. Naghavi, L. Lombez, I. Gerard, M. Bouttemy, P. Tran-Van, A. Etcheberry, G. Voorwinden, B. Dimmler, Thinning of CIGS solar cells: Part II: Cell characterizations, Thin Solid Films, 519 (2011) 7212-7215.

[80] E. Jarzembowski, M. Maiberg, F. Obereigner, K. Kaufmann, S. Krause, R. Scheer, Optical and electrical characterization of Cu(In,Ga)Se_2 thin film solar cells with varied absorber layer thickness, Thin Solid Films, 576 (2015) 75-80.

[81] M. Gloeckler, J.R. Sites, Potential of submicrometer thickness Cu(In,Ga)Se_2 solar cells, J. Appl. Phys., 98 (2005) 103703.

[82] M.H. Wolter, Optical investigation of voltage losses in high-efficiency Cu(In, Ga)Se_2 thin-film solar cells, in, University of Luxembourg 2019 (https://orbilu.uni.lu/handle/10993/39611), pp. 82-85.

[83] S. Rühle, Tabulated values of the Shockley–Queisser limit for single junction solar cells, Solar energy, 130 (2016) 139-147.

[84] S. Siebentritt, T.P. Weiss, M. Sood, M.H. Wolter, A. Lomuscio, O. Ramirez, How photoluminescence can predict the efficiency of solar cells, Journal of Physics: Materials, 4 (2021) 042010.
[85] R.T. Ross, Some thermodynamics of photochemical systems, The Journal of Chemical Physics, 46 (1967) 4590-4593.
[86] W. Metzger, I. Repins, M. Romero, P. Dippo, M. Contreras, R. Noufi, D. Levi, Recombination kinetics and stability in polycrystalline Cu(In,Ga)Se_2 solar cells, Thin Solid Films, 517 (2009) 2360-2364.
[87] M. Maiberg, R. Scheer, Theoretical study of time-resolved luminescence in semiconductors. I. Decay from the steady state, J. Appl. Phys., 116 (2014).
[88] S.J. Heise, J.L. Salas, Charge separation effects in time-resolved photoluminescence of Cu(In,Ga)Se_2 thin film solar cells, Thin Solid Films, 633 (2017) 35-39.
[89] A. Kanevce, D. Kuciauskas, T.A. Gessert, D.H. Levi, D.S. Albin, Impact of interface recombination on time resolved photoluminescence (TRPL) decays in CdTe solar cells (numerical simulation analysis), in: 2012 38th IEEE Photovoltaic Specialists Conference, IEEE, 2012, pp. 000848-000853.
[90] T.P. Weiss, F. Ehre, V. Serrano-Escalante, T. Wang, S. Siebentritt, Understanding Performance Limitations of Cu(In,Ga)Se_2 Solar Cells due to Metastable Defects—A Route toward Higher Efficiencies, Sol. RRL, 5 (2021).
[91] T.P. Weiss, O. Ramírez, S. Paetel, W. Witte, J. Nishinaga, T. Feurer, S. Siebentritt, Metastable defects decrease the fill factor of solar cells, Phys. Rev. Appl., 19 (2023) 024052.
[92] F. Babbe, L. Choubrac, S. Siebentritt, The optical diode ideality factor enables fast screening of semiconductors for solar cells, Sol. RRL, 2 (2018) 1800248.
[93] T. Kirchartz, F. Deledalle, P.S. Tuladhar, J.R. Durrant, J. Nelson, On the differences between dark and light ideality factor in polymer: fullerene solar cells, J. Phys. Chem. Lett., 4 (2013) 2371-2376.
[94] S. Lany, A. Zunger, Light-and bias-induced metastabilities in Cu(In, Ga)Se_2 based solar cells caused by the (V_{Se}-V_{Cu}) vacancy complex, J. Appl. Phys., 100 (2006) 113725.
[95] K. Macielak, M. Maciaszek, M. Igalson, P. Zabierowski, N. Barreau, Persistent Photoconductivity in Polycrystalline Cu(In, Ga)Se_2 Thin Films: Experiment Versus Theoretical Predictions, IEEE Journal of Photovoltaics, 5 (2015) 1206-1211.

[96] U. Rau, K. Weinert, Q. Nguyen, M. Mamor, G. Hanna, A. Jasenek, H. Schock, Device analysis of Cu(In, Ga)Se_2 heterojunction solar cells-some open questions, MRS Online Proceedings Library, 668 (2001) H9. 1.

[97] S. Lany, A. Zunger, Metal-dimer atomic reconstruction leading to deep donor states of the anion vacancy in II-VI and chalcopyrite semiconductors, Phys. Rev. Lett., 93 (2004) 156404.

[98] S.-H. Wei, S. Zhang, Defect properties of $CuInSe_2$ and $CuGaSe_2$, Journal of Physics Chemistry of solids, 66 (2005) 1994-1999.

[99] S. Zhang, S.-H. Wei, A. Zunger, Katayama-Yoshida, Defect physics of the $CuInSe_2$ chalcopyrite semiconductor, Physical Review B, 57 (1998) 9642.

[100] J. Pohl, K. Albe, Intrinsic point defects in $CuInSe_2$ and $CuGaSe_2$ as seen via screened-exchange hybrid density functional theory, Physical Review B, 87 (2013) 245203.

[101] T.P. Weiss, B. Bissig, T. Feurer, R. Carron, S. Buecheler, A.N. Tiwari, Bulk and surface recombination properties in thin film semiconductors with different surface treatments from time-resolved photoluminescence measurements, Sci. Rep., 9 (2019) 1-13.

[102] M. Burgelman, P. Nollet, S. Degrave, Modelling polycrystalline semiconductor solar cells, Thin Solid Films, 361 (2000) 527-532.

[103] K.L. Luke, L.J. Cheng, Analysis of the interaction of a laser pulse with a silicon wafer: Determination of bulk lifetime and surface recombination velocity, J. Appl. Phys., 61 (1987) 2282-2293.

[104] T. Otaredian, Separate contactless measurement of the bulk lifetime and the surface recombination velocity by the harmonic optical generation of the excess carriers, Solid·State Electron., 36 (1993) 153-162.

[105] F. Werner, D. Colombara, M. Melchiorre, N. Valle, B. El Adib, C. Spindler, S. Siebentritt, Doping mechanism in pure $CuInSe_2$, J. Appl. Phys., 119 (2016) 173103.

[106] A. Sproul, Dimensionless solution of the equation describing the effect of surface recombination on carrier decay in semiconductors, J. Appl. Phys., 76 (1994) 2851-2854.

[107] E. Jarzembowski, F. Syrowatka, K. Kaufmann, W. Fränzel, T. Hölscher, R. Scheer, The influence of sodium on the molybdenum/Cu(In, Ga)Se_2 interface recombination velocity, determined by time resolved photoluminescence, Appl. Phys. Lett., 107 (2015) 051601.

[108] M. Nichterwitz, T. Unold, Numerical simulation of cross section electron-beam induced current in thin-film solar-cells for low and high injection conditions, J. Appl. Phys., 114 (2013) 134504.
[109] J. Van Delft, D. Garcia-Alonso, W. Kessels, Atomic layer deposition for photovoltaics: applications and prospects for solar cell manufacturing, Semicond. Sci. Technol., 27 (2012) 074002.
[110] T. Dullweber, J. Schmidt, Industrial silicon solar cells applying the passivated emitter and rear cell (PERC) concept—A review, IEEE journal of photovoltaics, 6 (2016) 1366-1381.
[111] L. Guo, S. Vijayaraghavan, X. Duan, H.G. Menon, J. Wall, L. Kong, S. Gupta, L. Li, F. Yan, Stable and efficient Sb_2Se_3 solar cells with solution-processed NiO_x hole-transport layer, Solar Energy, 218 (2021) 525-531.
[112] D. Xiao, X. Li, D. Wang, Q. Li, K. Shen, D. Wang, CdTe thin film solar cell with NiO as a back contact buffer layer, Sol. Energy Mater. Sol. Cells, 169 (2017) 61-67.
[113] Y. Cao, X. Zhu, H. Chen, X. Zhang, J. Zhouc, Z. Hu, J. Pang, Towards high efficiency inverted Sb_2Se_3 thin film solar cells, Sol. Energy Mater. Sol. Cells, 200 (2019) 109945.
[114] Y. Qin, J. Song, Q. Qiu, Y. Liu, Y. Zhao, L. Zhu, Y. Qiang, High-quality NiO thin film by low-temperature spray combustion method for perovskite solar cells, Journal of Alloys Compounds, 810 (2019) 151970.
[115] L. Xu, X. Chen, J. Jin, W. Liu, B. Dong, X. Bai, H. Song, P. Reiss, Inverted perovskite solar cells employing doped NiO hole transport layers: A review, Nano Energy, 63 (2019) 103860.
[116] R. Singh, P.K. Singh, B. Bhattacharya, H.-W. Rhee, Review of current progress in inorganic hole-transport materials for perovskite solar cells, Applied Materials Today, 14 (2019) 175-200.
[117] J. T ü rck, H.J. Nonnenmacher, P.M. Connor, S. Siol, B. Siepchen, J.P. Heimfarth, A. Klein, W. Jaegermann, Copper (I) Oxide (Cu_2O) based back contact for p ‐ i ‐ n CdTe solar cells, Prog. Photovolt: Res. Appl., 24 (2016) 1229-1236.
[118] J. Wang, T.B. Daunis, L. Cheng, B. Zhang, J. Kim, J.W. Hsu, Combustion Synthesis of p-Type Transparent Conducting $CuCrO_{2+x}$ and Cu:CrO_x Thin Films at 180° C, ACS Appl. Mater. Interfaces, 10 (2018) 3732-3738.
[119] Z.-K. Yu, W.-F. Fu, W.-Q. Liu, Z.-Q. Zhang, Y.-J. Liu, J.-L. Yan, T. Ye, W.-T. Yang, H.-Y. Li, H.-Z. Chen, Solution-processed CuO_x as an efficient hole-extraction layer for inverted planar heterojunction perovskite solar cells, Chin. Chem. Lett., 28 (2017) 13-18.

[120] M.I. Hossain, F.H. Alharbi, N. Tabet, Copper oxide as inorganic hole transport material for lead halide perovskite based solar cells, Solar Energy, 120 (2015) 370-380.
[121] W. Shen, C. Yang, X. Bao, L. Sun, N. Wang, J. Tang, W. Chen, R. Yang, Simple solution-processed CuO_x as anode buffer layer for efficient organic solar cells, Materials Science Engineering: B, 200 (2015) 1-8.
[122] Z. He, Y. Liu, S. Lin, S. Shi, S. Sun, J. Pang, Z. Zhou, Y. Sun, W. Liu, Energy band alignment in molybdenum Oxide/Cu(In, Ga)Se_2 interface for high-efficiency ultrathin Cu(In, Ga)Se_2 solar cells from low-temperature growth, ACS Applied Energy Materials, 3 (2020) 3408-3414.
[123] M. Heinemann, J. Berry, G. Teeter, T. Unold, D. Ginley, Oxygen deficiency and Sn doping of amorphous Ga_2O_3, Appl. Phys. Lett., 108 (2016) 022107.
[124] M. Saifullah, K. Kim, R. Shahzad, J. Gwak, J.-S. Cho, J.-S. Yoo, J.H. Yun, J.H.J.S.E.M. Park, S. Cells, Insertion of the AGS layer at the CIGSe/ITO interface: A way to reduce the formation of the GaO_x interfacial phase in CIGSe solar cells, Sol. Energy Mater. Sol. Cells, 178 (2018) 29-37.
[125] W. Witte, S. Paetel, R. Menner, A. Bauer, D. Hariskos, The application of sputtered gallium oxide as buffer for Cu(In, Ga)Se_2 solar cells, physica status solidi –Rapid Research Letters, 15 (2021) 2100180.
[126] F. Pianezzi, S. Nishiwaki, L. Kranz, C.M. Sutter‐Fella, P. Reinhard, B. Bissig, H. Hagendorfer, S. Buecheler, A.N. Tiwari, Influence of Ni and Cr impurities on the electronic properties of Cu(In, Ga)Se_2 thin film solar cells, Prog. Photovolt: Res. Appl., 23 (2015) 892-900.
[127] K. Decock, P. Zabierowski, M. Burgelman, Modeling metastabilities in chalcopyrite-based thin film solar cells, J. Appl. Phys., 111 (2012) 043703.
[128] K. Decock, S. Khelifi, M. Burgelman, Modelling multivalent defects in thin film solar cells, Thin Solid Films, 519 (2011) 7481-7484.
[129] J.H. Werner, J. Mattheis, U. Rau, Efficiency limitations of polycrystalline thin film solar cells: case of Cu(In, Ga)Se_2, Thin Solid Films, 480 (2005) 399-409.
[130] M. Gloeckler, A. Fahrenbruch, J. Sites, Numerical modeling of CIGS and CdTe solar cells: setting the baseline, in: 3rd World Conference onPhotovoltaic Energy Conversion, 2003. Proceedings of, IEEE, 2003, pp. 491-494.

[131] T. Wang, F. Ehre, T.P. Weiss, B. Veith‐Wolf, V. Titova, N. Valle, M. Melchiorre, O. Ramírez, J. Schmidt, S. Siebentritt, Diode Factor in Solar Cells with Metastable Defects and Back Contact Recombination, Adv. Energy. Mater., (2022) 2202076.
[132] M. Nichterwitz, D. Abou-Ras, K. Sakurai, J. Bundesmann, T. Unold, R. Scheer, H. Schock, Influence of grain boundaries on current collection in Cu(In, Ga)Se_2 thin-film solar cells, Thin Solid Films, 517 (2009) 2554-2557.
[133] J. Kavalakkatt, D. Abou-Ras, J. Haarstrich, C. Ronning, M. Nichterwitz, R. Caballero, T. Rissom, T. Unold, R. Scheer, H.W. Schock, Electron-beam-induced current at absorber back surfaces of Cu(In, Ga)Se_2 thin-film solar cells, J. Appl. Phys., 115 (2014) 014504.
[134] S. Shirakata, T. Nakada, Time-resolved photoluminescence in Cu(In, Ga)Se_2 thin films and solar cells, Thin Solid Films, 515 (2007) 6151-6154.
[135] I. Khatri, H. Fukai, H. Yamaguchi, M. Sugiyama, T. Nakada, Effect of potassium fluoride post-deposition treatment on Cu(In, Ga)Se_2 thin films and solar cells fabricated onto sodalime glass substrates, Sol. Energy Mater. Sol. Cells, 155 (2016) 280-287.
[136] T.P. Weiss, R. Carron, M.H. Wolter, J. Löckinger, E. Avancini, S. Siebentritt, S. Buecheler, A.N. Tiwari, Time-resolved photoluminescence on double graded Cu (In, Ga) Se_2–Impact of front surface recombination and its temperature dependence, STAM, 20 (2019) 313-323.
[137] W. Metzger, I. Repins, M. Romero, P. Dippo, M. Contreras, R. Noufi, D. Levi, Recombination kinetics and stability in polycrystalline Cu(In, Ga)Se_2 solar cells, Thin Solid Films, 517 (2009) 2360-2364.
[138] W.K. Metzger, I.L. Repins, M.A. Contreras, Long lifetimes in high-efficiency Cu(In, Ga)Se_2 solar cells, Appl. Phys. Lett., 93 (2008) 022110.
[139] L. Gütay, D. Regesch, J.K. Larsen, Y. Aida, V. Depredurand, A. Redinger, S. Caneva, S. Schorr, C. Stephan, J. Vidal, Feedback mechanism for the stability of the band gap of $CuInSe_2$, Physical Review B, 86 (2012) 045216.
[140] Y. Sun, S. Lin, W. Li, S. Cheng, Y. Zhang, Y. Liu, W. Liu, Review on alkali element doping in Cu(In, Ga)Se_2 thin films and solar cells, Engineering, 3 (2017) 452-459.
[141] L. Zhang, Q. He, W.-L. Jiang, F.-F. Liu, C.-J. Li, Y. Sun, Effects of substrate temperature on the structural and electrical properties of Cu(In, Ga)Se_2 thin films, Sol. Energy Mater. Sol. Cells, 93 (2009) 114-118.

[142] M. Sood, A. Urbaniak, C. Kameni Boumenou, T.P. Weiss, H. Elanzeery, F. Babbe, F. Werner, M. Melchiorre, S. Siebentritt, Near surface defects: Cause of deficit between internal and external open‐circuit voltage in solar cells, Progress in Photovoltaics: Research Applications, 30 (2022) 263-275.

[143] P.M. Salome, B. Vermang, R. Ribeiro‐Andrade, J.P. Teixeira, J.M. Cunha, M.J. Mendes, S. Haque, J. Borme, H. Águas, E. Fortunato, Passivation of interfaces in thin film solar cells: Understanding the effects of a nanostructured rear point contact layer, Adv. Mater. Interfaces, 5 (2018) 1701101.

[144] F. Werner, B. Veith-Wolf, C. Spindler, M.R. Barget, F. Babbe, J. Guillot, J. Schmidt, S. Siebentritt, Oxidation as key mechanism for efficient interface passivation in Cu(In, Ga)Se_2 thin-film solar cells, Phys. Rev. Appl., 13 (2020) 054004.

[145] D.G. Buldu, J. de Wild, T. Kohl, G. Brammertz, G. Birant, M. Meuris, J. Poortmans, B. Vermang, Study of Ammonium Sulfide Surface Treatment for Ultrathin Cu(In, Ga)Se_2 with Different Cu/(Ga+ In) Ratios, Phys. Status Solidi, 217 (2020) 2000307.

[146] A. Gerhard, W. Harneit, S. Brehme, A. Bauknecht, U. Fiedeler, M.C. Lux-Steiner, S. Siebentritt, Acceptor activation energies in epitaxial $CuGaSe_2$ grown by MOVPE, Thin Solid Films, 387 (2001) 67-70.

[147] S. Siebentritt, L. Gütay, D. Regesch, Y. Aida, V. Deprédurand, Why do we make Cu(In, Ga)Se_2 solar cells non-stoichiometric?, Sol. Energy Mater. Sol. Cells, 119 (2013) 18-25.

[148] C. Stephan, S. Schorr, M. Tovar, H.-W. Schock, Comprehensive insights into point defect and defect cluster formation in $CuInSe_2$, Appl. Phys. Lett., 98 (2011) 091906.

[149] A. Jeong, J.M. Choi, H.J. Lee, G.Y. Kim, J.K. Park, W.M. Kim, S. Kuk, Z. Wang, D.J. Hwang, H. Yu, Transparent back‐junction control in Cu(In,Ga)Se_2 absorber for high‐efficiency, color‐neutral, and semitransparent solar module, Prog. Photovolt: Res. Appl., 30 (2022) 713-725.

[150] J. Keller, L. Stolt, O. Donzel-Gargand, T. Kubart, M. Edoff, Wide‐Gap Chalcopyrite Solar Cells with Indium Oxide‐Based Transparent Back Contacts, Sol. RRL, 6 (2022) 2200401.

[151] J. Keller, W.C. Chen, L. Riekehr, T. Kubart, T. Törndahl, M. Edoff, Bifacial Cu (In, Ga) Se2 solar cells using hydrogen‐doped In_2O_3 films as a transparent back contact, Progress in Photovoltaics: Research Applications, 26 (2018) 846-858.

[152] Y.-S. Son, H. Yu, J.-K. Park, W.M. Kim, S.-Y. Ahn, W. Choi, D. Kim, J.-h. Jeong, Control of structural and electrical properties of indium tin oxide (ITO)/Cu(In,Ga)Se_2 interface for transparent back-contact applications, The Journal of Physical Chemistry C, 123 (2019) 1635-1644.

[153] M.D. Heinemann, V. Efimova, R. Klenk, B. Hoepfner, M. Wollgarten, T. Unold, H.W. Schock, C.A. Kaufmann, Cu(In,Ga)Se_2 superstrate solar cells: prospects and limitations, Prog. Photovolt: Res. Appl., 23 (2015) 1228-1237.

[154] T. Nakada, Y. Hirabayashi, T. Tokado, D. Ohmori, T. Mise, Novel device structure for Cu(In,Ga)Se_2 thin film solar cells using transparent conducting oxide back and front contacts, Solar energy, 77 (2004) 739-747.

[155] S. Siebentritt, L. Gütay, D. Regesch, Y. Aida, V. Deprédurand, Why do we make Cu(In, Ga)Se_2 solar cells non-stoichiometric?, Solar Energy Materials Solar Cells, 119 (2013) 18-25.

[156] E.A. Cochran, D.-H. Park, M.G. Kast, L.J. Enman, C.K. Perkins, R.H. Mansergh, D.A. Keszler, D.W. Johnson, S.W. Boettcher, Role of combustion chemistry in low-temperature deposition of metal oxide thin films from solution, Chem. Mater., 29 (2017) 9480-9488.

[157] M.-G. Kim, M.G. Kanatzidis, A. Facchetti, T.J. Marks, Low-temperature fabrication of high-performance metal oxide thin-film electronics via combustion processing, Nature materials, 10 (2011) 382-388.

[158] A. Varma, A.S. Mukasyan, A.S. Rogachev, K.V. Manukyan, Solution combustion synthesis of nanoscale materials, Chem. Rev., 116 (2016) 14493-14586.

[159] L. Krückemeier, U. Rau, M. Stolterfoht, T. Kirchartz, How to report record open‐circuit voltages in lead‐halide perovskite solar cells, Adv. Energy. Mater., 10 (2020) 1902573.

[160] P.T. Erslev, J.W. Lee, W.N. Shafarman, J.D. Cohen, The influence of Na on metastable defect kinetics in CIGS materials, Thin Solid Films, 517 (2009) 2277-2281.

[161] T. Wada, N. Kohara, S. Nishiwaki, T. Negami, Characterization of the Cu(In,Ga)Se_2/Mo interface in CIGS solar cells, Thin Solid Films, 387 (2001) 118-122.

[162] S.-T. Kim, V. Bhatt, Y.-C. Kim, H.-J. Jeong, J.-H. Yun, J.-H. Jang, Formation of $MoSe_2$ layer and Ga grading in flexible Cu(In,Ga)Se_2 solar cell via Na diffusion, Journal of Alloys Compounds, 899 (2022) 163301.

[163] Y.-I. Kim, K.-B. Kim, M. Kim, Characterization of lattice parameters gradient of $Cu(In_{1-x}Ga_x)Se_2$ absorbing layer in thin-film solar cell by glancing incidence X-ray diffraction technique, Journal of Materials Science Technology, 51 (2020) 193-201.
[164] J. Guillemoles, Stability of $Cu(In,Ga)Se_2$ solar cells: a thermodynamic approach, Thin Solid Films, 361 (2000) 338-345.
[165] D. Cahen, R. Noufi, Free energies and enthalpies of possible gas phase and surface reactions for preparation of $CuInSe_2$, Journal of Physics Chemistry of Solids, 53 (1992) 991-1005.
[166] A.K. Mondal, R. Deivasigamani, L.K. Ping, M.A. Shazni Mohammad Haniff, B.T. Goh, R.H. Horng, M.A. Mohamed, Heteroepitaxial Growth of an Ultrathin β-Ga_2O_3 Film on a Sapphire Substrate Using Mist CVD with Fluid Flow Modeling, ACS omega, 7 (2022) 41236-41245.
[167] K. Kikuchi, S. Imura, K. Miyakawa, H. Ohtake, M. Kubota, Properties of Ga_2O_3/Ga_2O_3: Sn/CIGS for visible light sensors, in: Journal of Physics: Conference Series, IOP Publishing, 2015, pp. 012009.
[168] H. Xue, Q. He, G. Jian, S. Long, T. Pang, M. Liu, An overview of the ultrawide bandgap Ga_2O_3 semiconductor-based Schottky barrier diode for power electronics application, Nanoscale research letters, 13 (2018) 1-13.
[169] K. Kikuchi, S. Imura, K. Miyakawa, M. Kubota, E. Ohta, Electrical and optical properties of Ga_2O_3/$CuGaSe_2$ heterojunction photoconductors, Thin Solid Films, 550 (2014) 635-637.
[170] T. Nakada, Microstructural and diffusion properties of CIGS thin film solar cells fabricated using transparent conducting oxide back contacts, Thin Solid Films, 480 (2005) 419-425.
[171] S.-C. Yang, T.-Y. Lin, M. Ochoa, H. Lai, R. Kothandaraman, F. Fu, A.N. Tiwari, R. Carron, Efficiency boost of bifacial $Cu(In,Ga)Se_2$ thin-film solar cells for flexible and tandem applications with silver-assisted low-temperature process, Nature Energy, 8 (2023) 40-51.
[172] T. Hölscher, M. Placidi, I. Becerril-Romero, R. Fonoll-Rubio, V. Izquierdo-Roca, A. Thomere, E. Bailo, T. Schneider, H. Kempa, R. Scheer, Effects of ITO based back contacts on $Cu(In,Ga)Se_2$ thin films, solar cells, and mini-modules relevant for semi-transparent building integrated photovoltaics, Sol. Energy Mater. Sol. Cells, 251 (2023) 112169.
[173] J. Keller, N. Shariati Nilsson, A. Aijaz, L. Riekehr, T. Kubart, M. Edoff, T. Törndahl, Using hydrogen‐doped In_2O_3 films as a transparent back contact in $(Ag,Cu)(In,Ga)Se_2$ solar cells, Prog. Photovolt: Res. Appl., 26 (2018) 159-170.

[174] H. Yan, Y. Guo, Q. Song, Y. Chen, First-principles study on electronic structure and optical properties of Cu-doped β-Ga_2O_3, Physica B: Condensed Matter, 434 (2014) 181-184.
[175] C. Zhang, Z. Li, W. Wang, Critical Thermodynamic Conditions for the Formation of p-Type β-Ga_2O_3 with Cu Doping, Materials, 14 (2021) 5161.
[176] J. Zhang, S. Zhu, C. Gao, C. Gao, X. Liu, Low Temperature Producing Copper‐Doped Gallium Oxide as Hole Transport Layers of Perovskite Solar Cells Enhanced by Impurity Levels, Sol. RRL, 6 (2022) 2100861.
[177] Y. Zhang, J. Yan, Q. Li, C. Qu, L. Zhang, W. Xie, Optical and structural properties of Cu-doped β-Ga_2O_3 films, Materials Science Engineering: B, 176 (2011) 846-849.
[178] T. Gustafson, N. Giles, B. Holloway, C. Lenyk, J. Jesenovec, J. McCloy, M. McCluskey, L. Halliburton, Cu^{2+} and Cu^{3+} acceptors in β-Ga_2O_3 crystals: A magnetic resonance and optical absorption study, J. Appl. Phys., 131 (2022) 065702.
[179] J. Zhang, S. Zhu, Q. Yang, C. Gao, X. Liu, Copper Doped $In_xGa_{2-x}O_3$ Nanocrystals as Efficient Hole Transport Materials of Perovskite Solar Cells by Regulating Energy Levels, Sol. RRL.
[180] Y. Liu, Y. Sun, W. Liu, J. Yao, Novel high-efficiency crystalline-silicon-based compound heterojunction solar cells: HCT (heterojunction with compound thin-layer), PCCP, 16 (2014) 15400-15410.
[181] L.M. Mansfield, A. Kanevce, S.P. Harvey, K. Bowers, C. Beall, S. Glynn, I.L. Repins, Efficiency increased to 15.2% for ultra‐thin Cu(In, Ga)Se_2 solar cells, Prog. Photovolt: Res. Appl., 26 (2018) 949-954.
[182] B. Vermang, J.T. Wätjen, V. Fjällström, F. Rostvall, M. Edoff, R. Gunnarsson, I. Pilch, U. Helmersson, R. Kotipalli, F. Henry, Highly reflective rear surface passivation design for ultra-thin Cu(In, Ga)Se_2 solar cells, Thin Solid Films, 582 (2015) 300-303.
[183] T. Schneider, J. Tröndle, B. Fuhrmann, F. Syrowatka, A. Sprafke, R. Scheer, Ultrathin CIGSe solar cells with integrated structured back reflector, Sol. RRL, 4 (2020) 2000295.
[184] S. Yang, J. Zhu, X. Zhang, X. Ma, H. Luo, L. Yin, X.J.P.i.P.R. Xiao, Applications, Bandgap optimization of submicron‐thick Cu(In, Ga)Se_2 solar cells, Prog. Photovolt: Res. Appl., 23 (2015) 1157-1163.

[185] A. Laemmle, R. Wuerz, M. Powalla, Efficiency enhancement of Cu(In,Ga)Se_2 thin‐film solar cells by a post‐deposition treatment with potassium fluoride, physica status solidi ‐ Rapid Research Letters, 7 (2013) 631-634.
[186] J. Eid, H. Liang, I. Gereige, S. Lee, J.V. Duren, Combinatorial study of NaF addition in CIGSe films for high efficiency solar cells, Prog. Photovolt: Res. Appl., 23 (2015) 269-280.
[187] I. Khatri, H. Fukai, H. Yamaguchi, M. Sugiyama, T.J.S.E.M. Nakada, S. Cells, Effect of potassium fluoride post-deposition treatment on Cu(In,Ga)Se_2 thin films and solar cells fabricated onto sodalime glass substrates, Sol. Energy Mater. Sol. Cells, 155 (2016) 280-287.
[188] A. Stephens, A. Aberle, M. Green, Surface recombination velocity measurements at the silicon-silicon dioxide interface by microwave‐detected photoconductance decay, J. Appl. Phys., 76 (1994) 363-370.
[189] A. Chirilă, S. Buecheler, F. Pianezzi, P. Bloesch, C. Gretener, A.R. Uhl, C. Fella, L. Kranz, J. Perrenoud, S. Seyrling, Highly efficient Cu (In, Ga)Se_2 solar cells grown on flexible polymer films, Nature materials, 10 (2011) 857-861.
[190] A.G. Aberle, T. Lauinger, J. Schmidt, R. Hezel, Injection‐level dependent surface recombination velocities at the silicon‐plasma silicon nitride interface, Appl. Phys. Lett., 66 (1995) 2828-2830.
[191] T. Kirchartz, U. Rau, What makes a good solar cell?, Adv. Energy. Mater., 8 (2018) 1703385.
[192] T. Kirchartz, U. Rau, Electroluminescence analysis of high efficiency Cu(In,Ga)Se_2 solar cells, J. Appl. Phys., 102 (2007) 104510.
[193] P. Jackson, R. Wuerz, D. Hariskos, E. Lotter, W. Witte, M. Powalla, Effects of heavy alkali elements in Cu(In, Ga)Se_2 solar cells with efficiencies up to 22.6%, physica status solidi –Rapid Research Letters, 10 (2016) 583-586.
[194] Y.H. Chang, R. Carron, M. Ochoa, A.N. Tiwari, J.R. Durrant, L. Steier, Impact of RbF and NaF Postdeposition Treatments on Charge Carrier Transport and Recombination in Ga‐Graded Cu(In,Ga)Se_2 Solar Cells, Adv. Funct. Mater., 31 (2021) 2103663.
[195] U. Rau, J. Werner, Radiative efficiency limits of solar cells with lateral band-gap fluctuations, Appl. Phys. Lett., 84 (2004) 3735-3737.
[196] O. Ramírez, J. Nishinaga, F. Dingwell, T. Wang, A. Prot, M. Hilaire Wolter, V. Ranjan, S. Siebentritt, On the origin of tail states and V_{OC} losses in Cu (In,Ga)Se_2, Sol. RRL, (2022).

[197] A.M. Bothwell, J. Wands, M.F. Miller, A. Kanevce, S. Paetel, P. Tsoulka, T. Lepetit, N. Barreau, N. Valdes, W. Shafarman, Non‐Radiative Recombination Dominates Voltage Losses in Cu(In,Ga)Se_2 Solar Cells Fabricated Using Different Methods, Sol. RRL, (2023).

[198] R. Carron, S. Nishiwaki, T. Feurer, R. Hertwig, E. Avancini, J. Löckinger, S.C. Yang, S. Buecheler, A.N. Tiwari, Advanced alkali treatments for high‐efficiency Cu(In,Ga)Se_2 solar cells on flexible substrates, Adv. Energy. Mater., 9 (2019) 1900408.

[199] M.H. Wolter, R. Carron, E. Avancini, B. Bissig, T.P. Weiss, S. Nishiwaki, T. Feurer, S. Buecheler, P. Jackson, W. Witte, How band tail recombination influences the open‐circuit voltage of solar cells, Prog. Photovolt: Res. Appl., 30 (2022) 702-712.

[200] T. Feurer, R. Carron, G. Torres Sevilla, F. Fu, S. Pisoni, Y.E. Romanyuk, S. Buecheler, A.N. Tiwari, Efficiency improvement of near‐stoichiometric $CuInSe_2$ solar cells for application in tandem devices, Adv. Energy. Mater., 9 (2019) 1901428.

[201] S. Suckow, T.M. Pletzer, H. Kurz, Fast and reliable calculation of the two‐diode model without simplifications, Prog. Photovolt: Res. Appl., 22 (2014) 494-501.

[202] Marc Burgelman, Koen Decock, Alex Niemegeers, Johan Verschraegen, S. Degrave, SCAPS manual (2020) 20-21.

[203] Z. Sárosi, W. Knapp, A. Kunz, K. Wegener, Evaluation of reflectivity of metal parts by a thermo-camera, InfraMation proceedings, (2010) 475-486.

[204] L. Gouillart, A. Cattoni, W.C. Chen, J. Goffard, L. Riekehr, J. Keller, M. Jubault, N. Naghavi, M. Edoff, S. Collin, Interface engineering of ultrathin Cu(In,Ga)Se_2 solar cells on reflective back contacts, Prog. Photovolt: Res. Appl., 29 (2021) 212-221.

[205] O. Poncelet, R. Kotipalli, B. Vermang, A. Macleod, L.A. Francis, D. Flandre, Optimisation of rear reflectance in ultra-thin CIGS solar cells towards>20% efficiency, Solar Energy, 146 (2017) 443-452.

[206] K. Wang, Y. Tian, H. Jiang, M. Chen, S. Xu, Surface Treatment on Nickel Oxide to Enhance the Efficiency of Inverted Perovskite Solar Cells, International Journal of Photoenergy, 2019 (2019) 1-7.

[207] M. Imran, H. Coskun, N.A. Khan, J. Ouyang, Role of annealing temperature of nickel oxide (NiO_x) as hole transport layer in work function alignment with perovskite, Appl. Phys. A, 127 (2021) 1-8.

[208] T. Liu, K. Chen, Q. Hu, R. Zhu, Q. Gong, Inverted perovskite solar cells: progresses and perspectives, Adv. Energy. Mater., 6 (2016) 1600457.
[209] J. Castillo-Saenz, N. Nedev, B. Valdez-Salas, M. Bernechea, E. Martínez-Guerra, I. Mendivil-Palma, M. Curiel-Alvarez, D. Mateos, O. Perez-Landeros, Effect of oxidation temperature on the properties of NiO_x layers for application in optical sensors, Thin Solid Films, 734 (2021) 138849.
[210] D. Pokhrel, X. Mathew, K. Khanal Subedi, A. Patel, A.B. Phillips, E. Bastola, A. Abudulimu, M.K. Jamarkattel, S. Rijal, A. Quader, Bifacial CdTe Solar Cells with Copper Chromium Oxide Back‐Buffer Layer, Sol. RRL, 6 (2022) 2200501.
[211] H. Rao, S. Ye, W. Sun, W. Yan, Y. Li, H. Peng, Z. Liu, Z. Bian, Y. Li, C. Huang, A 19.0% efficiency achieved in CuO_x-based inverted $CH_3NH_3PbI_{3-x}Cl_x$ solar cells by an effective Cl doping method, Nano Energy, 27 (2016) 51-57.
[212] D. Wang, R. Yang, L. Wu, K. Shen, D. Wang, Band alignment of CdTe with MoO_x oxide and fabrication of high efficiency CdTe solar cells, Solar Energy, 162 (2018) 637-645.
[213] H. Lin, W. Xia, H.N. Wu, Y. Gao, C.W. Tang, MoO_x back contact for CdS/CdTe thin film solar cells: Preparation, device characteristics, and stability, Sol. Energy Mater. Sol. Cells, 99 (2012) 349-355.
[214] M.T.S.K.A. Sen, P. Bronsveld, A. Weeber, Thermally stable MoO_x hole selective contact with Al_2O_3 interlayer for industrial size silicon solar cells, Sol. Energy Mater. Sol. Cells, 230 (2021) 111139.
[215] J. Bullock, A. Cuevas, T. Allen, C. Battaglia, Molybdenum oxide MoO_x: A versatile hole contact for silicon solar cells, Appl. Phys. Lett., 105 (2014) 232109.
[216] J. Dréon, Q. Jeangros, J. Cattin, J. Haschke, L. Antognini, C. Ballif, M. Boccard, 23.5%-efficient silicon heterojunction silicon solar cell using molybdenum oxide as hole-selective contact, Nano Energy, 70 (2020) 104495.